

A close-up, low-angle photograph of a turbine blade assembly. The blades are arranged in a circular pattern, radiating from a central hub. The lighting is dramatic, highlighting the metallic surfaces and the intricate details of the blades. The background is dark, making the blades stand out.

Impact of turbine performance on the operating conditions of a 10 MW OTEC plant

Master Thesis

Pieter André van Strijp

Delft University of Technology

Impact of turbine performance on the operating conditions of a 10 MW OTEC plant

Master Thesis

by

Pieter André van Strijp

in partial fulfillment of the requirements for the degree of

Master of Science
in Mechanical Engineering

at the Delft University of Technology.
to be defended publicly on Friday October 26, 2018 at 11:00 AM

Student number: 4151186

Thesis committee:	Dr.ir. C. A. Infante Ferreira,	TU Delft, supervisor
	Prof. dr. ir. T.J.H. Vlugt,	TU Delft
	Dr. ir. H. Polinder,	TU Delft
	Ir. J.A. Kirkenier,	Bluerise, supervisor

*This thesis is confidential and cannot be made public until October 26, 2023.
Op dit verslag is geheimhouding van toepassing tot en met 26 October 2023.*

An electronic version of this thesis is available at <http://repository.tudelft.nl/>.



Abstract

One of the world greatest priorities is to move to a sustainable world, while the global energy demand is growing. Ocean Thermal Energy Conversion (OTEC) is a base-load renewable electricity technology that has the potential to contribute to a sustainable power supply on a world-wide scale. OTEC creates sustainable power utilizing the temperature difference in different depths in the ocean. The relative small temperature difference between the heat source (upper layer of the ocean) and cold sink (lower layer of the ocean) is the power resource. To obtain cost effective electricity from this small temperature difference is one of the major challenges of this technology. In order to determine an optimum power plant under specific environmental conditions, a techno-economic optimization model is developed, where the geometries of the components is input in the off-design model. The off-design model determines the operating conditions of the OTEC cycle with respect both the working fluid, the geometry of the components and the mass flows of the system. Nowadays, a simulation model predicts the steady state point of a test set-up at the TU Delft, despite of a lack of knowledge in the off-design performance of the OTEC cycle. Especially in the off-design performance of the turbine. To investigate the influence of the turbine performance on a 10 MW OTEC power plant, the off-design model is now equipped with an axial turbine and applicable for larger scales. As a result, the model determines the pressure drop over the turbine and the performance of the turbine. The model uses the currently best correlations for the heat transfer and the pressure drop prediction of the components to predict the influence of the off-design turbine performance on the overall performance of the system. Ultimately, the cost per produced kW as optimization criterion is calculated and compared for the different power plants during warm seawater temperature fluctuations over a year or seawater mass flow fluctuations. As a final conclusion, the influence of the turbine is calculated to the overall power performance. The results of varying the warm seawater temperature results in a specific power curve, which shows proportional behavior to the temperature difference. The turbine influences the pressure drop in the system and therefore it is recommended to optimize the position of the vanes, especially when the vapor flow is higher than its design value. Ultimately, the different power curves are derived for every specific power plant. Within the relatively small range of temperature differences, the non-linear effect of the off-design performance of the turbine is too small. This leads to the conclusion, the seasonal fluctuation of sea water temperature difference have a significant impact on the net power production, while the performance of the turbine is rather constant. Variations in seawater mass flows show non-linear characteristics. The turbine performance influences the cycle performance, especially if the seawater mass flows drop significantly. This results that the cycle efficiency drops non-linearly downwards as the mass flows decrease. Finally, the turbine performance remains constant during off-design conditions. Therefore, the accessibility of a thermal energy from the ocean is one step closer. This is an important step in creating a renewable energy powered world.

Acknowledgements

I would first like to thank my thesis supervisor Ir. Carlos Infante Ferreira from the Delft University of Technology. The various conversations with him gave me a lot of useful help in my thesis and he gave the necessary feedback for my report. Furthermore, I would like to thank Joost Kirkenier from Bluerise B.V. for his guidance. He was always helpful when I needed more technological knowledge. Next to this, he had taken me into the development of the company itself, which was very interesting. Apart from my daily supervisors, I would like to thank Bram Harmsen from Bluerise B.V. The major part of my thesis was programming the on-design and off-design model and he helped me with his programming skills to solve my software issues in the Python model. Furthermore, I would also like to thank all Bluerise colleagues, for my entire time at Bluerise, where it was interesting with the many discussions we had.

Pieter van Strijp
Delft, October 2018

Nomenclature

Roman symbols

\hat{a}	Amplitude	(m)
A	Heat transfer area	(m^2)
A_0	Plate area	(m^2)
A_f	Cross-sectional area	(m^2)
A_{hex}	total heat transfer area	(m^2)
A_p	Effective heat transfer area	(m^2)
c	Concentration	(-)
c_p	Specific heat capacity at constant pressure	($\frac{J}{kgK}$)
c_v	Specific heat capacity at constant volume	($\frac{J}{kgK}$)
C	Cost	(€)
d	Diameter	(m)
d_g	Channel gap	(m)
d_p	Plate thickness	(m)
d_s	Specific diameter	(-)
D	Mass diffusivity	($\frac{m^2}{s}$)
E_{HEX}	Effectiveness	(-)
E	Energy flow	($\frac{J}{s}$)
f	Fanning friction factor	(-)
f_{wet}	Wetted area factor	(-)
f_{VTG}	Multiplier of the Stodola Constant	(-)
F_{CU}	Fraction copper losses	(-)
g	Gravitational acceleration	($\frac{m}{s^2}$)
\dot{G}	Mass flow rate per cross-sectional area	($\frac{kg}{m^2s}$)
i	Control volume number	(-)
h	Enthalpy	($\frac{J}{kg}$) \rightarrow ($\frac{m^2}{s^2}$)
K	Resistance factor	(-)
L	Characteristic length	(m)
L_p	Port-to-port length	(m)
m	Mass	(kg)
\dot{m}	Mass flow rate	($\frac{kg}{s}$)
\dot{m}_{red}	Reduced mass flow	($\frac{kg \cdot K^{\frac{1}{2}}}{skPa}$)
M	Total mass	(kg)
M_{molar}	Molar mass	($\frac{kg}{mol}$)
N	Rotational speed	(RPM)
N_{ch}	Number of channels	(-)

Continued on next page

– continued from previous page

N_s	Specific speed	(–)
p	Corrugation pitch	(m)
p_{cp}	Compressed plate pitch	(m)
P	Pressure	(bar)
P_{ar}	Relevant parameter	(bar)
P_r	Pressure ratio	(–)
PF	Power factor	(–)
PL	Partial load	(–)
q	Vapour quality	(–)
Q	Thermal energy	(J)
\dot{Q}	Heat transfer	(W)
s	Entropy	$\left(\frac{J}{kgK}\right)$
S	Slip	(%)
SP	Size Parameter	(m)
t	Time	($year$)
T	Temperature	(K)
<i>Torque</i>	Torque	(Nm)
u	Velocity	$\left(\frac{m}{s}\right)$
U	Overall heat transfer coefficient	$\left(\frac{W}{m^2K}\right)$
U	Blade velocity	$\left(\frac{m}{s}\right)$
v	Specific volume	$\left(\frac{m^3}{kg}\right)$
V	Volume	(m^3)
V	Absolute velocity	$\left(\frac{m}{s}\right)$
\dot{V}	Volume flow rate	$\left(\frac{m^3}{s}\right)$
V_r	Volume ratio	(–)
W	Work	(J)
W	Relative velocity	$\left(\frac{m}{s}\right)$
\dot{W}	Power	(W)
W_p	port-to-port width	(m)
Y_{design}	Stodola's Constant	$\left(\frac{Pa*s^2}{kg*m^3}\right)$
Z	Compressibility factor	(–)

Greek symbols

α	Heat transfer coefficient	$\left(\frac{W}{m^2K}\right)$
β	Chevron angle to flow direction	(°)
β_{flow}	Chevron angle perpendicular to flow	(°)
γ	Corrugation aspect ratio/heat capacity ratio	(–)
δ	Thickness	(m)
Δ	Difference	(–)
ϵ	Void fraction	(–)
ζ	Thermodynamic index	(–)
η	Efficiency	(–)
η_I	Carnot efficiency	(–)

Continued on next page

– continued from previous page

κ	Thermal diffusivity	$\left(\frac{m^2}{s}\right)$
λ	Thermal conductivity	$\left(\frac{W}{mK}\right)$
Λ_{wave}	Corrugation wavelength	(m)
μ	Dynamic viscosity	$\left(\frac{kg}{ms}\right)$
ν	Kinematic viscosity	$\left(\frac{m^2}{s}\right)$
ξ	Friction factor	$(-)$
π	Number pi	$(-)$
ρ	Density	$\left(\frac{kg}{m^3}\right)$
σ	Surface tension	$\left(\frac{N}{m}\right)$
ϕ	Enlargement factor	$(-)$
Φ	Mass flow Coefficient	$\left(\frac{kg^{\frac{1}{2}} m^{\frac{3}{2}}}{sPa^{\frac{1}{2}}}\right)$
Ω	Wave number	$(-)$

Subscripts

0	Total, basic or reference	E	Entering
1	Start change of state	f	Saturation liquid
2	End change of state	fluid	Fluid
a	Ammonia	fric	Frictional
acc	Acceleration	fg	Latent
ad	Adiabatic	g	Saturation vapor or Gas
av	Average	gap	Through channel gap
c	Critical	gear	Gearbox
calc	Calculated	gen	Generator
component	Component	gross	Gross
cond	Condenser	h	Hydraulic
conv	Convection	hex	Heat exchanger
corr	Corrected	hw	Hot medium
cw	Cooling water	hy	Hydrostatic
cm	Cooling medium	H	Hot
cycle	Cycle	H ₂ O	Water
C	Cold	ideal	Ideal gas law
des	on-design	in	Inlet
depth	Deep sea water	is	Isentropic
duty	Duty	I	Maximum
eff	Effective	l	Liquid
ele	Elevation	load	Load
elec	Electrical	L	Leaving
env	Environment	LMTD	Logarithmic mean temperature difference
eq	Equivalent	LO	Liquid only
evap	Evaporator	m	Mix
exp	Experimental		

Continued on next page

– continued from previous page

man	Manifolds and ports	sep	Separator
max	Maximum	sp	Single phase
mech	Mechanical	sub	Subcooled
mix	Mixer	surface	Surface sea water
mod	Model	stator	Stator
net	Net output	S	System
NH ₃	Ammonia	t	Turbine
ori	Orifice	thermal	Thermal
out	Outlet	tot	Total
off	Off-design	tp	Two-phase
p	Plate	tt	Total-to-total
pump	Pump	ts	Total-to-static
r	Ratio	v	Vapor
rec	Recuperator	valve	Valve
red	Reduced	VDI	VDI Heat atlas
rotor	Rotor	w	Water
rw	Return water	wall	Wall
s	Specific or isentropic	wet	Wetted
sat	Saturation condition	wf	Working fluid

Superscripts

– Averaged

Dimensionless numbers

Ma	Mach number
Nu	Nusselt number
Pr	Prandtl number
Re	Reynolds number
Sc	Schmidt number

Acronyms

cv	Control volumes	ORC	Organic Rankine Cycle
CFD	Computational Fluid Dynamics	OTEC	Ocean Thermal Energy Conversion
DE	Differential Evolution	PHE	Plate Heat Exchanger
EoS	Equation of State	P&ID	Piping & Instrumentation Diagram
GA	Genetic Algorithm	ST	Steam Turbine
GT	Gas Turbine	SWAC	Seawater Air Conditioning
HT	Hydro Turbine	TLCC	Total life-cycle cost
LCOE	Levelized Cost of Energy	VTG	Variable turbine geometry
LMTD	Logarithmic Mean Temperature Difference	WT	Wind Turbine
NTU	Number of Transfer Units		

Contents

1	Introduction	1
1.1	Ocean Thermal Energy Conversion	2
1.1.1	Benefits	4
1.2	Bluerise B.V.	4
1.3	Relevance	5
1.4	Objectives	5
1.5	Methodology	6
1.6	Thesis outline	7
2	Overview and setup of the OTEC cycle	9
2.1	Power cycles	9
2.2	Kalina cycle	10
2.3	Working fluids	11
2.3.1	Ammonia	12
2.3.2	Ammonia-water	12
2.3.3	Thermodynamic and transport properties	13
2.4	Dimensionless quantities	15
2.4.1	Flow characteristics	15
2.4.2	Mass transfer	15
2.5	Heat exchanger	16
2.5.1	Geometry of the heat exchanger	17
2.5.2	Heat transfer	19
2.5.3	Heat transfer correlations	20
2.5.4	Condenser	21
2.5.5	Pressure drop	23
2.6	Overall system calculations	27
3	Turbine	29
3.1	Turbine performance quantification	29
3.2	Scope	30
3.3	Operating range	33
3.4	Performance maps	34
3.5	Design performance turbine	36
3.6	Effect of the multiple parameters	37
3.6.1	N_s	37
3.6.2	V_r	37
3.6.3	SP	38
3.6.4	Optimum specific speed	38

3.7	Off-design modelling of the turbine	39
3.7.1	Stodola	39
3.7.2	Turbine isentropic efficiency	41
3.7.3	Gearbox and generator off-design efficiency.	43
3.7.4	Qualitative considerations	43
3.8	Discussion turbine	46
4	Model of the 10 MW OTEC plant	47
4.1	Model methodology.	48
4.2	On-design model approach	49
4.3	Steady state thermodynamic cycle	49
4.4	Sizing components	52
4.4.1	Cost correlations	52
4.4.2	Heat exchangers.	53
4.4.3	Turbine	55
4.4.4	Separator	55
4.4.5	Other components	55
4.4.6	Scaling effects	55
4.5	Inputs of the on-design model	56
4.6	Techno-economic optimization	57
4.6.1	Optimization algorithm	57
4.7	On-design optimization results.	59
5	Off-design of the OTEC model	63
5.1	Model decomposition	63
5.2	Assumptions	64
5.3	Mathematical model	65
5.3.1	Heat exchangers.	67
5.3.2	Numerical solver heat exchangers	67
5.3.3	Separator	70
5.3.4	Valve.	71
5.3.5	Turbine	71
5.3.6	Mixer	73
5.3.7	Pump	73
5.4	Numerical model	74
5.4.1	Input of the model	74
5.4.2	Solving Algorithm.	75
5.4.3	Fast calculation method	78
5.5	Discussion off-design model	78
6	Results	79
6.1	Validation	79
6.1.1	Heat exchanger pressure drop	80
6.1.2	Separator	80
6.1.3	Turbine	80
6.1.4	Full model validation.	81
6.1.5	Analysis solver	82

6.2	Influence of the temperature variation	84
6.2.1	On-design results	85
6.2.2	Off-design optimization	86
6.2.3	Results	88
6.2.4	Conclusion	89
6.3	Influence of the seawater mass flows variation	89
6.3.1	Off-design optimization	89
6.3.2	Results	90
6.3.3	Conclusion	91
7	Conclusion and Recommendations	93
7.1	Conclusions	93
7.2	Limitations	94
7.3	Recommendations for further investigations.	95
A	Piping & Instrumentation Diagram	97
B	Correlations analysis	99
B.1	Heat exchanger correlations.	99
B.1.1	Recuperator	100
B.1.2	Evaporator	100
B.1.3	Condenser	101
B.2	Turbine trends comparison	103
C	Transport properties of ammonia-water	107
C.1	Mixture critical temperature and pressure	107
C.2	Liquid properties for ammonia-water	108
C.2.1	Specific heat capacity	108
C.2.2	Thermal conductivity	108
C.2.3	Dynamic viscosity of liquid mixtures	109
C.2.4	Surface tension for mixtures	109
C.2.5	Density for liquid mixture	109
C.3	Vapor properties for ammonia-water	110
C.3.1	Specific heat capacity	110
C.3.2	Thermal conductivity	111
C.3.3	Dynamic viscosity.	111
C.3.4	Density	111
D	Optimal operating conditions	113
D.1	Evaporator outlet vapour quality	113
E	Additional model information	117
E.1	On-design model	117
E.1.1	Pressure drop calculations for the sea water pipes	117
E.1.2	Cost correlations	118
E.1.3	Results	119

E.2	Off-design model	125
E.2.1	Recuperator	125
E.2.2	Heat exchangers.	125
E.2.3	perfect insulation or separation in the separator	127
E.3	Optimum off-design pressure drop	128
F	Model decomposition	131
E.1	Heat exchangers	131
E.2	Other components	132
	Bibliography	133



Introduction

The growing global energy demand is one of the reasons to install more energy generating capacity, but the move to a sustainable world has become one of the greatest priorities. The ever-increasing demand for energy, scarcity of traditional energy sources and severe environmental issues are, perhaps, the biggest global challenges that need immediate actions since climate change became one of the largest threats facing mankind today [32]. Therefore, the question is how to solve this demand of energy in a sustainable way. At this moment, climate change is already affecting every country on the planet. The change in climate is disrupting economies, threatening communities and ways of living. One of the main reasons is the risks associated with global warming, primary caused by burning large amounts of fossil fuels [74]. That is the main reason for seeking a sustainable solution of generating energy, to have no CO₂ emissions. With advances in technology over the last decades, electricity production from renewable sources has, in many cases, become competitive with electricity produced by fossil fuels. This makes electricity generated from renewable sources a viable alternative from an economic perspective. Besides an environmental and economic argument in favor of renewable energy, the integration of more renewable energy often makes sense from a geopolitical perspective as well. Specially for tropical islands, to provide a continuous base load, without being dependent on the import of fossil fuels.

The ocean covers 70% of the the earth's surface [11]. As a result, the ocean can be compared to a large solar collector and therefore it actually serves as big battery of energy. This makes it the largest source of renewable heat available on the planet which creates a big opportunity for renewable energy generation. To use this energy, OTEC is one of the promising renewable energy technologies. It utilizes the thermodynamics of cycles working with heat exchangers and use the temperature differences between different depths in the ocean, which occur naturally in the ocean as the driving force.

The closed cycle OTEC power plant concept was first proposed by French Engineer Jacques Arsene D'Arsonval in 1881 [26]. Since then many advancements have been made in the development of this technology. The three most common OTEC systems are: open-cycle, closed-cycle and hybrid cycle, all requiring a working fluid, condenser and evaporator within the system.

Concerns with efficiency losses due to bio fouling, system power requirements and heat exchanging systems have lead to exploration through case studies and analysis. While OTEC systems have been studied since 1881 there have been few full-scale implementations. There are still, however, a number of studies being conducted, especially in Japan, regarding the implementation of this renewable large scale technology.

In tropical regions the upper layer of the ocean is held nearly constant at a temperature of 27 °C balancing incoming heat radiation from the sun with outgoing heat due to evaporation, convection, and long-wavelength radiation. Therefore the tropics are the best option for OTEC. Figure 1.1 shows the potential areas for the OTEC plants.

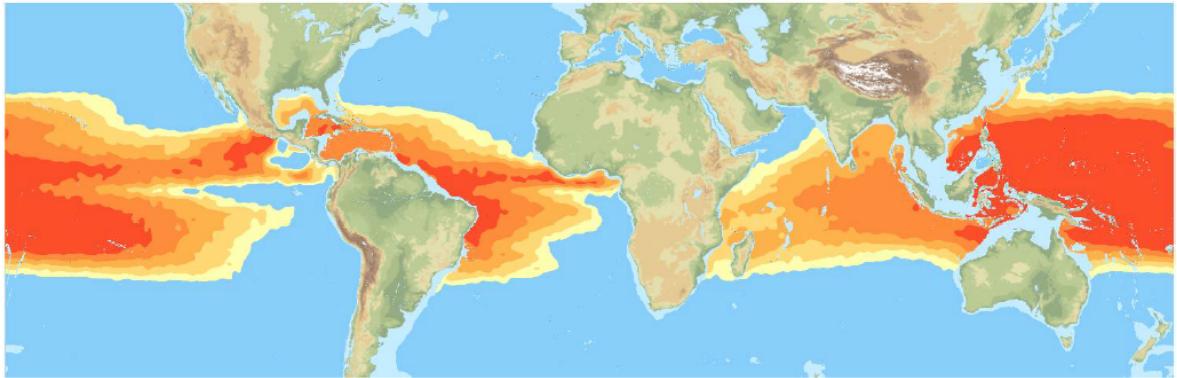


Figure 1.1: Resource potential for OTEC plants for location with a large enough temperature gradient and a deep enough sea. Copy right 2014 by Bluerise B.V. [49].

1.1. Ocean Thermal Energy Conversion

The Rankine cycle is a common power cycle for the production of electricity. The Rankine cycle is a thermodynamic power cycle that uses the heat difference between a cold and a hot source to produce mechanical work, see figure 1.2. The OTEC cycle is based on the Rankine cycle, the difference between the different power stations is the heat source that is used. The heat source could be for example coal, nuclear, heat of the flue gasses of a gas turbine, geothermal, or in this example the surface layer of the ocean.

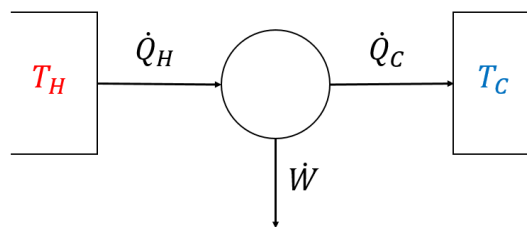


Figure 1.2: The classical Carnot heat engine [28].

Since OTEC uses a low temperature heat source and through this a small temperature difference is used, the Carnot efficiency is low, see formula 1.1, which indicates the maximum

theoretical efficiency of a (reversible) thermodynamic cycle. The OTEC system utilizes very low grade energy and yields very low efficiency of about 3–5%. Therefore, generating high capacity power requires enormous quantity of seawater and pumping energy that could decrease the cost-effectiveness of this technology. Since the hot source is the surface water of the ocean, this surface is about 27–29 °C and the cold source is coming from the depth of the ocean. Due to these low temperatures a water cycle is impossible, because it is impossible to vaporize water without operating at vacuum conditions. Thence the working fluid is something other than water, namely an organic fluid. Which fluid is doubtful, since it has some advantages and disadvantages. A recommended working fluid is ammonia since it has a boiling point at the conditions of OTEC. Rankine cycles that use an organic working fluid are called Organic Rankine Cycles (ORC)¹. In this field is done a lot of research, but not for what concerns OTEC system, which has not yet been investigated a lot.

$$\text{Carnot efficiency} = \eta_I = 1 - \frac{T_C}{T_H} \quad (1.1)$$

The working principle is quite simple and based on the Rankine cycle and the main components are the evaporator, turbine, generator, condenser and pump. An overview of the OTEC cycle is given in figure 1.3. Firstly, the working fluid is evaporated by heat extraction of the warm sea water and when it is vaporized, the working fluid is expanded over a turbine to generate electricity. Thereafter, the condenser extracts heat from the cycle by the cold sea water. After that, the sub-cooled working fluid is then pumped back to the boiler to start the cycle from the beginning.

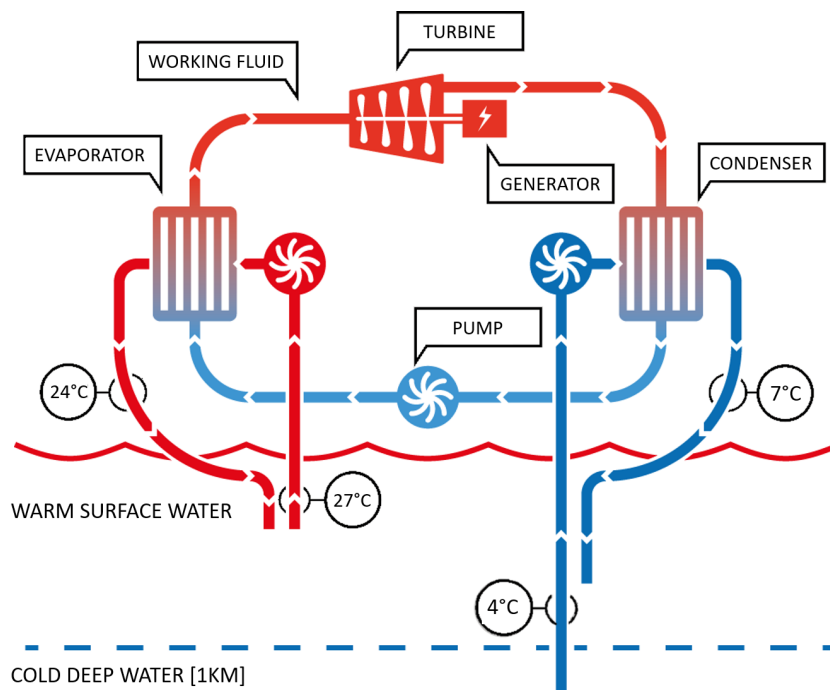


Figure 1.3: Working principle of the closed OTEC cycle, its main components and temperature levels (image courtesy of Bluerise).

¹Although ammonia is not an organic substance, Rankine cycles operating on ammonia are still considered ORC's because of the similar operating conditions with true ORC's

1.1.1. Benefits

OTEC has the benefits of clean production of energy with no carbon emissions during production and the source is free, warm and cold seawater. These benefits are not different between other renewable energy resources, like solar or wind energy. The main benefit of OTEC is that it has a vast potential, it can provide a base-load power. Even if there is no sun and wind, energy will be produced, since the OTEC system generates power 24 hours of every day. The need for an energy storage is less necessary, in comparison with the fluctuating energy production methods, like sun and wind energy, due to the weather conditions. The other benefits in comparison to other renewables are the immense resource, the maximum available energy is not limited by land, water, environmental impact, human impact, OTEC is dispatchable, meaning that its power can be ramped up and down quickly to compensate for fluctuating power demand or supply from other intermittent renewables. For this reason, OTEC is the perfect partner in energy production to other renewables like solar and wind.

1.2. Bluerise B.V.

Bluerise B.V. is a start-up company located in Delft, the Netherlands. Bluerise B.V. main business is the OTEC, but next to that they do also research on seawater air conditioning (SWAC), agriculture, aquaculture, desalination and the cooling of data centres. All these applications use the deep sea water and thus the deep-water pipe can be combined for multiple purposes. Bluerise has, in cooperation with the Technical University of Delft, an experimental set up. This set up is used to develop the different applications.

At this moment Bluerise is developing a project for the islands of Curaçao and Jamaica. There are several plans to build an operational OTEC pilot plant of 500 kW with some other applications to complete the Ecopark. The next step for Bluerise is to develop and build the 10-25 MW offshore OTEC power plant. The analysis in this report is a part of that development. Figure 1.4 shows the current projects of OTEC systems in the world.

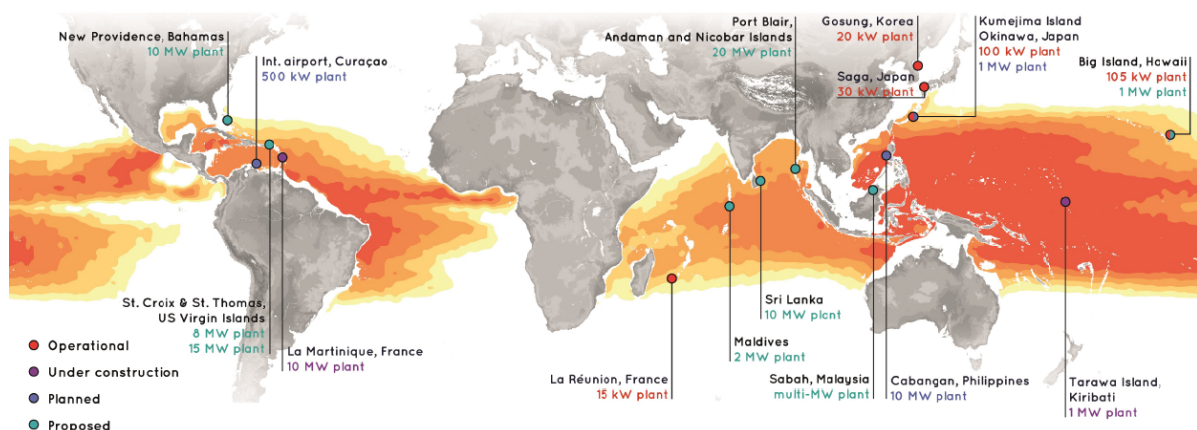


Figure 1.4: Current OTEC plants or planned projects around the world [22].

1.3. Relevance

In 1981 Kostors and Vincent have already said that OTEC is a solution to the energy crisis [51]. However, there is currently no plant with a large energy production. The disadvantages of OTEC in comparison to the traditional fossil fuels energy production are too obvious. The capital costs of OTEC technology are very high, making it difficult to compete with these traditional groups. Bluerise and other companies who are doing research on OTEC are improving the feasibility of OTEC, by reducing the costs. The OTEC plant has in operational condition low costs, no purchase of fuel and electricity, therefore the investment of the plant is the main cost.

There are several methods to reduce the costs of the OTEC plant.

- Optimized heat exchangers, to improve the efficiency of heat transfer. Which lead to minimum purchase requirements due to the size of the heat exchanger.
- Optimized turbine design, the work range of the turbine in the OTEC setup is really small, the temperature gradient is low, thus the pressure drop is quite low as well. It is recommended to design a turbine with a very high isentropic efficiency in this small range.
- Which thermodynamic cycle is used, which working fluid has the highest efficiency and is resistant to the fluctuations of the temperature gradient, see figure 1.5.

These temperature fluctuations at each location have potentially a high impact on the performance of an OTEC plant since the overall temperature difference is relatively low.

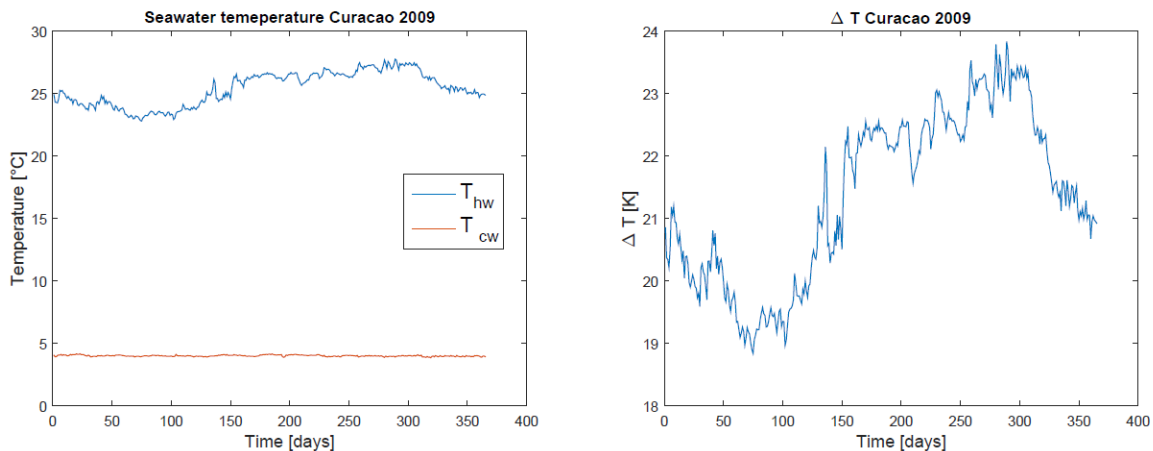


Figure 1.5: Sea water temperatures in Curaçao during 2009. On the left the sea water fluctuations of the warm surface water and cold water from 1000 m depth. On the right the temperature gradient over the year.

1.4. Objectives

The research objective is to improve the OTEC system of Bluerise and to positively impact the capital cost for OTEC plants. It will improve the implementation possibilities for advanced cycles, which is beneficial to make OTEC more available on the tropical islands. There is an existing simulation model for Bluerise's OTEC system, where the code is based on the geometry of the components of the OTEC experimental set-up located at TU Delft.

The main objective of this study is to analyze the influence of the off-design performance of the turbine on the overall performance of the OTEC power cycle. The off-design performance of the OTEC is so important, because seasonal temperature fluctuations have quite some impact on the conditions of the cycle and this has not been previously extensively investigated. The following research question is investigated in this report:

What is the impact of the turbine performance on the operating conditions of the 10 MW OTEC plant?

With accompanying sub-questions:

- What are the best correlations to predict the performance of the OTEC demo set-up the best?
- What are the optimum geometries at specific environmental conditions?
- What is the favorable working range of the turbine?
- How can we determine the pressure drop over the turbine?
- How is the existing model applicable for larger scales than the OTEC set-up scale?
- What is the influence of varying the warm seawater temperature?
- What is the influence of varying the seawater mass flows?
- Can we improve the performance of the total cycle, by adjusting the position of the vanes?
- Does the maximum heat input lead to the maximum net power output?

The conditions of the turbine for an OTEC power plant are given in table 1.1.

Table 1.1: Conditions for the turbine for the 10 MW_e OTEC Power plant

Parameter	Symbol	Unit	10 MW
Mass flow	\dot{m}	$\frac{kg}{s}$	440.0
Total inlet Temperature	T_{in}	K	293.8
Total inlet Pressure	p_{in}	bar	8.8
Static outlet Pressure	p_{out}	bar	6.4
Volume ratio	V_r	–	1.32
Enthalpy drop	Δh	$\frac{J}{kg}$	35000
Working fluid	NH_3	–	Ammonia

1.5. Methodology

This study aims at assessing the performance of the turbine in off-design conditions. This is done by evaluating the influence of varying the warm seawater temperature or seawater mass flows in an off-design model of a gross 15 MW OTEC power plant. In order to derive an optimum geometry for specific environmental conditions, a techno-economic optimization model is used using a thermodynamic model for the thermodynamic cycles in Cycle Tempo [16] that is optimized by an optimization routine that is implemented in Python. The optimum geometry is used as input for the off-design model. Therefore, the

existing off-design model is made applicable for larger scales and is equipped with a turbine instead of an orifice. As a result, the model is able to determine the pressure drop over the turbine and the performance of the turbine. The validation of the created model is based on the data reported by Goudriaan and Kuikhoven. Ultimately, the cost per produced kW as optimization criterion can be compared for the different geometries during warm seawater temperature fluctuations over a year or seawater mass flow fluctuations. As final conclusion, the role of the turbine can be emphasized to the overall performance of the cycle.

1.6. Thesis outline

- Chapter 2 gives an overview of the OTEC cycle and the set-up of the model. The selection of the working fluid is explained. Thereafter the heat exchangers geometry is introduced and the prediction of the heat transfer and pressure drop is discussed.
- Chapter 3 is a state of the art review about turbines for ORC systems and the modelling of the turbine is introduced.
- Chapter 4 describes the method of modelling the OTEC cycle and introduces the on-design model. Finally, with the results a geometry can be determined for the 10 MW OTEC cycle.
- Chapter 5 continues with the model, the off-design model is discussed.
- Chapter 6 shows a full model validation of the model. The results of varying the environmental temperature or the seawater mass flows are shown and the influence of the off-design performance of the turbine is discussed.
- Chapter 7 presents the conclusions and recommendations of this study.

2

Overview and setup of the OTEC cycle

This Chapter describes the working principles of the conventional OTEC system, which operates like a traditional Rankine Cycle, see figure 1.3. The working fluid is explained and the heat transfer prediction is introduced.

This thesis is a follow up to the research of Goudriaan and Kuikhoven [33][52]. These two research projects model the total OTEC demo set-up at the TU Delft. The configuration of the OTEC demo set-up is a more complex version of the traditional Rankine cycle, because a separator and recuperator are added. Therefore, the more complex Kalina cycle is introduced. To complete the OTEC demo model, it is necessary to add a turbine module. Only with this improved OTEC model, we are able to simulate a commercially upscaled plant with realistic performance and power output. Further, the heat transfer method applied in the present study will be described, which is based on heat transfer coefficient correlations by Goudriaan and Kuikhoven [33][52]. Therefore additional dimensionless quantities are introduced.

2.1. Power cycles

A thermodynamic cycle consists of thermodynamic processes transferring heat and work with varying conditions, like flow pressure and flow temperature, to return after one cycle into the initial state [14]. Heat and work are converted through the system by the working fluid. The heat from a warm source is converted into useful work and the remaining heat is disposed to a cold sink. This thermodynamic cycle is the power cycle, which is a closed system for the OTEC application. This means that the working fluid is conserved. During a closed cycle, the system returns to its original thermodynamic state.

The OTEC cycle is based on the traditional thermodynamic Rankine cycle, where the working fluid consists of a combination of steam and water. The cycle consists of four processes to convert the heat into mechanical work [58]. The steps between the points 1-2 and 3-4 are adiabatic processes and 2-3 and 4-1 are isobaric processes, see figure 2.1.

In the first step of the thermodynamic cycle 1-2, the pump increases the pressure of the working fluid. In the following step 2-3, the heat source heats the working fluid. In the third step 3-4, the expanding working fluid in the turbine generates work output. In the final step

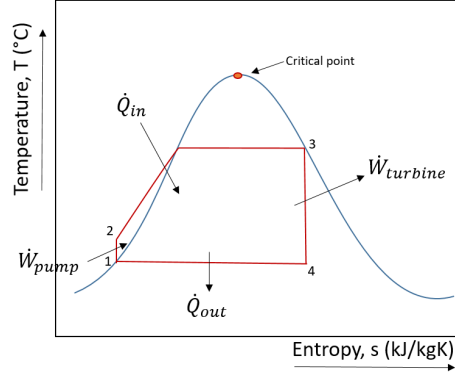


Figure 2.1: Power cycle

4-1, the cold source cools the working fluid and therefore the initial state is reached. Therefore, the complete thermodynamic cycle is described by the first law of thermodynamics, leading to the following equation:

$$\Delta E = E_{out} - E_{in} = 0 \quad (2.1)$$

The total cycle makes use of the mass- and energy equations 2.2 and 2.3.

$$\frac{dM}{dt} = \dot{m}_{in} - \dot{m}_{out} \quad (2.2)$$

$$\frac{dE}{dt} = \dot{m}_{in} * h_{in} - \dot{m}_{out} * h_{out} + \dot{Q}_S - \dot{W}_S, \quad (2.3)$$

where \dot{m} is the mass flow in $[\frac{kg}{s}]$, $\frac{dE}{dt}$ is the rate of change of energy, \dot{Q}_S is the rate of heat to the system and \dot{W}_S is the rate of useful work produced by the system, all in $[\frac{J}{s}]$.

2.2. Kalina cycle

In comparison with the traditional Rankine cycle, we discuss the Kalina cycle, in which a separator and a recuperator are added, see figure 2.2. The Kalina cycle is the configuration of the OTEC demo set-up, so also the configuration of the existing model.

The separator divides the working fluid liquid phase from the vapour phase. This ensures that the working fluid flow to the turbine is vapour only, so that the flow is dry enough before it enters the turbine¹. Because of this, the Kalina cycle has the possibility to handle partial evaporation in the evaporator. Therefore, the model will be applicable for mixtures. In general, a mixture contains two fluids with a different volatility and mainly the more volatile fluid is expanded over the turbine. Therefore, the Kalina cycle is more flexible and can be optimized for a specific source. The concentration of the two fluids gives the ability to improve the performance of the power cycle. Therefore, using the Kalina cycle can be an improvement for the OTEC system [44]. The Kalina cycle performs better if the heat source has a finite capacity. Since it has the ability to take full advantage of the temperature difference between the particular heat source and available sink. In practise, the gravity plays

¹More explanation about dry fluids in section 2.3

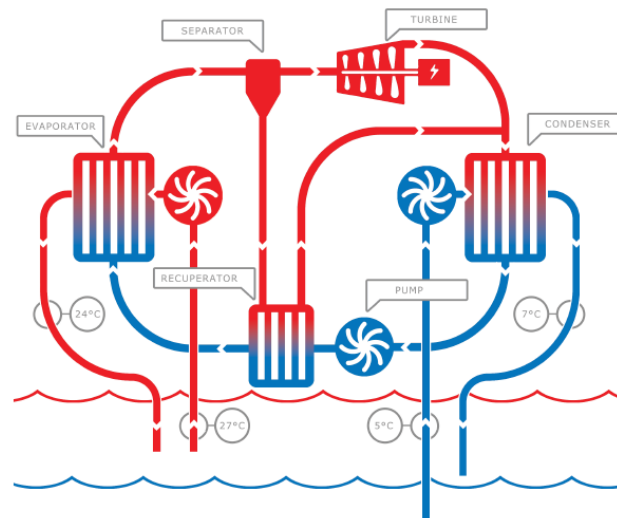


Figure 2.2: Layout of Kalina cycle used in the OTEC system [49].

the main role of the separation method in the separator. In the OTEC setup, the separator is a vertical wire-mesh separator. Further, the recuperator ensures that more heat is used as input for the system and therefore less sea water is needed. Thereafter, the pressure is reduced with a turbine and in the mixer the two flows are coming together, which ensures that the flow is a perfect mix of vapor and liquid before the condenser.

2.3. Working fluids

The selection of the working fluid is important for the OTEC system. The performance of the heat exchanger is directly linked to the working fluid. In figure 2.3, three different types of working fluid are shown, namely a dry, a wet and an isentropic working fluid. For the OTEC cycle, there is an optimal type of fluid, which should be selected. Using a wet working fluid, gives the possibility that the medium is too wet in the turbine and results in too much damage and therefore a short life duration. For this reason, wet fluids usually need to be superheated, while many organic fluids, which may be dry or isentropic, do not require superheating. In the dry situation, the medium is superheated after the turbine. This sounds ideal, but a lot of cooling is necessary to have full condensation at the outlet of the condenser. The most ideal fluid would be an isentropic fluid, mostly organic fluids. The maximum work is achievable and the turbine outlet is always dry enough. Another advantage of organic working fluids is that the turbine built for ORC's typically requires only a single-stage expander, resulting in a simpler, more economical system in terms of capital costs and maintenance [15]. An extra advantage is that most of them condense at ambient temperatures at pressures above atmospheric, so organic Rankine cycles have no problems with air getting into the cycle. Nevertheless, these types of fluids have some disadvantages, like being more toxic and more expensive [15].

For the OTEC system, there are multiple criteria for the working fluid. The fluid should be able to operate in a specific pressure range with a high heat transfer coefficient and operating at low volume flow is recommended. The fluid should be safe, for example non-flammable, nontoxic, noncorrosive, good for the environment and preferably as cheap as

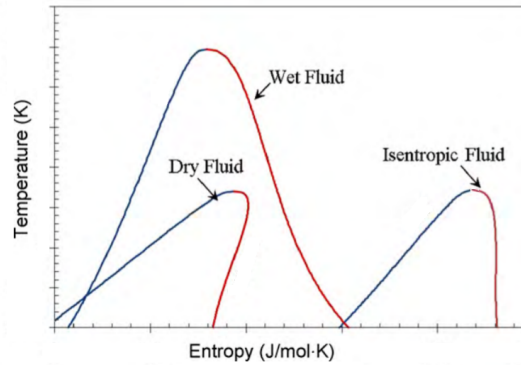


Figure 2.3: Temperature versus entropy, three working fluids, dry, wet and isentropic [59].

possible. In literature, a lot of research is done into which working fluid is favorable for OTEC systems. The thermo-economic optimization of Kirkenier [48] concludes that the most advantageous working fluid is ammonia or a mixture of ammonia with water. The difference of using a mixture or a pure working fluid will be discussed in the following subsections, since the influence of using a mixture is significant [52].

2.3.1. Ammonia

The research of Ganic and Wu [30] shows that ammonia is the best working fluid for an OTEC plant. Ammonia has some disadvantages, like being toxic and having problems with turbine seals and materials, but in this research it is still concluded that ammonia is the optimal working fluid for OTEC. The main reason is the high thermal conductivity of ammonia, which is essential in OTEC applications. Because the heat exchangers play an important role in the purchase costs. Further, ammonia has a molar mass, M_{molar} , of $17 \frac{g}{mol}$, so steam turbines can be used and in this field of technology a lot of research is already done. Also, ammonia is a common working fluid in the process industry. The demo setup at the TU Delft uses ammonia as working fluid, so validation is possible. Therefore, we assume that ammonia is a proper working fluid, since ammonia results in a good temperature match between the working fluid and heat source in the heat exchangers and has shown competitive power generation ability with another Organic Rankine Cycles [86].

2.3.2. Ammonia-water

A mixture of ammonia and water as working fluid is considered in order to improve the efficiency from low enthalpy heat sources. Figure 2.4 compares the working fluid mixture with a pure fluid. The properties of a mixture are more complex to investigate, but the research of Angelino and Colonna [5] shows that it has its advantages.

In a mixture working fluid, it is possible to follow the warm and cold seawater temperature slopes, which are called the temperature glides. During the evaporation process, the mixture working pair as zeotropic working fluid has the advantage to evaporate non-isothermally. The temperature rises during evaporation, because the concentration of the working fluid is changing, since ammonia is more volatile. This means ammonia has a lower boiling point, which results in a smaller ammonia fraction in the liquid phase at the

end of the evaporator relative to the inlet. Hence, the temperature glide adapts better to the profile of the heat source, which decreases the logarithmic mean temperature difference (LMTD) for the evaporator, with the result that the working fluid is almost at the temperature of the source fluid when leaving the heat exchanger. For the condenser, in the condensation phase this effect is the other way around. Ultimately, the benefits are that the amount of power that can be extracted from a given heat and cold source pair is larger, so less sea water needs to be used and enables an increase of the high pressure level in the cycle. Therefore, the performance of the the cycle may be improved. The research of Zhang concludes that ammonia-water mixture is environmentally friendly and safe enough for engineering application. Several stainless steels as well as titanium do not suffer from corrosion caused by ammonia-water [92].

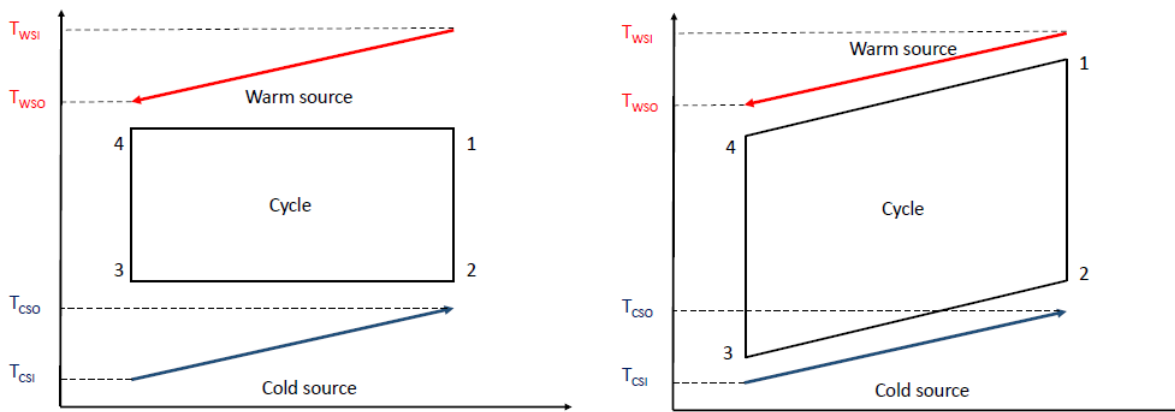


Figure 2.4: T-S diagram for (on the left) a pure fluid (on the right) a non-azeotropic mixture [33].

Ammonia-water is a zeotropic or non-azeotropic mixture [88], which means that fractions of water and ammonia have different boiling points. This results in a very soluble mixture. For ideal mixtures, the thermophysical properties can be obtained by combining the properties of each component. In practice, the properties of a mixture of fluids are more complex and the real characteristics are hard to determine.

2.3.3. Thermodynamic and transport properties

In the OTEC cycle, multiple properties of the working fluid vary, namely pressure, temperature and concentration. In the operating range of the OTEC cycle, it is important to obtain accurate thermodynamic- and transport properties of the fluid with an acceptable computational time, since optimization should be possible. For each fluid, a separate model is used to determine the thermodynamic and transport characteristics. The investigation of which library or model is most favorable is adopted from Goudriaan and Kuikhoven [33][52].

Ammonia-water mixture

Equation of state

An equation of state relates the thermodynamic properties of a fluid to each other to describe its thermal equilibrium state. Rattner & Garimella developed a correlation which is mainly used for ammonia-water mixtures. It seems the best option in comparison with its computational time [68][52]. It is one of the most complete and is thermodynamically

cally consistent. This correlation is totally validated in the range ($230 \leq T \leq 500 \text{ K}$ and $20 \leq P \leq 5000 \text{ kPa}$), so useful for the conditions of the OTEC set-up.

Transport properties

The implementation of Rattner & Garimella is unfortunately not enough for our cycle. It does not take the transport properties for the working fluid into account. Therefore, Conde is selected [52] to obtain the specific heat capacity, density, thermal conductivity, dynamic viscosity and the surface tension of the working fluid. Appendix C explains Conde in more detail. In the vapor phase, an ideal behavior is assumed. For the non-ideal behavior, correlations are used to compensate them, see appendix C. The Shamsedinov's correlation is used to compensate the mixing effects with an excess term [52].

Pure ammonia

Using a working fluid of pure ammonia, the thermodynamic properties are rather easy to obtain. In this situation, CoolProp is chosen as the model. CoolProp is an open source thermophysical property library and specializes in pure fluid properties. Using the CoolProp model, still correlations are needed, see appendix C. Table 2.1 shows the implemented models and correlations for different properties of ammonia by CoolProp.

Table 2.1: An overview of the applied models and correlations to calculate the thermophysical properties of ammonia with CoolProp [52].

Property	Implemented model
Thermodynamic properties: Equation of state	Tillner-Roth et al., 1993 [79]
Thermal conductivity	Tufeu et al., 1984 [81]
Viscosity	Fenghour et al., 1995 [25]
Surface tension	Mulero et al., 2012 [60]

Pure water

For pure water, CoolProp is used to calculate the thermophysical properties. In addition to CoolProp some correlations are needed, see appendix C. Table 2.2 shows the implemented models and correlations for different properties of water by CoolProp.

Table 2.2: An overview of the applied models and correlations to calculate the thermophysical properties of water in addition to CoolProp [52].

Property	Implemented model
Thermodynamic properties: Equation of state	Wagner et al., 2002 [84]
Thermal conductivity	Huber et al., 2012 [40]
Viscosity	Huber et al., 2009 [39]
Surface tension	Mulero et al., 2012 [60]

2.4. Dimensionless quantities

During modelling the components of the OTEC cycle, the behavior of the fluid should be described. In complex situations, analytic solutions are hard to determine and empirical correlation methods are used. Therefore, the OTEC model uses correlations. Heat transfer in two-phase flows is a complex phenomenon to describe, hence we introduce the heat transfer coefficient. Using this coefficient, it is not necessary to determine the complete complex physics. Correlations for heat transfer coefficients are developed for plate heat exchangers, which are valid for certain ranges. These correlations are obtained by experimental research and data fits. To describe the effects and characteristics of a flow, several dimensionless quantities are used.

2.4.1. Flow characteristics

The most common quantities to describe the flow characteristics in heat exchangers are the Reynolds and Prandtl number.

$$Re = \frac{\rho u L}{\mu} \quad (2.4)$$

$$\text{Prandtl number} = Pr = \frac{c_p \mu}{\kappa}, \quad (2.5)$$

where ρ is the density in $[\frac{kg}{m^3}]$, u is the velocity of the flow in $[\frac{m}{s}]$, L is characteristic length $[m]$, μ is the dynamic viscosity $[\frac{kg}{m*s}]$, κ is the thermal diffusivity $[\frac{m^2}{s}]$ and c_p is the specific heat in $[\frac{J}{kgK}]$. The Reynolds number is the ratio between the inertial and the viscous forces. In other words, the acceleration of a mass in respect to the forces to the friction between layers of any real fluid. The Reynolds number is used to define the regime of turbulence of a flow. In two-phase mixture flows the Reynolds number takes different forms. Other reports make use of an other form of the Reynolds number, namely the equivalent form in equation 2.6. The equivalent form describes both phases with the vapor fraction and a mass flux. The Prandtl number is the ratio between viscous and thermal diffusion rate.

$$Re_{eq} = \frac{\dot{G}_{eq} * L}{\mu_l} \quad (2.6)$$

$$\dot{G}_{eq} = \dot{G} \left[(1 - q) + q * \left(\frac{\rho_l}{\rho_v} \right)^{0.5} \right], \quad (2.7)$$

where \dot{G} is the mass flow rate per cross-sectional area in $[\frac{kg}{m^2*s}]$, q is the vapor quality, μ_l is the viscosity of the liquid phase.

2.4.2. Mass transfer

Next to the heat transfer, mass transfer occurs in mixtures and two-phase fluids during condensation or evaporation. Water and ammonia exchange mass through diffusion. The ammonia vapor and liquid transfer mass via absorption through their interface. Geschiere [31] concludes that the Schmidt number is relevant, since mass transfer plays a role in heat transfer processes.

$$Sc = \frac{\mu}{\rho D} \quad (2.8)$$

The physical interpretation of the Schmidt number is the ratio of momentum diffusivity (viscosity) over mass diffusivity. It is also called the mass transfer equivalent of Prandtl's number, since it only contains fluid properties [31]. The D is the mass diffusivity in [$\frac{m^2}{s}$].

2.5. Heat exchanger

In the OTEC cycle, the heat from the hot source, which is the upper layer of the ocean water, is transferred to the working fluid through the evaporator. It evaporates the working fluid, with the result that a vapour flow is created. Which can flow to the turbine to produce power by expansion of the working fluid. The heat from the working fluid is extracted through the condenser, which uses the deep sea water of the ocean to cool down the working fluid.

A few degrees of sub-cooling prevent condensate pump cavitation. Therefore, the working fluid flow from the condenser into the cycle pump has to be in fully liquid phase. If ever the vapor doesn't condensate properly, the liquid phase could accumulate at the end of the heat exchanger. Since the inlet flow of the condenser is constant, the pressure will rise. Until enough hydrostatic pressure is build up to push the liquid through. In the OTEC demo set-up, a buffer tank is placed to ensure that this accumulation occurs outside the condenser. Finally, this results in a pure liquid phase is flowing to the pump. Excessive condensate sub-cooling decreases the operating efficiency of the plant, since the sub-cooled condensate should be reheated up to heat source temperature [2]. Therefore, excessive sub-cooling should be minimized in optimal situation. In the situation of excessive sub-cooling, the pressure level of the condenser is too high. From this we can conclude, the performance of the condenser is the driving factor of the outlet pressure of the turbine and the pressure level a good indicator of the condensation performance [31]. Geschiere [31] examines the optimal condenser pressure with an iteration loop, whereby no vapor and no sub-cooling is present at the outlet of the condenser. These calculations are time-consuming, so it is not practical to use in a model that includes all components.

A large share of the total module cost of the investment of the OTEC cycle is due to the heat exchangers. Therefore, optimization of the heat exchangers should be performed. Key characteristics regarding heat transfer are the effectiveness, heat transfer coefficient and pressure drops. The effectiveness is the ratio between the actual heat and the maximum heat that could be exchanged in an infinite heat exchanger. The most common heat exchangers are the shell & tube and the plate heat exchangers. The selection of a heat exchanger depends on the sizing and financial costs. The construction type depends on the fluids, operating pressures, temperatures, fouling and clean-ability, fluids and material compatibility, corrosiveness of the fluids, how much leakage is permissible from one fluid to the other fluid, available heat exchanger manufacturing technology and financial costs [72]. In the OTEC demo set-up, plate heat exchangers are used and in the large scale OTEC plant plate heat exchangers will be used again. Plate heat exchangers are suitable in the conditions of the OTEC cycle, due to the small pressure difference between the two median and the fouling factors of ammonia and water are good enough. Hence, with the reason

that the compactness is high and therefore the plate heat exchanger is cheaper than shell & tube heat exchangers, the plate heat exchanger is a proper choice [72].

2.5.1. Geometry of the heat exchanger

The geometry of the plate heat exchanger depends on the research of manufacturers, since a lot of research is done to find the optimal configurations with a specific geometry. Therefore, the geometry will be taken over from the manufacturers data. The flow in the heat exchanger is single pass [78], see figure 2.5.

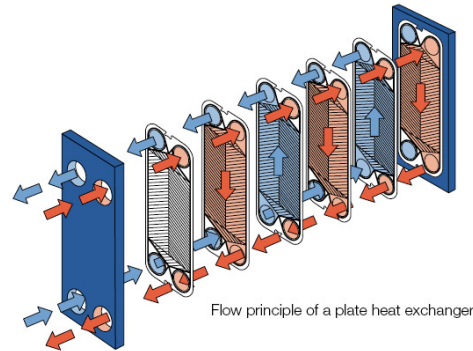


Figure 2.5: Counter current single pass plate heat exchanger arrangement [1].

The plate heat exchangers geometry is determined by several parameters. The effective heat transfer area, A_p , is obtained by multiplying the plate area, A_0 , with an enlargement factor, ϕ . The enlargement factor symbolizes the enlargement of the heat transfer area, so it represents the ratio of the corrugated area and the projected area. This factor depends on the corrugation characteristics of the geometry.

$$A_p = \phi * A_0 \quad (2.9)$$

Figure 2.6 shows the dimensions of a chevron plate. The chevron plates have a sinusoidal corrugation with a chevron angle, β . The corrugations are mirrored in the center plane of the plate, making the pattern symmetrical. The type of heat exchanger is important in how the definition of the geometry is used. In the gasketed heat exchanger, the corrugated zone is mirrored over the horizontal mid plane, while the corrugated zone is mirrored over the vertical mid plane in the brazed heat exchanger. Next to this, it introduces the effective length and width, $L_{p,eff}$ & $W_{p,eff}$, which are not equal to the port-to-port length and width, L_p & W_p , but are derived by adding or subtracting the port diameter. Subsequently, the plate area can be derived with equation 2.10.

$$A_0 = W_{p,eff} * L_{p,eff} \quad (2.10)$$

To determine the enlargement factor we have to zoom in on the geometry of the corrugated plate. Figure 2.7 shows the geometry of the plate heat exchanger and some parameters are introduced, which eventually lead to the geometry equations, see equations 2.9-2.18.

Figure 2.7a shows the sinusoidal corrugation of the plate. The chevron angle is the angle between the corrugation and the main flow direction and perpendicular to the flow direction is represented by the β_{flow} . The parameter, p , corresponds to the corrugation pitch,

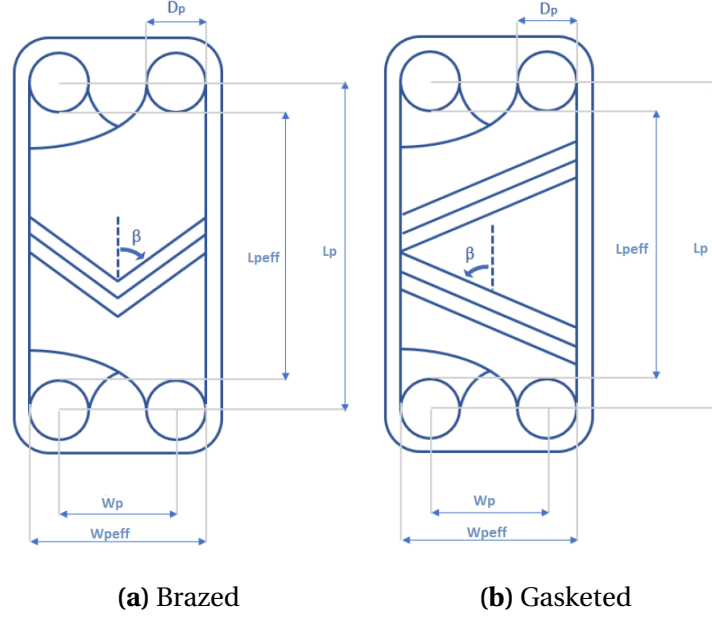


Figure 2.6: Length, width and chevron angle definitions of heat exchanger plates [20].

which is the corrugation length in the main flow direction. The plate pitch, p_{cp} , in literature also called the corrugation depth [53], is the total thickness of corrugation of the plate. From the plate pitch and the known plate thickness, d_p or δ_{wall} , the channel gap is defined as d_g , the cavity between the plates, see figure 2.7b. The channel gap is a decisive parameter and is important for the flow characteristics. The last parameter is the wavelength, Λ_{wave} , the corrugation length in the direction of the corrugation pattern. Since the plate has a specific corrugation, the chevron angle is fixed, whereof the pitch and wave length are dependent. Hence, the enlargement factor is imposed, see the following equations:

$$\Omega = \frac{\pi(p_{cp} - d_p)}{\Lambda_{wave}} = \frac{\pi d_g}{\Lambda_{wave}} = \frac{2\pi \hat{a}}{\Lambda_{wave}} \quad (2.11)$$

$$\phi(\Omega) = \frac{1}{6} \left(1 + \sqrt{1 + \Omega^2} + 4\sqrt{1 + \frac{\Omega^2}{2}} \right) \quad (2.12)$$

The rest of the geometry characteristics consists of the diameters. First, we have the equivalent diameter, where the amplitude is known from the manufacturer, see figure 2.7b. With the enlargement factor the hydraulic diameter is derived, which is a modified length and is used in multiple literature studies for plate heat exchangers.

$$d_{eq} = 4 * \hat{a} = 2 * d_g \quad (2.13)$$

$$d_h = \frac{d_{eq}}{\phi} \quad (2.14)$$

$$\gamma = \frac{d_{eq}}{\Lambda_{wave}}, \quad (2.15)$$

where d_{eq} is the equivalent diameter, d_h is the hydraulic diameter in [m] and \hat{a} is the corrugation amplitude in [m]. The parameter γ is the corrugation aspect ratio, which indicates

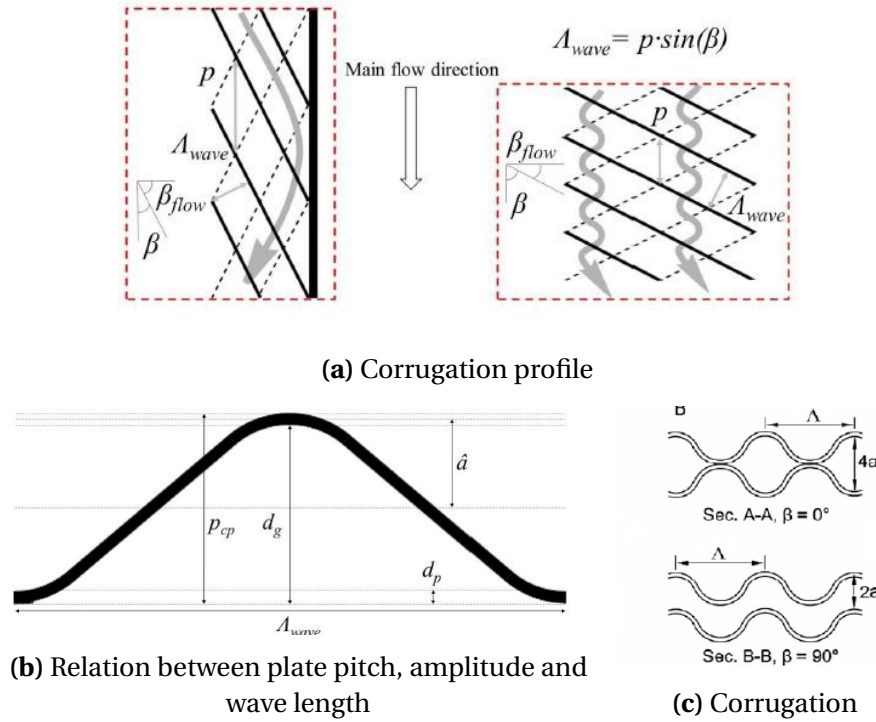


Figure 2.7: Geometry of the plate heat exchanger [78].

the degree of surface corrugation. The equations 2.16-2.18 are the equations to calculate the velocity and mass flux through the plates.

$$u_p = \frac{\dot{V}_{gap}}{2 * \hat{a} * W_{p,eff}} \tag{2.16}$$

$$A_f = W_{p,eff} * d_g \tag{2.17}$$

$$\dot{G} = \frac{\dot{m}}{A_f * N_{ch}} \tag{2.18}$$

The A_f is the cross-sectional area for flow per channel in [m^2], and N_{ch} are the number of channels per fluid for one plate heat exchanger. These equations are important to describe the flow characteristics.

2.5.2. Heat transfer

The first law of thermodynamics has been used to calculate the heat flow of the heat exchanger, see equation 2.19. \dot{Q}_{load} is the heat load of the water flow through the condenser or evaporator in [W]. The c_p is assumed to be the average value of the in- and outlet of the water side in [$\frac{J}{kg * K}$].

$$\dot{Q}_{load} = \dot{m}_{water} * c_p * (T_{in} - T_{out}) = \dot{m}_{water} * (h_{in} - h_{out}), \tag{2.19}$$

Subsequently, the heat transfer to the working fluid can be determined, see equation 2.20.

$$\dot{Q}_{duty} = U_{hex} * A_{hex} * \Delta T_{LMTD} = \dot{m}_{wf} * (h_{in} - h_{out}) \tag{2.20}$$

The coefficient U_{hex} is the overall heat transfer coefficient in [$\frac{W}{m^2 \cdot K}$], which actually represents the degree of performance and equation 2.21 shows that it depends on several components. The parameter A_{hex} is the total heat transfer area in [m^2], which is determined by the number of plates and the geometry of the plates. The ΔT_{LMTD} is the logarithmic mean temperature difference between the in- and outlet of the heat exchanger in [K], which is shown in equation 2.22.

$$\frac{1}{U_{hex}} = \frac{1}{\alpha_{fouling}} + \frac{1}{\alpha_{conv,warm}} + \frac{1}{\alpha_{conv,cold}} + \frac{\delta_{wall}}{\lambda_{wall}} \quad (2.21)$$

$$\Delta T_{LMTD} = \frac{(T_{warm,in} - T_{cold,out}) - (T_{warm,out} - T_{cold,in})}{\ln\left(\frac{T_{warm,in} - T_{cold,out}}{T_{warm,out} - T_{cold,in}}\right)}, \quad (2.22)$$

where $\frac{1}{\alpha_{fouling}}$ is the fouling resistance in [$\frac{m^2 K}{W}$]. The fouling of the working fluid side is neglected, since this side is closed. In a closed circuit, the accumulation of unwanted material on solid surfaces leading to the detriment of function will not happen. Therefore, the fouling only depends on the water side, which reduces the thermal efficiency of the heat exchanger. The coefficient α_{conv} is the convective heat transfer coefficient of the fluid in [$\frac{W}{m^2 K}$], δ_{wall} is the thickness of the wall in [m] and the λ_{wall} is the thermal conductivity of the plate material in [$\frac{W}{mK}$].

Kuikhoven and Goudriaan [33][52] investigated which heat transfer correlations are optimal in the OTEC model and validated the correlations with experimental data. Table 2.3 shows an overview of the selected correlations in the heat exchangers by Kuikhoven and Goudriaan. In appendix B.1 the research findings are shown, in which the different correlations which are found in the literature are compared and the best performing correlations are selected.

Table 2.3: Correlations of the fluids in the OTEC Cycle, [33]

Component	Heat transfer correlations	
Evaporator	1. Two phase (wf-side)	Ayub (direct expansion) [9]
	2. Single phase (wf-side)	Donowski & Kandlikar [24]
	3. Single phase (water-side)	GoudKuik [33][52]
Condenser	1. Two phase (wf-side)	Winkelmann [87]
	2. Single phase (wf-side)	Donowski & Kandlikar [24]
	3. Single phase (water-side)	GoudKuik [33][52]
Recuperator	1. Single phase (wf-side)	Donowski & Kandlikar [24]

2.5.3. Heat transfer correlations

Table 2.4 shows the correlations for the single phase and the two phase heat transfer coefficients.

The correlations for the single phase use the Reynolds and Prandtl numbers to determine the convective heat transfer coefficient. In the two phase regime, the correlations obtain the Nusselt number and with equation 2.23 the convective heat transfer coefficient is derived. The Nusselt number is the ratio of convective to conductive heat transfer across the

Table 2.4: The one and two phase heat transfer correlations

One phase		
Source	Heat transfer correlation	Validation range
Donowski & Kandlikar [24]	$\alpha_{sp} = \frac{\lambda}{d_{eq}} * 0.02875 * Re^{0.78} * Pr_r^{\frac{1}{3}}$	Re > 200
GoudKuik [33][52]	$\alpha_{sp} = \frac{\lambda}{d_{eq}} * 0.291 * Re^{0.72} * Pr_r^{\frac{1}{3}}$	400 < Re < 1800
Two phase		
Source	Heat transfer correlation	Validation range
Ayub direct expansion [9]	$Nu_{tp} = 0.025 * C * \left(\frac{Re_l^2 * h_{fg}}{L_p} \right)^{0.4124} * \left(\frac{P}{P_c} \right)^{0.12} * \left(\frac{65}{\beta} \right)^{0.35}$ C = 0.0675 for direct expansion C = 0.1121 for flooded evaporators	No limit defined
Winkelmann [87]	$Nu_{tp} = 16.8 * Re_{eq}^{0.29} * Pr_{liq}^{\frac{1}{3}}$	10 < Re < 1100

boundary. Next to this, the correlation of Ayub uses the latent heat of vaporization, h_{fg} and the critical pressure of the working fluid, P_c .

$$\alpha_{tp} = Nu_{tp} * \frac{\lambda_l}{L}, \quad (2.23)$$

where L is the characteristic length scale of the flow [m] and λ_l is the thermal conductivity in [$\frac{W}{mK}$].

2.5.4. Condenser

In appendix B.1 is concluded that the correlation of Winkelmann gives the most accurate prediction of the system behaviour for the two phase working fluid side. Geschiere investigated the influence of the mass transfer on the heat transfer. He concluded that the interface, vapor fraction and liquid fraction have their own temperature. With respect to the heat transfer coefficient, this leads to an effectively much lower driving force and thus locally a much lower heat flow. Despite that the heat transfer prediction is accurate using the vapor and liquid flow including the effect of mass transfer. The prediction remains doubtful, since the theory on the film thickness in mixture flow in plate heat exchangers is unclear. Therefore, Geschiere proposes a correlation for two-phase condensing convective heat transfer coefficient for the flow in brazed heat exchangers based on the mass transfer between the two phases. The Schmidt number, see equation 2.8, is added to the correlation to describe the mass transfer influence. The convective heat transfer coefficient correlation is given in equation 2.24. The exponent of the Prandtl number is different in comparison with other correlations. Which could be a result of taking the Schmidt number into account. The Schmidt number has some influence on the correlation, which normally is taking into account the Prandtl number. The Prandtl number and Schmidt numbers are not totally independent of each other, since the parameters overlap. This behaviour should be further investigated, but is beyond this research.

$$Nu = 1.16 * Re_{eq}^{0.48} * Pr_l^{-0.50} * Sc_l^{0.17} \quad (2.24)$$

The correlation of Geschiere is investigated to improve the accuracy of the heat transfer prediction of the condenser. Figure 2.8 shows the results of the heat transfer correlation of

Geschiere in comparison with the previous work done by Goudriaan [33] and Kuikhoven [52] for the working fluid mass flow of 10 g/s.

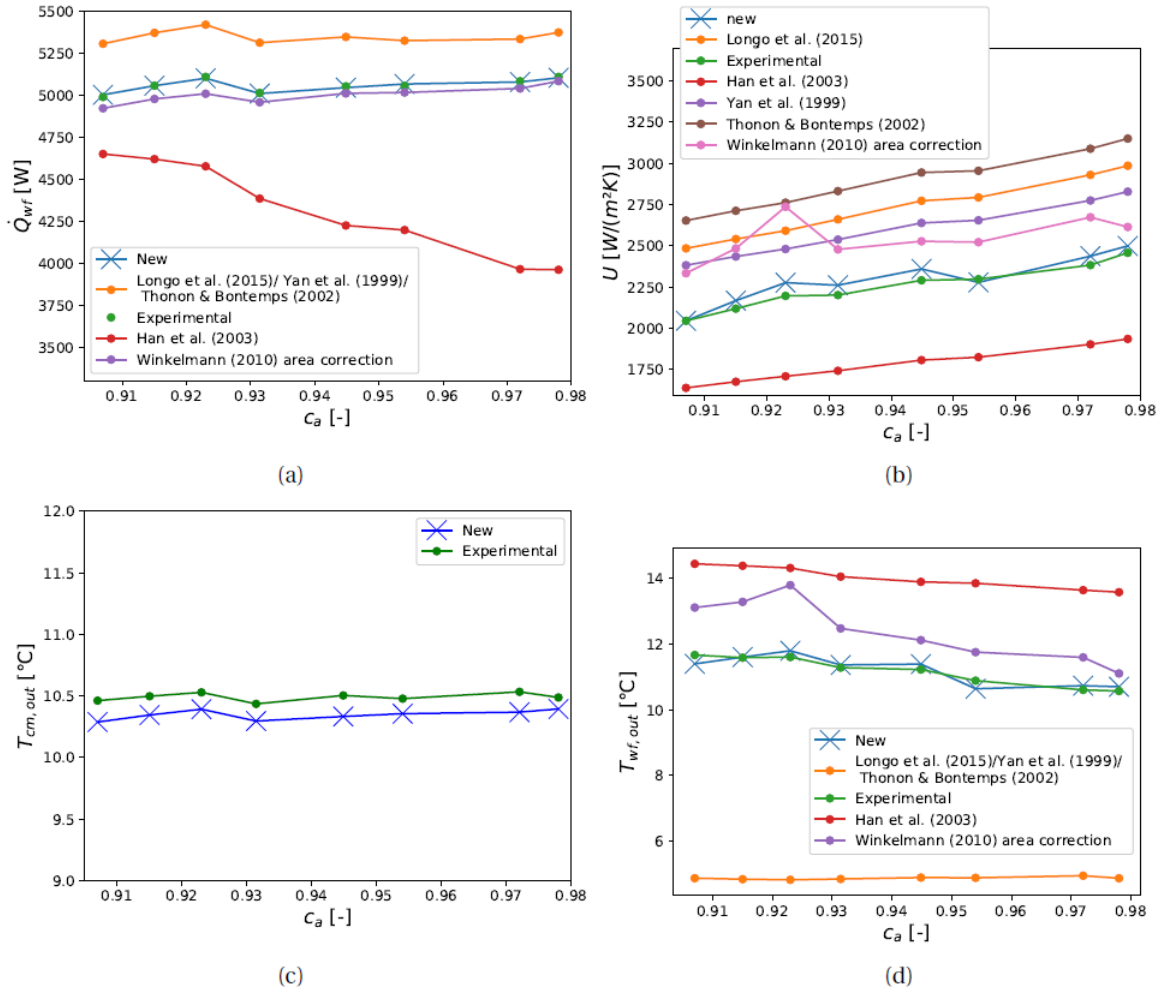


Figure 2.8: Condenser parameters compared to correlations mentioned in Goudriaan [33] and Kuikhoven [52] for $\dot{m}_{wrf} = 10$ g/s: (a) Heat transferred from the working fluid side (b) The overall heat transfer coefficient (c) The outlet temperature of the cooling medium (d) The working fluid outlet temperature [31]. New is the correlation given in equation 2.24.

For the 10 $\frac{g}{s}$ working fluid mass flow data set, the results show good agreement with the experimentally measured data. Geschiere concludes that the proposed heat transfer correlation is still reasonably accurate for other working fluid mass flows. Nevertheless, the correlation works properly in the range of different working fluid concentrations, but for the case of pure ammonia the correlation shows more inaccuracy. Figure 2.9 shows the comparison of the Winkelmann correlation and the correlation of Geschiere for the pure ammonia cases. Note that the heat input of all experimental data is not equal, so the trends do not symbolize anything.

The heat transfer correlation improves the results in comparison with Winkelmann. Extrapolation to other mass flows leads to decent results as well. The correlation of Geschiere is a promising heat transfer correlation to describe the heat transfer in the condenser. Geschiere states that the proposed correlation has the following accuracies: the temper-

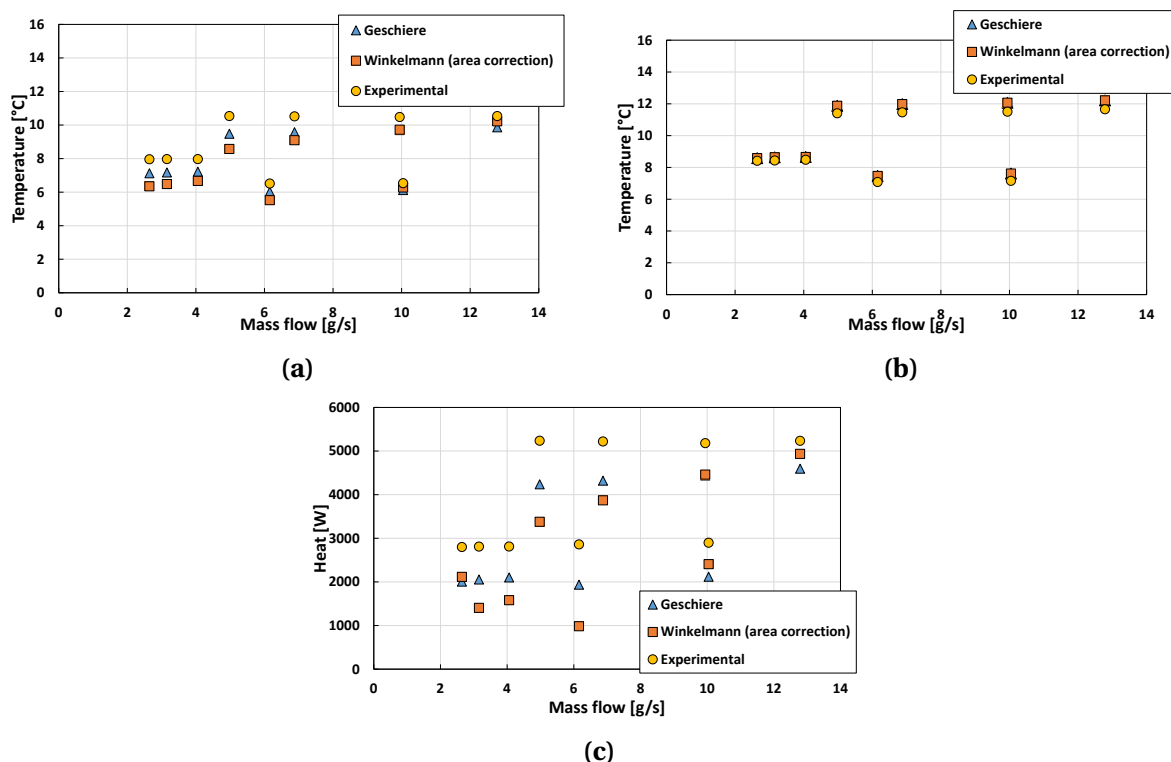


Figure 2.9: Comparison of the Winkelmann correlation to the correlation of Geschiere for different pure ammonia mass flows: (a) Cold water outlet temperature (b) Working fluid outlet temperature (c) Transferred heat. Note that the Winkelmann correlation uses a area correction, which will be discussed in more detail in section 5.3.2. Note that the heat input of all tests is not equal, so the trends do not symbolize anything.

ature of the working fluid stays within 2.4% accuracy, the cooling medium temperature doesn't exceed 2.7% and the cooling medium heat transfer is within 3%. The deviation will be different if we are only interested in the pure fluid situation and repeat all pure ammonia tests. The tests from figure 2.9 lead to a deviation of 4% for the working fluid outlet temperature, 8% for the water outlet temperature and 20% for the total heat transfer of the condenser. Despite these deviations, the heat transfer prediction is improved by the correlation of Geschiere in comparison with the correlation of Winkelmann. For this reason equation 2.24 has been used to predict the condensation heat transfer coefficient.

2.5.5. Pressure drop

In both the rating and sizing problems of heat exchangers, limitations are generally defined by economic considerations or by process limitations. Therefore, the pressure drop and the heat transfer coefficient are important. While the pressure drop in a single-phase flow in plate heat exchangers has been studied extensively, the industry lacks basic information on fluid flow evaporating or condensing in plate heat exchangers. Therefore, the model of Goudriaan and Kuikhoven assumes that the pressure drop is constant over the heat exchanger. A pressure drop is inevitably incurred in each fluid stream as it passes through the heat exchanger. Its estimation is critical to the overall design and selection of a heat exchanger. In order to predict the pressure drop on both the water and working fluid side

correctly, pressure drop correlations have been implemented in the model.

The research of Dahlgren [20] investigates the pressure drop of plate heat exchangers. The pressure drop depends on several components, namely the pressure drop due to friction, acceleration and elevation. The pressure drop results from the sum of all other pressure losses due to inlet/outlet flow distribution and includes the pressure drop in ports and manifolds [77], see equation 2.25.

$$\Delta P_{tot} = \Delta P_{fric} + \Delta P_{acc} + \Delta P_{ele} + \Delta P_{man}, \quad (2.25)$$

where ΔP_{fric} is the frictional pressure drop. This pressure drop is due to the friction along the plate walls, where the fluid flows through. This is the most important part of the pressure drop as concluded by Yan and Lin [89] for the evaporator and by Yan et al [90] for the condensers. These reports concluded that around 93-99% of the pressure drop occurs by friction, which means other factors that influence pressure drop can be neglected when sizing the heat exchangers. The frictional pressure drop is given by the following equation:

$$\Delta p_{fric} = \frac{\xi \dot{G}^2}{2\rho_{av}d_h} L_p = \frac{2f\dot{G}^2}{\rho_{av}d_h} L_p, \quad (2.26)$$

where ξ is the friction factor. In the literature it is also common to use the Fanning friction factor $f = \xi/4$. This factor is a function of the plate surface corrugation pattern, flow Reynolds number and fluid properties. Equation 2.26 is usable for single and two phase flow correlations. As the density of a fluid is not constant during condensation and evaporation, the density, ρ_{av} , should be determined by equation 2.27.

$$v_m = \frac{1}{\rho_{av}} = \frac{(1 - q_{av})}{\rho_l} + \frac{q_{av}}{\rho_v} \quad (2.27)$$

For two phase situation, boiling or condensation, the estimation of the friction factor becomes complicated. In literature, there is no unanimity for developing more precise two-phase flow friction factor correlations for PHEs [77]. Some survey reports recommend power law curve fitting for the friction factor. Ayub [9] and Focke et al [27] conclude that the geometry has influence on the pressure drop. The chevron angle is a major parameter since it affects the flow through the plates.

Dahlgren compares the single phase Fanning friction fraction correlation and validates its own correlation by some experimental experiments. Dahlgren gives the following correlations for the Fanning friction factor for single phase flow, equation 2.28.

$$f_{water} = 2.285 * Re_{water}^{-0.19} \quad (2.28)$$

Figure 2.10, shows the single phase Fanning friction factor correlation comparison. The correlation of equation 2.28 is similar to the correlation of Martin [57] proposed by VDI [8]. Therefore, the VDI correlation is used, since it has been validated in a wider range. Next to this, Gudjonsdottir [34] concluded that VDI Heat Atlas pressure drop calculation is a good correlation for the range of chevron angles around 60°. Equation 2.30 gives the VDI Heat Atlas correlation. Note that the Reynolds in this equation of the VDI Heat Atlas is with the hydraulic diameter, d_h , see equation 2.29. The friction factor is calculated with β_{flow} , which is the chevron angle of the plates measured from the vertical flow direction, while β is the chevron angle measured from the horizontal direction.

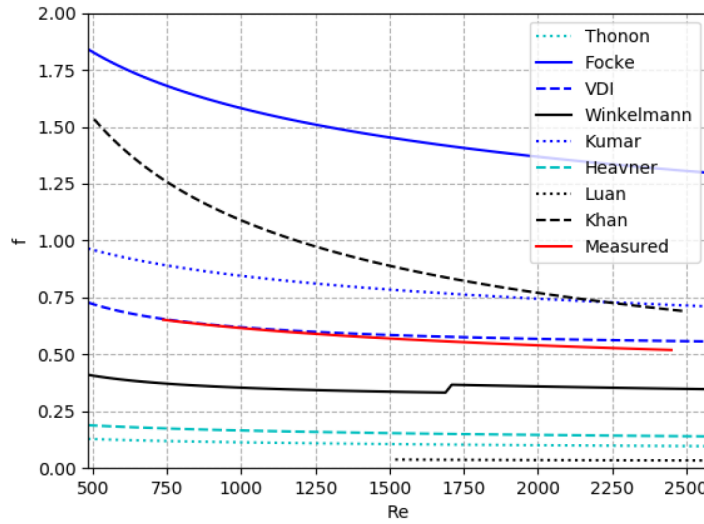


Figure 2.10: Fanning friction factor correlation comparison for single phase flow [20].

$$Re_{VDI} = \frac{\dot{G} * d_h}{\mu_l} \quad (2.29)$$

$$\frac{1}{\sqrt{\xi}} = \frac{\cos(\beta_{flow})}{\sqrt{0.18 \tan(\beta_{flow}) + 0.36 \sin(\beta_{flow}) + \xi_0 / \cos(\beta_{flow})}} + \frac{1 - \cos(\beta_{flow})}{\sqrt{\xi_1 * 3.8}} \quad (2.30)$$

$$\xi_0 = \frac{64}{Re_{VDI}} \quad (2.31)$$

$$\xi_1 = \frac{597}{Re_{VDI}} + 3.85 \quad (2.32)$$

For the two phase correlation, a distinction should be made between the evaporator and the condenser, since the boiling effect is different to the condensation effect. Dahlgren obtained a correlation for the Fanning friction factor on the working fluid side in the condenser, see equation 2.33 and the comparison in figure 2.11. For the evaporator, Ayub [9] proposes an other correlation, see equation 2.34.

$$f_{tp,wf,cond} = 270000 * Re_{eq,wf}^{-1.5} \quad (2.33)$$

$$f_{tp,wf,evap} = (n/Re^m)(-1.89 + 6.56 * R - 3.69 * R^2), \quad (2.34)$$

where:

$$R = \beta_{flow}/30$$

$m = 0.137$	$n = 2.99$	for $Re \leq 4000$
$m = 0.172$	$n = 2.99$	for $4000 < Re \leq 8000$
$m = 0.161$	$n = 3.15$	for $8000 < Re \leq 16,000$
$m = 0.195$	$n = 2.99$	for $Re > 16,000$

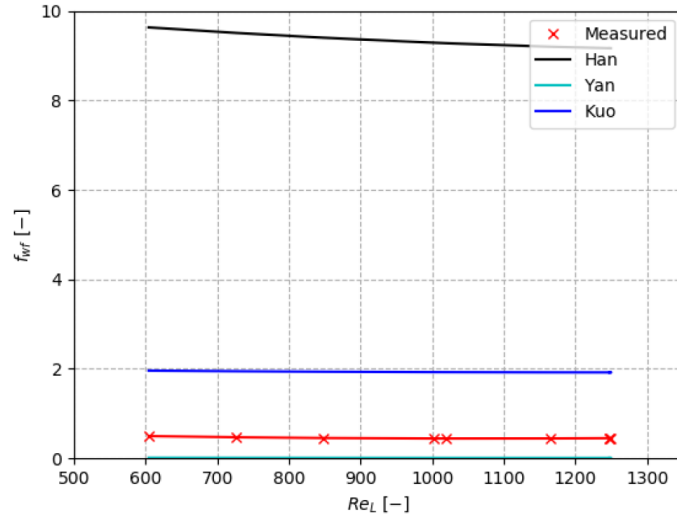


Figure 2.11: Fanning friction factor correlation comparison for condensing flow [20].

The other components of the pressure drop are given in the following equations:

$$\Delta P_{acc} = G^2 * v_m * \Delta q \quad (2.35)$$

$$\Delta p_{ele} = \frac{gL_p}{v_m} \quad (2.36)$$

$$\Delta p_{man} = 1.5 * \left(\frac{u_{av}^2}{2v_m} \right)_l \quad (2.37)$$

Dahlgren assumes that the pressure drop by elevation has influences on the total pressure drop next to the frictional pressure drop. The Δp_{acc} is usually negligible for single phase flows [77], but for two phase flows it can be assumed by equation 2.39. The pressure drop in the inlet and outlet manifolds and ports can be estimated from the empirical correlation. It is approximately 1.5 times the head due to the flow expansion at the channel inlet [89], same as for the one phase flow.

$$\epsilon = \left[1 + \frac{1-q}{q} (\rho_v / \rho_l)^{2/3} \right]^{-1} \quad (2.38)$$

$$\Delta p_{acc} = G^2 \left(\left[\frac{(1-q_{out})^2}{\rho_l(1-\epsilon_{out})} + \frac{q_{out}^2}{\epsilon_{out}\rho_v} \right] - \left[\frac{(1-q_{in})^2}{\rho_l(1-\epsilon_{in})} + \frac{q_{in}^2}{\epsilon_{in}\rho_v} \right] \right), \quad (2.39)$$

where ϵ_{in} and ϵ_{out} are the inlet and outlet void fractions, and q_{in} and q_{out} the inlet and outlet vapour qualities.

Yan et al [90] concluded that the pressure drop normally increases with the mass flux and that the increase in pressure drop is more significant than in heat transfer coefficient. Also for a lower mass flux an increase of the heat transfer coefficient was found with a small increase in the quality of the vapor in the condenser. Finally a higher pressure in the working fluid results in a slightly lower heat transfer coefficient, especially in the high vapor quality regime [89]. The effects of the pressure drop are small or even lower with an increasing of the system pressure.

2.6. Overall system calculations

In practice, the efficiency of the OTEC cycle is not so high as mentioned in the introduction. To analyze the cycle it is important to analyze the performance. The first law of thermodynamics is a version of the law of conservation of energy. Energy can be converted from the source to something else, but can be neither created nor destroyed. In addition to the first law of thermodynamics, we will use the second law of thermodynamics. The second law of thermodynamics states that the total entropy can never decrease over time for an isolated system. In real cases, there is some converted energy with the surroundings. Therefore the total entropy always increases and the process is irreversible. The gross efficiency is the ratio of external work achieved compared to the total energy expenditure, see equation 2.40.

$$\eta_{gross} = \frac{\dot{W}_{t,gross}}{\dot{Q}_{evap}} \quad (2.40)$$

Next to the gross efficiency, the net or thermal efficiency of the cycle can be derived, see equation 2.41, which is estimated as the net power produced by the cycle divided by the heat duty of the evaporator. The net power of the cycle is the gross power produced by the turbine minus the consumed power of the working fluid pump, see equation 2.42.

$$\eta_{thermal} = \frac{\dot{W}_{net}}{\dot{Q}_{evap}} \quad (2.41)$$

$$\dot{W}_{net} = \dot{W}_{t,gross} - \dot{W}_{pump, wf} \quad (2.42)$$

As soon as we look at the entire system, i.e. from the initial input to the final output, we can compute the overall thermal efficiency, equation 2.43.

$$\eta_{overall} = \frac{\dot{W}_{gen} - W_{pumps}}{\dot{Q}_{evap}}, \quad (2.43)$$

where W_{gen} is the produced power produced by the turbine generator and W_{pumps} is the total consumed power by the pumps, see equation 2.44.

$$\dot{W}_{pumps} = \dot{W}_{pump, H} + \dot{W}_{pump, C} + \dot{W}_{pump, wf} \quad (2.44)$$

Ultimately, the system efficiency can be derived, see equation 2.45.

$$\eta_{system} = \frac{\dot{W}_{gen} - W_{pumps}}{\dot{W}_{t,gross}}, \quad (2.45)$$

This thesis will focus on the influence of the turbine on the performance of the cycle. In the existing model of Goudriaan and Kuikhoven [33][52], the turbine component is missing, since the demo set-up has an orifice instead of a turbine. For the up-scaling of the model, it is necessary that a turbine will be used instead of the orifice. In the next chapter the turbine will be introduced.

3

Turbine

The turbine is a major component of the OTEC power cycle. Turbine's efficiency plays a key role in the design optimization of power cycles, like ORC's. The turbine is used to expand a vapour flow from the separator, which results in the rotating of the turbine blades. Its power is the main output of the OTEC cycle. Most literature focuses on the optimal efficiency that could be derived, but less literature focuses on the estimation of the real power production. In general, during design optimization the turbine efficiency is assumed as given, without checking the off-design performance. The importance of predicting real efficiency values becomes evident if the optimization of the thermodynamic cycle parameters, like mass flow, temperatures, kind of working fluid, is done to maximize the performance of the whole cycle. This chapter describes the working principles and reviews the literature about turbines. Finally, it introduces the method for modelling the turbine.

3.1. Turbine performance quantification

The inlet fluid contains a certain amount of energy in the form of kinetic, pressure and internal energy. The achievable extracted energy determines the power output of the turbine, which is the most important parameter with given designed cycle and the economical constraints. Therefore we determine the turbines efficiency, work and isentropic enthalpy drop. The power output of the turbine can be determined by:

$$\dot{W}_t = \dot{m} * (h_{in} - h_{out}), \quad (3.1)$$

where \dot{W}_t is the power delivered by the turbine in [W], \dot{m} is the mass flow in [$\frac{kg}{s}$], h_{in} and h_{out} are the respective in- and outlet enthalpies in [$\frac{J}{kg}$]. The outlet enthalpy depends on the performance, i.e. the isentropic efficiency, of the turbine. In general, the outlet enthalpy is unknown in off-design conditions. Figure 3.1a shows an expansion process by means of an enthalpy-entropy diagram. The process shows the changes in total energy, recall that the total energy is defined as $h_0 = h + \frac{u^2}{2}$. The ideal process, where the isentropic efficiency is equal to 100%, is represented by an isentropic change of state from start to end pressure, i.e. the same as for the real process. In such case a so called total-to-total, *tt*, efficiency is used, see equation 3.2.

$$\eta_{is,tt} = \frac{\text{Actual change in energy}}{\text{Ideal change in energy}} = \frac{h_{01} - h_{02}}{h_{01} - h_{02s}} \quad (3.2)$$

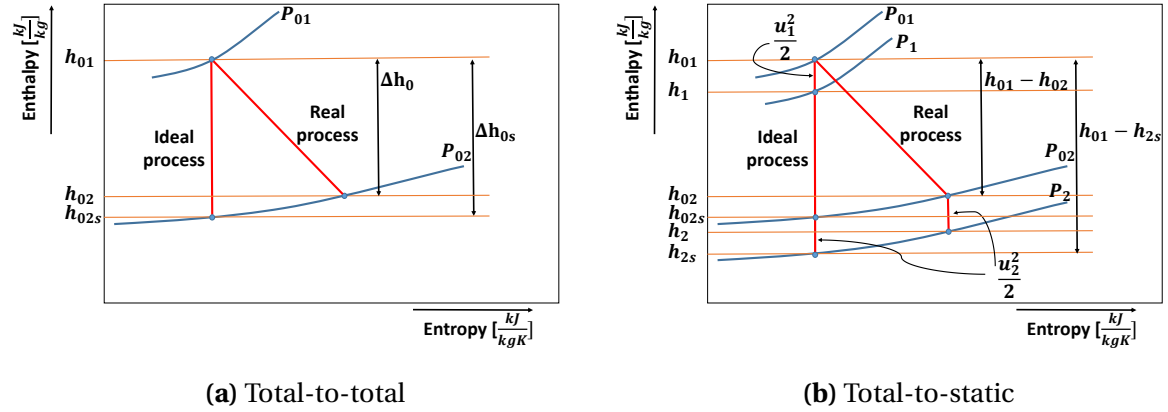


Figure 3.1: Expansion process. Turbine actual and isentropic work in an enthalpy versus entropy diagram. The 0 stands for the total energy, 1 and 2 for the start and end of the change of state and *s* for the isentropic case.

In certain cases the kinetic energy that is contained in the fluid can not be used, for example a turbine where the kinetic energy in the exhaust gases is not contributing to the total energy produced. In such case a so called total-to-static, *ts*, isentropic efficiency is used, see equation 3.3. Figure 3.1b shows the difference in the total and static energy. Thus, both figures show the work lost due to irreversibility and as soon as the $u_2 > 0$, the total-to-static efficiency is always smaller than the total-to-total efficiency.

$$\eta_{is,ts} = \frac{h_{01} - h_{02}}{h_{01} - h_{2s}} = \frac{h_{01} - h_{02}}{h_{01} - h_{02s} + \frac{u_2^2}{2}} \quad (3.3)$$

In the most studies about the turbine design, the total-to-static efficiency is used, so that the diffuser part can be left behind. The designing of a diffuser for a turbine is complicated matter which could be a study on itself. Therefore, using the total-to-static efficiency can be seen as a conservative estimate of the obtainable efficiency.

3.2. Scope

Table 1.1 gives the operating condition for the turbine. A variation of the warm seawater temperature ensures that the evaporation pressure changes, with the result that the conditions of the turbine changes. To describe the inlet flow, we can introduce the mass flow coefficient, see equation 3.4. In the turbine performance, this parameter is widely used and it represents the relative measure of its efficiency at allowing fluid flow. It describes the relation between the pressure and the corresponding flow rate [37].

$$\Phi = \frac{\dot{m}}{\sqrt{\frac{P}{v}}} = constant \quad (3.4)$$

The vapor flow is the driving force to rotate the blades of the turbine, which are connected to the shaft of the turbine. With the result that the shaft will rotated with a rotational speed, which subsequently is connected to the rotor of a generator. Between the turbine shaft and the generator, an optional gearbox is capable of controlling the rotational speed to its favorable speed. Thereafter, the stator of the generator is connected to the electricity grid. In grid connected systems the generator voltage and frequency are locked to the grid system,

which has a frequency of 50-60 *Hz*. Changing the energy output from the turbine does not affect the frequency and voltage but will cause the output current to increase resulting in an equivalent change in the generator output power. As soon as the generator will be connected to the grid, its speed should be run up so that its output frequency matches the grid before the connection is made. As soon as the rotational speed is not matching the synchronous speed, a torque will be present. Equation 3.5 gives the torque in [*Nm*], which is the power of the turbine divide by the angular velocity of the rotor. The relative motion between the stator's rotating field and the rotor speed is called the slip, *S*, see equation 3.6.

$$Torque = \frac{\dot{W}_t}{2 * \pi * N_{rotor}} \quad (3.5)$$

$$S = \frac{N_{stator} - N_{rotor}}{N_{stator}} * 100 \quad (3.6)$$

The rotor current and hence the torque are proportional to the slip within the stable operating region. A positive torque corresponds to a lower rotor speed than the synchronous speed, which is undesirable because it costs energy from the grid. At that moment the generator should not be connected to the grid. This situation is present during start-up situation. As soon as the stator is connected to the grid it provides the necessary rotating field, but the rotor shaft is driven by the turbine at a speed faster than the synchronous speed so that a negative torque is produced. With the result that the rotor will induce a current in the stator and the generator supplies energy output to the grid. At the synchronous speed the slip is zero, and no electricity would be consumed by the turbine or produced by the generator. Figure 3.2 shows the behavior of the torque and the rotational speed. Note that the torque applied at 0 to 100 % slip is not applied during start-up conditions. The absorbing phase means that energy is consumed by the turbine and in the generating phase a opposite effect is present.

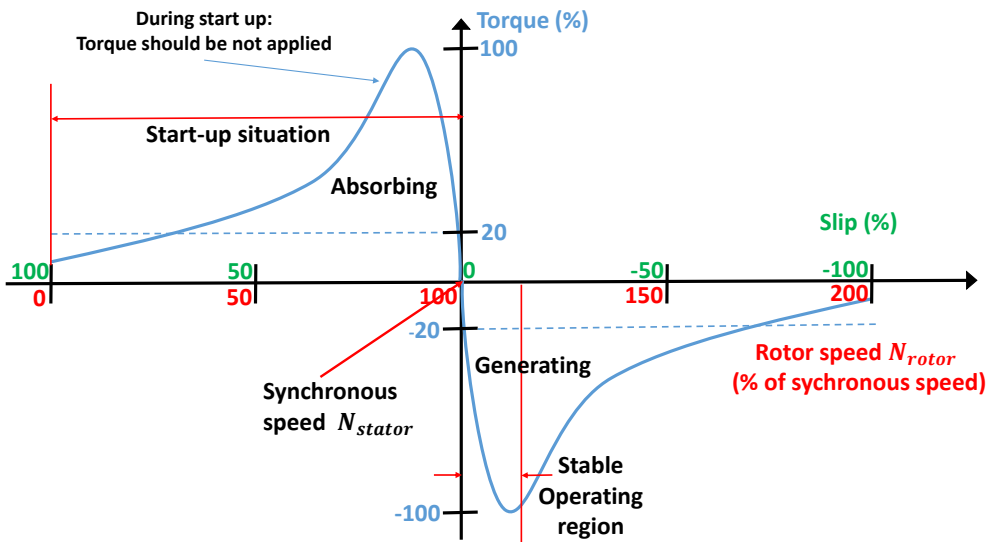


Figure 3.2: Torque and speed characteristics generator

Fig 3.2 shows the working principle of an induction motor, what makes it possible to operate at constant speed [82]. Next to this, no pressure control is necessary to operate at constant turbine speed. Therefore, an inline and bypass pressure reducing valves are unnecessary, which is favorable since all energy can be used.

In the ORC field each turbine is designed *ex novo* because each plant differs in the available thermal power and in the temperature of both the heat source and the cooling medium. Turbines can operate with different fluids in a large range of pressure and volume ratio's. Each optimized turbine design has its specific size and power output. The choice of the expansion machines strongly depends on the cycle operating conditions, type of working fluid and the range of net power output. In general, expansion machines can be categorized into two types as the volumetric type (i.e. scroll, screw, reciprocating piston and rotary vane expanders) and velocity type (i.e. axial flow and radial inflow turbines). The type of turbines available for this type of systems are the velocity expanders instead of the volumetric expanders. These turbines are classified as axial flow and radial inflow based on their flow path as shown in figure 3.3.

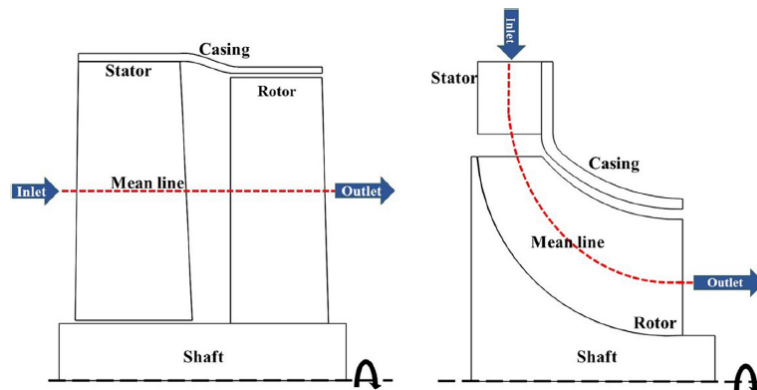


Figure 3.3: Schematic diagram of axial flow (left) and radial inflow (right) turbines [67]

Dankerlui [21] mentions that the design rotational speed for a single flow axial turbine can vary between 2577-5155 *RPM* to obtain high efficiencies. Next to this, he mentions that for single flow it is impossible to operate any radial configuration without a gearbox and multiple flow is unfeasible because of the complex connections between the radial stages. In OTEC systems, the temperature difference is small. This means that one stage turbines can be used according to Macchi and Perdichizzi [56]. Therefore we focus on single flow turbines.

Radial inflow turbines exhibit unique advantages of high efficiency, compact structure and light weight compared to the axial turbine when employed in the small scale applications [66]. Lazzaretto and Manente [54] compare the isentropic efficiencies between axial and radial turbines in different situations and conclude that radial turbines hold higher isentropic efficiencies at high volumetric ratios, which is the ratio of the volume flow between the outlet and inlet. However, table 1.1 shows that the volume ratio in OTEC conditions is small. In addition, radial turbines have also disadvantages. Kostors and Vincent [51] mention maximum turbine diameters for radial inflow architectures from 0.6 m up to 1.32 m. The difference in these values is due the different working conditions, which result in other mechanical stresses due to other temperatures and pressures. Dankerlui mentions this is right at the limit of what is possible to manufacture and therefore radial turbines are preferable for a 10MW OTEC set-up. Despite the fact that a radial turbine sounds hopeful, an axial turbine is the type of turbine which is preferred for 10 to 25 MW OTEC applications. Multiple literature studies conclude these preferences [21][34][56]. The advantages of an axial turbine are high power capacity, high efficiency at large scale and flexibility of operation under partial admission for off-design [67].

Axial turbines are common in the energy sector, such as geothermal turbines, biomass steam turbines, hydro axial-flow turbines and wind turbines. Approximately 90% of the electricity produced comes from axial-flow turbines around the world. Figure 3.4 shows the wide range of applications of axial turbines deployed in the energy production. Despite these many experiences with axial turbines, it is different for the OTEC application, since the conditions are different than for the applications from figure 3.4. Because of this there is a lack of knowledge of this range in literature.

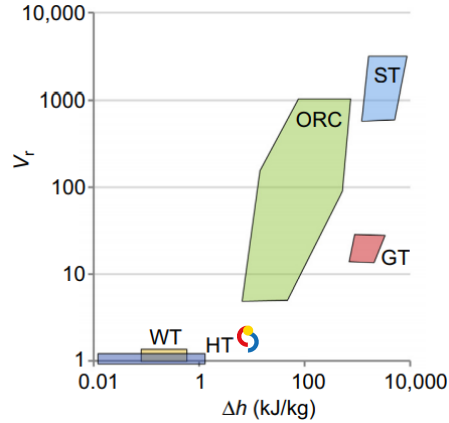


Figure 3.4: Range of application of commercial axial flow turbines: Gas Turbine (GT), Steam turbine (ST), Hydro Turbine (HT), Wind Turbine (WT) [55]. The BlueRise logo represents the range of the turbines in 10 MW OTEC plants. The y-axis gives the volumetric ratio and the x-axis represents the enthalpy drop over the turbine.

The choice for an axial turbine is confirmed by the gas turbines performance of Walsh [85]. This author categorized the range for radial and axial turbines with the reduced mass flow, see equation 3.7. The reduced mass flow is proportional to the given earlier mass flow coefficient. The reduced mass flow is a parameter which is more often encountered in turbine performance studies. Note that Walsh uses the reduced mass flow in $[kg * K^{\frac{1}{2}} s^{-1} kPa^{-1}]$. With the result that the values from table 1.1 give a higher reduced mass flow than the 0.5 of the boundary for axial turbines. Therefore, only axial turbine configurations are considered at this capacity.

$$\dot{m}_{red} = \frac{\dot{m} * \sqrt{T}}{P} \quad (3.7)$$

3.3. Operating range

Turbines range from micro scale to very big machines, therefore Astolfi and Macchi [6] introduce three parameters as independent variables for parametric analysis of axial-flow turbines. Equations 3.8-3.10 give the three suggested variables, the volumetric ratio (V_r), the size parameter (SP) and the specific speed (N_s). The volumetric ratio is the ratio between the inlet and outlet volume flow of the turbine in isentropic case. The size parameter tells more about the geometry of the turbine and it is actually a kind of measure for how large the diameter of the turbine will be, see more in the study of Astolfi and Macchi [6].

$$V_r = \frac{\dot{V}_{out,is}}{\dot{V}_{in}} \quad (3.8)$$

$$SP = \frac{\dot{V}_{out,is}^{0.5}}{\Delta h_{is}^{0.25}} \quad (3.9)$$

$$N_s = \frac{N}{60} * \frac{\dot{V}_{out,is}^{0.5}}{\Delta h_{is}^{0.75}}, \quad (3.10)$$

where \dot{V} is the volume flow in [$\frac{m^3}{s}$], Δh_{is} is the isentropic enthalpy drop over the turbine in [$\frac{J}{kg}$] and N is the shaft output speed in [RPM]. Further, V_r is the volumetric ratio [-], SP is the size parameter [m] and N_s is the specific speed, which is a dimensionless number to give more information about the performance of the turbine. It is an indication if the turbine performs on the design rotational speed or if it runs far from its optimal design conditions.

Using the operating environmental conditions and the given parameters, the ranges of the OTEC system can be derived. Table 3.1 shows the ranges where the turbine will operate in OTEC conditions. It is assumed that the mass flow can vary +- 50% from the design mass flow of table 1.1.

Table 3.1: Ranges of specific parameters for the turbine for a 10 MW OTEC Cycle

Parameter	Range	Unit	Parameter	Range	Unit
\dot{m}	220-660	$[\frac{kg}{s}]$	N	2577-5155 [21]	$[RPM]$
P_{in}	6.7-11.3	$[bar]$	Φ	0.07-0.35	$[\frac{kg^{\frac{1}{2}} m^{\frac{3}{2}}}{sPa^{\frac{1}{2}}}]$
T_{in}	285-302	$[K]$	V_r	1.2-1.9	$[-]$
P_{out}	5.4-8.5	$[bar]$	SP	0.41-0.96	$[m]$
Δh_{is}	27.5-38.0	$[kJ/kg]$	N_s	0.10-0.34	$[-]$

3.4. Performance maps

The turbine model will be the main difference with the model of Goudriaan and Kuikhoven [33][52]¹. At this moment there is no axial turbine installed in the experimental OTEC setup. A valve with a manually adjustable opening is fitted instead, to simulate the pressure drop normally induced by a turbine. With a certain fluid flow through a fixed constricted area, the pressure drop in the experimental setup is fixed. Therefore, in the existing model the pressure drop is an input of the model.

Many studies in the literature compare the effects of the working fluid on the plant performance for a fixed turbine efficiency, whereas little focus is given to the off-design performance efficiency charts of the turbines. Designing a turbine means finding the optimal velocities and rotor and stator angles, which leads to specific velocity triangles. Dankerlui [21] investigates the design of a turbine for OTEC applications and figure 3.5 shows the velocity triangles of his design.

When designing the blades of a turbine, the degree of reaction and velocity ratio are important factors. The degree of reaction is defined as the ratio of isentropic enthalpy change in stator to the rotor. The velocity ratio is the ratio of the blade velocity, U and the absolute velocity, V_2 . In turbine design studies, it is mainly about optimize the design to achieve the highest total-to-static efficiency, the same in the study of Dankerlui. He shows that

¹The turbine is a new component with respect to the report of Goudriaan and Kuikhoven

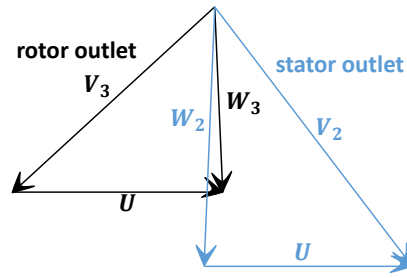


Figure 3.5: Velocity triangles of 1 stage turbine with design angles of Dankerlui [21].

the total-to-static efficiency for a single stage axial turbine lies between 89.1% and 91.2%. However, the total-to-total efficiency is required. In the literature there are several efficiency charts to determine the achievable total-to-total isentropic efficiency. These charts are based on both inflow methods of turbines, radial or axial. In general maps, the influence of the compressibility and turbine size is shown through the volumetric expansion ratio and size parameter. These maps can be included in a general design optimization of the turbine, and especially the whole power cycle. Which results in the optimum design without assumptions on turbine efficiency. The primary numerical classification of a turbine is its specific speed. It describes the speed of the turbine and its maximum efficiency with respect to the conditions and the flow rate of the turbine. The specific speed is derived by the flow conditions and the desired shaft output speed and therefore independent of turbine geometry. For the scaling of the power cycle, the specific speed is also an ideal parameter. The specific speed can be used to reliably scale an existing design of known performance to a new size with corresponding performance.

One of the promising performance maps of the total-to-total efficiency is of Astolfi and Macchi [6], which is based on the Craig and Cox losses [18]. In this research, the ideal gas law is used with a fixed heat capacity ratio. The heat capacity ratio is the ratio of the heat capacity at constant pressure (c_p) to heat capacity at constant volume (c_v). For ideal gas it is denoted as the $\gamma = \frac{c_p}{c_v}$ and it symbolizes the isentropic expansion factor. For the assumption that it is valid to use the ideal gas law, the compressibility, Z is important. The turbine operates far away from the critical point, where the non-ideal behavior is the greatest. For the OTEC conditions the compressibility is around the 0.91 [-] [21]. There is a deviation in the compressibility factor from ideal behavior, which is expected especially at the inlet of the turbine. Nevertheless, Dankerlui [21] concludes that usage of similarity parameters for ideal gas is still viable. Next to the compressibility, the heat capacity ratio should have no influence to conclude the ideal gas law is valid. The heat capacity ratio in the OTEC ranges is around the 1.43 [-]. Figures 3.6a and 3.6b show the influence of the heat capacity ratio. Despite, that the figures are with the total-to-static efficiency and with a size parameter which deviates from the OTEC range, we can conclude that the influence of the heat capacity ratio increases with an increase of volumetric ratio or increase of pressure ratio. Thus, the influence of the heat capacity ratio can be neglected in the range of OTEC.

The research of Da Lio et al. [19] is not using the ideal gas law, but uses RefProp. It is focused on ORC turbines, and thereby useful because it uses the same working fluids as other OTEC researches. Da Lio states that the efficiency is a function of five independent variables: specific speed, specific diameter, Reynolds number, Mach number and specific heat ratio [19]. The specific diameter, d_s , in [-] is given in equation 3.11. Notice that the

specific diameter is a dimensionless number using the size parameter and the root mean square diameter, d , in $[m]$. The Mach number is the ratio of flow velocity past a boundary to the local speed of sound.

$$d_s = d * \frac{\Delta h_{is}^{0.25}}{\dot{V}_{out,is}^{0.5}}, \quad (3.11)$$

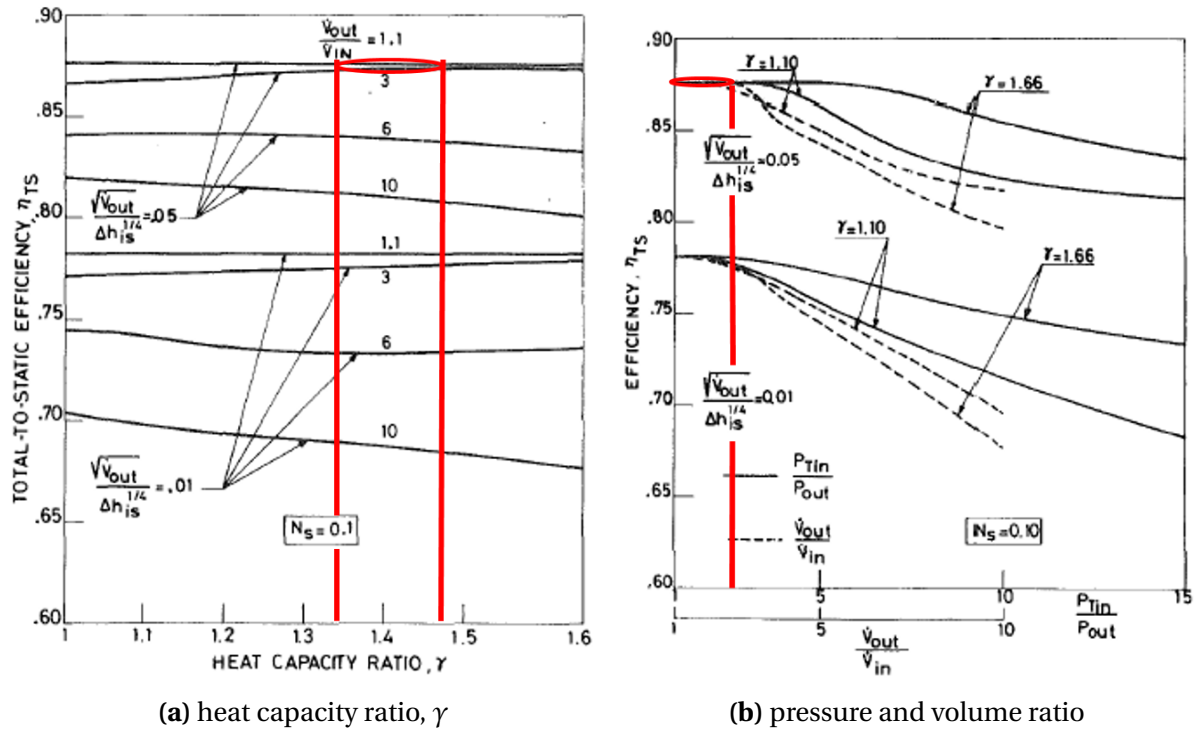


Figure 3.6: Influence of the efficiency of a turbine. Note that different volumetric flow rate ratios, different heat capacity ratios and different turbine dimensions are used [56]. The red marks highlighted the most corresponding OTEC range.

Vonk [83] mentions that the Reynolds number is negligible, since the flow regime is fully developed in the operating conditions of the turbine. Further, Vonk says the efficiency predictions for axial turbines using the ideal gas law are quite consistent, while Da Lio predicts slightly lower efficiency's using the RefProp database. Thereafter, Vonk reports that the efficiencies show more or less the same trend, indicating that although there may be absolute differences between the charts, the relative error of the predicted total-to-total efficiency's are expected small. Thus, the total-to-total efficiency prediction of these different authors leads to the same in the range of OTEC and the chart by Astolfi and Macchi [6] is used as an indication of the design turbine performance.

3.5. Design performance turbine

Astolfi and Macchi [6] concluded that there is a lack of availability of numerical data to estimate the design efficiency of turbines in the scientific literature. Therefore, they use these maps and make a dedicated numerical tool for estimation of the isentropic efficiency. An own performance map of the isentropic efficiency is obtained using the specific speed, size parameter and the volumetric flow rate as inputs, see figure 3.7. For this report the data

of the report of Astolfi and Macchi [6] are used for the design turbine performance and to show the off-design performance deviation. Astolfi and Macchi validate the data set in their research. Because the heat capacity ratio has less influence, the ideal gas law is acceptable and the data set is validated, therefore it is assumed that it is valid to use the data set of Astolfi and Macchi.

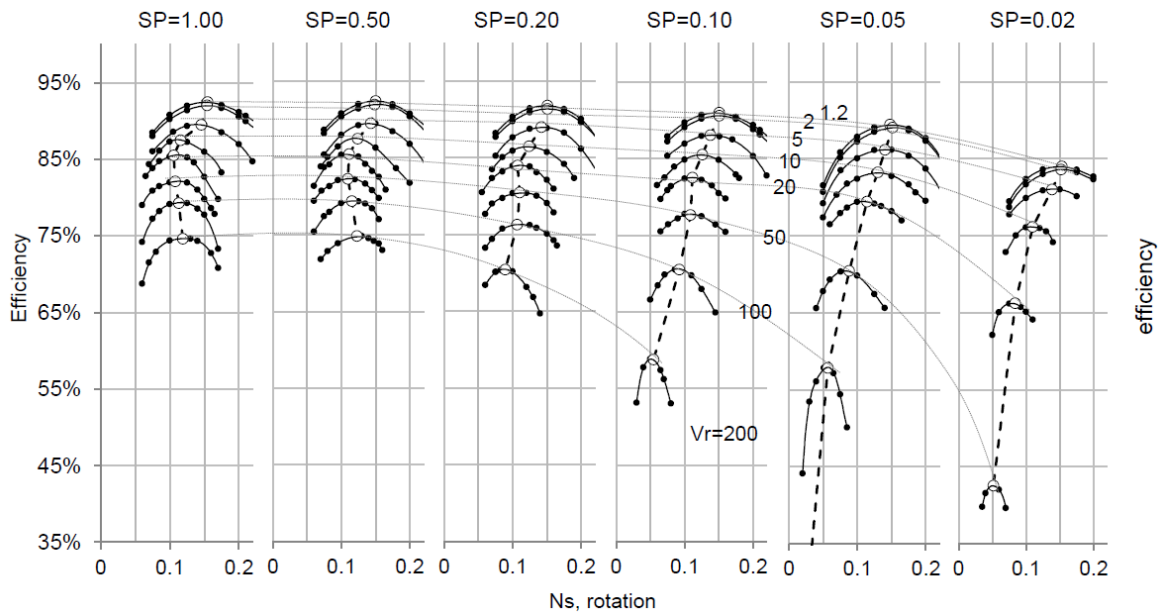


Figure 3.7: Results for the single stage turbines. Black markers (•) are representative of the optimal configuration for each combination of SP , V_r and N_s . White markers (○) identify the turbine designs at optimized rotational speed [6].

3.6. Effect of the multiple parameters

The suggested parameters of Astolfi and Macchi have each its own effect of the efficiency losses breakup. For better understanding of the effects of the parameters, a parametric analyses is presented in figure 3.8. The first shows the effect of the specific speed at fixed SP and V_r . The other figures focus on varying the V_r and SP at optimized rotational speed. Note that figures not use the same corresponding values, so the highest possible efficiencies are not the same in each figure.

3.6.1. N_s

Fig 3.8a shows that the secondary and leakage losses are together with a small specific speed and the kinetic losses with a high specific speed. The optimum for the specific speed is around the 0.15. The efficiency drops as the turbine does not run at the optimal specific speed, therefore the rotational speed must always be optimized.

3.6.2. V_r

The breakdown of efficiency losses in fig 3.8b shows that the maximum attainable efficiency is a decreasing function of V_r . The effects of the volume ratio is noticed at the velocities through the turbine, but the effects will be small since the flow is always subsonic in the range of OTEC. Therefore, high efficiency can be attained since the height over the diameter of the turbine design is favourable in the OTEC range [6]. In supersonic flows, which are

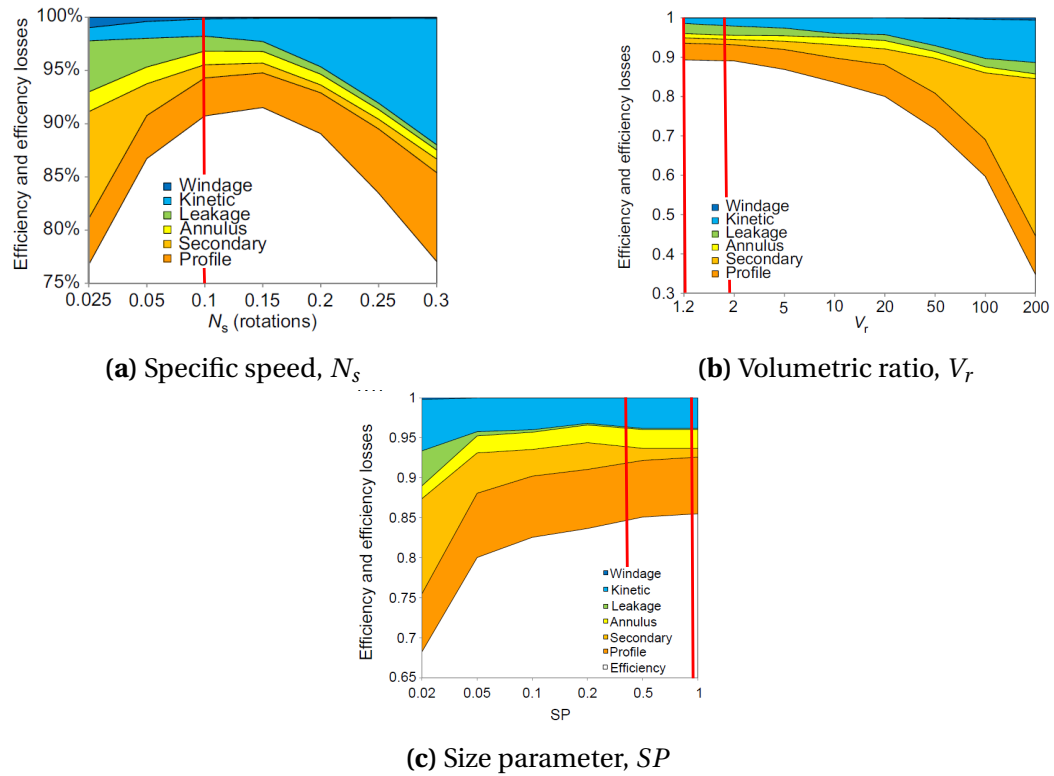


Figure 3.8: Parametric analysis of the efficiency losses breakup for a single stage axial turbine. Note that the figures (a, b and c) use other values than the specific OTEC range, nevertheless the effect of the relevant parameter can be investigated. The red lines represent the values from table 3.1. [55].

common in high volumetric ratios, the kinetic losses are high. The additional losses due transonic and supersonic flow conditions are the loss phenomena such as shock waves, which reduce turbine efficiency and ask a specific turbine design. In these situations a turbine with more stages is recommended.

3.6.3. SP

Small size parameters lead to very small volume flow rates at the turbine inlet. Due to geometrical limits, the diameter will be smaller together with an increase of rotational speed in order to maintain the optimal value of specific speed. These two effects result in a strong efficiency drop for small turbines with a considerable increase of secondary and leakage losses, see figure 3.8c. The OTEC conditions ensure that the system will operate in the region of large SP values, therefore it is able to keep the losses small.

3.6.4. Optimum specific speed

In figure 3.7, the white markers identify the turbine designs at optimized rotational speed. Vonk [83] introduces a fitted correlation to obtain these highest possible efficiencies, which from now on is independent of the specific speed. Equations 3.12 to 3.15 show the correlation of Vonk.

$$a = -17.335, b = -0.31176, c = -13.4053, d = 9.4899, e = 109.9875 \quad (3.12)$$

$$m = \left(\frac{1}{SP} * (SP - 0.002) \right)^{0.5} \quad (3.13)$$

$$n = \frac{-1}{(SP * 68)^{1.4}} \quad (3.14)$$

$$\eta_{is,t} = \frac{a * V_r^b + \frac{c * \log(V_r)}{\log(d)} + m * e + n * V_r}{100} \quad (3.15)$$

3.7. Off-design modelling of the turbine

From now, the design performance of the turbine is derived, and we can continue with the off-design part. This will play a major role in the quantification of the impact of the turbine in variable environmental conditions. The turbine is in fact a nozzle with a certain throttling condition, which is determined on the basis of the inlet conditions, the turbine blades and the high back pressure. High back pressure means that the outlet pressure of the turbine is higher than atmospheric pressure. The throttling behavior is present over turbines, but also over the orifice in the demo set-up. In the existing model, the pressure drop over the orifice, which was observed in the OTEC demo set-up, was a necessary parameter, but a fixed pressure drop does not symbolize the reality correctly. Therefore, the turbine and orifice are modelled like a nozzle [71]. In the OTEC system, no pressure control is available and the pressure drop can be controlled with the adjustable turbine vanes. In off-design conditions the mass flow coefficient will change continuously as soon as the conditions change. Stodola introduces a method to use this mass flow coefficient to determine the pressure drop. This method is widely used in off-design performance calculations [13][29]. Especially in cases where the thermodynamic aspect is the most important, which in this thesis is also the main goal to quantify.

3.7.1. Stodola

The law of Ellipse, or Stodola's cone law is a method to estimate the highly non-linear dependence of extraction pressures with a flow for multiple or single stage turbines with high back pressure, when the turbine nozzles are not choked. A choked flow is if the Mach number is equal to one, a compressible flow effect takes place, because of this the flow velocity is limited. The limiting case of the Venturi effect is when a fluid reaches the state of choked flow, where the fluid velocity approaches the local speed of sound. A choked flow is the result of the Venturi effect, see figure 3.9. Venturi effect occurs when a fluid flows through a constricted area, which is present in the orifice or turbine. Dankerlui [21] concludes that the turbine in an OTEC cycle has subsonic flow, since the Mach number is lower than one, the flow is non-choked. The molecular weight of ammonia ($17 \frac{kg}{kmol}$) is close to that of the water ($18 \frac{kg}{kmol}$) and therefore it is possible to use normal back-pressure turbines and no special materials are needed for ammonia [61].

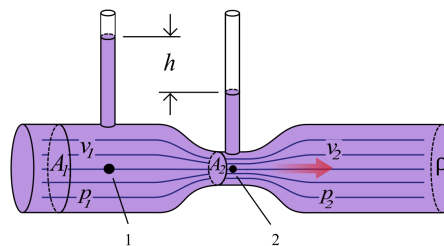


Figure 3.9: Venturi Effect [70]

The method of Stodola is important in turbine off-design calculations, widely used in steam turbines but also in ORC comparison literature studies [91] and states that equation 3.16 applies. Figure 3.10a shows the proportionality of the elliptical equation and shows that if the back pressure drops the nozzle chokes due to sonic conditions, thereafter the curve is flat. The ellipses at various pressures create a cone, see figure 3.10b [75]. The axes are made relative to the pressure and mass flow of table 1.1.

$$\Phi \propto \sqrt{1 - \left(\frac{P_{out}}{P_{in}}\right)^2} \text{ or } \Phi = K * \sqrt{1 - \left(\frac{P_{out}}{P_{in}}\right)^2} \quad (3.16)$$

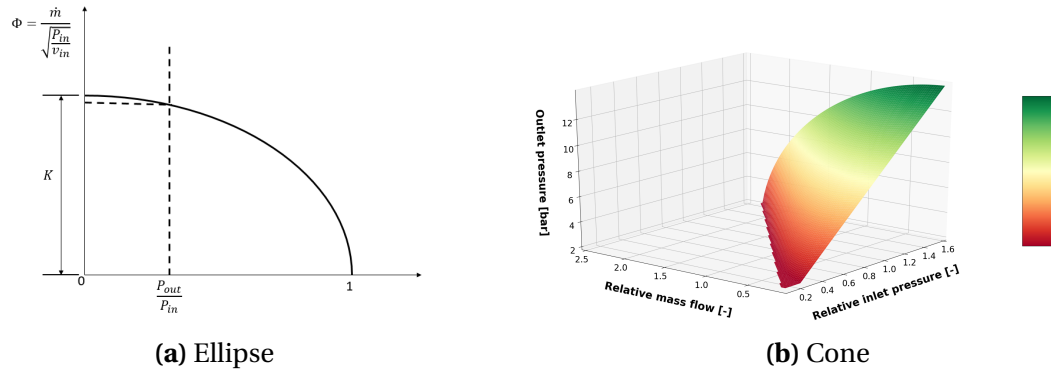


Figure 3.10: Stodola

The proportionality of Stodola's Ellipse, equation 3.16, can be restated as:

$$\frac{\Phi_{in,off-design}}{\Phi_{in,on-design}} = \frac{\sqrt{1 - \left(\frac{P_{out,off-design}}{P_{in,off-design}}\right)^2}}{\sqrt{1 - \left(\frac{P_{out,on-design}}{P_{in,on-design}}\right)^2}} \quad (3.17)$$

In on-design situation, a parameter can be obtained which is constant for all loads, the Stodola Constant Y_{design} , see equation 3.18. The Stodola Constant symbolizes the design of the nozzle area and influences the pressure levels of the turbine. This coefficient depends directly on the ratio between inlet and outlet pressures of the turbine. By some algebraic rearrangements of equation 3.17, the equation of the inlet pressure, see equation 3.19, or outlet pressure, see equation 3.20, can be achieved. In equations 3.19 and 3.20, the mass flow coefficient is computed with the present conditions.

$$Y_{on-design} = \frac{P_{in,on-design}^2 - P_{out,on-design}^2}{P_{in,on-design}^2 * \Phi_{on-design}^2} \quad (3.18)$$

$$P_{in} = \frac{P_{out}}{\sqrt{1 - \Phi^2 * Y_{on-design}}} \quad (3.19)$$

$$P_{out} = P_{in} * \sqrt{1 - \Phi^2 * Y_{on-design}} \quad (3.20)$$

Once the method of calculation of the pressure levels uses equation 3.19, then the solving the system is backwards. The method will be implicit, since the mass flow coefficient contains the inlet pressure. Equation 3.20 is, of course, explicit. As already mentions the

Stodola Constant symbolizes the passing area of the turbine and therefore the position of the blades. Thus, a variation of the Stodola constant, Y_{design} , symbolizes the variation of the position of the blades. This is called in literature, the variable turbine geometry (VTG). Therefore, the f_{VTG} can be introduced, which is the multiplier of the Stodola Constant. A variation of $\pm 50\%$ of the design value shows good agreement with the range of OTEC. An increase of the Stodola Constant corresponds to an increase of the pressure drop, so a decrease of the mass flow. In other words, an increase of the Stodola Constant means tightening the nozzle. From now, an optimization of the off-design model is necessary to find the optimal position of the vanes for every specific environmental condition, which will be discussed in more detail in section 5.3.5. In the off-design model, the turbine will be used equation 3.20, which is explicit, so no further reduction is necessary. With the mass flow coefficient, the equation is completed and results in:

$$P_{out} = P_{in} * \sqrt{1 - \frac{\dot{m}_{in}^2 * v_{in}}{P_{in}} * Y_{on-design}} \quad (3.21)$$

Ultimately, the non-linear relations of the pressure drop and pressure ratio are derived, see equations 3.22 and 3.23.

$$\Delta P = P_{in} * \left(1 - \sqrt{1 - \frac{\dot{m}_{in}^2 * v_{in}}{P_{in}} * Y_{on-design}} \right) \quad (3.22)$$

$$P_r = \frac{1}{\left(1 - \sqrt{1 - \frac{\dot{m}_{in}^2 * v_{in}}{P_{in}} * Y_{on-design}} \right)} \quad (3.23)$$

As soon as the variation of the mass flow rate through the turbine is small, Ray [69] concludes that the turbine stage efficiency is approximately constant and does not change significantly for small deviations from design conditions. Therefore, the thermodynamic index, $\zeta = [\gamma * (2 - \eta_{is}) + \eta_{is}] / \gamma$, is reasonably constant. Assuming an identical law of expansion for both design and off-design conditions yields equation 3.24 [69]. With this formula, an initial guess of the mass flow in off-design conditions can be made and therefore less iterations are needed.

$$\dot{m} = \frac{\dot{m}_{des}}{\sqrt{P_{inlet,des}^\zeta - P_{outlet,des}^\zeta}} * \sqrt{P_{inlet}^\zeta - P_{outlet}^\zeta} \quad (3.24)$$

3.7.2. Turbine isentropic efficiency

As soon as the turbine operates in off-design conditions, the velocity of the turbine blades varies, which results in other velocity triangles of the turbine. As soon as the exit velocity of the stator decreases, the velocity ratio increases. A negative incidence angle of the rotor is the result, which leads that vapor flow strikes the suction side of the blade. Hereby, the degree of reaction and the leakage loss increase and therefore the efficiency reduces [71]. To determine the off-design efficiency of the turbine, a off-design performance map is required. A map of the isentropic efficiency of the turbine is mostly a function of the mass flow coefficient or reduced mass flow. However, OTEC operates in a low pressure ratio range with high volumetric flows and figure 3.4 shows that this is not in the range of normal applications of axial turbines. This results in that there is a lack of off-design performance

maps of the range of OTEC. Therefore, a performance map should be made of the turbine by means of a correlation. The correlation should reflect the efficiency changes due to changes in the conditions of the turbine, so it evaluates the off-design efficiency relative to the design efficiency. Despite the lack of knowledge of correlations for the performance prediction, there are two correlations that have been selected to investigate the applicability. The correlation of Keeley [46], see equation 3.25 and the correlation of Jüdes et al. [43], see equation 3.26.

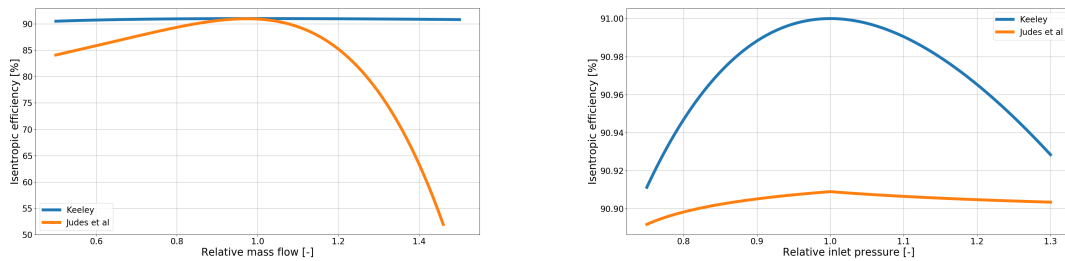
$$\eta_{is} = \eta_{is,des} * \sin \left[0.5 * \pi * \left(\frac{\dot{m}_{in} * \rho_{in,des}}{\dot{m}_{in,des} * \rho_{in}} \right)^{0.1} \right] \quad (3.25)$$

$$\eta_{is} = \eta_{is,des} * \left(-1.0176 * \left(\frac{\dot{m}}{\dot{m}_{des}} \right)^4 + 2.4443 * \left(\frac{\dot{m}}{\dot{m}_{des}} \right)^3 - 2.1812 * \left(\frac{\dot{m}}{\dot{m}_{des}} \right)^2 + 1.0535 * \left(\frac{\dot{m}}{\dot{m}_{des}} \right) + 0.701 \right) \quad (3.26)$$

At partial-load operation, the efficiency prediction of Jüdes et al. must be adjusted with respect to changes in the outlet quality, Δq . When the exiting quality is lower than 1, this adjustment is carried out using the equation 3.27.

$$\eta_{is,corr} = \eta_{is} - \frac{1}{2} * \Delta q \quad (3.27)$$

The correlation of Keeley is mostly used in the off-design performance prediction studies in the field of ORC, like Calisi [13], Gabbrielli [29] and Yoon [91]. The correlation of Jüdes et al is mostly used in the performance predictions of steam turbines, like Gudjonsdottir [34] and Jüdes and Tsatsaronis [42]. The comparison of the correlations of Keeley and Jüdes et al. is shown in figure 3.11, where the mass flow or inlet pressure are assumed to be constant.



(a) The efficiency versus the relative mass flow at constant inlet pressure (b) The efficiency versus the relative inlet pressure at constant mass flow.

Figure 3.11: Comparison of the correlations of Jüdes et al and Keeley.

It can be concluded that the correlations disagree with each other. In the correlation of Keeley, more effect is visible of variation in the inlet pressure, while Jüdes et al. show more variation in performance with a variation of the mass flow. The correlation of Jüdes et al. seems more a correlation based on experimental data and the effect of operating outside its design area is more present. Therefore, the correlation of Jüdes et al. will be selected.

After the isentropic efficiency is obtained, the outlet enthalpy of the turbine can be computed with equation 3.2 and finally the power output of the turbine can be determined with equation 3.1. With the equation of state all the other properties of the outflow can be derived. The mechanical work is converted to electrical work with a generator. Between the turbine and generator, a gearbox is optional.

3.7.3. Gearbox and generator off-design efficiency

The gearbox is a transmission machine between the turbine and the generator, which provides controlled application of the power. The gearbox ensures speed and torque conversions from a rotating power source to the generator, for this it uses gears and gear trains. After this, the generator converts the motive power into electrical power for use in an external circuit. The gearbox and generator work with a specific efficiency, which depends on the partial load. Therefore, equations 3.28 and 3.29 can be used to derive the performance of the gearbox and generator. The equations are derived from the research of Haglind [36] and use the partial load as depending factor of the performance. In the equation of the generator, the efficiency is the ratio of the electrical power to the mechanical power. A fraction of the total losses in design are the copper losses, F_{CU} . We assume the value of F_{CU} is 0.43, which gives a good agreement of the off-design efficiency of the generator [36].

$$\eta_{gear,off} = \frac{PL * \eta_{gear,des}}{PL * \eta_{gear,des} + (1 - \eta_{gear,des})} \quad (3.28)$$

$$\eta_{gen,off} = \frac{\dot{W}_{elec}}{\dot{W}_{mech}} = \frac{PL * \eta_{gen,des}}{PL * \eta_{gen,des} + (1 - \eta_{gen,des}) * [(1 - F_{CU} + F_{CU} * PL^2)]}, \quad (3.29)$$

where, PL stands for the partial load and is defined as the ratio of power out of the gear at part load to that in design. The figures 3.12a and 3.12b show the efficiencies versus the load.

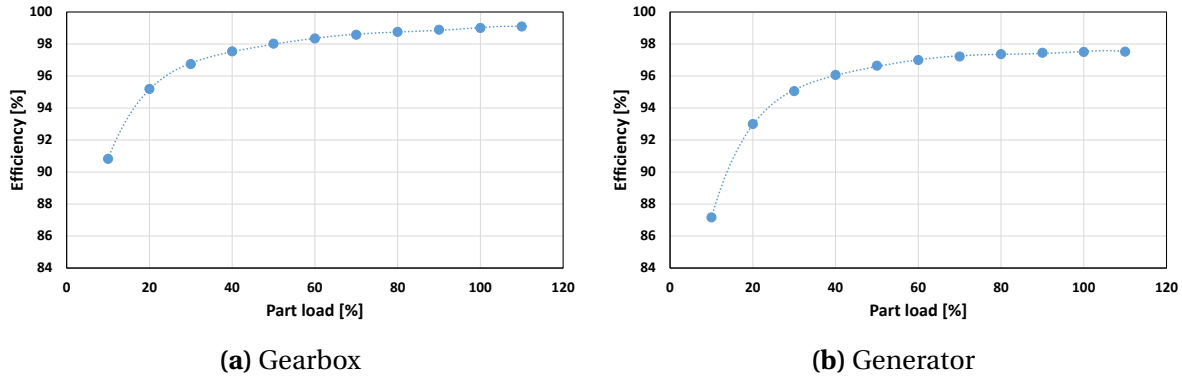


Figure 3.12: Efficiency versus load.

Ultimately, the power output to the electrical grid can be obtained with equation 3.30, using the efficiency of the turbine $\eta_{is,t}$, gearbox, η_{gear} and generator, η_{gen} .

$$\dot{W}_{gen} = \dot{m}_t * \eta_{gear} * \eta_{gen} * \eta_{is,t} * (h_{in} - h_{out,is}), \quad (3.30)$$

3.7.4. Qualitative considerations

Using the equations of sections 3.7.1 and 3.7.2 with the parameters and corresponding values from table 3.1, a qualitative analysis and the trends of the turbine efficiency are presented. The analysis starts with the influence of the inlet conditions on the pressure ratio and pressure drop over the turbine, see figures 3.13a-3.13d. The relative inlet pressure and relative mass flow are relative to the reference values from table 1.1.

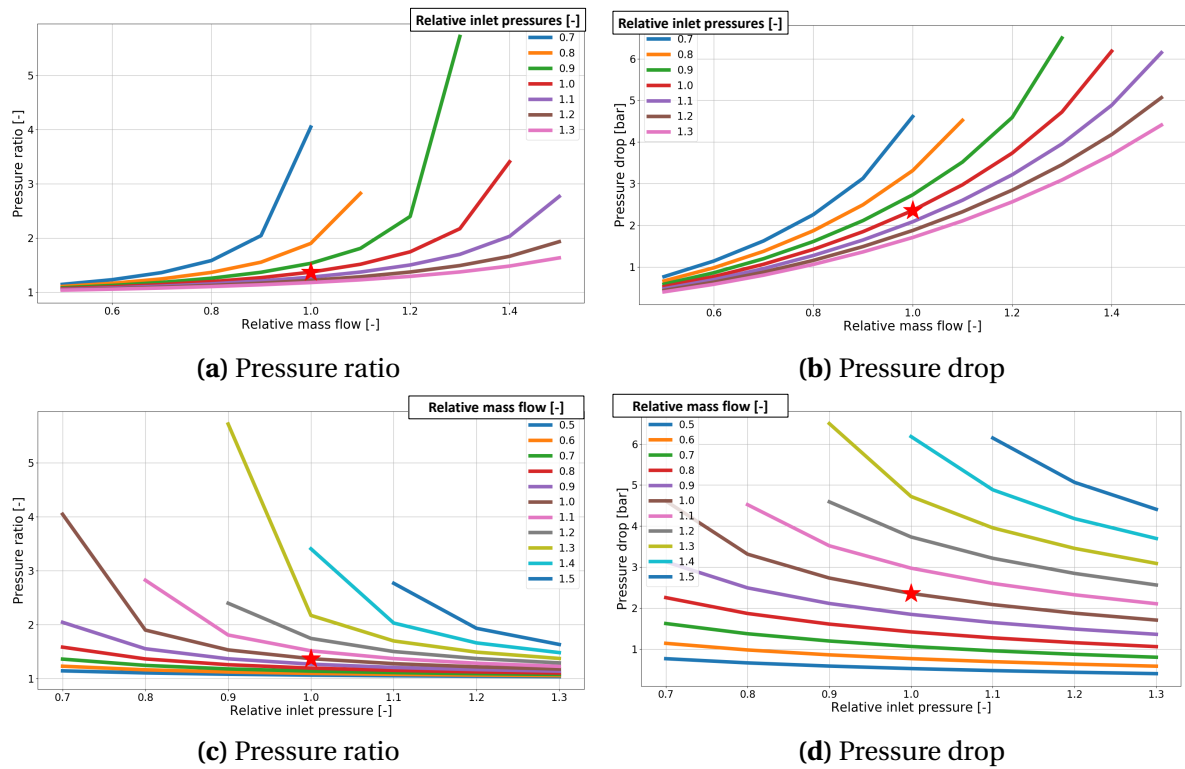


Figure 3.13: Influence inlet conditions, where the relative mass flow or relative inlet pressure is varied for different relative mass flows or inlet pressures of the turbine. The ★ represents the design point.

The influence of the inlet conditions is clear, a higher relative mass flow leads to a higher pressure ratio and pressure drop and the opposite applies to the relative inlet pressure. The influence of the relative mass flow and inlet pressure are both non-linear on the pressure drop and pressure ratio. This leads to the conclusion that the deviation from the design pressure ratio and pressure drop is larger for high relative mass flows and a small relative inlet pressure. The correlation of Jüdes et al. reflects the changes in off-design efficiency due to the changes in the conditions of the turbine. This results in that it is possible to draw a off-design performance map, see figure 3.14. It shows the isentropic efficiency of the turbine versus the relative inlet mass flow and relative inlet pressure.

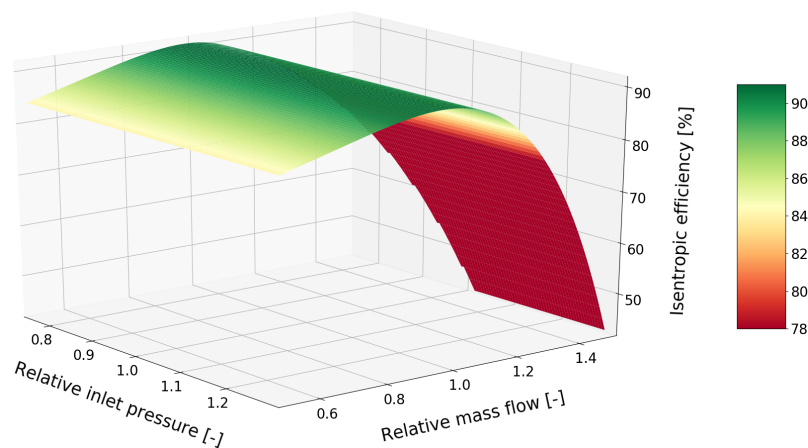


Figure 3.14: Efficiency versus relative mass flow and relative inlet pressure in OTEC ranges. Based on equations 3.26 and 3.27.

The behavior can be further explained on the basis of the Stodola ellipse, which can be visualized in a better way with figures 3.15a and 3.15b, which are in a 2D representation.

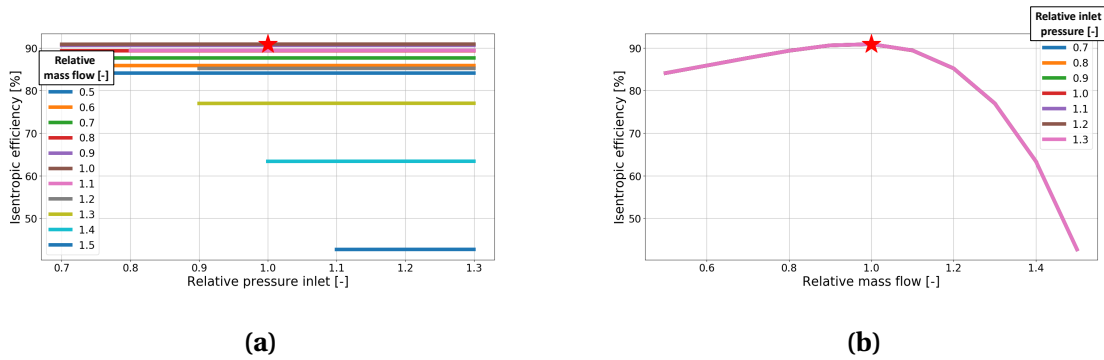


Figure 3.15: Efficiency versus (a) relative inlet pressure for different relative mass flows (b) relative mass flow for different relative inlet pressures. Based on equation 3.26. The ★ represents the design point.

Figure 3.15a shows that the influence of the inlet pressure for different relative mass flows compared to the design values is nihil in the range of OTEC. It is immediately noticeable that some mass flows are not possible at some inlet pressures. Figure 3.15b, shows the influences of the mass flow for different relative inlet pressures compared to the design mass flow. The effects of the relative mass flow are present and there is a clear optimum at the design mass flow. As soon as there is a deviation of mass flow, the performance of the turbine drops. The performance map is mostly given with the pressure ratio or pressure drop as reference parameter. Figures 3.16a and 3.16b show the efficiency versus the pressure ratio and pressure drop.

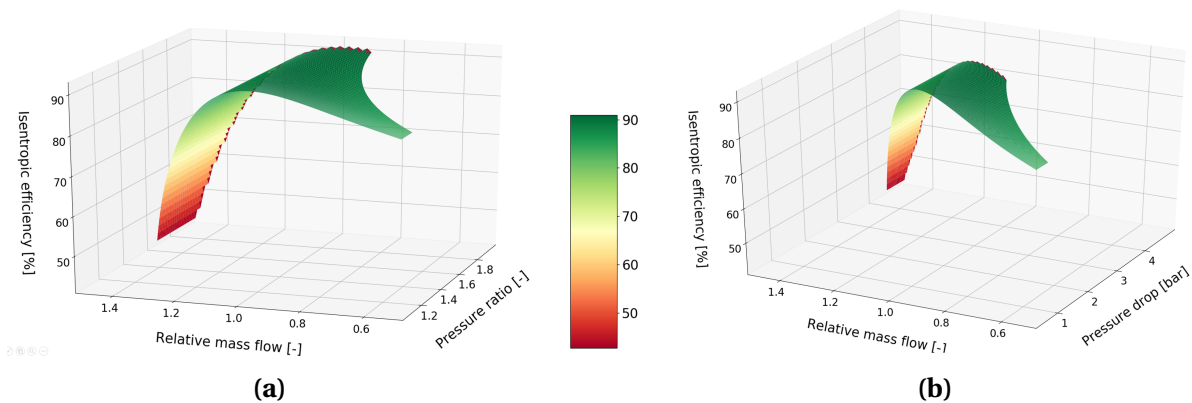


Figure 3.16: Efficiency versus the relative mass flow and (a) the pressure ratio or (b) the pressure drop. Based on equation 3.26.

In the range of OTEC, it can be concluded that a larger mass flow is more harmful than a smaller mass flow mass flow relative tot the design mass flow. The 2D representation of the figures 3.16a and 3.16b are given in figures 3.17a and 3.17b. Note that some pressure ratios or pressure drops are not possible at some mass flows. Finally, a qualitative analysis of the power output is derived. It is ignored whether the other components of the system are capable of providing the in and outlet conditions. Figures 3.17d and 3.17c show the behavior of the work output versus the relative inlet pressure or relative mass flow.

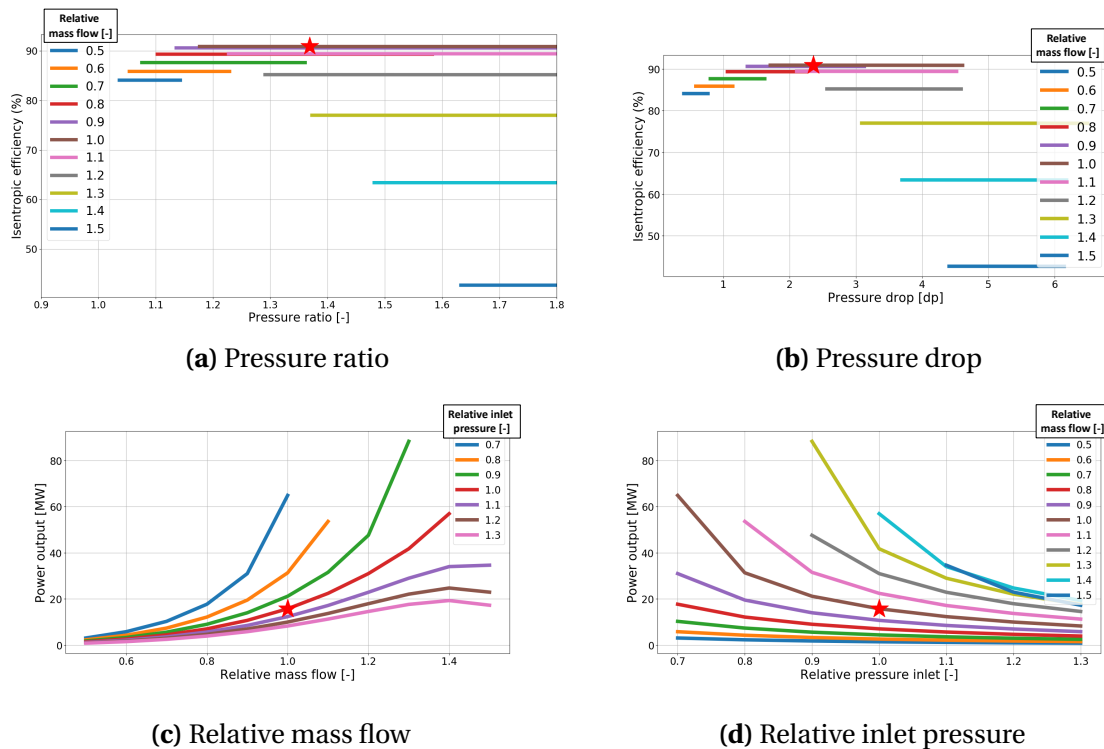


Figure 3.17: (a and b) Influence on the efficiency for different relative mass flows. (c and d) The influence on the power output. Based on equation 3.26. The ★ represents the design point.

Figure 3.17c shows that an increase of the relative mass flow results in an increase of the power output, which continues until the efficiency of the turbine drops to far, see on the right in the figure. The influence of the relative inlet pressure is negative to the power output, which is the result of the behavior shown in figures 3.13c and 3.13d. The inlet pressure and mass flow depend on each other and therefore, the influence of an increase or decrease of the mass flow is complex and will be investigated with the off-design model and will be presented in the final results.

3.8. Discussion turbine

The Stodola method is widely used in other ORC literatures, but the correlation of Jüdes et al. is mainly used in studies related to steam turbines. The correlation is based on experimental data of steam turbines in general, so the correlation of the specific OTEC turbine performance can differ. Therefore, the correlation is investigated to the trends. The study of Petrovic [63] investigates the off-design flow of axial low-pressure steam turbines in subsonic conditions. He shows that the pressure ratio increases with an increase of the reduced mass flow or mass flow coefficient, which also happens when the method of Stodola is used, see equation 3.23. In the study of Petrovic, the losses at off-design operating conditions are predicted with a calculation method based on the through-flow theory and the finite element solution procedure. The flow field and the turbine performance are predicted at the design load as well as for wide range of part loads. Next to the study of Petrovic, the study of Tsoutsanis [80] is examined to gain more certainty in the correlation of Jüdes et al. In the study of Tsoutsanis, the transient gas turbine performance is investigated with performance maps of the components. Finally, the correlation is compared to the study of Hue [38], where the inlet temperature of the turbine is fixed. In appendix, the comparison of the trends with using the Stodola method and the correlation of Jüdes et al. to these studies is shown and we can conclude that the trends are quite similar to the literature.

4

Model of the 10 MW OTEC plant

Goudriaan and Kuikhoven have numerically modeled the off-design performance of the OTEC demo set up. At this moment, the model is in the same scale as the demo set-up at the TU Delft and is validated by experimental data. For a commercial plant, we need to scale up the 0.0001 MW demo set-up a factor 100000. Therefore, it is necessary to scale-up the geometry of the off-design model. This chapter focuses on scaling up the OTEC plant to a 15 MW gross plant using an optimized on-design model. The specific correlations, selected in Chapter 2, are used and are assumed as the optimum correlation to predict the real values accurately. It is assumed that the correlations are still valid and independent from the geometric scale of the plant. After that, in this follow-up study we continue with the existing off-design model. Where all the geometries of the plant are used as input and thereafter the off-design model predicts a steady state of the thermodynamic cycle. Using the off-design model, results in more knowledge about the performance of the complete OTEC cycle.

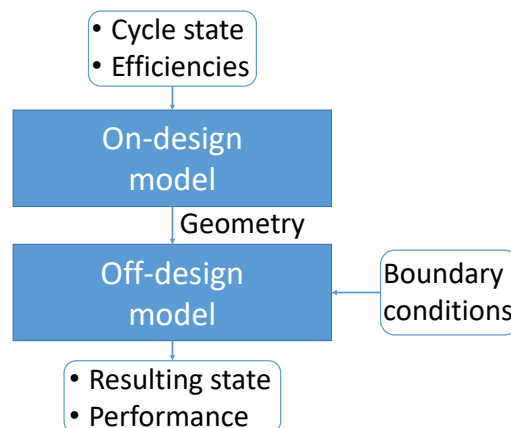


Figure 4.1: Collaboration of the on-design model with the off-design model

Figure 4.1 provides more insight into the cooperation of an on-design model with an off-design model. It also shows the order in which the models should be used. In the following section, the methodology of the modelling the OTEC plant is introduced. Then the on-design model approach is explained, what follows with the description of the on-design model. Through which in the next Chapter, the step to the upscaled off-design model is possible.

4.1. Model methodology

The research objective is to identify the practical and physical limitations of scaling up the plant and to determine the consequence of the turbine performance and efficiency. Nowadays, the benefits of using a mixture of water and ammonia over pure ammonia are ambiguous. Therefore, the result focuses on an ordinary Rankine cycle, so with pure ammonia as working fluid. The off-design model will have a Kalina configuration, so the model will also remain suitable for mixtures as working fluid.

In order to create a commercially optimized OTEC plant, where the influence of changed environment conditions can be compared, the geometries should be determined first. Therefore, an on-design model is used. An on-design model is a model in which you specify the state of the working fluid along the cycle, like pressure, temperature, mass flow rate, as well as the energy transfers in the system. The on-design model characterizes a design operating point. Assuming the component efficiencies, this kind of model permits to derive the geometries of the various components to realize the specified design conditions. The structure of the on-design model is derived from the model of Kirkenier [48]. The model optimizes the plant design to achieve the optimal costs per kW. The on-design and optimization step will be discussed in section 4.2.

The on-design optimization results in a plant design, where the geometries can be used as input in the off-design model. An off-design model is the opposite of an on-design model. It is a model into which you specify the geometries of the different components. In addition to the geometry, boundary conditions of the system are specified. The model will compute the resulting state of the working fluid. The pressures and temperatures of the working fluid are not inputs of the model, but outputs. This kind of model permits you to determine how an existing machine, sized for a specified design point, will behave if you operate outside this design point.

To complete the generic off-design tool of Goudriaan and Kuikhoven, a turbine model should be made instead of the current orifice model. The orifice symbolizes the pressure drop in the demo set-up, since no turbine is implemented. The turbine model influences the entire system, since the performance of the turbine is no longer considered as a fixed value. Each specific condition of the turbine will lead to its own turbine performance as described in Chapter 3. The whole off-design model will be discussed in Chapter 5.

Once the conditions are different than the design conditions, the off-design model should be optimized. The optimization variable is the net power output, since the purchase costs are fixed. This will lead to the lowest cost per kWh and the influence on the conditions can be derived now.

An overview of the total methodology of modelling the commercial OTEC plant is shown in figure 4.2.

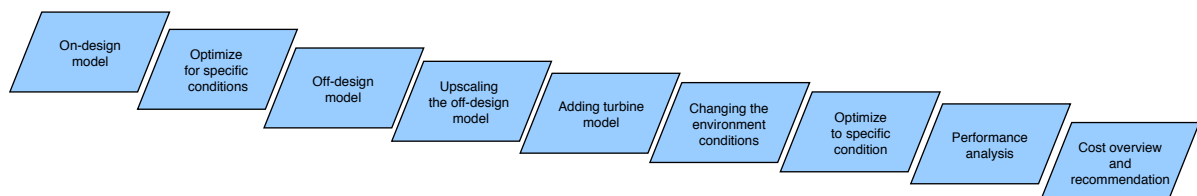


Figure 4.2: Methodology of the model

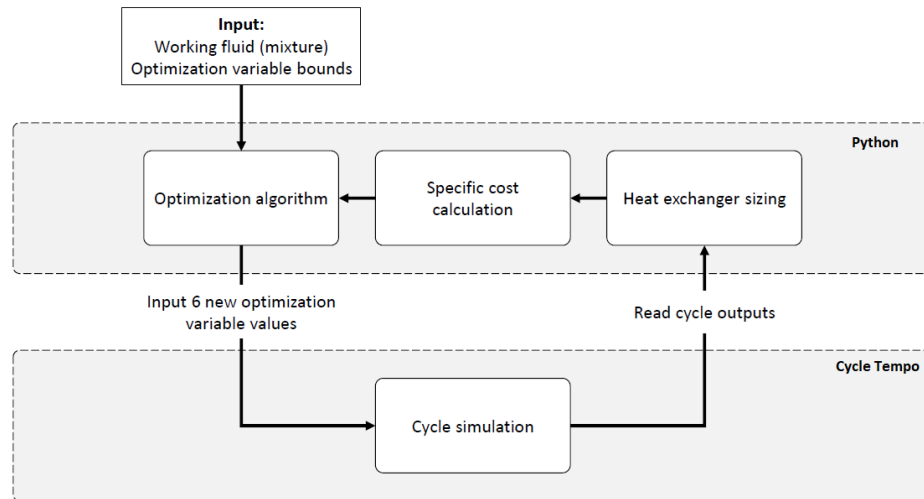


Figure 4.4: Optimized flowchart on the on-design.

Heat exchangers

The configuration of the on-design contains three heat exchangers, the condenser, evaporator and recuperator. The flow through the heat exchangers is counter-current and the energy equation is used to calculate an enthalpy in one of the inlets or outlets [4]. The heat exchangers have twenty different control volumes, so different vapour quality points resulting in nineteen zones with equal thermal load. These zones are used for the heat exchanger sizing process, see section 4.4.2. Kirkenier concludes that the pressure drop on the seawater side has a much larger influence on the net power production than the pressure drop on the working fluid side [48]. Therefore the seawater side pressure drop will be an optimization variable, so a design criterion in the heat exchanger sizing procedure. The working fluid pressure drop will be held constant at 0.1 bar, what is a reasonable value according to Kleute [49]. In the condenser, fully condensation is desired, therefore a 0.1K sub-cooling at the working fluid outlet is specified. Using the Kalina cycle configuration as an ORC, the recuperator is bypassed and the resulting cycle is a conventional ORC. Because of this, a vapour fraction of 100% can be set at the evaporators outlet. In appendix D.1, the choice for a vapor fraction of 100% is explained in more detail.

In the recuperator, the velocity of the flow is low, since the working fluid is fully liquid at both sides. For that reason, the pressure drop of both sides is assumed to be much lower, the setpoint is 0.03 bar. The recuperator uses a fixed temperature difference between the low temperature side to calculate the amount of recuperated energy. This difference is set to 2K. A smaller difference is possible, but an increase of the recuperator heat transfer area is required. This increases significantly the costs of the recuperator and not the amount of recuperated energy, so it is not beneficial.

Turbine

The OTEC cycle has a small pressure and volume flow ratio. Therefore, Kirkenier's model assumes a constant isentropic efficiency. The performance map of Astolfi concludes also that a constant design efficiency is valid. Figure 4.5 shows the sensitivity of the turbine design efficiency computed with the Astolfi performance map. The deviation in design efficiency is computed relative to the deviations in the Size Parameter and Volume ratio.

The deviation in specific speed is neglected, since the specific speed should be always optimized, see section 3.6. The values from table 3.1 are used to calculate the deviations of the design efficiency. An assumed constant efficiency is recommended in comparison with computational time. Otherwise, all iterations should occur twice, since the efficiency determination of the turbine requires the properties of the turbine and these are known after one Cycle Tempo iteration. The losses of the turbine, gearbox and generator are all included in the generator efficiency, which is set on 95%, since Haglind [36] and Ogriseck [61] show this is a reasonable value.

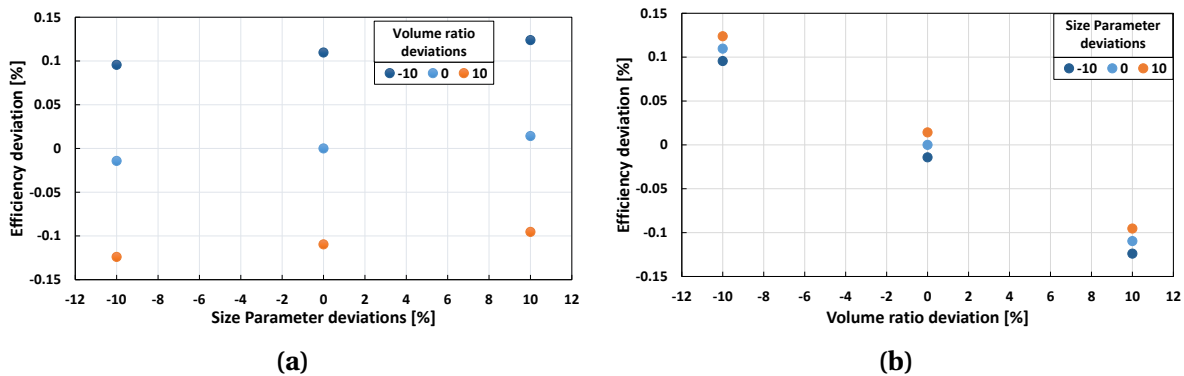


Figure 4.5: Turbine design efficiency sensitivity versus (a) Size Parameter deviation for different volume ratio deviations (b) Volume ratio deviation for different Size Parameter deviations

Seawater pipes

The total pressure in the seawater pipes is a value that can be optimized. It depends mainly on the inner diameter of the pipe. That is why the inner diameter of the pipe is one of the optimization variables. A large pipe diameter gives a lower pressure drop, which results in lower seawater pump costs. But at the same time a larger diameter pipe results in higher costs of the seawater pipe(s). The pressure drop in the seawater pipes is the sum of three components, namely the pressure drop due to friction in the pipe, a hydrostatic pressure drop due to the difference in density of the water at the different depths and a pressure drop due to entrance and exit losses. These different pressure drops are taken over from the thesis of Kirkenier [48], see appendix E.1.

$$\Delta P = \Delta P_{fric} + \Delta P_{hy} + \Delta P_{in} \quad (4.1)$$

The total pressure drop of the cold water pipe is maximized to 0.4 bar. The pressure limitation is a practical limitation and should never occur [49] and avoids simulation errors.

Pumps

The cycle contains three pumps, which are modeled by three liquid-only "Pump" models [4]. The cycle has a cold and warm seawater pump, which have an assumed isentropic efficiency of 80%. The working fluid pump has an isentropic efficiency of 70%. The isentropic efficiency is lower, due to the use of a more unconventional working fluid, namely pressurized ammonia [48]. The working fluid pump has a fixed discharge pressure, which is one of the optimization variables. The pressure difference over the seawater pump compensates the total pressure loss of the seawater pipe and the pressure drop of the seawater side of the heat exchanger. The pumps have purely liquid phase, because as soon as the fluid

is not pure liquid cavitation can occur. Cavitation is the formation of vapor bubbles in a liquid, small liquid-free zones, that are the consequence of forces acting upon the liquid. When subjected to higher pressure, the voids implode and can generate an intense shock wave. The pump is sensitive for this effect. A few degrees of sub-cooling prevent condensate pump cavitation, excessive condensate depression decreases the operating efficiency of the plant. The sub-cooled condensate must be reheated in the heat exchanger, which in turn requires more heat from the heat source [2].

Separator and mixer

The on-design configuration is based on the fact that it should be suitable for both pure and mixtures as working fluid. For that reason, the configuration is based on the Kalina model. Some mixtures will not evaporate completely if the cycle temperature is maximized. Because it is undesirable to send liquid through the turbine, a separator, recuperator and mixer are added in the on-design configuration. The pressure drop of the separator should be around 0.1 bar, which is based on manufacturer data and an extensive OTEC design report by Cable in 2010 [12]. Furthermore, the heat duty is assumed to be zero as heat transfer to the environment of the separator is negligible. The separator function is modelled by setting the vapor fraction on the vapor (top) and liquid (bottom) outlets to 100% and 0% respectively.

4.4. Sizing components

The components in the power cycle require a specific size to achieve the up-scaled on-design conditions. After a cycle iteration, Cycle Tempo provides certain quantities. Using these quantities, the components can be designed to the proper scale. Thereafter, the costs of the obtained scale can be determined. Since the costs are the main objective of the optimization, the design procedure is always cost-driven. Ultimately, the optimum plant with specific geometries is obtained and serves as input for the off-design model. First the cost correlations will be discussed and thereafter the different components, which need to be scaled, will be discussed.

4.4.1. Cost correlations

The cost of each component of the cycle can be calculated using the derived dimensions of the components. The specific cost calculation is based on the cost analysis of Kleute [49]. This analysis has been done by Bluerise B.V. for a 10 MW offshore OTEC power plant. The cost correlations are based on the reference cost and a power factor, which are used to describe the cost scaling behaviour, see equation 4.2.

$$C_{component} = C_0 * \left(\frac{P_{ar}}{P_{ar0}} \right)^{PF}, \quad (4.2)$$

where C_0 is the reference cost, P_{ar} is the relevant parameter, P_{ar0} is the value of the relevant parameter corresponding to the reference cost and PF is the power factor. All reference costs and power factor are given in appendix E.1.2. The relevant parameters vary depending on the unit which is used.

4.4.2. Heat exchangers

The software module Cycle Tempo will give a heat duty and a temperature difference as outputs of the cycle and the UA can be derived with equation 2.20. The UA is an input for the sizing of the heat exchanger, which has an unit of W/K . Next to the UA , the seawater side pressure drop is a design criterion. The seawater side pressure drop is an optimization variable, so it is an imposed specification per iteration. Equations 2.20 and 2.21 are used to obtain the performance of the heat exchanger. Equation 2.25 is used to check if the pressure drops are within the specifications. The design procedure of the heat exchanger is shown in figure 4.6. The structure of the design procedure derived from Sinnott and Towler [73], and gives the geometry of the specific heat exchanger.

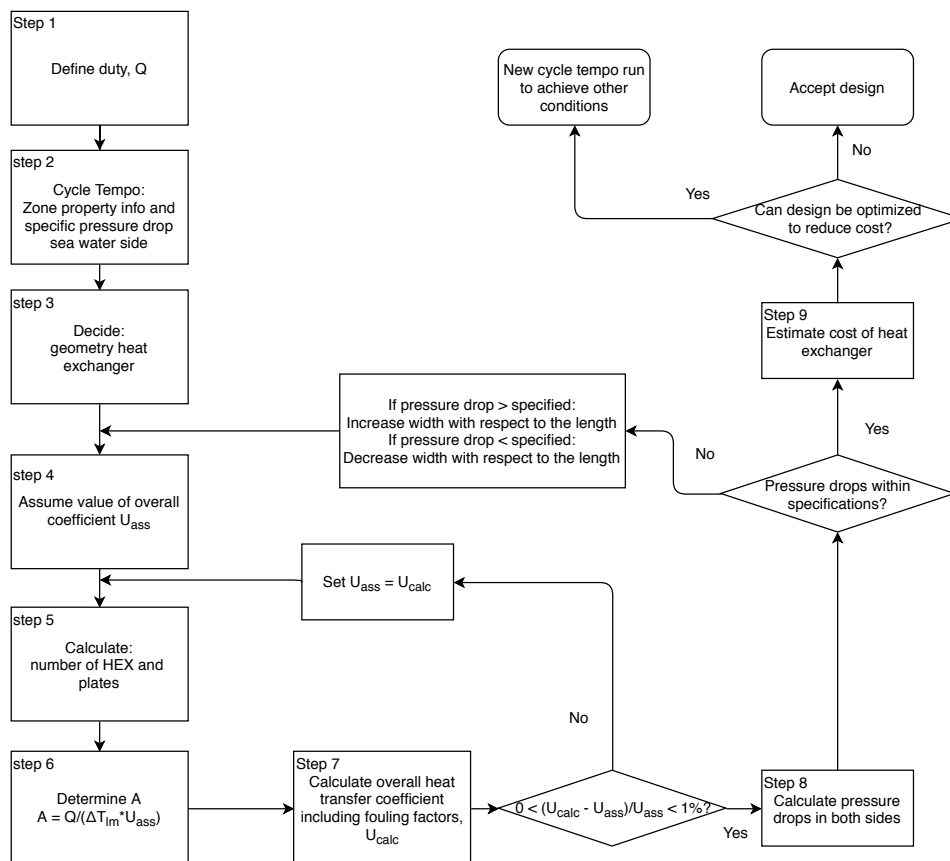


Figure 4.6: Design procedure heat exchanger

In step 3 of the procedure, the geometry of the heat exchanger should be selected. Based on manufacturer quotes and to hold the geometry the most similar to the demo set-up, the plates are made from titanium [50]. The thermal conductivity of titanium is $16.3 \frac{W}{mK}$. The geometry of one individual plate is adapted from the demo set-up at the TU Delft. In section 2.5.1, the structure of the plate geometry is discussed and it is assumed that the plate thickness is 0.4 mm , the channel gap is 2.02 mm and the chevron angle is 57.5° . Table 4.1 gives the ranges of the geometry, which are usual for plate heat exchangers. The maximum size of the heat exchanger is determined with the maximum heat transfer area per heat exchanger, 1500 m^2 [73]. The number of heat exchangers is determined by using this maximum size. The sizing of the heat exchanger starts with a fixed width of the plate and

an initial guess of the ratio between the width and the length of the plate. Now, in step 5 with an assumed overall heat transfer coefficient, the number of plates and number of heat exchangers can be computed. The chosen geometry variables are shown in table 4.2.

Table 4.1: Realistic ranges of geometry.

Parameter	Unit	Range
L_p/W_p	$\frac{m}{m}$	2-3 [73]
Plate thickness	mm	0.4 - 3.0 [8]
		Soft plates < 45
Chevron Angle	$^\circ$	Hard plates > 45
		22–65 [9]
Plate Pitch	mm	1.9 - 8.0 [8]
Size HEX	m^2	0.03-1500 [73]

Table 4.2: Geometry values of the model.

Parameter	Unit	Value
Port to port width		Variable to optimize
Port to port length		Variable to optimize
Port diameter	m	$\frac{2}{3} * W_p$ [20]
Plate thickness	mm	0.40
Chevron Angle	$^\circ$	57.5
Corrugation wavelength	mm	6.67
Channel gap	mm	2.02
Corrugation pitch	mm	7.50
Plate Pitch	mm	2.42
Number of plates		Variable to optimize

1

Finally, the total area can be computed and that results in the costs of the heat exchangers using the cost correlations. The optimization variables, high pressure level, low pressure level and pressure drop of the sea side are the most decisive variables for the costs of the heat exchangers.

Effectiveness heat exchanger

The performance calculation of a heat exchanger is a typical problem in the performance analysis. The method to describe the performance of a heat exchanger is done with the effectiveness, E_{HEX} :

$$E_{HEX} = \frac{\dot{Q}}{\dot{Q}_{max}} \quad (4.3)$$

The effectiveness is the ratio between the actual heat transfer and the maximum possible heat transfer. As high as possible effectiveness is favorable, but this is accompanied with a large heat transfer area. An infinite heat transfer area gives an effectiveness equal to one. The downside of this is that a larger heat transfer area makes the heat exchanger more expensive and the pressure drop will be higher. Therefore, there is an optimum between the effectiveness, pressure drop and the costs in the design phase. The plate heat exchanger has a counter-current arrangement, since this yields in the highest effectiveness [35]. Once the heat transfer area is infinite, the outlet hot medium temperature is equal to the inlet temperature of the cold medium. Therefore, the maximum temperature difference is the difference between the cold and hot inlet temperature, see equation 4.4.

$$\dot{Q}_{max} = (\dot{m} * c_p)_{min} * \Delta T_{max} \text{ with } \Delta T_{max} = T_{warm,in} - T_{cold,in} \quad (4.4)$$

The effectiveness is included in the on-design model optimization. The effectiveness gives in the off-design model more insight into whether a designed geometry performs well.

¹In a gasketed heat exchanger, the effective length and the effective width in figure 2.6 are not valid anymore. The method of calculation, with adding or subtracting the port diameter, no longer corresponds to reality. Therefore in the validation, the effective length scales are measured [20]. In the off-design model, this is not used, but the method of brazed heat exchangers is still used.

4.4.3. Turbine

The turbine is sized with the same Size Parameter (SP) as described in Chapter 3, see equation 3.9. The SP value is computed from the conditions in the Cycle Tempo simulation. The mass flow through the turbine and pressure levels of the turbine are the defining parameters of the turbine geometry. These values are the inputs for the off-design model. The SP value can be compared to the reference parameter to compute the cost of the turbine, see section 4.4.1. The pressure drop over the turbine is a consequence of the optimization of the on-design, since the low and high pressure level are optimization variables. The optimal pressure drop for a specific condition is found.

4.4.4. Separator

The pressure drop of the separator is the only effect that depends on the size of the separator. The pressure drop should be as small as possible, it depends on the areas of the in and outlet ports of the separator. To ensure that the pressure drop over the separator is the same for both scales, the areas have to be scaled to compensate for the mass flow. The scale factor of the area ports is given in equation 4.5. The diameter of the in- and outlet port should be changed in such a way that the same pressure drop in the separator is reached, since the velocity will be the same.

$$d_{new} = d_{old} * \sqrt{\frac{\dot{m}_{new}}{\dot{m}_{old}}} \quad (4.5)$$

4.4.5. Other components

The sizing of the mixer is not important, since the geometry of the mixer is not included in the on-design and off-design model. Finally, the working fluid pump and seawater pumps, their pressure drops are obtained by the cycle. The pressure drop of the working fluid pump is derived from the optimization variables high and low pressure level of the cycle and the known condenser pressure drop. Therefore, the pressure drop of the working fluid is not influenced by the sizing. The required power of the working fluid pump can be compared to the reference required power. Herewith, the cost of the working fluid pump can be computed. Thus, the sizing of the pumps in the on-design model depends on the work that the pumps require. The geometry of the pump is not important for the off-design model, since the isentropic efficiency will only depend on the fluid properties, which will be explained in more detail in the next Chapter.

4.4.6. Scaling effects

In Geschiere [31], it is concluded that if the cycle is up-scaled the assumption of neglecting the surface tension is still valid. In the existing model, the correlation of Winkelmann was used and not Geschiere's. For the correlation of Winkelmann, the area of the condenser should be corrected by the wetted area factor [33]. This gives a better representation of the available heat transfer area. Equation 4.7 gives the corrected area, which uses the fitted factor from equation 4.6. The fit relates the wetted area factor with the concentration of the working fluid. The method of fitting the wetted correction factor is derived from Kim [47]. The correction factor accounts the influence of the change in surface tension of the working fluid. Since the correlation of Geschiere is selected instead of Winkelmann, the wetted

surface correction factor is not used anymore. As soon as the Winkelmann correlation is selected, the assumption is made that the correction factor is still valid, since the wetted surface correction factor is Reynolds number dependent.

$$f_{wet} = 0.0362 * c_{wf}^2 - 0.034 * c_{wf} + 0.0251 \quad (4.6)$$

$$A_{wet} = A * f_{wet} * Re^{0.58} \quad (4.7)$$

Other scaling effects in flows are not included in previous Bluerise reports and also this report does not focus on the scaling effects in flow regimes. As soon as the OTEC plant is scaled up, the assumption remains that the condenser gets an ideal mixing flow from the mixer instead of non-ideal mixing of vapor and liquid [52]. The uneven flow distribution over the plates, which probably occurs in the small demo setup, is less present in the up-scaled version, because the flow speed of the working fluid is higher. As a result, the flow distribution over all the plates is improved.

4.5. Inputs of the on-design model

In the techno-economic evaluation, an offshore 15 MW gross power OTEC plant is optimized. A gross power of 15 MW is necessary to have approximately 10 MW net power output. In order to evaluate the OTEC plant, a techno-economic optimization model is created using a thermodynamic model build with Cycle Tempo and an economic model is implemented in Python. Table 4.3 shows the inputs of the on-design model. The input summary is suitable for mixture as working fluid, but also if pure ammonia is chosen. In addition to the discussed variables, the temperature and mass flows of the hot and cold sources are also needed. The temperatures are assumed to be constant and the mass flows are optimization variables.

Table 4.3: Summary of fixed and variable parameters of the on-design OTEC cycle model [48].

Component	Variable	Value
Evaporator	$T_{H,in}$	Variable
	ΔP_H	Optimization variable
	ΔP_{wf}	0.1 [bar]
	Heat transfer coefficient	Correlations (section 2.5)
	q_{out} (vapor fraction)	Optimization variable ²
Condenser	$T_{C,in}$	Variable
	ΔP_C	Optimization variable
	ΔP_{wf}	0.1 [bar]
	Heat transfer coefficient	Correlations (section 2.5)
	q_{out} (Vapor fraction)	0 [%]
Recuperator	$\Delta T_{sub-cooling}$	0.1 [K]
	$\Delta P_{both\ sides}$	0.03 [bar]
	ΔT_{low}	2 [K]
Turbine	Isentropic efficiency	91 [%]
	P_{outlet}	Optimization Variable

Continued on next page

²In the case of pure ammonia, the vapour fraction will be 100 [%] (appendix D.1)

– continued from previous page

Generator	Mechanical efficiency	95 [%]
	\dot{W}_{out}	15 [MW]
Cold seawater pump	\dot{m}_C	Optimization Variable
	Isentropic efficiency	80%
	ΔP	Pump (section 4.3)
Hot seawater pump	\dot{m}_H	Optimization Variable
	Isentropic efficiency	80 [%]
	ΔP	Pump (section 4.3)
Cycle pump	Isentropic efficiency	70 [%]
	P_{outlet}	Optimization Variable
Working fluid	Mass flow	Cycle Tempo
	Mixture composition	100 [%] ammonia
Separator and mixer	ΔP	0.1 [bar]
	$q_{out, top}$	1.0
	$q_{out, bottom}$	0.0
Water pipes	d_{in}	Optimization Variable
	$\Delta P_{cw, pipe, max}$	0.4 [bar] (constraint)
Environment	T_{env}	288.15 [K]
	P_{env}	1.01325 [bar]

4.6. Techno-economic optimization

The model performs a techno-economic optimization, which determines the optimal conditions of the plant in terms of €/kW. In this section, the optimization variables and the optimization algorithm will be discussed.

The optimization strategy of this model is similar to Astolfi et al. [7]. The optimization variables are:

- Warm water mass flow
- Cold water mass flow
- High pressure level, which is after the working fluid pump
- Low pressure level, which is after the turbine
- Pressure drop of the water side of both heat exchangers
- Water pipe inner diameter

If the working fluid is a mixture, the optimization variables can be extended with:

- Evaporator outlet vapor fraction. If the working fluid is a mixture
- Ammonia-water concentration

4.6.1. Optimization algorithm

The optimization algorithm, which is used in the optimization is based on the Scipy [41] implementation of a Differential Evolution (DE). The Differential Evolution is a method that belongs to the Genetic algorithms (GA). These methods are widely used if system parameters are unknown or if multiple local minima exist [45]. Figure 4.7 shows the structure of a GE.

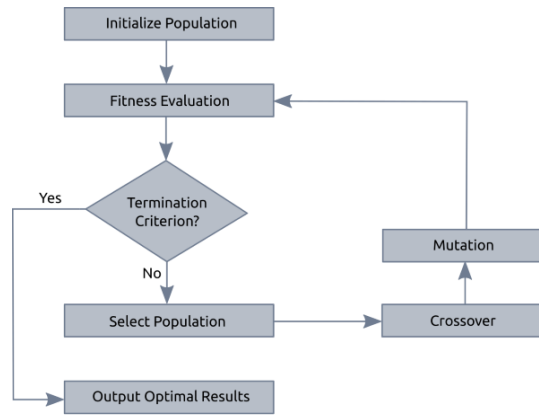


Figure 4.7: Basic structure of Genetic Algorithm

The Differential Evolution (DE) algorithm is a new heuristic approach with three advantages, namely finding the true global minimum regardless of the initial parameter values, fast convergence and using only a few control parameters. The DE algorithm is a population based algorithm, like genetic algorithms, using similar operators, namely selection, crossover and mutation [45]. First, the selection step selects the old initial guesses according to their fitness, how better fitness the greater the chance to be selected. Subsequently, a new initial guess is formed from the old initial guesses with a cross over in the crossover step. The cross over has a specific crossover probability or recombination constant. If no cross over is performed, the new initial guess is an exact copy of the old initial guess. At last, the mutation step mutates a new initial guess at each locus with a mutation probability. The optimization has a maximum number of generations over which the entire population is evolved, which is set by the maxiter. The Scipy default settings are taken over in the DE, since the global minimum is founded with these settings and the computational time is acceptable. The population size is a multiplier for setting the total population size. The tol is the relative tolerance for convergence, it determines when the iteration stops. Finally, the solving strategy has influence on how the iteration guesses originate. The strategy, 'best1bin', is the default setting of Scipy's DE. In this strategy two members of the population are randomly chosen. Their difference is used to mutate the best member. Table 4.4 shows an overview of the DE settings.

Table 4.4: Differential evolution algorithm settings of the model

Setting	Value
Population size	15
Maxiter	1000
Tol	0.01
Mutation	0.5-1
Recombination	0.9
Solving Strategy	'best1bin'

A differential evolution algorithm is used as the global optimizer. At the start of an optimization run, the optimizer is configured and its bounds are set. Table 4.5 shows the bounds of each optimization variable. Note that in using pure ammonia as working fluid, the evaporator outlet and ammonia-water concentration are omitted in the optimization.

Table 4.5: Bounds of the differential evolution in the on-design optimization.

Optimization variable	Unit	Bounds
Warm water mass flow	$[\frac{kg}{s}]$	7500-60000
Cold water mass flow	$[\frac{kg}{s}]$	7500-60000
High pressure level	$[bar]$	7.5-12.0
Low pressure level	$[bar]$	4.5-7.5
Pressure drop water side	$[bar]$	0.01-0.5
Water pipe diameter	$[m]$	2.0-5.0
Evaporator outlet vapor fraction	$[-]$	0.1-1.0
Ammonia-water concentration	$[-]$	0.9-1.0

4.7. On-design optimization results

For a specific boundary condition, the optimization results in an optimum costs per installed capacity. Figures 4.8 shows the convergence of the optimization run for a specific environment condition, namely pure ammonia as working fluid, a warm water temperature of 27 °C and a cold water temperature of 5 °C. This results in the standard scenario plant, namely a plant which is designed for the condition of $15MW_{gross}@\Delta T22K$ and $T_H = 27^\circ C$. This leads to the optimized operating conditions of the OTEC cycle, see figure 4.9 for an overview of the cycle. Figure 4.10 shows an overview of the optimum cost per component and finally figure 4.11 shows the optimization variables convergence.

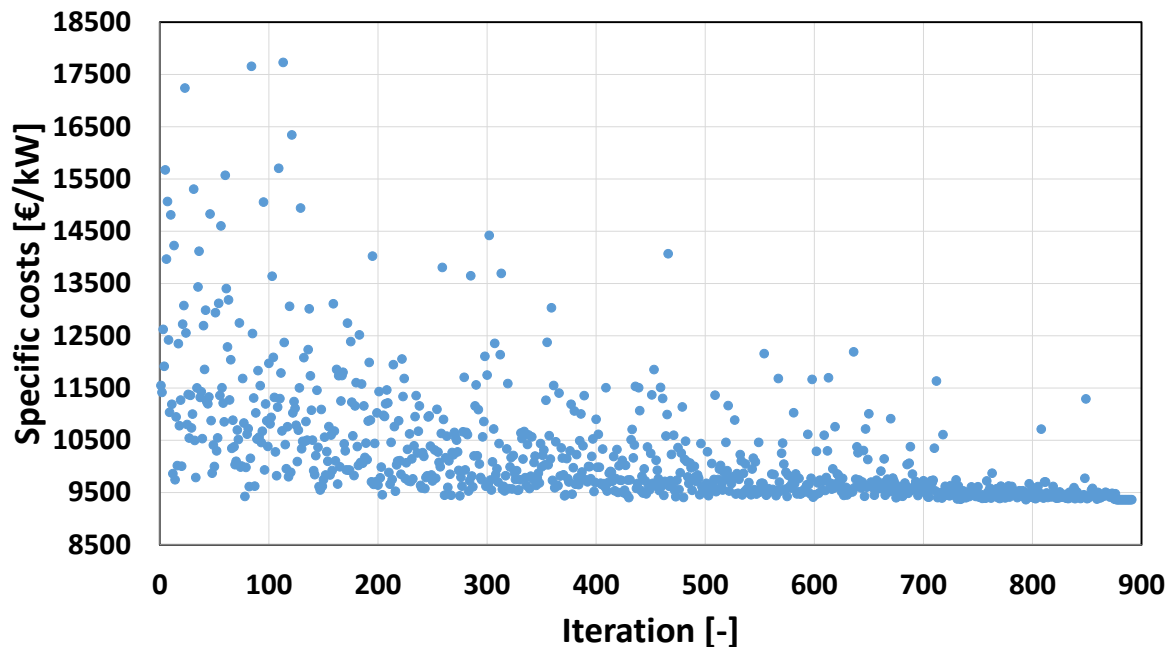


Figure 4.8: Convergence of the optimization run. Single stage ORC for $15MW_{gross}@\Delta T22K$ and $T_H = 27^\circ C$.

Kalina cycle

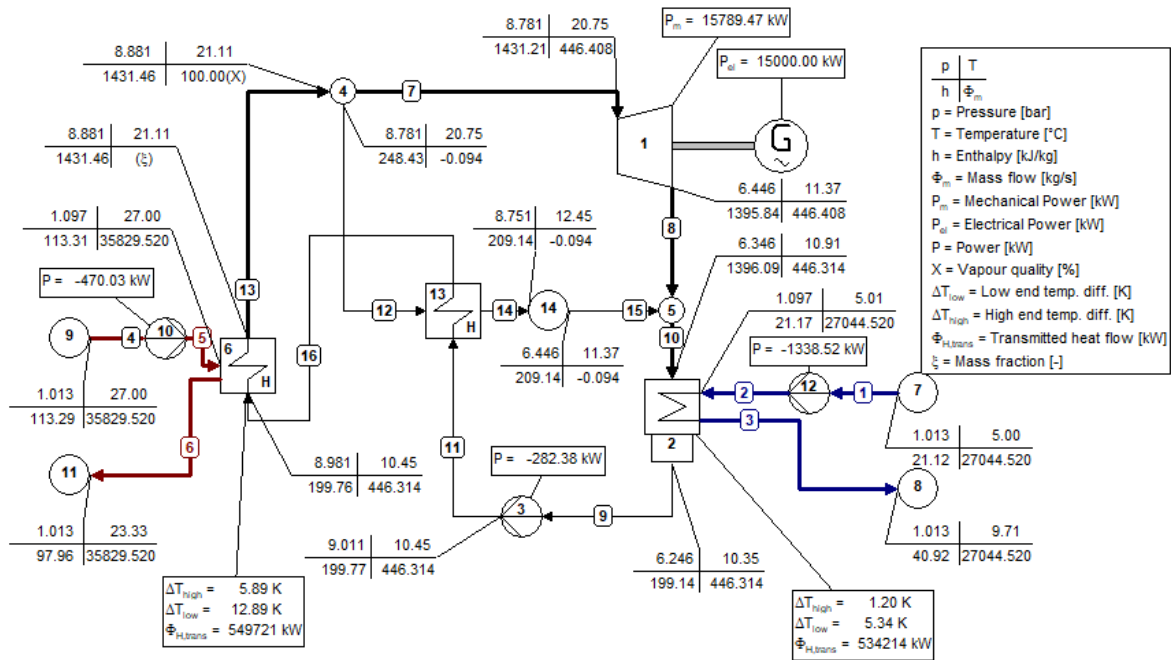


Figure 4.9: Cycle tempo model showing the optimal result for the single stage ORC for $15MW_{gross}$ @ $\Delta T22K$ and $T_H = 27^{\circ}C$.

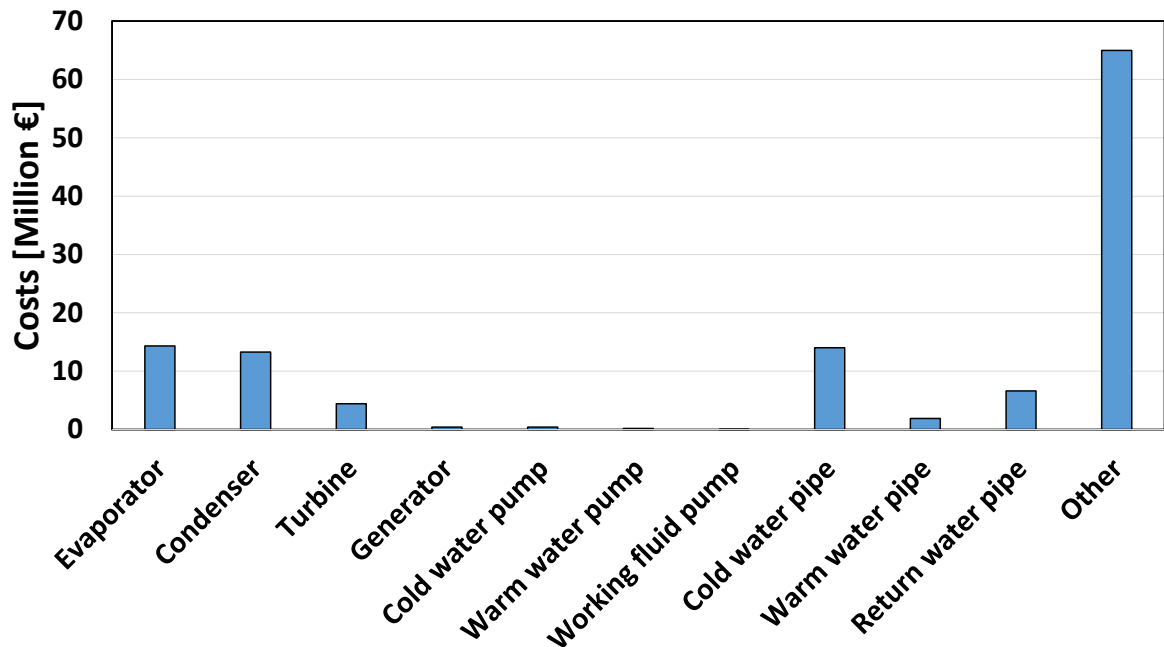


Figure 4.10: Cost per component overview for the optimal result for the single stage ORC for $15MW_{gross}$ @ $\Delta T22K$ and $T_H = 27^{\circ}C$.

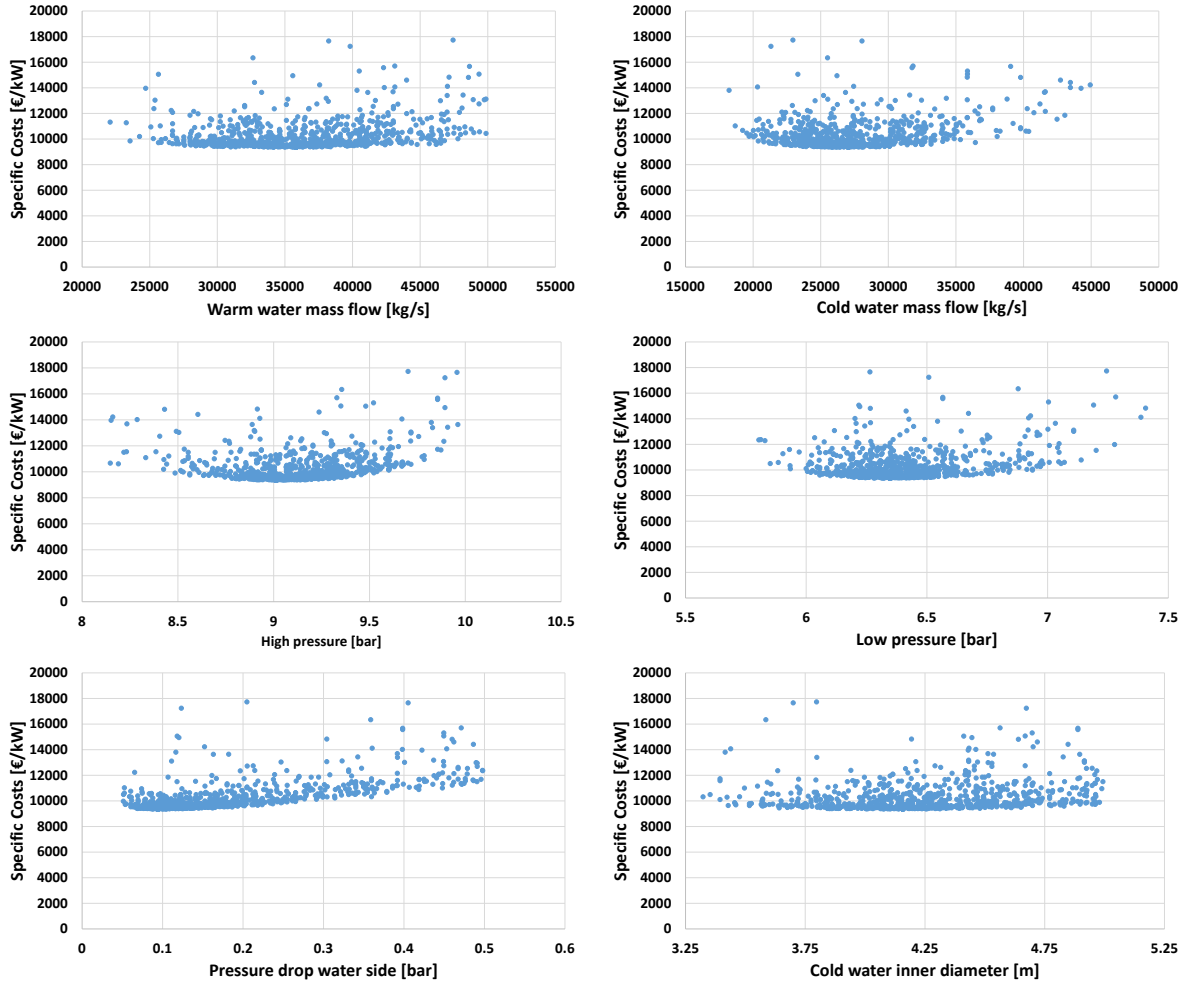


Figure 4.11: Optimization results for the single stage ORC for $15MW_{gross}$ at ΔT_{22K} and $T_H = 27^\circ C$. Every subplot shows a single optimization variable vs specific cost.

With the total power production and the total costs, the specific costs and the Levelized Costs of Energy (LCOE) can be derived. The LCOE is a measure of an energy production source. It is an economic assessment of the average total cost, which includes the operating and building costs over its lifetime, divided by the total energy output. With the LCOE, the break-even or the feasibility can be obtained of a project. The LCOE can be derived with equation 4.8.

$$LCOE = \frac{\text{sum of cost over lifetime}}{\text{sum of electrical energy produced over lifetime}} = \frac{TLCC}{\sum_{t=1}^n \frac{Q_t}{(1+r)^t}}, \quad (4.8)$$

where, TLCC stands for the total life-cycle cost, which contains the investment, operations and maintenance expenditures. The Q_t is the energy output in year t . Further, the LCOE is based on a 8.0% discount rate, r and a lifetime of the plant of 30 years [48]. The optimization algorithm has a total plant cost and a net power production of approximately 120 M€ and 14 MW. The share of the heat exchangers in the installed costs is circa 50% of the components, which is a reasonable value. If the OTEC plant continuously operates at design conditions, this results in a specific cost of approximately $9500 \frac{\text{€}}{\text{kW}}$ and a LCOE of $0.12 \frac{\text{€}}{\text{kWh}}$, which are comparable to Kirkenier and Vroom [48][50].

5

Off-design of the OTEC model

The on-design model results in specific geometry of the components, which are in addition of the boundary conditions the inputs of the off-design model. The modelling of the off-design model of the OTEC set-up of Bluerise starts with the research of Goudriaan and Kuikhoven. The off-design model from their research is able to predict with a small deviation the steady state conditions of the demo setup at the TU Delft. In the following sections, the structure of the off-design model will be discussed. The numerical algorithms are explained, which determine the output conditions in the heat exchangers. At last, the solving algorithm for the total off-design model is discussed. The model is built in a modular way, such that in the future the off-design model is suitable that all the components can be replaced by other components. The off-design model is suitable for pure or mixture working fluids. The cycle can be an ordinary Rankine cycle instead of a Kalina cycle, since the flow through several subsystems can be zero.

5.1. Model decomposition

The OTEC system consists of several components, which are given in figure 5.1. All the subsystems which are covered in this report are shown. In the report, the numbering in the figure is adopted for the start condition of the flows.

The system boundary is derived from the parameters, which are known and can be input or output values. In the off-design model, in addition to the known sea water conditions, the geometries of the components are given as input parameters to model a specific OTEC plant. The conditions of the working fluid are unknown, which can be optimized. The ammonia-water concentration, the mass flow of the working fluid and mass flows of the seawater sides are optimization variables, since operators are able to fine-tune these variables to achieve the highest power output. Together with these variables, Chapter 3 introduces that the position of the blades of the turbine can vary and also should be optimized. Table 5.1 shows the inputs, variables and outputs of the off-design model.

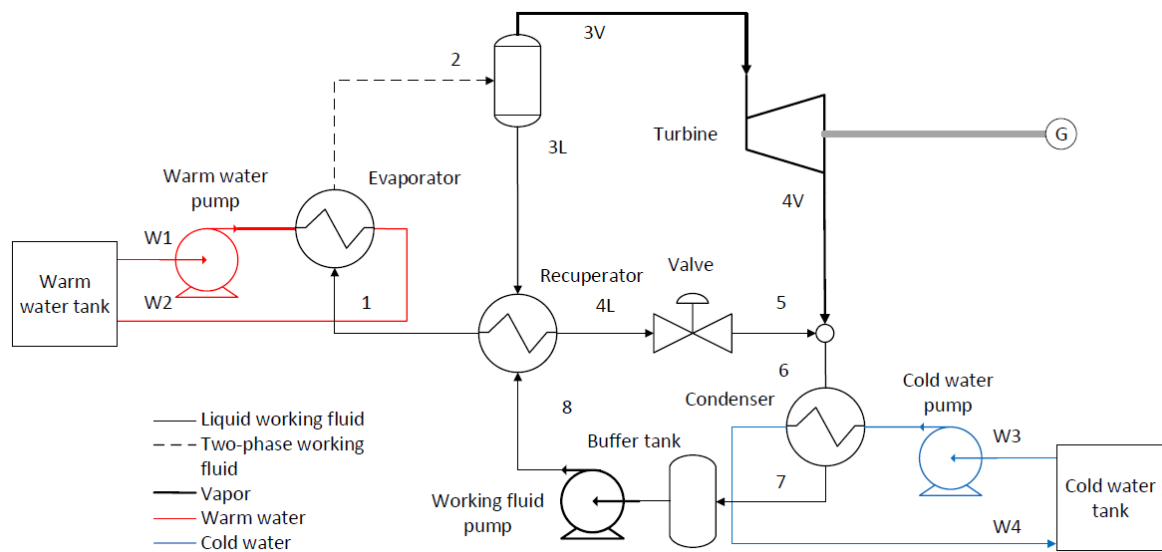


Figure 5.1: Process flow diagram (PFD) of the experimental OTEC setup [33].

Table 5.1: Overview of the inputs, optimization variables and outputs of the model.

Inputs	Variable	Outputs
Inlet temperatures of the water flows	Mass flow rate of the working fluid	Overall heat transfer coefficients of the HEX's
Inlet pressures of the water flows	Mass flow rates of the water flows	Thermal efficiency of the cycle
Fixed components geometry	Ammonia-water concentration	Turbine isentropic efficiency
	Position of the blades of the turbine	Power input of cycle pump
		Pressure drops of the HEX's
		Power output of the cycle

5.2. Assumptions

In order to simplify the complexity of the system, it is necessary to make further assumptions. The assumptions of Goudriaan and Kuikhoven are in most cases taken over, which will be clarified in the next paragraphs.

Assumptions for the entire system

In the following list we mention the assumption of the entire system:

- Well insulated, so no external heat transfer to the environment.
- No height difference between the components, so that the potential energy difference can be neglected.
- All flows are steady state, inviscid and fully developed.
- The vapor flow is assumed to be 100% ammonia in a mixture working fluid, because ammonia is more volatile than water.

These assumptions are realistic and not far from the reality and needed to simplify the model to achieve the first results for the entire system.

Assumptions for the heat exchangers

In the heat exchanger, assumptions are made to describe the heat transfer. All heat exchangers are plate heat exchangers. A temperature gradient is the driving force to have heat transfer from the warm side to the cold side. Thus, the main transfer is convection, either convective boiling or nucleate boiling will be the dominant form of evaporation depending on the flow regime of the fluid [52]. Due to the low Reynolds numbers in the system, gravity controlled condensation is the dominant form of condensation. The energy accumulation in the heat exchangers walls is negligible. In the evaporator and condenser, the pressure drop of the sea water side is computed in the model¹. The working fluid pressure drops in each heat exchanger remains a constant. The assumptions for the heat exchanger are:

- A fixed heat transfer area is assumed.
- The fluid flows are one-dimensional.
- The water flow of the hot and cold source is single phase.
- Single phase liquid flow in the recuperator.
- Radiation is negligible due to the low temperatures of the fluids.
- In the case of two phase flow a perfect mixing of vapor and liquid is assumed in the working fluid.

Assumptions for the pump

The assumptions to determine the work of the pump are:

- No delay in the electrical-to-mechanical transmission for the pumps.
- In the pump only single phase flow is present
- The pump characteristic of Goudriaan is used for the working fluid pump, but once the upscaled geometry is used the working fluid pump has a constant isentropic efficiency of 70% [48].

Assumptions for the other components

The other components of the OTEC cycle have some assumptions that are used to learn more about the outlet streams. The separator and valve play an important role as soon as a mixture is used as working fluid. The assumptions are:

- The valve is assumed ideal, i.e. $h_{out} = h_{in}$.
- Perfect separation of phases in the separator.

5.3. Mathematical model

The off-design steady state operating condition is calculated by the mathematical model. In this section, we explain the mathematical modules of the OTEC system. Figure 5.2 gives an overview of the process flow of the model and which parameters per component are used as input or output. The model is decomposed into several components, with each component having its own method of calculation. In appendix F, the decomposition of the several sub components are given. It gives an overview of the in and outputs per component.

¹In the research of Goudriaan and Kuikhoven, the pressure drop was assumed to be constant. In this thesis, this assumption is not present anymore and the pressure drop will be computed.

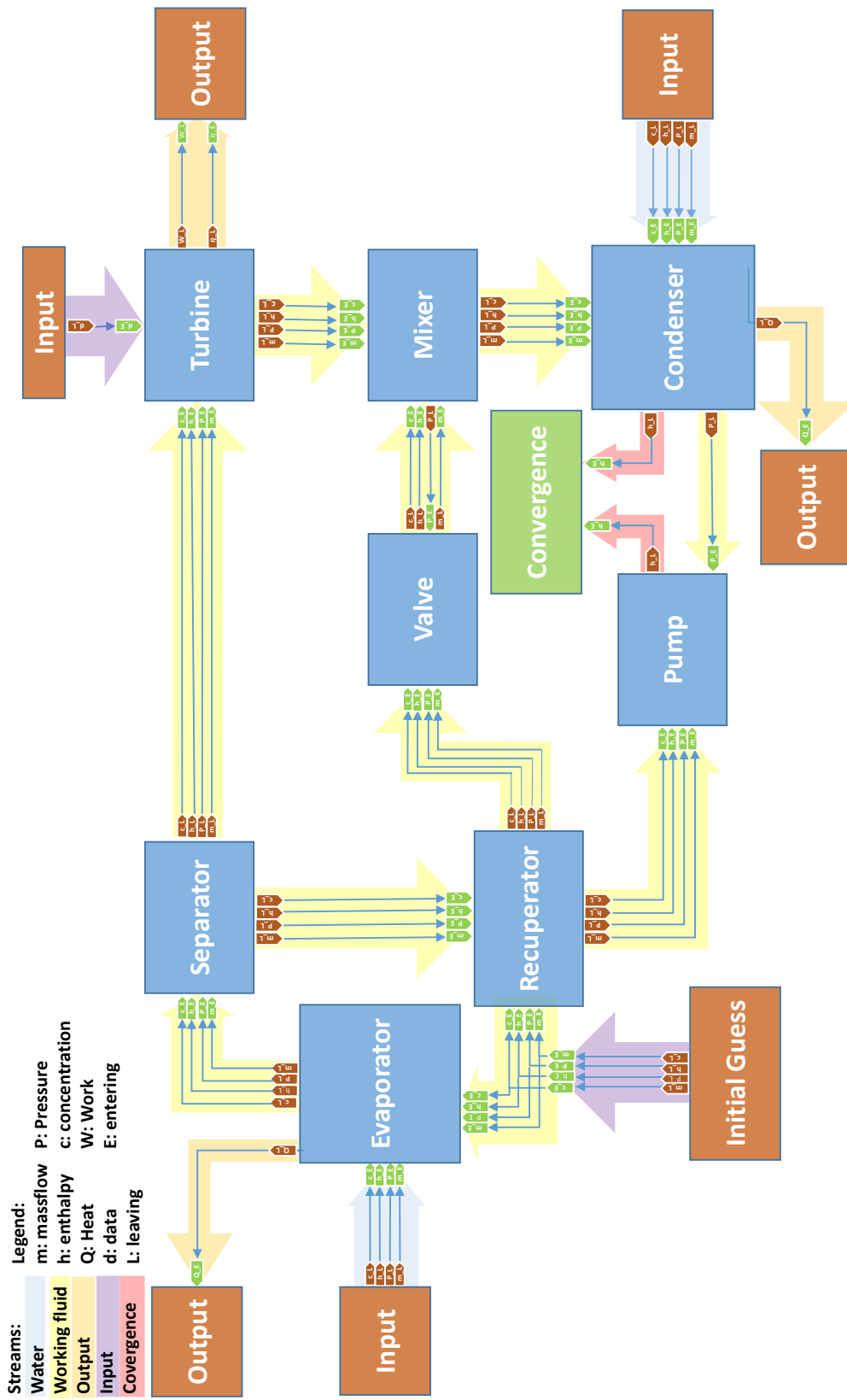


Figure 5.2: Flow chart of mathematical model with all in- and outputs of every component.

5.3.1. Heat exchangers

The Kalina cycle for OTEC has three heat exchangers and they all apply the same energy and mass balances. The energy balance is given in equation 5.1 and in equations 5.2 - 5.4 the mass balance conditions are shown.

Energy conservation

$$\dot{Q}_{load} = \dot{Q}_{duty}, \quad (5.1)$$

where \dot{Q}_{duty} is the transferred heat to the working fluid, see equation 2.20 and \dot{Q}_{load} is the heat load of the water source, see equation 2.19.

Mass conservation

$$\dot{m}_{wf} = \dot{m}_{NH_3} + \dot{m}_{H_2O} \quad (5.2)$$

$$\dot{m}_{wf} = \dot{m}_l + \dot{m}_v \quad (5.3)$$

$$\dot{m}_v = q * \dot{m}_{wf}, \quad (5.4)$$

where \dot{m} is the mass flow in [$\frac{kg}{s}$]. The index wf stands for the working fluid and l and v for the liquid and vapor part of the working fluid. The index NH_3 and H_2O stands for the specific component of the working fluid and q is the vapor quality in [$\frac{kg}{kg}$].

5.3.2. Numerical solver heat exchangers

In chapter 2, the equations, which are necessary to model the heat exchangers, are given. In this section, the method to solve the energy balance for the heat exchanger is explained and therefore the output conditions. First, the method for the evaporator and condenser are described, followed by the algorithm of the recuperator.

Evaporator and Condenser

The algorithm to solve the outlet conditions of the heat exchanger is the same for the condenser and evaporator. The research of Goudriaan and Kuikhoven [33][52] concludes that the LMTD method with enough control volumes, cv 's, works properly in these components. Once the thermophysical properties of the fluid are constant, the LMTD method is most appropriated to evaluate the performance. If the number of control volumes is high enough, the LMTD method with control volumes can be used for the one phase and two phase regimes of the working fluid. A number of 100 control volumes is sufficient to obtain an accuracy of 0.0001 Kelvin for the outlet temperature convergence. Since the number of cv 's is high enough, the assumption to approximate constant properties over each cv is valid. Hereby, the LMTD method linearises the properties of the fluid flows. Taking the evaporator as an example, equations 5.5 - 5.10 show the algorithm steps for the LMTD method and figure 5.3 shows the LMTD approach per cv . First, the available heat load of the hot water side is determined. The inlet temperature is known, as well the heat transfer area by the imposed geometry. The corresponding heat load can be derived by a guessed hot water outlet temperature, see equation 5.5.

$$\dot{Q}_H = \dot{m}_H c_{p,H,av} (T_{H,in} - T_{H,out}) \quad (5.5)$$

$$\dot{Q}_{cv} = \frac{\dot{Q}_H}{N_{cv}} \quad (5.6)$$

$$\Delta h_{cv} = \frac{\dot{Q}_{cv}}{\dot{m}_{wf}} \quad (5.7)$$

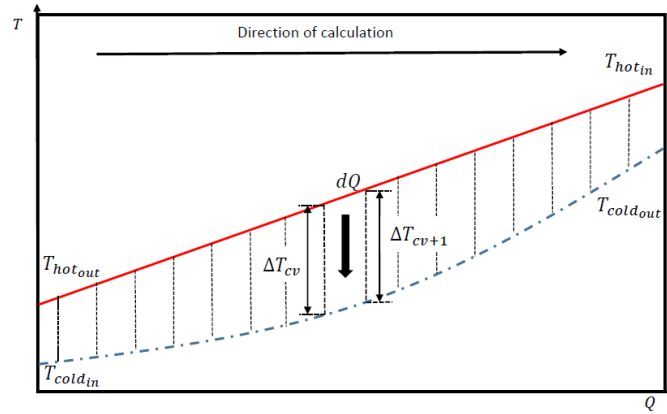


Figure 5.3: Control volume with LMTD approach for a counter-current flow evaporator [33].

The assumption that the system is well insulated, results in that the total heat load is transferred to the working fluid. As a result, the heat load per control volume determines the enthalpy difference per control volume, which can be used to determine the properties for the next control volume. The enthalpy difference should be added up with the previous control volume to derive the next control volume, see equation 5.8. If the corresponding pressure is known, the temperature of this new control volume can be derived.

$$h_{cv+1} = \frac{Q_{cv}}{\dot{m}} + \Delta h_{cv} \quad (5.8)$$

As soon as the pressure drop will be computed, the pressure of each cv is unknown. If the pressure drop is assumed constant, the pressure of each cv is also unknown, since the area distribution is unknown before the iterations. The area distribution is necessary to distribute the pressure drop over the cv's. The pressure drop is more flow length dependent than depending on the energy. That is why, the distribution of the pressure drop along the flow length gives a better representation of the reality than that it is linear over the cv's. In the first iteration, the pressure drop is an initial guess and the distribution is linear. In the next iterations, the per cv calculated pressure drop is used, since the pressure drop and area distribution are known. Because of this the pressure drop is no longer linearized over the cv's compared to the existing model². The area distribution per control volume is known from the previous iteration, which is valid since the difference between the iterations is small and the error of this method is acceptable. At this stage the properties of the inlet and outlet per control volume are known. Using this information, the log mean temperature difference of all control volumes can be determined, see equation 5.9.

$$LMTD_{cv} = \frac{\Delta T_{cv+1} - \Delta T_{cv}}{\ln\left(\frac{\Delta T_{cv+1}}{\Delta T_{cv}}\right)} \quad (5.9)$$

The vapor quality can be determined, since it is a function of the pressure and enthalpy. Thereafter, the vapor mass flow and the new concentration can be derived. In section 2.5, we introduce the single and two-phase heat transfer coefficients. Using equation 2.21, the overall heat transfer per control volume can be derived. Subsequently, the required area is

²The method of using the area as driven-factor to distribute the pressure drop is a change with respect to the reports of Goudriaan and Kuikhoven.

calculated to transfer the heat per control volume, see equation 5.10.

$$A_{cv} = \frac{Q_{cv}}{U_{cv} * LMTD_{cv}} \tag{5.10}$$

This approach is repeated for all control volumes. After all, the total sum of all control volume area's is compared to the imposed area, which results in a relative area error. This error should be minimized to an error of $10^{-6}\%$. Once the calculated area is not equal to the imposed area, the initial guess of the water outlet temperature is not correct and a new estimation is proposed. Relative to the existing model, more control of the temperature guess are implemented, see appendix E.2.2. The loop continues, until the calculated area equals the fixed area of the specific heat exchangers within the convergence criterion. This control volume approach is used in the evaporator and condenser. The only difference is that the enthalpy per control volume is added or subtracted. Figure 5.4 shows the algorithm of the evaporator and condenser.

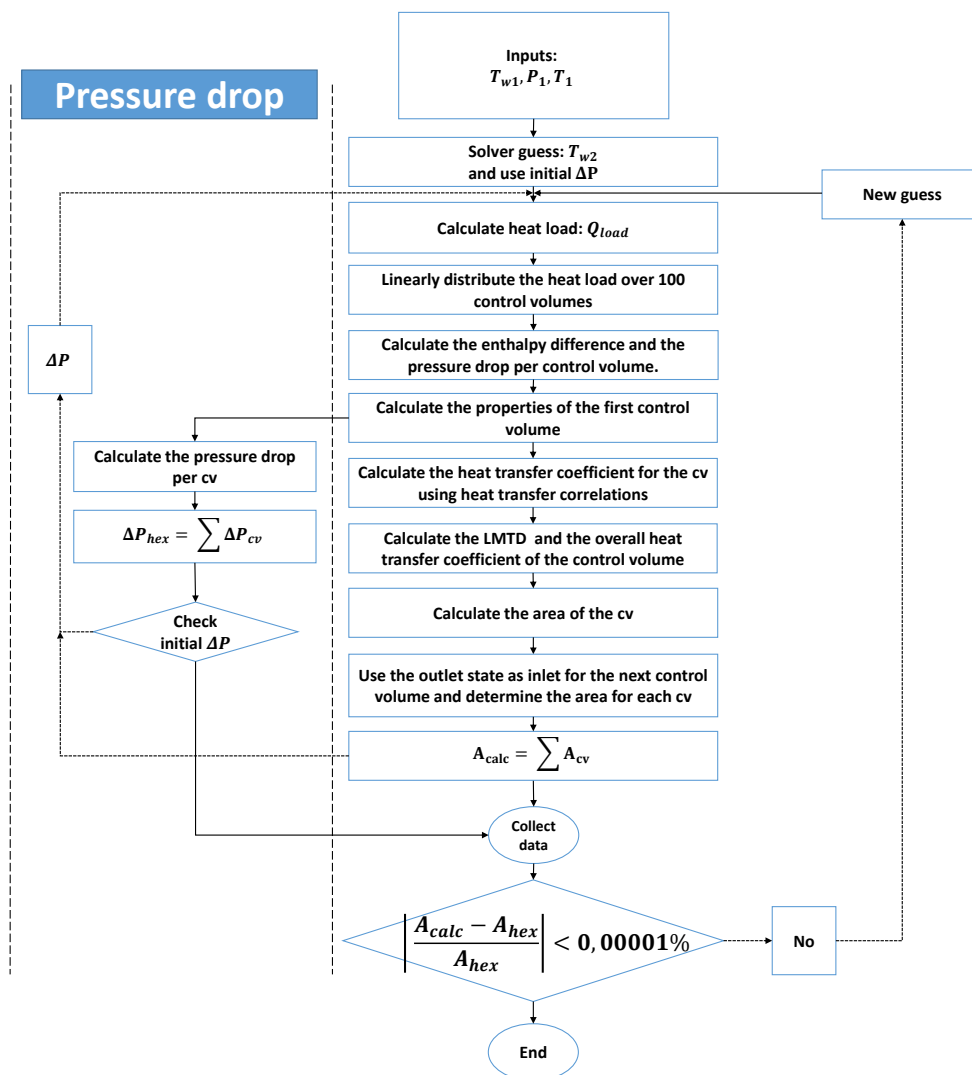


Figure 5.4: Heat transfer algorithm. Notice that if the correlation of Winkelmann is used, the A_{hex} should be corrected with the wetted area factor.

In condenser, the outlet vapour fraction and the degree of sub-cooling are checked. An error will occur as soon as the working fluid flow is too much sub-cooled or has a certain vapor quality at the outlet of the condenser. With the result that a new iteration is performed.

Recuperator

In the recuperator, an iterative loop is in comparison with the condenser and evaporator not necessary. The only condition for the linearization of the recuperator is that the number of control volumes is large enough. Goudriaan concludes that a number of 500 control volumes is necessary in comparison with the computation time to decrease the error enough [33]. The streams of the recuperator are both single phase. Therefore, linearization is valid in the recuperator, since the temperature difference between the hot and cold side per control volume is almost equal, $\Delta T_{cv} \approx \Delta T_{cv+1}$. Hence, the temperature difference over the control volume is equal to the logarithmic temperature difference. The algorithm of the recuperator starts with the distribution of the area over the number of control volumes. Hereby, the control volumes are area dependent instead of energy dependent. Therefore, the pressure drop can be linearized. Hereafter, the overall heat transfer coefficient is calculated using the correlations described in section 2.5. Finally, the heat for the control volume is calculated and the enthalpy value per control volume can be derived. This method is repeated for each control volume. As soon as the iteration behaves like an ordinary Rankine cycle, the mass flow through the recuperator is zero. Therefore, a minimum mass flow through the recuperator is implemented, see appendix E.2.1.

5.3.3. Separator

In the off-design model, the exact method of separation is not modelled, but only the effect of the separator. The separator splits the vapor fraction from the liquid fraction, to ensure a pure vapour stream. Liquid is avoided in the turbine, which should decrease the turbine performance significantly. The residual liquid flow is send to the recuperator to recuperate the residual heat. The vapor and liquid mass flows can be derived with the mass balance, see equation 5.11. Since the assumption of perfect separation is made, the vapor stream has a concentration of 100% ammonia in mixtures as working fluid. By means of the species balance, the mass fraction of ammonia in the liquid stream is derived. Once the pressure of the outlet is known, the properties of the liquid outlet of the separator can be determined with the derived concentration and a vapor quality of zero, which means pure liquid phase. The outlet temperature of the vapor stream can be calculated in two ways, due to the assumption of ideal separation or perfect insulation. As soon as the insulation of the separator is perfect, the properties of the vapour outlet flow can be solved with the energy balance, see equation 5.12.

Mass conservation

$$\dot{m}_{wf} = \dot{m}_v + \dot{m}_l = q_{in} * \dot{m}_{in} + (1 - q_{in}) * \dot{m}_{in} = \dot{m}_{H_2O} + \dot{m}_{NH_3} \quad (5.11)$$

Energy conservation

$$\dot{m}_{wf} * h_{in} = \dot{m}_l * h_l + \dot{m}_v * h_v, \quad (5.12)$$

where q is the vapor quality [-], \dot{m} is the mass flow [$\frac{kg}{s}$] and h is the enthalpy [$\frac{J}{kg}$].

The pressure loss of the inlet and outlet ports creates a pressure drop in the streams. The

pressure drop can be approximated as one velocity head for the inlet and a half velocity head for the outlet, see equations 5.13 and 5.14 [17].

$$\Delta P_{in} = \frac{\dot{m}_{in}^2}{2 * \rho_{in} * A_{in}^2} \quad (5.13) \quad \Delta P_{out} = \frac{\dot{m}_{out}^2}{4 * \rho_{out} * A_{out}^2} \quad (5.14)$$

Kuikhoven [52] concludes that the assumption of perfect separation or perfect insulation has no significant effect on the outputs of the separator. Nevertheless, the trend in temperature of the orifice is less correct when perfect separation is proposed instead of perfect insulation. In the demo set-up, there is an orifice instead of a turbine to symbolize the pressure drop of the turbine. Kuikhoven's research focuses on mixtures as working fluid, while this thesis will focus on pure ammonia. Therefore, the assumption of perfect separation or insulation is examined again, see appendix E.2.3. In the case of pure ammonia, it can be concluded that the difference between perfect insulation or separation seems no longer has an effect.

5.3.4. Valve

The function of the valve is that the liquid flow from the recuperator has the same pressure as the turbine outlet. Thus, it expands the liquid flow to a lower pressure level. Due to the ideal valve assumption, the valve presents no heat losses. With the known pressure, enthalpy and concentration, all properties of the flow to the mixer can be obtained from the equation of state.

Mass conservation

$$\dot{m}_{in} = \dot{m}_{out} \quad (5.15)$$

Energy conservation

$$h_{in} = h_{out} \quad (5.16)$$

5.3.5. Turbine

In Chapter 3, the off-design model of the turbine is introduced and it is mentioned that the turbine is modelled like a nozzle. The pressure drop depends on the turbine design and inflow conditions, see equation 3.22. The performance of the turbine will depend on the degree of deviation from the design conditions. An efficiency correction method is used in the off-design calculation, see equations 3.26 and 3.27. As soon as the efficiency is derived, the real output and conditions of the outlet of the turbine can be obtained.

The turbine design depends on the conditions of the turbine in on-design conditions. In Chapter 3, the three parameters, SP , V_r and N_s are introduced, which are used to obtain the on-design performance of the turbine in the performance map of Astolfi and Macchi [6]. The performance map is implemented in the off-design model as feedback for the off-design performance, see figure 5.5. Fig 5.5a presents the design performance map of the specific Size Parameter, with the obtained off-design turbine performance. Fig 5.5b shows a detail of figure 5.5a, where only the range is shown where OTEC is applicable. This gives a representation of the deviation of the off-design performance compared to the design performance map with emphasis on the specific speed. By means of an interpolation function, the optimal rotational speed is obtained from the design performance map. The interpolation is done by a regular grid interpolator made by Scipy [41]. Fig 5.5c shows the contour map of the maximum attainable efficiency at optimized rotational speed and optimal results, with also herein the the obtained off-design performance. In this figure, the cooperation of the Size Parameter and volumetric flow is clearly visible.

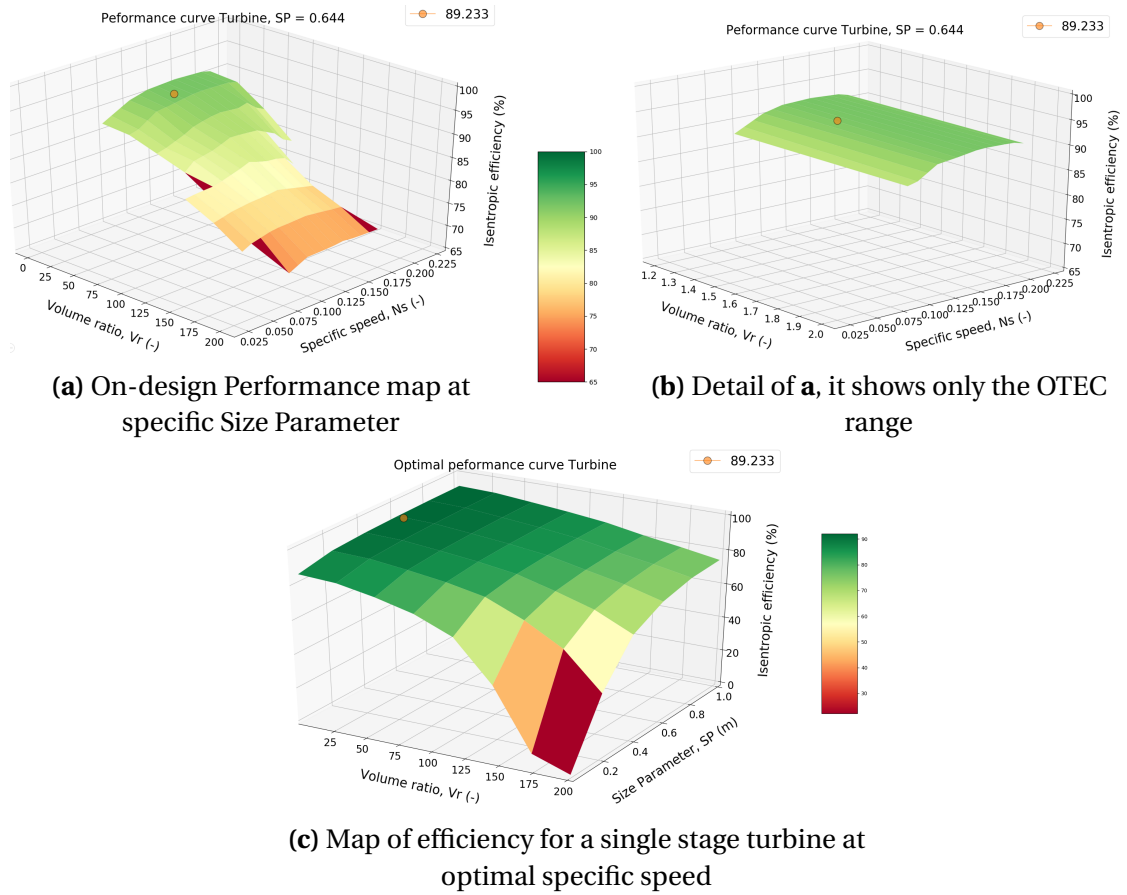


Figure 5.5: Feedback of the off-design performance.

Pressure drop over the turbine

In Chapter 3 is mentioned that the pressure drop over the turbine is an important parameter for the power output and is introduced that the pressure drop is a result of the resulting vapor mass flow, the achieved turbine inlet conditions and the Stodola constant, Y_{design} . As soon as the environmental conditions deviate from the design conditions, the optimal position of the vanes can change, which results in a specific pressure drop in the system. Hence, the position of the vanes should be optimized to have the most net power output at specific environmental conditions. The Stodola constant implies the position of the vanes, so if the Stodola constant varies the opening of the vanes varies. A multiplier of the Stodola constant, f_{VTG} , represents a factor for the vane opening, which operates in the opposite direction, the larger the multiplier, the narrower the nozzle. Ultimately, this results in that it is possible to control the pressure drop over the turbine and therefore the vapor mass flow. The performance map in figure 3.14 shows that it is more harmful to have a higher mass flows than a smaller mass flows relative to the design mass flow through the turbine. As soon as the warm seawater temperature rises, the heat load increases, which results in that the pressure drop or vapor mass flow increases in the turbine. Therefore, it is important to adjust the position of the vanes to regulate the pressure drop over the turbine, i.e. change of the vapor mass flow. For this reason, tightening of the nozzle is required, with the result that the pressure drop increases instead of the vapor mass flow, which is better for the performance of the turbine. As soon as the plant operates below design conditions, the vanes can be regulated with the result that the pressure drop can be reduced, so that the vapor mass flow increases.

Optimal rotational speed turbine

The optimal specific speed can be investigated with the optimal efficiency derived by using the correlation of Vonk [83], see equation 3.12. From this, the optimal rotational speed can be investigated, so that it can be examined whether the turbine is suitable for the size of the cycle. The rotational speed that is assumed in this report is 3600 rounds per minute. This value is derived from that it is suitable to the connection with the grid. Namely this has a frequency of 60 Hz. If the rotational speed should be higher a gearbox is necessary. For efficiency losses and purchase costs this is not desirable. Next to this, the feedback of the optimal rotational speed gives some information how much the optimal rotational speed varies in off-design conditions. Therefore, a conclusion can be made if the turbine can operate at constant or variable rotational speed.

5.3.6. Mixer

The mixer uses the same balances as the separator. The energy content of the working fluid stream should be lower than at the inlet of the separator, since some energy is consumed in the recuperator and/or turbine stage. The conditions of both mixer inlets are known, so the outlet properties can be determined with the mass and energy balance. The same pressure drop as the on-design model is assumed in the off-design model.

5.3.7. Pump

The work that the pump consumes can be derived by equation 5.17. As soon as the isentropic efficiency is known, the inlet enthalpy can be derived, see equation 5.18.

$$\dot{W} = \dot{m} * (h_{in} - h_{out}) = \frac{\dot{V} * \Delta P}{\eta_{is,pump}} \quad (5.17)$$

$$h_{in} = h_{out} - \frac{h_{out} - h_{in,is}}{\eta_{is}}, \quad (5.18)$$

The isentropic enthalpy can be derived with the known outlet entropy of the pump and the known pressure levels. Goudriaan [33] proposes a correlation for the isentropic efficiency, which is derived by experimental research and data fits, see equation 5.19. It symbolizes the isentropic efficiency of the working fluid pump of the demo set-up.

$$\eta_{is,pump} = (-0.11 * \rho_{av} + 79.6)/100, \quad (5.19)$$

where, ρ_{av} is the average density of the in- and outlet of the pump. Because of this, the isentropic efficiency depends on the density of the flows. A deviation of the density results in a deviation of the isentropic efficiency.

The deviation of the outlet density of the pump is investigated. The experimental data consists of two sets, in which the conditions of the demo set-up differ. The working principle of the working fluid pump is an oscillating pump, whereby the pressure is higher in the pump and with a damper a more or less constant working fluid mass flow is regulated. Therefore, the outlet pressure of the damper describes the outlet pressure of the pump. Unfortunately, the pressure sensor after the damper was not in use during the experiments. Therefore, the model is executed with two different pressures. The first pressure represents the pressure of the pressure sensor before the damper. The second pressure represents the pressure

derived from the evaporator pressure with assumed pressure drop over the recuperator. Figure 5.6 shows the deviation of the outlet density of the pump.

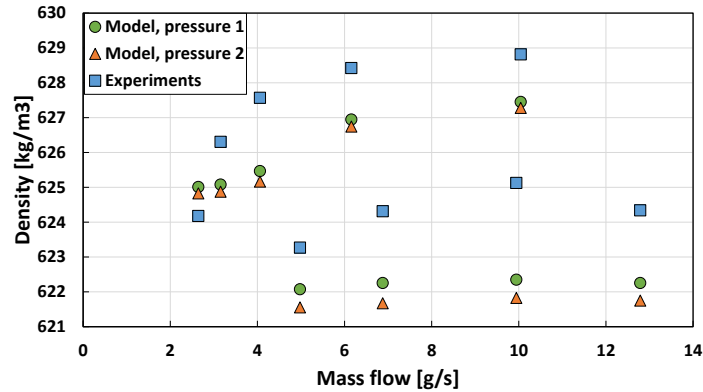


Figure 5.6: Comparison of the model versus the experimental data for the outlet density of the pump. The experiments consists of two different data sets, in which a different pressure drop in the cycle was used. The difference between pressure 1 and 2 depends on which pressure sensor is used.

The average deviation of the density is around the 0.3% for both modelled pressures. The deviation of the energy balance of the whole cycle is influenced by the work input of the cycle pump. The influence of the density is very small, since the work input of the pump is relatively small with respect to the heat input of the evaporator. Therefore, it can be concluded that use of the correlation of Goudriaan is valid.

The working principle of the pump in the OTEC demo set-up is not realistic for a commercially pump, since the efficiency is very low. In the on-design model, the isentropic efficiency is an assumed fixed value and Kleute mentions that the cycle is mainly sensitive to fluctuations of the seawater pump efficiency and not for the working fluid pump [49]. Therefore, it is valid to assume that the working fluid pump has a fixed isentropic efficiency for the upscaled plant. For further research, it is recommended to investigate a pump characteristics of a more upscaled pump. The pump characteristics of Goudriaan are used for the validation steps of the off-design model.

5.4. Numerical model

The main cycle is calculated with an overarching solver algorithm. It solves an unique steady state condition at some initial conditions. The solver has to converge to an unique solution, which should be equal to the reality. The founded steady state can be validated with the demo set-up of the OTEC cycle. Other algorithms, like the solver for the properties of the heat exchanger, are inside the main cycle algorithm. This section will discuss the inputs of the model for the different components and the solving algorithm.

5.4.1. Input of the model

On top of the inputs of the model conditions, like mass flows, working fluid concentration and water conditions from table 5.1, the model needs also additional inputs and initial guesses. In table 5.2, an overview of the additional inputs is shown. In appendix E.2, additional initial numbers are given and explained in more detail. To achieve exactly the same model results, these initial inputs are important.

In addition to the additional inputs, the off-design model uses also a input value, which

Table 5.2: Additional inputs for the off-design model

Component	Required input/initial guess	Value/Name
Evaporator	Geometry	See section 2.5
	Control volumes	100
	Heat transfer correlations	
	Two phase (wf-side)	Ayub (direct expansion)[9]
	Single phase (wf-side)	Donowski & Kandlikar[24]
	Single phase (water-side)	GoudKuik[33][52]
	Pressure drop correlation	
Single phase (water-side)	VDI [57]	
Condenser	Geometry	See section 2.5
	Control volumes	100
	Heat transfer correlations	
	Two phase (wf-side)	Geschiere [31]
	Single phase (wf-side)	Donowski & Kandlikar[24]
	Single phase (water-side)	GoudKuik[33][52]
	Pressure drop correlation	
Single phase (water-side)	VDI [57]	
Recuperator	Geometry	See section 2.5
	Control volumes	500
	Heat transfer correlations	
	Single phase (wf-side)	Donowski & Kandlikar[24]
Separator	Radius of the ports	See section 4.4.4
Turbine	On-design conditions	See section 4.4.3

symbolizes the required vapor fraction at the outlet of the evaporator. As a result, the working fluid mass flow is no longer an optimization input variable. The first initial working fluid mass flow is determined by the correlation of Ray [69], see equation 3.24. Thereafter, the working fluid mass flow is determined with the vapor mass flow of the iteration with the smallest error. This vapor mass flow is divided with the chosen input value to determine the working fluid mass flow.

5.4.2. Solving Algorithm

Goudriaan and Kuikhoven compare a differential evolution solver with a particle swarm optimization and the brute force algorithm. They choose for the differential evolution as solver. A brute force optimization, where the model uses every possible input, leads to the same result. But the brute force optimization uses a lot more iterations and therefore the differential evolution is preferred, since fast convergence is an important criterion of the off-design model. In section 4.6.1, the differential evolution (DE) is introduced. The DE has recently proven to be an efficient method for optimizing real-valued multi-model objective functions. An additional advantage of the DE is that it is very simple to understand and to implement. The DE consists of different settings with its own rules. First, the population size is determined by 10 times the number of parameters. Next, the crossover constant or recombination should be set at 0.9 for real-world optimization problems [64].

Usually the crossover probability must be considerably lower than one. If no convergence can be achieved a higher value helps [76]. At last, the mutation factor or weighting factor varies randomly between 0.5-1 in each generation. This improves significantly the con-

vergence behavior, especially for noisy objective functions. The population size correlates with the mutation factor. The larger the population size is, the smaller the mutation factor should be. Table 5.3 shows an overview of the differential evolution settings of the off-design model. In the table, the bounds of the off-design model are also introduced and the convergence criterion, where the solver accepts the steady state condition of the cycle.

The strategy, 'best1bin', is chosen, which is also the default setting of Scipy's DE. The 'best1bin' is the best solution found so far, since it has usually a fast convergence speed and performs well when solving unimodal problems. However, they are more likely to get stuck at a local optimum and thereby lead to a premature convergence when solving multimodal problems [65].

An objective function is a function to be maximized or minimized in optimization theory. In this objective function, the inputs are the guess pressure and temperature of the working fluid inlet conditions of the evaporator. The parameter which is optimized is the enthalpy error. To calculate the enthalpy error, there will be a forward and backward loop. The forward loop, which follows the direction of the evaporator and a backward loop, which is going over the recuperator to the inlet of the cycle pump. The inlet enthalpy of the cycle pump from the backward loop can be compared with the inlet enthalpy of the cycle pump from the forward calculation. The resulting difference between the enthalpies is used as the cycle error and is fed back to the solver. The solver will evaluate the guessed input values of the evaporator.

Table 5.3: Differential evolution algorithm settings of the model

Setting	Value	
Population size	20	
Mutation	0.5-1	
Recombination	0.9	
Solving Strategy	'best1bin'	
Bounds	Pressure	7.0-10.0 [bar]
	Temperature	288.15-295.15 [K]
Convergence criterion	Enthalpy error	< 50 [$\frac{J}{kg}$]

The convergence criterion is the enthalpy error, which may be not larger than $50 \frac{J}{kg}$. If the convergence criterion is not met, new initial guesses are made for the inlet of the evaporator. This iteration continues until the convergence criterion is reached. In this situation, the inlet pressure and temperature are accepted as the solutions for the operating condition of the cycle. The mass and energy balance is continuously monitored. In the model, several breakpoints are implemented, which are checks to ensure that the solver only converges to realistic solutions. Furthermore, the breakpoints speed up the convergence, since the iteration stops if an error occurred. Table 5.4 gives the errors, which can possibly occur in the model. The sub-cooling and vapour fraction errors are dependent on how much sub-cooling or vapour fraction is present. Thereafter, the solver detects the different values of the iterations and evaluates the iterations so that this leads to convergence of the model. Some errors are able to be turned off, since some errors can occur in reality in some situations. Figure 5.7 shows the solution algorithm, where the state points in the algorithm come from figure 5.1.

Table 5.4: Possible breakpoints in the model

Component	Error
Heat exchangers	No solution found
	Optimization not successfully
Evaporator	No vapor outlet
	Super-heated vapor
Turbine	Pressure outlet not found
Recuperator	Temperature cold stream higher than hot stream
	Temperature cold stream lower than sea water stream inlet
Condenser	Temperature inlet hot stream lower than inlet cold stream
	Too much sub-cooling
	Outlet contains a vapor fraction
Pump	Enthalpy out of range
	Temperature inlet higher than outlet
	Pressure inlet higher then outlet
All components	Mass balance
	Energy balance

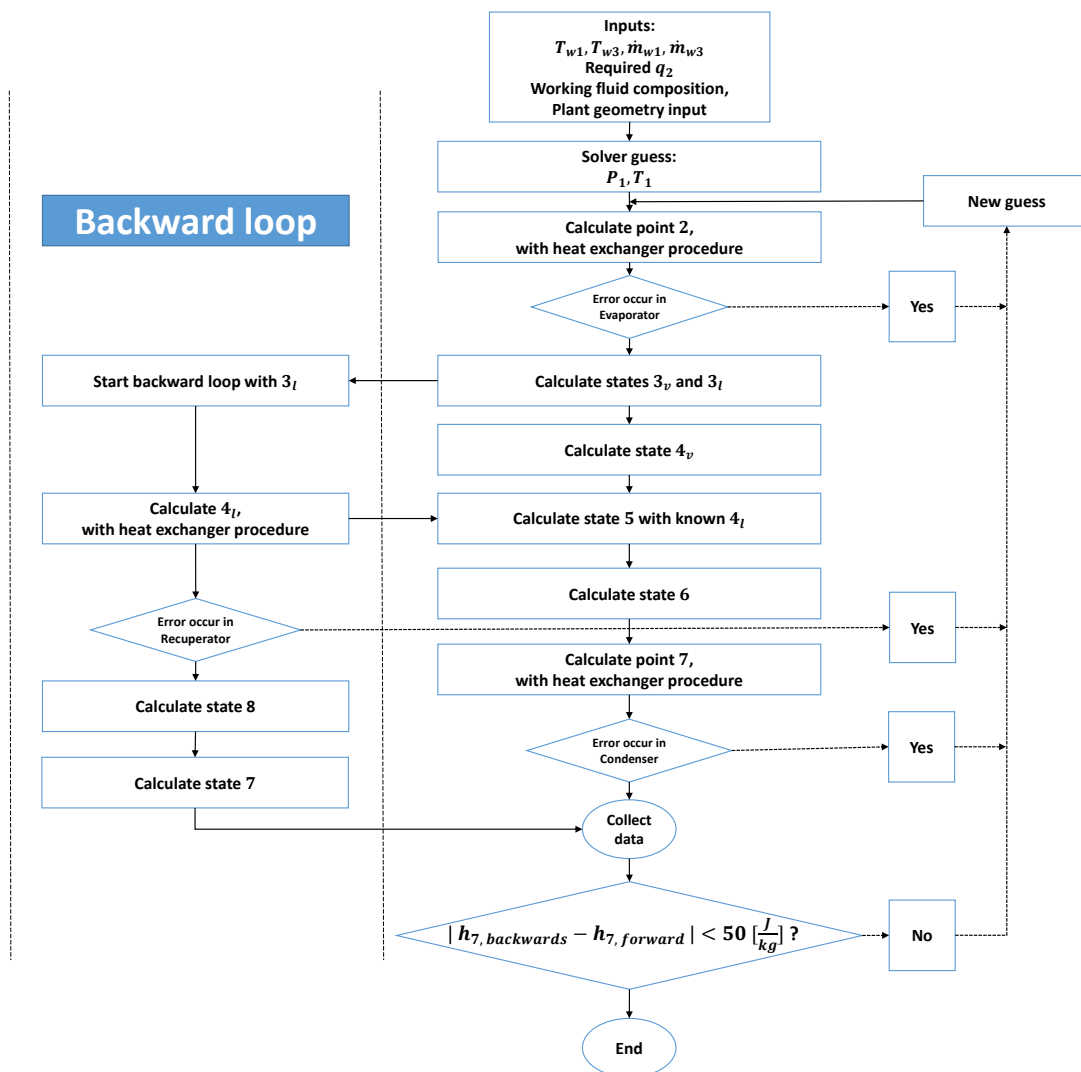


Figure 5.7: Kalina cycle solution algorithm.

5.4.3. Fast calculation method

The model needs multiple iterations to find the steady state condition. Therefore, any saving of calculation time in each iteration is desirable. The number of equation of state calls is enormous per loop iteration. As soon as less calls can be occurred, the computational time reduces. In the model an option is applied, which can be selected before the start of solving the model. The method is the fast calculation method. In this method, the properties of the evaporator and condenser are not determined for every control volume, but are equal to the average of the first and last cv. Hereby, a fast estimation of the correctness of the guess outlet temperature of the water side can be realized. As soon as the area error comes near the convergence criterion of the area error, the fast calculation method is turned off and the properties of each control volume will be determined. In section 5.3.2, the area error is explained in more detail. The method ensures that the computational time decreases with at least 15%. The run time of the entire model depends on the convergence criterion, but the model usually needs at least 3 hours. Therefore, the computational time can be significantly improved by the method. The difference between an iteration with or without the fast method is on average $2.31e-5$. Table 5.5 shows the average deviation of the fast calculation method of a specific parameter in one random iteration. The specific parameter is the average of that parameter in all calculated state points.

Table 5.5: Deviation of the fast calculation method

Parameter	T	P	\dot{m}	h	s	q
Average deviation [%]	$8.32e^{-6}$	$4.22e^{-8}$	$2.95e^{-5}$	$4.36e^{-5}$	$3.83e^{-5}$	$1.86e^{-5}$

Therefore, it can be concluded that the fast calculation is acceptable. Nevertheless, the advice is to use the 'slow' method for the final run and for testing to use the fast method. Since the fast calculation method uses less computational time, it is possible to get faster more insight into several runs with different settings.

5.5. Discussion off-design model

The configuration of the on-design and off-design model is a Kalina cycle. In ordinary Rankine cycles, a reflux of the working fluid through the evaporator with a drum is proposed. With the result that, the value of the vapor fraction at the outlet of the evaporator can be different and still sends a pure vapor stream to the separator. Because of this, it allows the Kalina cycle to continue to work as an ordinary Rankine cycle. Therefore, the in on-design optimization set value, which was set to 1.0, can be re-investigated. In the off-design model, the influence of the working fluid mass flow is small on the net power output, but the controllability is better if the value is lower than 1.0. Therefore, the results will be produced with a vapor fraction of 0.7. In the most literature studies of modelling an ORC, an imposed fluid sub-cooling is assumed [23]. Such hypotheses make the off-design models not fully deterministic and can mislead the performance predictions. In the existing model, the influence of the charge, the total mass of working fluid, is not included and the sub-cooling to the working fluid pump is imposed. Therefore, the role of the buffer tank or liquid receiver is neglected. It is recommended to implement the buffer tank as part of the off-design model, which makes the model more realistic. Especially when the OTEC demo set-up is converted into a pure ammonia ORC. As soon as the working fluid is evaporated to full vapor, the saturated amount of liquid in the buffer tank is no longer self-evident. Therefore, the model of Dickes [23] is recommended and the cooperation of the working fluid pump and the buffer tank can be examined.

6

Results

In Chapter 4, the on-design model is introduced, which can be used to derive a power plant in the optimal technical and economical performance of the OTEC applications. Subsequently, the geometries of the components can be used as input in an off-design model, which is discussed in Chapter 5. Hereby, the off-design model can be used for the analysis of the gross 15 MW OTEC plant. The off-design performance is analyzed, which means the influence of changes of the environmental conditions. The influence of the seawater inlet temperatures on the performance of the cycle is investigated and different design conditions of the warm seawater are compared. Next to this, the influence of the seawater mass flows is explored. In the whole off-design analysis, the focus will be on the turbine off-design performance and the thermodynamic influence of the turbine on whole OTEC cycle. Before the off-design model can serve as a numerical tool, it should be validated.

6.1. Validation

A sense of confidence and usability of numerical models can be attained with verification and validation. These independent procedures engage together to check the numerical model. Verification checks if the model is correctly built, so verification is concerned with the system is well-engineered, error-free and so on. Verification helps to determine whether the software is of high quality, but it will not ensure that the system is useful. Validation checks if the model is correct and is concerned with checking that the model predicts the reality correctly. Verification and validation of numerical models of natural systems is impossible, since natural systems are never closed and because model results are always non-unique [62]. However, models can be confirmed with experiments, since a demonstration of agreement between observation and prediction is possible. Models can only be evaluated in relative terms and their predictive value is always open to question. The verification and validation of the off-design model is a follow-up from the theses of Goudriaan and Kuikhoven [33][52], where different components of the off-design model have been validated. The experiment data has been taken over from Dahlgren [20], Goudriaan [33] and Kuikhoven [52]. Therefore, the method of measurement and the deviation of measurement the data is not included in this thesis. The experiments are done with the small scale set-up at the TU Delft and table 6.1 shows the data, which has been used in the validation steps.

Table 6.1: Parameters of the experimental set-up

Test number		1	2	3	4	5	6	7	8	9
\dot{m}_{wf}	$[\frac{g}{s}]$	4.1	3.2	2.6	6.2	10.0	5.0	6.9	9.9	12.8
\dot{V}_{hot}	$[\frac{L}{s}]$	0.3	0.3	0.3	0.6	0.6	0.3	0.3	0.3	0.3
ρ_{hot}	$[\frac{kg}{m^3}]$	996.5	996.5	996.5	996.5	996.5	996.5	996.5	996.5	996.5
T_{hot}	$[^{\circ}C]$	27	27	27	27	27	27	27	27	27
\dot{V}_{cold}	$[\frac{L}{s}]$	0.225	0.225	0.225	0.45	0.45	0.22	0.23	0.22	0.22
ρ_{cold}	$[\frac{kg}{m^3}]$	1000.0	1000.0	1000.0	1000.0	1000.0	1000.0	1000.0	1000.0	1000.0
T_{cold}	$[^{\circ}C]$	5	5	5	5	5	5	5	5	5
NH ₃	$[%]$	100	100	100	100	100	99.9	99.9	99.9	99.9
Δp_{ori}	$[bar]$	3.81	3.82	3.83	3.86	4.83	2.22	2.20	2.17	2.11

6.1.1. Heat exchanger pressure drop

The pressure drop of the heat exchangers is researched by Dahlgren [20] and proposes pressure drop correlations for the single and two-phase flow of the condenser. For the single phase flow, the correlation from equation 2.28 is proposed and for the two phase flow, the correlation from equation 2.33 is proposed. Dahlgren concludes that the single phase correlation is valid in the Reynolds number range of $725 < Re < 2472$ and that the trend is similar to the VDI single phase correlation, see figure 2.10 [57]. Therefore, the numerical model uses the VDI correlation for the single phase water flow pressure drop, since the validation range is wider for this correlation. For the two phase flow, Dahlgren concludes that the correlation is validated in a range of $52 < \dot{G}_{wf} < 84$ and has a maximum error of 5% with respect to the measured Fanning friction factors. However, figure 2.11 shows that the Fanning friction factor does not correspond with any of the existing correlations. Therefore, it is concluded that two phase correlation is not valid to use, since the correlation is not validated in a larger range. In addition to the small validation range, the variation of the vapor fraction was small and therefore the correlation seems also not valid enough. Ultimately, the pressure drop of the seawater side is the most important, since the sizing of the heat exchanger depends on the seawater side pressure drop, see section 4.4.2. Therefore, it is assumed that the heat exchanger pressure drop of the working fluid side in the off-design model can be taken over from the on-design model. In further research, it is recommended to find a pressure drop correlation for the working fluid side, so that this assumption is no longer necessary.

6.1.2. Separator

The influence of the assumption of perfect separation or insulation in the separator is discussed in section 5.3.3. In the case of pure ammonia, it can be concluded that the difference between perfect insulation or separation seems no longer has an effect and therefore the validation of the separator in the thesis of Kuikhoven is still valid.

6.1.3. Turbine

The performance map of Astolfi and Macchi [6] is used in the design phase. Astolfi and Macchi say this about the validity of its performance map: "*The correlations can be used for a preliminary estimation of turbine performance in the numerical optimization of ORC even if the results are affected by inaccuracy mainly related to the quality of efficiency losses correlations and the simplified volumetric behavior assumed in the generation of the performance maps*". In the off-design model, the correlation of Jüdes et al. [43] is used to

evaluate the off-design performance of the turbine relative to the design efficiency. The correlation is widely used in steam and ORC studies and in Chapter 3 and appendix B.2, the trend of the turbine efficiency is compared to the studies of Tsoutsanis, Petrovic and Hue [80][63][38]. From this, the correlation seems to have realistic trends and therefore it is assumed that this correlation is valid.

6.1.4. Full model validation

The next step is the full model validation of the off-design model. Since the sub-components are validated, the full cycle should automatically be validated as well. That is because the cooperation of the sub-components only consists of process stream transport. The model is able to predict the experimental outputs with an average deviation around 4%, as shown in table 6.2. The full model validation test is executed for the experimental data of test number eight and the average of all tests is shown in the last column.

Table 6.2: Model outputs for test case 8 and the average deviation of all tests. Note that due to the lack of some data, some parts have been left empty.

Component	Variable	Unit	Experimental measured	Model	Deviation [%]	Average deviation [%]
Evaporator	T_1	$^{\circ}\text{C}$	17.43	17.95	3.03	5.13
	p_1	bar	8.96	9.11	1.68	2.10
	T_2	$^{\circ}\text{C}$	21.10	21.89	3.71	2.97
	p_2	bar	8.96	9.10	2.45	2.11
	T_{w2}	$^{\circ}\text{C}$	23.10	22.88	0.94	0.41
	p_{w2}	bar	0.99	0.98	0.08	1.86
	q_2	-	0.42	0.43	2.02	4.69
	\dot{Q}_{evap}	W	5123	5170	0.92	4.22
Separator	T_{3l}	$^{\circ}\text{C}$	20.87	21.88	4.85	2.83
	p_{3l}	bar	8.87	9.10	2.68	2.21
	T_{3v}	$^{\circ}\text{C}$	20.88	21.88	4.78	3.24
	p_{3v}	bar	8.87	9.10	3.68	2.37
Turbine	T_{4v}	$^{\circ}\text{C}$	14.71	15.69	6.67	8.40
	p_{4v}	bar	6.61	6.93	4.85	5.49
	$\dot{W}_{turbine}$	W	0	0	-	-
Recuperator	T_{4l}	$^{\circ}\text{C}$	12.58	12.63	0.40	9.51
	p_{4l}	bar	8.67	9.09	2.60	2.21
	\dot{Q}_{rec}	W	254	250	1.65	-
Valve	T_5	$^{\circ}\text{C}$	11.96	12.65	5.83	10.69
	p_5	bar	6.61	6.93	4.85	5.47
Mixer	T_6	$^{\circ}\text{C}$	-	13.50	-	-
	p_6	bar	-	6.93	-	-
Condenser	T_7	$^{\circ}\text{C}$	10.55	11.97	13.55	15.81
	p_7	bar	6.59	6.93	5.02	5.50
	T_{w4}	$^{\circ}\text{C}$	10.48	10.50	0.28	1.22
	p_{w4}	bar	0.95	0.95	0.01	1.78
	\dot{Q}_{cond}	W	-5188	-5201	0.26	2.92
Cycle pump	T_8	$^{\circ}\text{C}$	12.11	12.62	4.17	4.51
	p_8	bar	8.99	9.12	1.45	-
	\dot{W}_{pump}	W	32.57	31.26	4.02	-
Average deviation					3.33	4.17

6.1.5. Analysis solver

The over-arching solver of the off-design model should give the unique and correct steady state operating point. Therefore, an analysis of the solver gives an indication of how reliable the solver algorithm is, but it can also show whether the solver algorithm can be improved. The explanation of the solver is given in section 5.4.2 and the Kalina cycle solution algorithm is shown in figure 5.7. The solver should converge to the minimum and not its local minimum. Therefore, an analysis of the solver indicates whether the solver is working properly with the current settings of the solver. The solver should have a clear optimum, which makes the outcome of the model no coincidence. As soon as the optimum of the solution is clear, the tolerance of the error is small enough. Figure 6.1 shows the convergence of the solver of a specific run in a 3D plot. In the figure, each iteration is shown with corresponding enthalpy error. The color of the scatters represents the accuracy of the iteration, how greener how better and redder how more worse the solution is. Notice that highest values in the graph are imposed values of the breakpoints, thus artificial values. How earlier they occur in the solving algorithm, the higher the value, so the errors in the evaporator have the highest values.

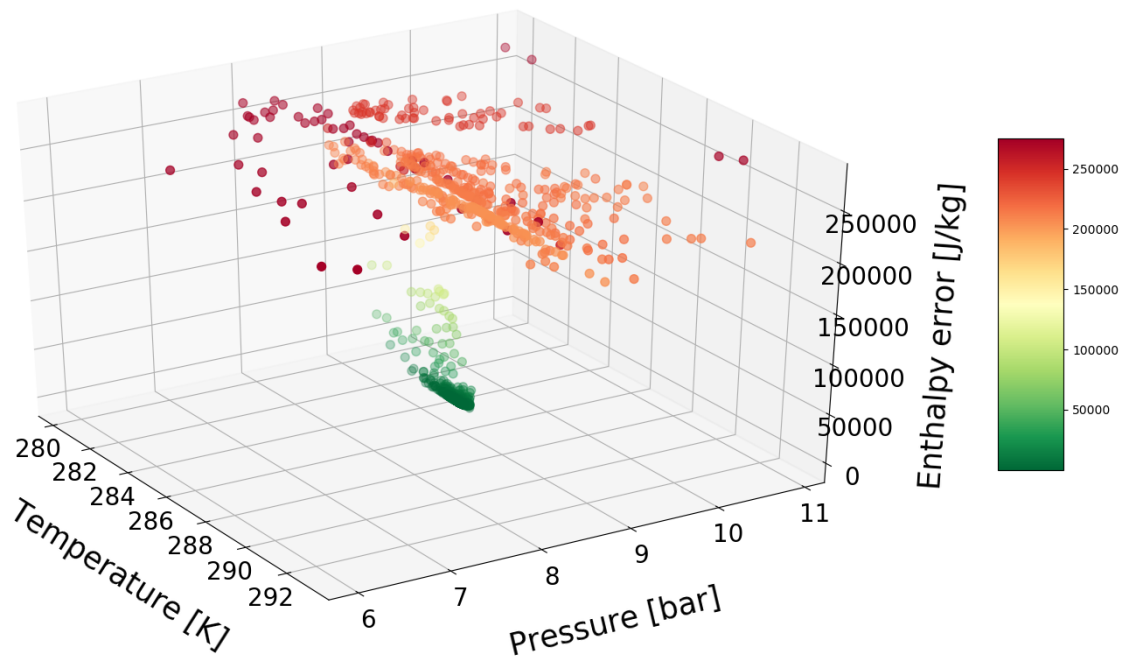
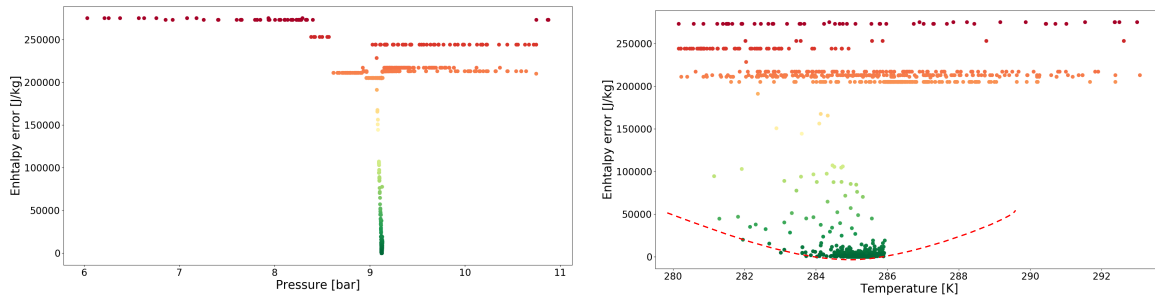


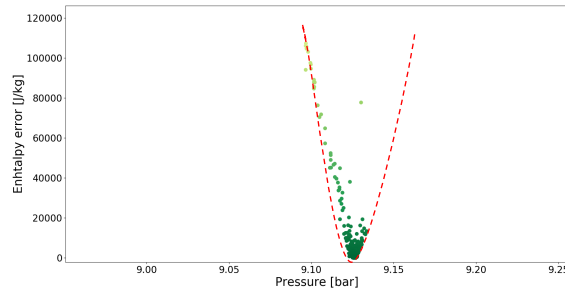
Figure 6.1: Convergence of the solver in a 3D plot, in which each iteration is shown with corresponding enthalpy error.

From figure 6.1, it can be concluded that there is a clear optimum in the solver. Figure 6.2 gives a more detailed representation of the analysis of the solver. Figures 6.2a and 6.2b show the same values as figure 6.1, but in a 2D representation. The red line in figure 6.2b represents the optimum which can be observed. Figure 6.2c shows a zoom-in of figure 6.2a, so that a clear optimum can be observed. Subsequently, figures 6.2d and 6.2e show the convergence values of the solution. It can be concluded that if the tolerance of the error is set low enough, there is one unique solution of the convergence. Finally, figure 6.3 shows the iterated guesses of all iterations. It is very clearly that more iterations are performed around the convergence values.

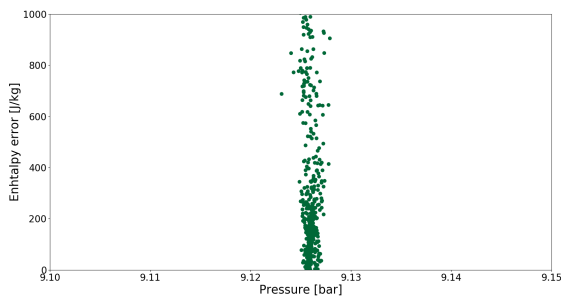


(a) Pressure versus the enthalpy error

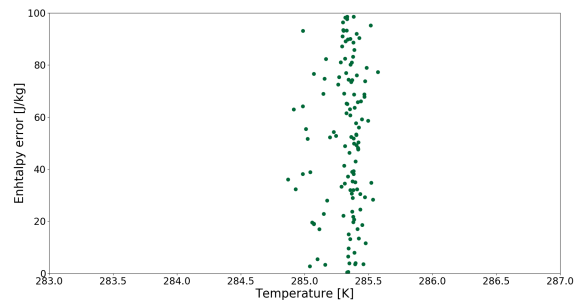
(b) Temperature versus the enthalpy error



(c) A detail plot of figure 6.2a



(d) The convergence value of the pressure



(e) The convergence value of the temperature

Figure 6.2: Analysis of the solver. The color represents the accuracy of the iteration, how greener how better and how redder how more worse the solution is.

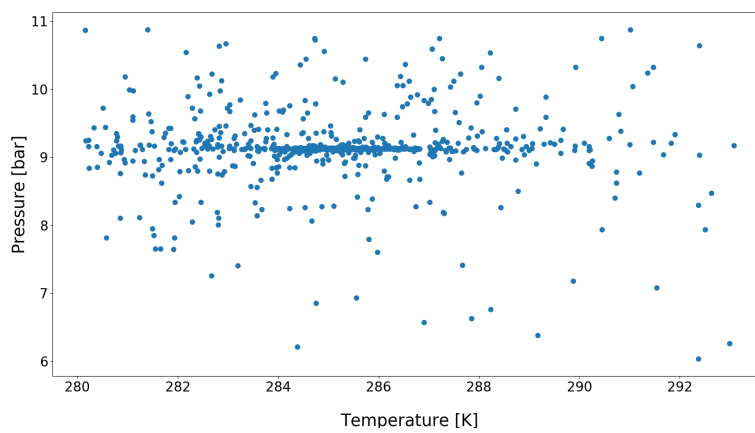


Figure 6.3: An overview of the iterated guesses of all iterations. The temperature versus the pressure

6.2. Influence of the temperature variation

In the potential areas for the OTEC plants, the seawater temperatures fluctuate. These temperature fluctuations at each location have potentially a high impact on the performance of an OTEC plant since the overall temperature difference is relatively low. Therefore, it is interesting to investigate the off-design performance with varying temperatures. Figure 6.4 shows the monthly temperature variation, which is used in the analysis of the off-design performance. The temperatures are derived from World Ocean Atlas 2013 [3].

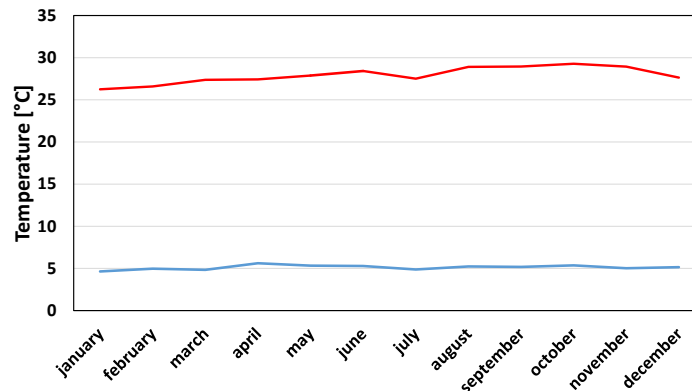


Figure 6.4: Temperature of the warm and cold seawater at 10 m and 1000 m depth at Curaçao, near the airport on the north side. [3]

From figure 6.4, it can be concluded that the fluctuation of the cold seawater during a year is small. However, the variation of the warm seawater temperature is significant, which leads to a fluctuation in the temperature difference, see figure 6.5. This temperature difference is the driving force of the OTEC cycle.

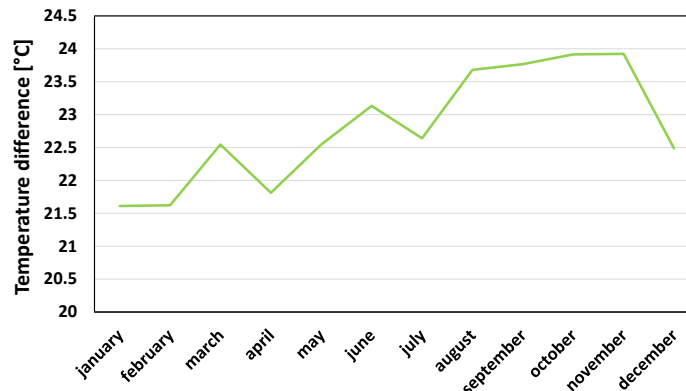


Figure 6.5: Temperature difference between 10 m and 1000 m depth at Curaçao, near the airport on the north side. [3]

The influence of these fluctuations is investigated with the off-design model. The geometry of the components, which is the input for the off-design model will be derived by the optimized on-design model, see Chapter 4. The environmental conditions will be varied during the power plant design phase, whereby different power plants are obtained for the specific environmental condition. Table 6.3 introduces the three scenario's, where the first scenario is with the lowest temperature difference. This results in that this plant is the largest plant since the 15MW gross power is been set during the design phase. Then, the standard scenario with a temperature difference of 22K and finally the best scenario with a temperature difference of 24K. Hereafter, the off-design model is optimized by optimization of the pressure drop over the turbine and a specific power curve is obtained for each

plant. During the off-design simulations, the mass flows of the seawater sides are kept constant in this research. In section 6.2.1, the on-design results will be discussed, section 6.2.2 gives the off-design optimization and section 6.2.3 gives the final results. Finally, the results are compared and a recommendation is made.

Table 6.3: Overview of the input variables for the numerical model to analyze the off-design performance of the OTEC set-up.

Model inputs	Case study 1: $\Delta T = 20^\circ\text{C}$		Case study 2: $\Delta T = 22^\circ\text{C}$		Case study 3: $\Delta T = 24^\circ\text{C}$	
Geometry	On-design plants of 15MW_{gross} @ $\Delta T = 20/22/24^\circ\text{C}$					
\dot{m}_{cold}	On-design	kg/s	On-design	kg/s	On-design	kg/s
\dot{m}_{warm}	On-design	kg/s	On-design	kg/s	On-design	kg/s
\dot{m}_{wf}	Optimize	kg/s	Optimize	kg/s	Optimize	kg/s
f_{Nozzle}	Optimize	–	Optimize	–	Optimize	–
$T_{cold,in}$	5.0	$^\circ\text{C}$	5.0	$^\circ\text{C}$	5.0	$^\circ\text{C}$
$T_{warm,in}$	25.0	$^\circ\text{C}$	27.0	$^\circ\text{C}$	29.0	$^\circ\text{C}$
c_{NH_3}	100	%	100	%	100	%

6.2.1. On-design results

With the model introduced in Chapter 4, the optimized on-design conditions can be derived. The geometry of the components and the optimization variables of the on-design model are the results of the on-design optimization, see table 6.4. Every plant results in a specific design costs with a designed net power output, see figure 6.6. From the figure, it cannot yet be concluded that one of the three design conditions has an advantage over the others. Therefore, the off-design performance is important, since the power curves of the OTEC plant determine the performance of the designs throughout the year.

Table 6.4: Optimal on-design output values

Scenario	Unit	Plant 1	Plant 2	Plant 3
Design Temperature difference	[K]	20	22	24
Design warm seawater Temperature	[$^\circ\text{C}$]	25	27	29
x0: Warm water mass flow	[$\frac{\text{kg}}{\text{s}}$]	41618.9	35829.5	28861.6
x1: Cold water mass flow	[$\frac{\text{kg}}{\text{s}}$]	34346.0	27044.5	21382.1
x2: High pressure level	[bar]	8.57	9.01	9.50
x3: Low pressure level	[bar]	6.23	6.35	6.51
x4: Pressure drop water side	[bar]	0.10	0.09	0.11
x5: Water pipe diameter	[m]	4.73	4.16	3.65

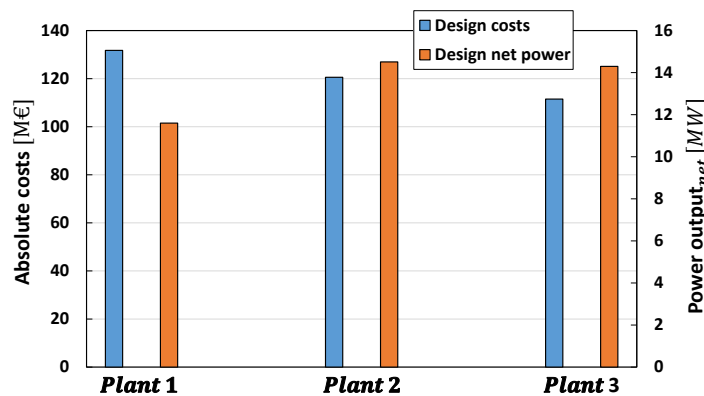


Figure 6.6: Absolute costs and net power of different plants.

6.2.2. Off-design optimization

The optimized design plant with specific components geometries serves as input for the off-design model. As soon as the environment conditions are changed, the off-design model reaches an other steady state operating point with a specific power output. In section 5.3.5 is introduced that the vane opening should be optimized to have the optimum relation between the vapor mass flow and the pressure drop over the turbine with respect to the net power output. Figure 6.7 shows the optimization of the off-design performance of plant 2 and in appendix E.3 the optimization of plants 1 and 3 are shown. The numbers at the points are the relative opening factor of the vanes and it can be concluded that a vane that is more open results in a lower pressure drop. The regulation of the vanes is more present in plants which operate at higher warm seawater temperature than design conditions, so plant 1 and 2. This is result of that it is more harmful to have vapor mass flows higher than the design mass flow, see Chapter 3. As soon as the plant operates below design conditions, the vanes can be regulated with the result that the pressure can be reduced and the vapor mass flow increases. In plant 2, this has an positive effect on the net power output, see figure 6.7. In plant 3, the reduction of the pressure drop cancels the positive effect, despite an increase of the isentropic efficiency of the turbine.

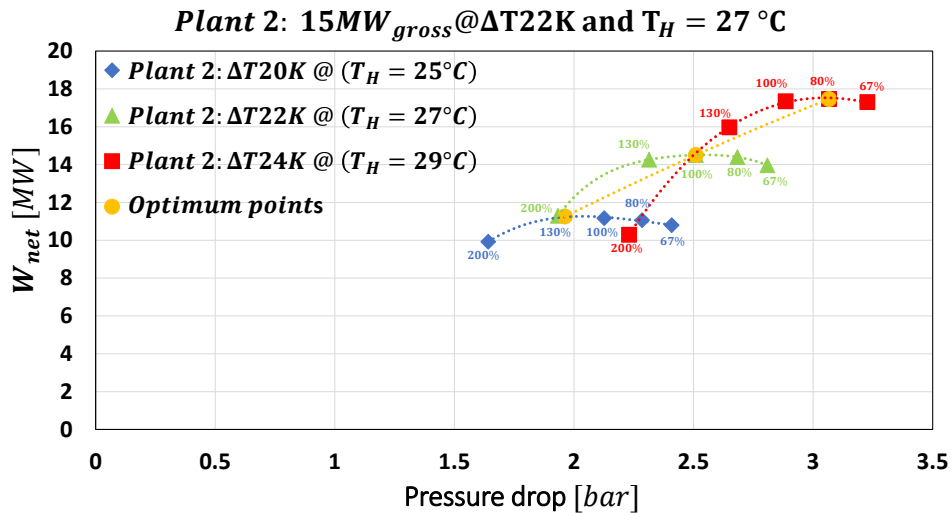


Figure 6.7: Optimization of plant 2 in specific environmental conditions. \blacklozenge shows the optimization with a warm seawater temperature of 25 °C, \blacktriangle of 27 °C, \blacksquare of 29 °C and \bullet shows the optimum operating points. The numbers at the points are the relative opening factor of the vanes, $\frac{1}{f_{VTG}}$.

The optimal operating points can be taken together and results in a specific power curve, see 6.8. It can be concluded that the power curve is proportional to the increase of the temperature difference, but the slopes of the different power plants are different.

The power curve depends on several aspects of the OTEC plant. The off-set in y-direction depends on the size of the plant, the slope depends on the freedom of the pressure drop in the system, which means there is the possibility of adjusting the position of the vanes. Finally, the curvature depends on the performance of the components in off-design. The curves seem to be almost linear, which means the non-linear effects of the components are not significant.

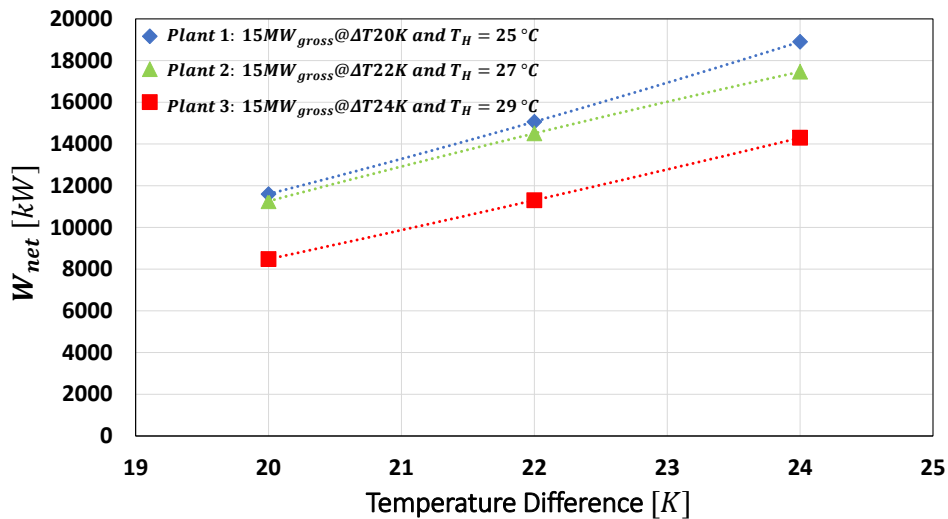


Figure 6.8: Net power curves: \blacklozenge plant 1, \blacktriangle plant 2 and \blacksquare plant 3.

The performance of the turbine, as already expected in section 3.7.4, is reasonably constant, see figure 6.9 where the efficiencies and pressure drops are shown of the optimal operating points. The non-linear behavior of the turbine is present, but can only be observed in detail level, see figure 6.9b. Figure 6.9c shows the proportionality of the pressure drop over the turbine in the plants. In plant 3, the adjustment of the position of the vanes is not favorable, which leads to the smallest slope.

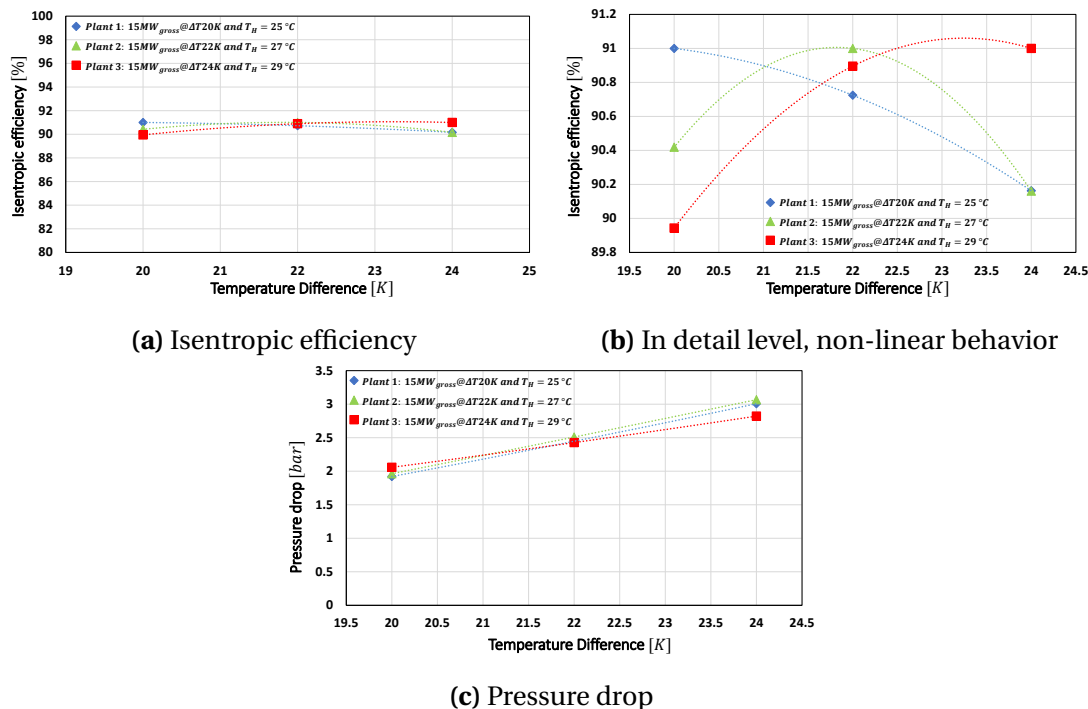


Figure 6.9: Optimal operating conditions of the turbine for the different power plants.

Optimization of the position of the vanes ensures that the vapor mass flow can be constant, but that the pressure ratio and pressure drop change significantly in off-design conditions. This results in that the specific speed with constant rotational speed varies and in plant 3, where no adjustability of the vanes is present, the specific speed remains almost constant, see figure 6.10. In section 3.6 is mentioned that the specific speed should always be opti-

mized duo to the increase of losses. As soon as it is favorable to vary the position of the vanes, it can be concluded that the turbine should be operate with a variable rotational speed, with the result that the torque remains stable, see figure 3.2 and equation 3.5.

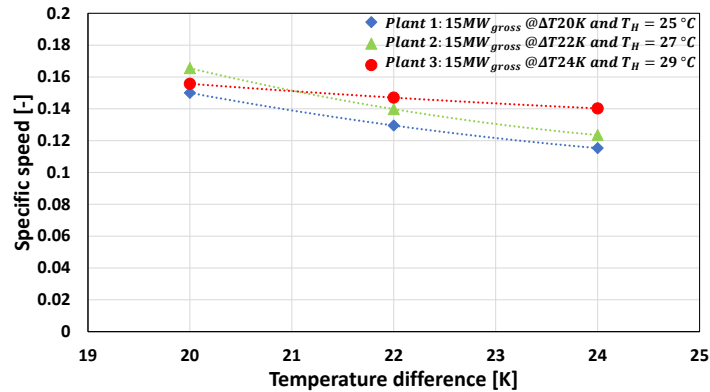


Figure 6.10: Specific speed of the optimal operating points

6.2.3. Results

Ultimately, the temperature curve of figure 6.4 and the specific power curve give a monthly average net power production, see figure 6.11.

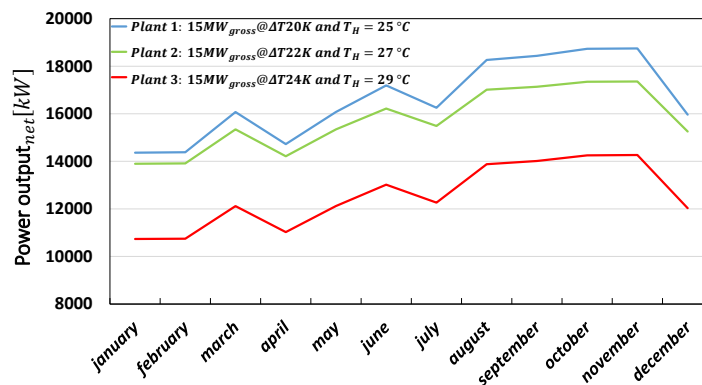


Figure 6.11: Monthly average net power output

With the monthly average power output, the total power production is obtained and the specific costs and the Levelized Cost of Energy (LCOE) can be derived, see section 4.7. In figure 6.12, the specific costs and the LCOE versus the temperature difference are shown for the different power plants.

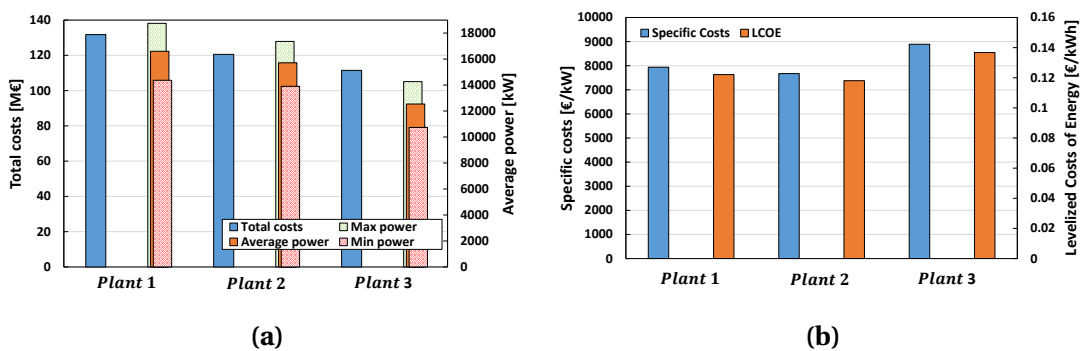


Figure 6.12: (a) Absolute costs and the average, maximum or minimum net power output of different plants (b) Specific costs and Levelized Cost of Electricity of different plants

6.2.4. Conclusion

The on-design results show that an increase in the design temperature of the warm seawater leads to different optimal plants and figure 6.6 even shows that this reduces the absolute costs. Subsequently in off-design conditions, figure 6.7 shows that there are optimal operating points and therefore the position of the vanes should be optimized in most cases. We can conclude that it is favorable to adjust the position of the vanes, especially when the power plant operates above design conditions. This is due to that it is harmful to have higher vapor flow through the turbine. Therefore, it might be that the degree of controllability of the pressure drop depends on whether has to operate below or above the design conditions. Ultimately, the power curves are derived for the plants and figure 6.8 shows that the power curves are proportional to the increase of the temperature difference, but that the slopes are different. The non-linear behavior of the turbine is too small to affect the non-linearity of the power curve. This leads to the conclusion, the seasonal fluctuation of seawater temperature difference have significant impact on the net power production, while the performance of the turbine is rather constant. Therefore, it is always favorable if the temperature is higher than the design temperature. However, the LCOE from figure 6.12b says more about the feasibility of the business case and we can conclude that it is most favorable to design on the average temperature of the location. Therefore, an analysis over overdimensioning of the OTEC plant is included in the LCOE calculation. Although the turbine seems to have little effect on the cycle performance, a turbine component in the off-design model is essential, because the turbine component influences the pressure drop in the cycle and therefore the right operating work point can be found.

6.3. Influence of the seawater mass flows variation

Nowadays, the business case of BlueRise of OTEC is mostly in co-operation with Seawater Air Conditioning (SWAC). The directly use of the cold sea water for SWAC is more beneficial, therefore it is likely that the water flow to the OTEC plant will be reduced in the future. For that reason, it is interesting to investigate the influence of a variation of the seawater flows. Table 6.5 shows the input for the case study with a variation of seawater mass flows.

Table 6.5: Overview of the input variables for the numerical model to analyze the off-design performance of the OTEC set-up.

\dot{m}_{sea}	25% or 50% or 75% or 100% or 120%
Power plant	On-design plant of $15MW_{gross}@\Delta T 22^{\circ}C$
\dot{m}_{wf}	Optimize [kg/s]
$T_{cold,in}$	5.0 [°C]
$T_{warm,in}$	27.0 [°C]
c_{NH_3}	100 [%]

6.3.1. Off-design optimization

The increase of seawater mass flows results in an increase of the power consumption of the seawater pumps. The seawater pumps are not included in the off-design model, therefore the power consumption change is derived with the on-design model in Cycle Tempo, see Chapter 4. The pipe diameter is kept constant, since the geometry of the power plant is

fixed. The power consumption of the working fluid pump is derived with the off-design model. Figure 6.13 shows the variation of power consumption of the pumps.

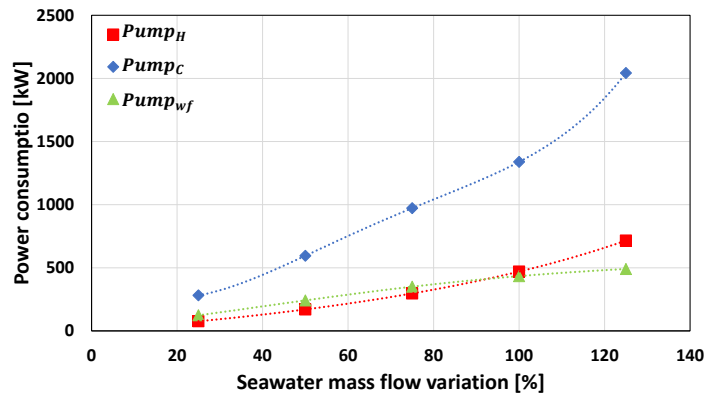


Figure 6.13: Power consumption variation. \blacklozenge $Pump_C$, \blacktriangle $Pump_{wf}$ and \blacksquare $Pump_H$.

The power consumption of the seawater pumps is non-linear, which is the result of the pressure drop due to pipe friction. This depends quadratically on the mass flow through the pipe. The same as with the research into variation of temperature differences, the off-design model should be optimized for the optimum pressure drop over the turbine. Figure 6.14 shows the optimization of the off-design model with variations of the seawater mass flows.

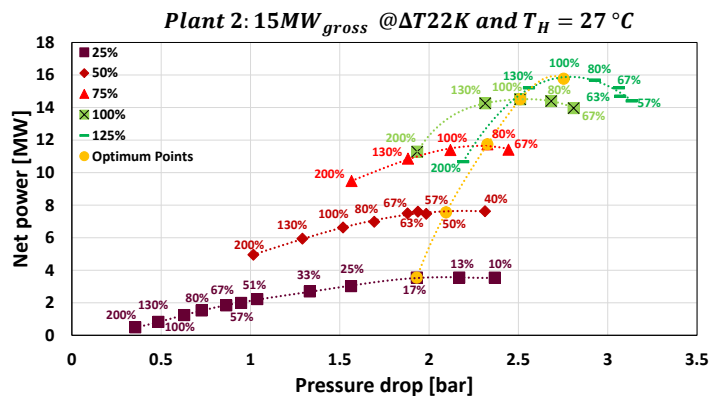


Figure 6.14: Optimization of plant 2 during variation of the seawater mass flow. The seawater mass flow is relative to the design mass flow. \blacksquare shows the optimization with a relative seawater mass flow of 25%, \blacklozenge of 50%, \blacktriangle of 75%, \blacksquare of 100%, \times of 125% and \bullet shows the optimum operating point. The numbers at the point are the relative opening factor of the vane, $\frac{1}{f_{VTG}}$.

6.3.2. Results

Figures 6.15 and 6.16 show the results of the optimum operating points of varying the seawater mass flow. Figure 6.15 shows the influence of the seawater mass flow variation on the turbine, where the vapor mass flow, the performance and the specific speed at constant rotational speed are shown. In Chapter 3, the trend of the correlation of Jüdes et al. is discussed and compared to the study of Hue [38]. The research into the influence of variations of the seawater mass flow shows that the trend of the turbine efficiency is like the trend of the study of Hue, see appendix B.2. Figure 6.16 shows the influence of the seawater mass flow variation on the cycle, where the net power output and the cycle efficiency are shown.

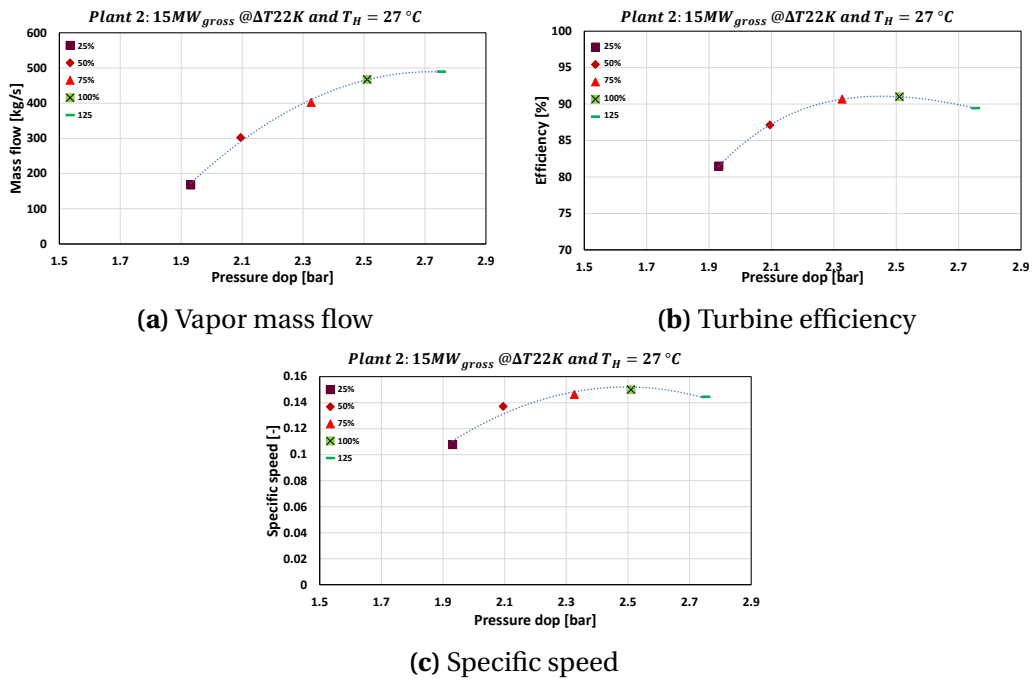


Figure 6.15: The influence of the mass flow variation on the turbine. The optimal operating point: ■ presents the relative seawater mass flow of 25%, ♦ of 50%, ▲ of 75%, ■ of 100% and — of 125%.

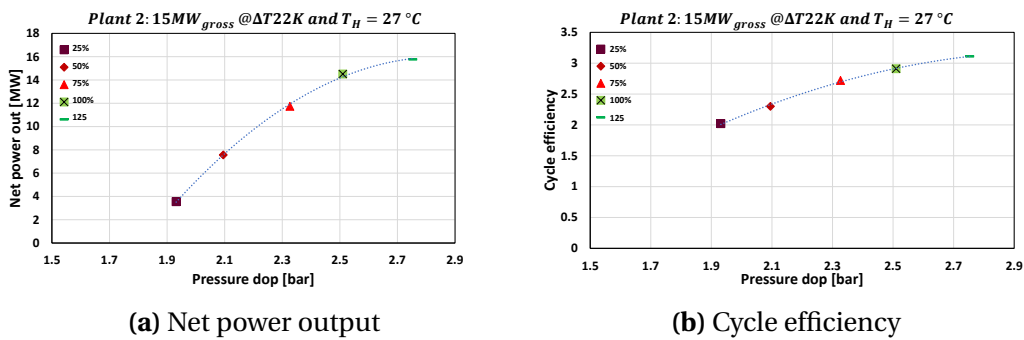


Figure 6.16: The influence of the mass flow variation on the cycle. The optimal operating point: ■ presents the relative seawater mass flow of 25%, ♦ of 50%, ▲ of 75%, ■ of 100% and — of 125%.

6.3.3. Conclusion

The optimization of the off-design model shows that a decrease of seawater mass flow results in a decrease of the pressure drop over the turbine, a decrease of the mass flow through the turbine and a drop in the performance of the turbine and that all these effects are non-linear. This results that the cycle have non-linear curves in the net power output and cycle efficiency. Therefore, it can be concluded that the turbine performance influences the cycle performance, especially as the seawater mass flow drops considerably. That is why, it is important to take into account the future of the seawater mass flows in the business case of the OTEC plant, since the performance of the cycle drops non-linear downwards as the mass flows decrease. Next to this, the specific speed is not constant, so once the seawater mass flow varies, the rotation speed should be adjusted.

7

Conclusion and Recommendations

7.1. Conclusions

This study investigates the off-design performance of an OTEC plant. Therefore, an off-design model is made and is validated with experiments on a small scale OTEC plant. The off-design conditions are symbolized by varying the warm seawater temperature and varying the seawater mass flows.

The heat transfer correlation for the condenser is re-investigated and the proposed correlation of Geschiere performs better than the correlation of Winkelmann, even with wetted area correction factor.

The pressure drop of the seawater mass flow in the heat exchangers can be predicted with the correlation of VDI, but a proper correlation of the working fluid side is still lacking in the literature.

The Stodola's method is selected as the best method to determine the pressure drop over the turbine, despite the fact that the method is used more in steam systems instead of ORC systems. The trend of the Stodola's method is similar to literature. The Stodola's method shows that a higher relative mass flow leads to a higher pressure ratio and pressure drop and the opposite applies to the relative inlet pressure. Both influences are non-linear and therefore the largest deviation of the pressure drop and pressure ratio is for a high relative mass flow and a small relative inlet pressure.

The range of OTEC is far away from the choking range, since the pressure ratio across a single turbine never exceeds 2.

The performance map of Astolfi and Macchi is valid to use as a tool to find the design turbine performance, since the influence of the heat capacity ratio can be neglected, the use of the ideal gas law is acceptable and the data is validated.

The performance map of the turbine in off-design is obtained using the correlation of Jüdes et al. The trend of the off-design efficiency of the turbine is similar to literature. We can conclude that it is more harmful to have high relative mass flows and the influence

of the relative inlet pressure is nihil for the performance of the turbine in the range of OTEC.

The on-design optimization shows that when the environmental conditions are varied, the optimum power plant is different. This leads to a specific power plant with specific mass flows.

Full model validation shows that the off-design model predicts the performance of the OTEC demo set-up with a small deviation and the Stodola's method predicts the pressure drop over the orifice well. The upscaled OTEC plant works at similar operating conditions, therefore the model seems to be accurate enough for the large scale application.

Varying the warm seawater temperature results in a proportional behavior in the power curve as expected. The non-linear effects of the off-design performance of the turbine are hardly visible, since the range of temperature difference is too small to have significant drops in the performance of the turbine. The three obtained power plant by means of a techno-economic optimization result in three different power curves. Hereby, the power curves of all plants are quite linear. Off-design optimization shows that it is favorable to adjust the position of the vanes, therefore there is a degree of controllability of the pressure drop. Which might be more favorable whether the plant has to operate above design conditions, due to it is more harmful for the turbine performance to have higher relative mass flows. This leads to the conclusion, the seasonal fluctuation of seawater temperature difference have significant impact on the net power production, while the performance of the turbine is rather constant and it is always favorable if the temperature is higher than the design temperature. However, the Levelized Costs of Energy shows that it is most favorable to design on the average temperature of the location.

Varying the seawater mass flows results in an other power curve, which shows non-linear characteristics. The turbine performance influences the cycle performance, especially if the seawater mass flows drop significantly. This results that the cycle efficiency drops non-linearly downwards as the mass flows decrease.

From now, it is possible to derive a power curve of the turbine for OTEC conditions, despite the uncertainties of the turbine performance quantification. The turbine performs reasonably constant in the range of OTEC, which leads that the power curves are quite linear. Therefore, the arrival of an OTEC plant is one step closer. This is an important step in creating a renewable energy powered world.

7.2. Limitations

The on- and off-design models use REFPROP thermodynamic library once pure ammonia is used. As soon as a mixture of ammonia with water as working fluid is used, the Rattner & Garimella library is used. At this time, Rattner & Garimella's properties are inaccurate in the range of higher ammonia concentrations. While, OTEC operates with higher concentrations of ammonia. Therefore, the results of this thesis focus on pure ammonia. However, mixtures are important in the investigation of the influence of the variation of the seawater temperature, since Kuikhoven mentions that ammonia-water has a more steady behaviour.

7.3. Recommendations for further investigations

The configuration of the demo set-up is a Kalina cycle, which can operate as an ordinary Rankine cycle, so the on-design and off-design model also use this configuration. In a lot of literature about a Rankine cycles, the configuration is different and a drum is placed after the evaporator. Whereby, the evaporator doesn't have to evaporate to full vapor, but a re-flux of working fluid is possible. Therefore, the evaporator is able to evaporate to a vapor quality around 70%, which is favorable for the heat transfer. It is recommended to investigate the influence of such re-design into the on-design and off-design models.

The correlations for the pressure drop in the condenser have been proposed by Dahlgren. Unfortunately, the pressure drop correlation for the working fluid side has not been sufficiently validated, whereby the off-design model is not able to calculate the working fluid pressure drop. The pressure drop of the seawater side is more important for the design phase of the heat exchanger. Still, it is recommended to investigate a pressure drop correlation for the working fluid side, so it could be implemented in the off-design model.

The performance maps of Astolfi and Macchi are used to derive the design performance of the turbine, but the applicability of these maps is uncertain. The data are widely used in the ORC literature, but these operates in other ranges. Therefore, it recommended to validate the data with turbine manufacturers. The same applies to the off-design performance of Jüdes et al. Because there is a lack of available literature about the OTEC range, it is recommended to produce an own power curve with CFD analysis.

The mass flow of the seawater is determined for a specific power plant in the on-design optimization. The optimization of the off-design model ignores the seawater mass flows, since it assumed to maximize the use of the seawater pipe. However, the optimal seawater mass flows will be different from the on-design setting as soon as the environmental conditions are changed. Therefore, it is recommended to take the seawater mass flows in the optimization of the off-design model.

The pump performance is modelled in the off-design model with the correlation of Goudriaan. As soon as the off-design model is upscaled, the correlation of Goudriaan is not valid anymore. Kleute mentions that the influence of the working fluid pump efficiency is negligible, therefore the off-design performance of the working fluid pump is neglected. Still, it is recommended to investigate the off-design performance of the working fluid pump.

The off-design model serves as tool to find the steady state operating point. The model is not able to serve as off-design tool for start-up or shut-down situations, since the model cannot handle a situation with no heat in- or out-put.

Some initial guesses are used in some components of the model. The estimates are set and are not yet overwritten with the found value of the best iteration. Once this is implemented, the computational time will be reduced.

The imposed sub-cooling is mostly used in literature studies of modelling an ORC. Such hypotheses make the off-design models not fully deterministic and can mislead the performance predictions. In the existing model, the influence of the charge, the total mass of working fluid, is not included and the sub-cooling to the working fluid pump is imposed. Therefore, the role of the buffer tank or liquid receiver is neglected. It is recommended to implement the buffer tank as part of the off-design model, the same as Dickes proposes and from then the cooperation of the working fluid pump and the buffer tank can be examined.

A

Piping & Instrumentation Diagram

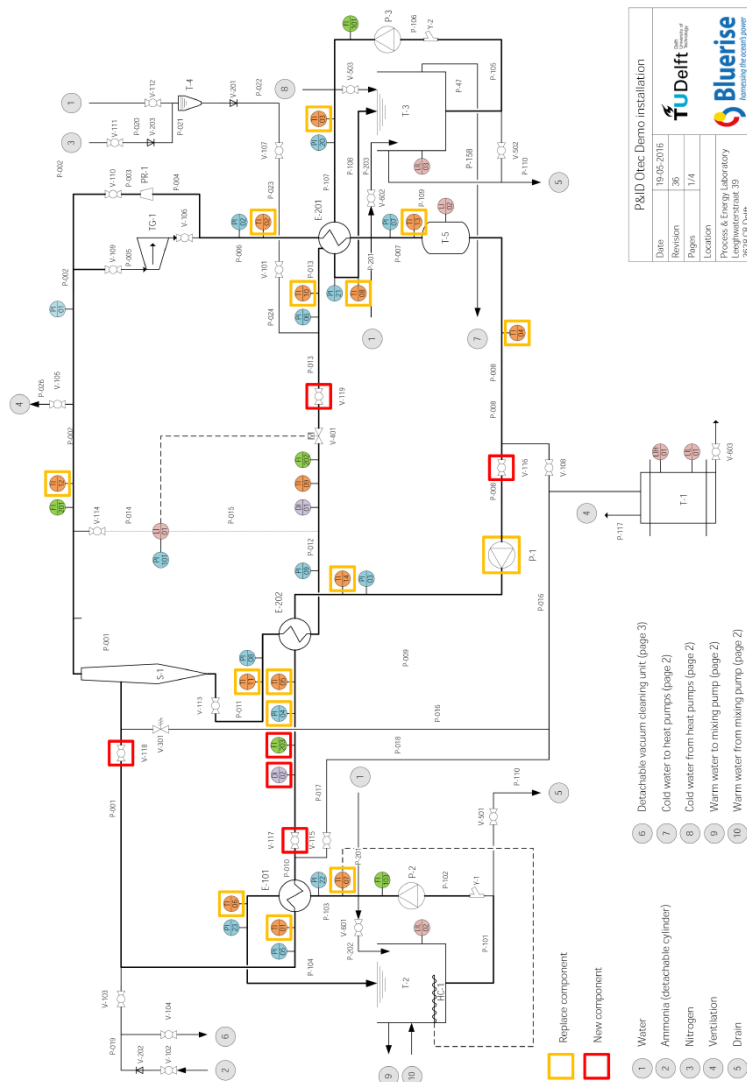


Figure A.1: Piping & Instrumentation Diagram (P&ID) of the OTEC demo set-up.
Copyright Bluerise B.V.

B

Correlations analysis

In the model, several correlations are selected, where the analysis is performed in other studies. Therefore, in this appendix the analysis is shown and explains the selected correlation. First, selection of the correlation for the heat transfer will be discussed and after that the correlation for the off-design performance of the turbine will be compared to other studies.

B.1. Heat exchanger correlations

In the research of Kuikhoven and Goudriaan are all possible correlation for the heat transfer investigate [52][33]. In this section are the results from their research discussed and shown which correlation performs the best and therefore is selected in the model of the OTEC cycle. In table B.1 are the conditions shown of the research of Kuikhoven and Goudriaan. In the next sections would for every heat exchanger shown which correlation performs the best and is selected with some explanation.

Table B.1: Conditions in the research of Goudriaan and Kuikhoven

Conditions		
m_{wf}	0.01	$[\frac{kg}{s}]$
m_{evap}	0.3	$[\frac{kg}{s}]$
$T_{evap,in}$	27	$[^{\circ}C]$
m_{cond}	0.225	$[\frac{kg}{s}]$
$T_{cond,in}$	5	$^{\circ}C$
$c_{ammonia}$	90 – 100	$[\%]$

For the single phase water side is a correlation fitted made in the research of Kuikhoven. With the equation B.1 the input amount of heat transfer could derive by experimental data by measure the inlet and outlet temperatures at a known mass flow, and by equation B.2 the performance of the heat exchanger can derived. From this experimental research a non linear correlation for the Nusselt number is derived. The result is the GoudKuik correlation. This correlation is shown in table 2.4. This correlation has a deviation of 5%.

$$Q_{exp} = \dot{m}_{water} * c_{p,water} * (T_{exp,in} - T_{exp,out}) \quad (B.1)$$

$$Q_{exp} = U_{exp} * A_{HEX} * \Delta T_{LMTD} \tag{B.2}$$

Now is discussed that all water flows are modelled by the correlation GoudKuik. The working fluid side is correlate in a different way, more with literature, which correlation performs the best is discussed separately per heat exchanger.

B.1.1. Recuperator

In the recuperator is the liquid flow from the separator used to preheat the flow after the pump. In both situation is the flow purely liquid, so one phase heat transfer at both sides. From figure B.1 can concluded that the Donowski & Kandlikar is the best performing correlation. This correlation is selected in the model in the situation there is single phase convective heat transfer coefficient on the working fluid side. The deviation is 1.83% for this correlation.

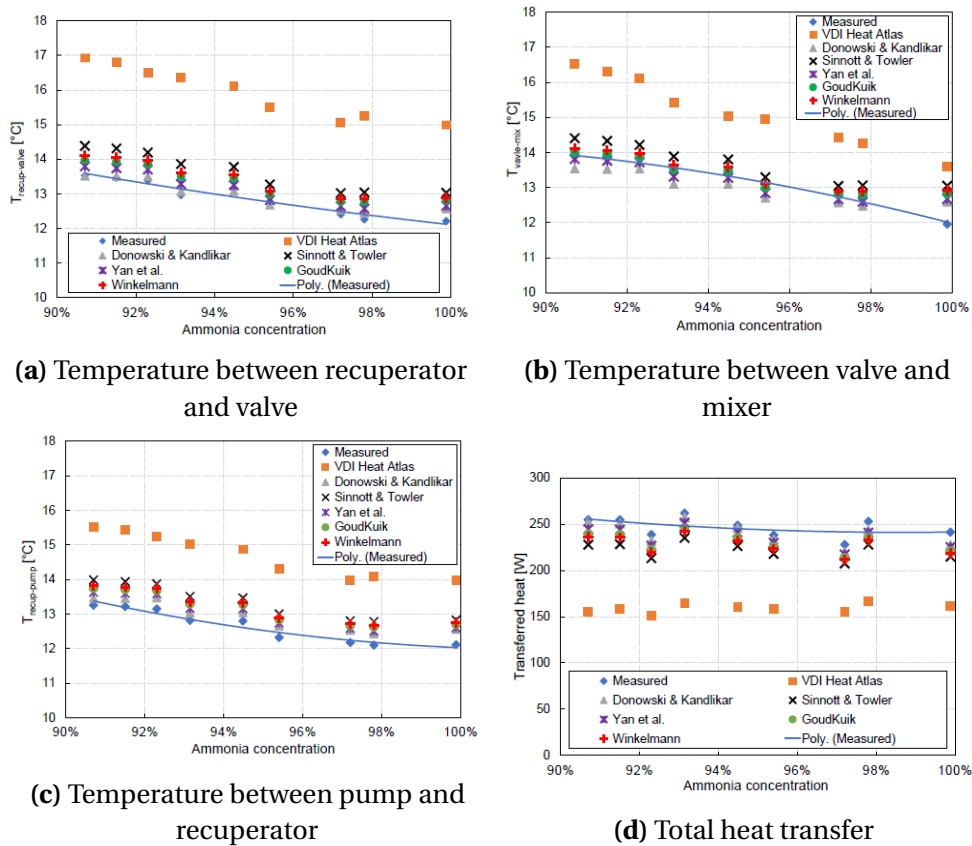


Figure B.1: Correlations results for the recuperator

B.1.2. Evaporator

Figure B.2 shows the results of the evaporator in the research of Goudriaan and Kuikhoven [52][33]. The correlation that shows the most realistic prediction could derive from this figures. The Ayub correlation for direct expansion is the best approximation of the experimental measurements. In the research is concluded that this correlation perform quite well. Ayub's correlation gave the breakdown in respect with the prediction of the vapor quality and this is crucial for the rest of the cycle and is therefore selected as correlation in

the evaporation. The deviation of this correlation is 1.98%, this value is also come from the research of Kuikhoven.

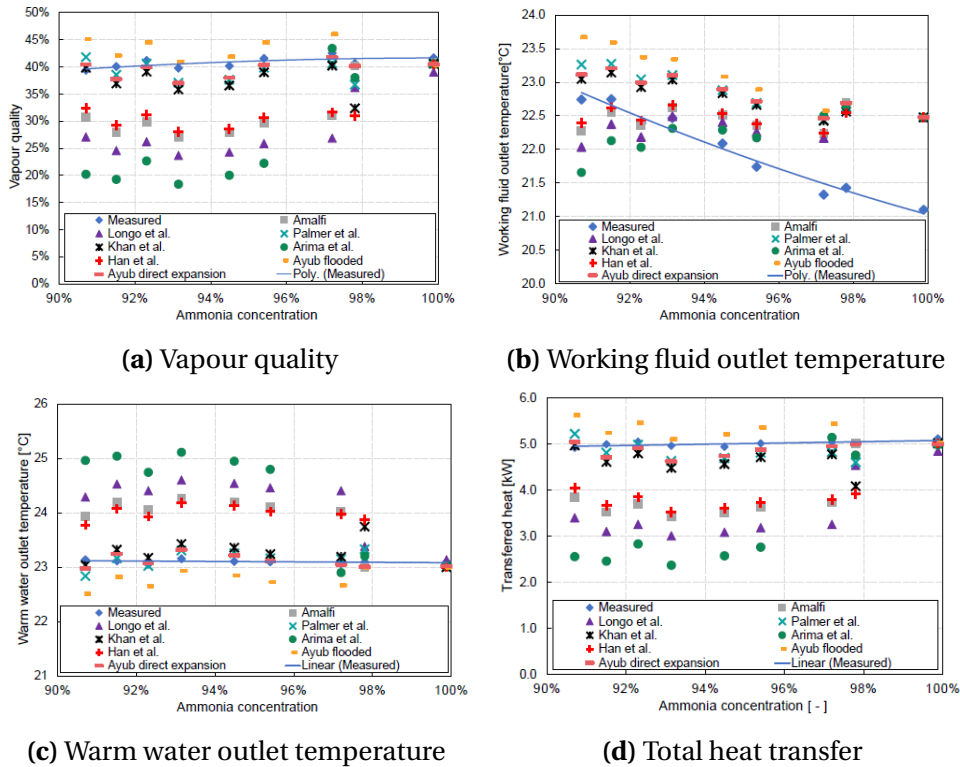


Figure B.2: Correlations results for the evaporator

B.1.3. Condenser

The results of the condenser are presented in figures B.3a, B.3b and B.3c. The correlations by Winkelmann, Longo et al, Yan et al and Thonon & Bontemps predict all the same output value. Only the Han et al predicts something else. The correlations lead to a completely sub-cooled liquid at the outlet of the condenser with a temperature equal to the cold water inlet temperature. So the area of the installed condenser is too large, because there is a lot of sub-cooling, see figure B.3d.

The experimental data however does not show that the working fluid temperature cools down until the cold water inlet temperature. This leads to the conclusion that not the area of the condenser is too large, but that the existing correlations over-predict the heat transfer of the two phase ammonia-water condensation. For this reason , a fitted correction factor is added to the Winkelmann correlation. This fitted correlation is taken over from Goudriaan [33]. Figure B.4 shows the results of this fitted correlation. This correlation is used is in the model as correlation for the two phase working fluid in the condenser. The deviation of this correlation is 1.20%.

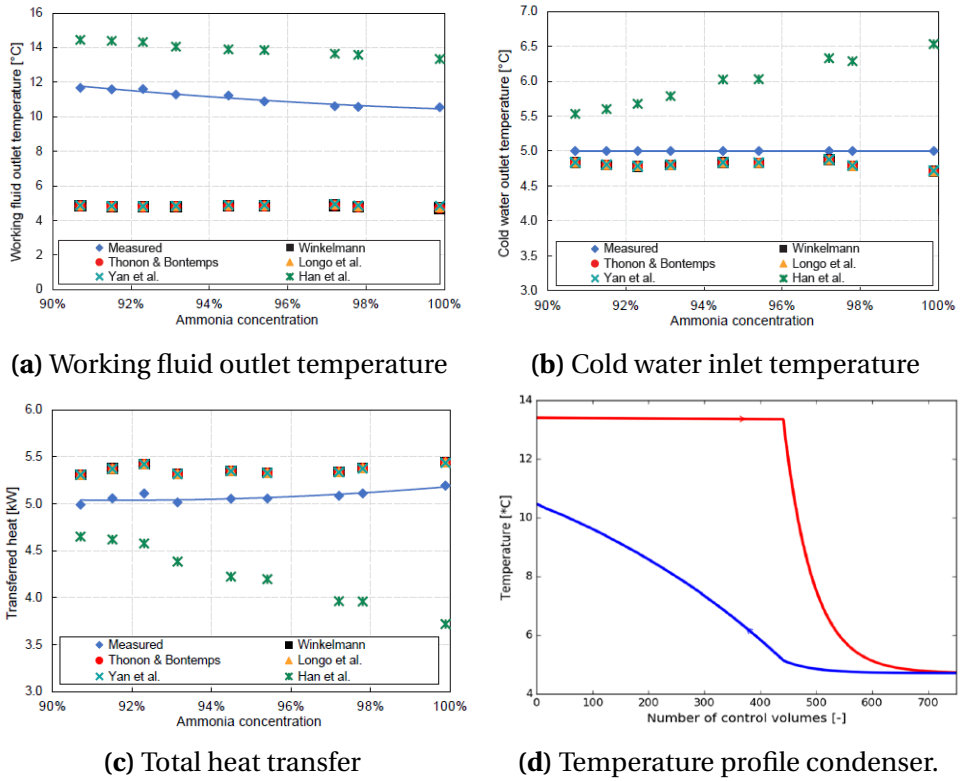


Figure B.3: Correlations results for the condenser. Note that in figure B.3d the correlation of Longo et al. is used.

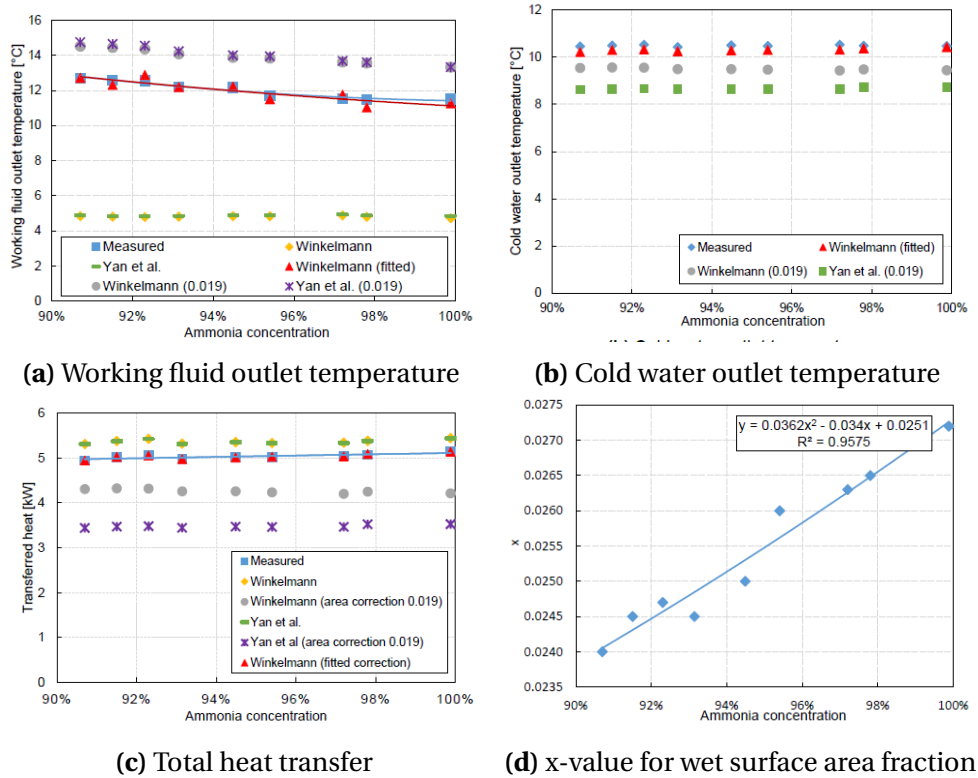


Figure B.4: Correlations results for the condenser

After the research of Goudriaan and Kuikhoven, Geschiere [31] investigates the condenser in more detail and made his own correlation to predict the heat transfer of the condenser. In figure B.5, the result of this correlation is shown.

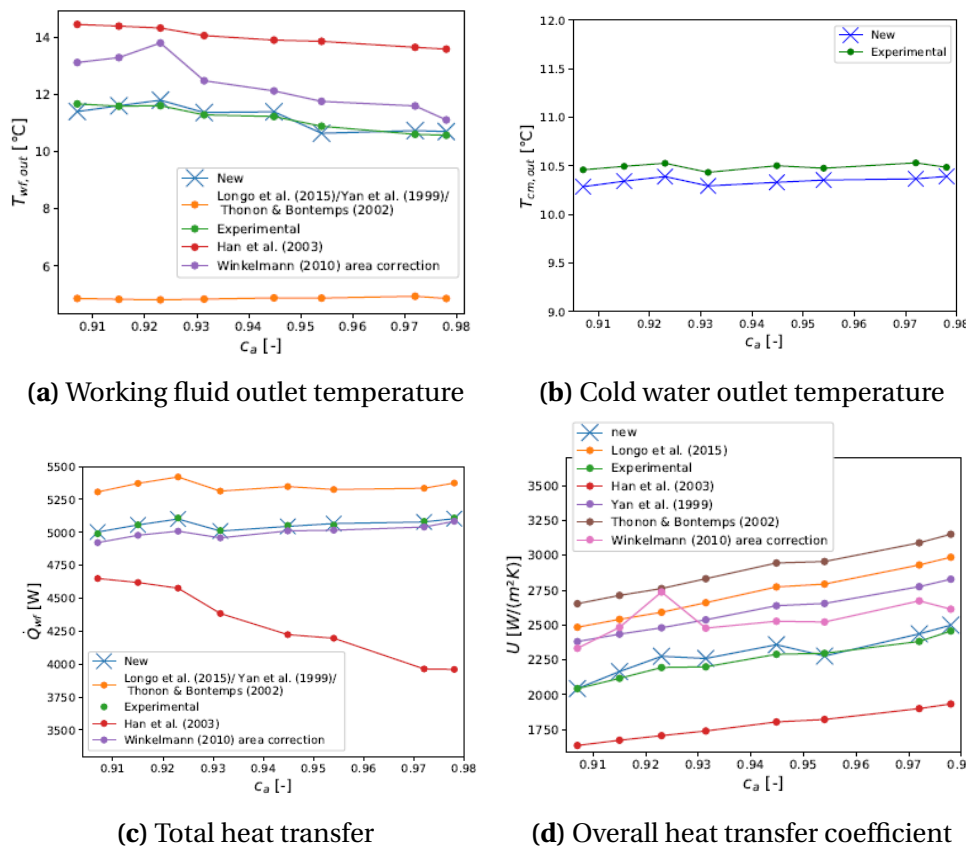
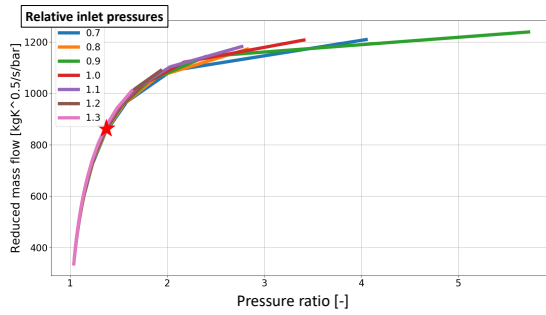


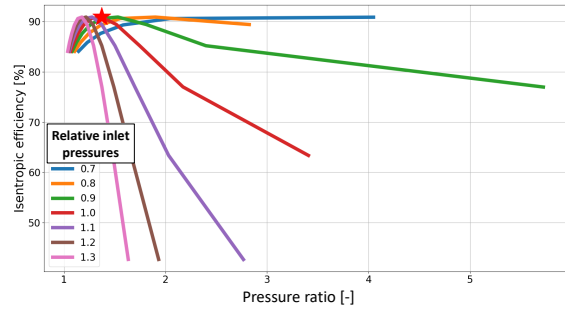
Figure B.5: Correlations results for the condenser, with new is the correlation of Geschiere [31].

B.2. Turbine trends comparison

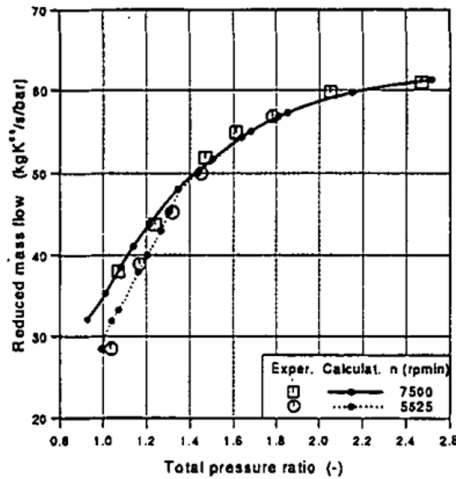
In the off-design calculations of the turbine, the Stodola method and the correlation of Jüdes et al. are used. To investigate the behavior of the behavior of the turbine, the trends will be compared to literature. In literature, the behavior of the turbine are mostly shown with the flow conditions and the pressure ratio. The flow conditions can be shown with the reduced mass flow or mass flow coefficient and it shows the behavior of the pressure ratio or pressure drop at specific inlet conditions. The trends can be compared to literature and therefore the studies of Petrovic [63] and Tsoutsanis [80] will be used, see figure B.6. In Tsoutsanis, the corrected mass flow rate is used, which is a polynomial function which is derived by map fitting. This parameter is similar than the reduced mass flow, so will be compared to that. Note that the conditions of OTEC are different, but the trend of the reduced mass flow seems similar to Petrovic and Tsoutsanis. The trend of the efficiency of Petrovic is like the trend of the relative inlet pressure of 0.7 and the other behaviors are similar to the behavior of the trends in the study of Tsoutsanis. Therefore, it can be concluded that the behavior of Jüdes et al. is quite similar to the literature.



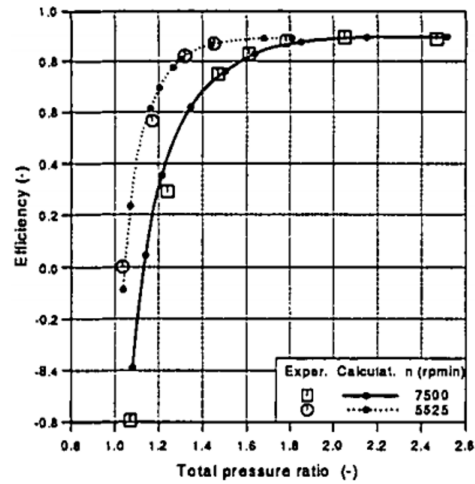
(a) The reduced mass flow



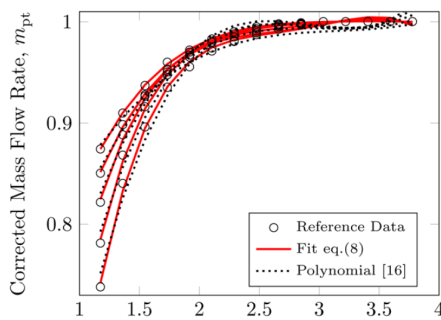
(b) The isentropic efficiency of the turbine



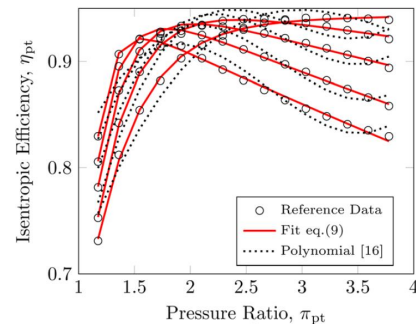
(c) The reduced mass flow



(d) The isentropic efficiency of the turbine



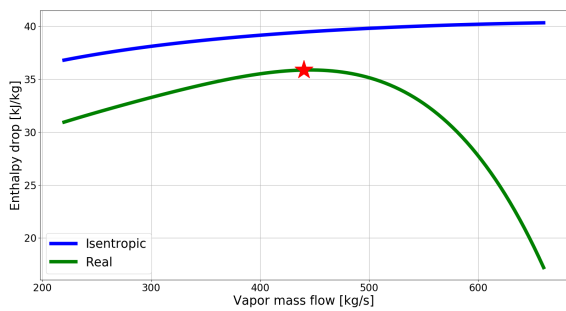
(e) The reduced mass flow



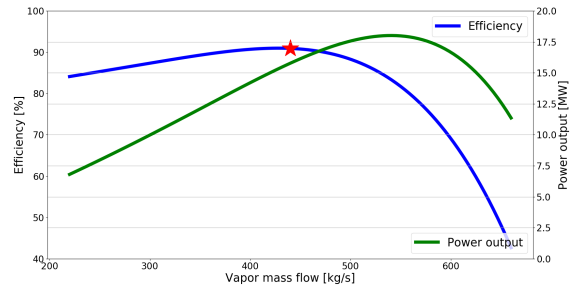
(f) The isentropic efficiency of the turbine

Figure B.6: Trends of the reduced mass flow and Isentropic efficiency [63][80]. The ★ represents the design point.

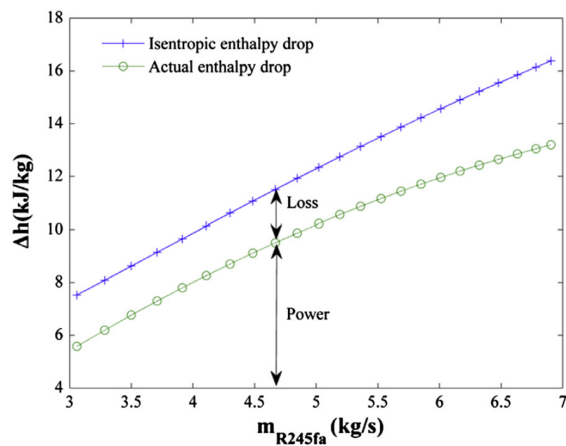
As soon as the inlet temperature of the turbine is fixed, the influence of the mass flow variation can be observed. Therefore, the study of Hue [38] is used, where the behavior of a turbine is investigated. Figure B.7 shows the comparison of the using the Stodola method and the correlation of Jüdes et al. to the research of Hue. The enthalpy drop is shown for the isentropic and real situation and the efficiency and power output of the turbine is presented. The trend shows that the loss part increases after the design point of the turbine, which is comparable to the literature and the deviation in turbine efficiency is shown as it operates in off-design.



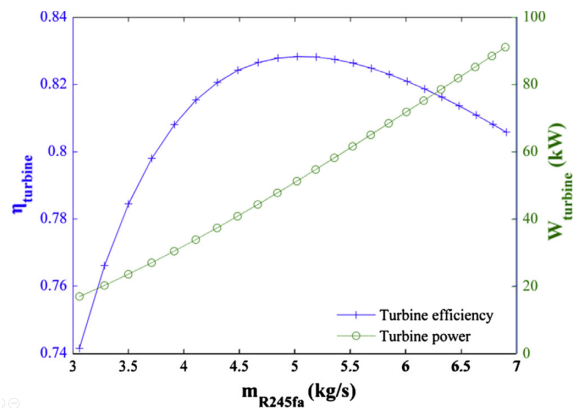
(a) Enthalpy drop



(b) The isentropic efficiency and power output of the turbine



(c) Enthalpy drop



(d) The isentropic efficiency and power output of the turbine

Figure B.7: Trends of the enthalpy drop and the efficiency and power output of the turbine [38]. The ★ represents the design point.

C

Transport properties of ammonia-water

In the model are the thermodynamic property database REFPROP and/or the method by Rattner implemented to obtain the thermodynamic properties of the ammonia-water mixture. Both methods do not include the transport properties of the ammonia-water mixture, so therefore the equations of Condé are implemented in the model. Condé developed equations to obtain the specific heat capacity, thermal conductivity, density, dynamic viscosity and the surface tension. The equations are used for the liquid phase and the vapour phase. The formulations by Condé for the vapour properties of ammonia-water assume ideal behaviour of the mixture in the vapour phase. In this appendix, the equations are given to determine the specific property.

C.1. Mixture critical temperature and pressure

The critical temperature and pressure can be determined with the following equations C.1 and C.2, where x is the concentration. The required parameters are given in table C.1.

$$T_{crit,mix} = \sum_{i=0}^4 a_i x^i \quad (C.1)$$

$$P_{crit,mix} = \sum_{i=0}^4 b_i x^i \quad (C.2)$$

Table C.1: Parameters to determine the critical temperature and pressure

i	a_i	b_i
0	647.14	220.64
1	-199.822371	-37.923795
2	109.035522	36.424739
3	-239.626217	-41.851597
4	88.689691	-63.805617

C.2. Liquid properties for ammonia-water

For all transport properties it is assumed that the mixture is in a vapour liquid equilibrium. this results in a saturation liquid solution and saturated vapour. So the properties are calculated with saturation temperature of the mixture. In this section are the different equations given to calculate the specific property of the saturated liquid solution.

C.2.1. Specific heat capacity

The following equations can be used to determine the liquid mixture specific heat capacity.

$$c_{p_{mix}}(T^*, x_{\text{NH}_3}) = x_{\text{NH}_3} c_{p_{\text{NH}_3}}(T_{\text{NH}_3}^*) + (1 - x_{\text{NH}_3}) c_{p_{\text{H}_2\text{O}}}(T_{\text{H}_2\text{O}}^*) \quad (\text{C.3})$$

Where the specific thermal capacities of the pure fluids are calculated by:

$$c_p(T^*) = A_{cp} + B_{cp}\tau^{-1} \quad (\text{C.4})$$

$$\tau = 1 - \theta = 1 - \frac{T^*}{T_{crit}} \quad (\text{C.5})$$

The parameters for the equation of the pure substances are:

Table C.2: Parameters for the pure substances

	A_{cp}	B_{cp}
NH ₃	3.875648	0.242125
H ₂ O	3.665785	0.236312

C.2.2. Thermal conductivity

The thermal conductivity saturated liquid ammonia can be calculated to according to the following equations:

$$\rho^* = \frac{\rho}{\rho_{crit, \text{NH}_3}} \quad (\text{C.6})$$

$$\lambda(\rho^*) = \sum_{i=0}^4 b_i \rho^{*, c_i} \quad (\text{C.7})$$

Table C.3: Parameters for the thermal conductivity equation

	$i = 0$	$i = 1$	$i = 2$	$i = 3$	$i = 4$
$b_i \rho \leq \rho_{crit}$	56.204417	-72.140043	133.084367	33.202225	15.190265
$b_i \rho \geq \rho_{crit}$	-278.262375	859.993184	-502.18171	86.142775	0.485818
c_i	0	1/3	2/3	5/3	16/3

In order to determine the thermal conductivity of the mixture the following correlation is used:

$$\lambda_{mix} = x_{\text{NH}_3} \lambda_{\text{NH}_3}(\rho_{\text{NH}_3}^*) + (1 - x_{\text{NH}_3}) \lambda_{\text{H}_2\text{O}}(T_{\text{H}_2\text{O}}^*) \quad (\text{C.8})$$

C.2.3. Dynamic viscosity of liquid mixtures

The following equations is proposed by Conde to approximate the dynamic viscosity of th mixture.

$$\ln(\eta_{mix}) = x_{\text{NH}_3} \ln(\eta_{\text{NH}_3, T_{\text{NH}_3}^*}) + (1 - x_{\text{NH}_3}) \ln(\eta_{\text{H}_2\text{O}, T_{\text{H}_2\text{O}}^*}) + \Delta\eta_{T_{mix}, x_{\text{NH}_3}} \quad (\text{C.9})$$

$$\Delta\eta_{T_{mix}, x_{\text{NH}_3}} = \left(0.534 - 0.815 \frac{T_{mix}}{T_{c, \text{H}_2\text{O}}}\right) F(x) \quad (\text{C.10})$$

$$F(x) = 6.38(1 - x_{\text{NH}_3})^{1.125x_{\text{NH}_3}} \left(1 - e^{-0.585 - x_{\text{NH}_3}(1 - x_{\text{NH}_3})^{0.18}}\right) \ln\left(\eta_{\text{NH}_3, T_{\text{NH}_3}^*}^{0.5} \eta_{\text{H}_2\text{O}, T_{\text{H}_2\text{O}}^*}^{0.5}\right) \quad (\text{C.11})$$

C.2.4. Surface tension for mixtures

The surface tension can be calculated by the following equation:

$$\sigma_{mix} = x_{\text{NH}_3} \ln(\sigma_{\text{NH}_3, T_{\text{NH}_3}^*}) + (1 - x_{\text{NH}_3}) \ln(\sigma_{\text{H}_2\text{O}, T_{\text{H}_2\text{O}}^*}) + \Delta\sigma_{T_{mix}, \text{NH}_3} \quad (\text{C.12})$$

$$\Delta\sigma_{T_{mix}, \text{NH}_3} = (\sigma_{\text{NH}_3, T_{\text{NH}_3}^*} + \sigma_{\text{H}_2\text{O}, T_{\text{H}_2\text{O}}^*}) F(x) \quad (\text{C.13})$$

$$F(x) = 1.442(1 - x_{\text{NH}_3}) \left(1 - e^{-2.5x_{\text{NH}_3}^4}\right) + 1.106x_{\text{NH}_3} \left(1 - e^{-2.5(1 - x_{\text{NH}_3})^6}\right) \quad (\text{C.14})$$

The surface tension of the pure substances is described by:

$$\sigma = \sigma_0(1 + b\tau)\tau^\mu \quad (\text{C.15})$$

With table C.4, the parameters for the equation can be found.

Table C.4: Parameters for the pure substances

	σ_0	μ	b
NH ₃	91.2	1.1028	0.0
H ₂ O	235.8	1.256	-0.625

C.2.5. Density for liquid mixture

The density of the liquid mixture can be calculated according to equation C.16

$$\rho_{mix} = x_{\text{NH}_3} \rho_{\text{NH}_3, T_{\text{NH}_3}^*} + (1 - x_{\text{NH}_3}) \rho_{\text{H}_2\text{O}, T_{\text{H}_2\text{O}}^*} + \Delta\rho_{T_{mix}, x_{\text{NH}_3}} \quad (\text{C.16})$$

Where the excess density can be described by:

$$\Delta\rho_{T_{mix}, x_{\text{NH}_3}} = \left(x_{\text{NH}_3}(1 - x_{\text{NH}_3}) - Ax_{\text{NH}_3}^2(1 - x_{\text{NH}_3})\right) \rho_{\text{NH}_3, T_{\text{NH}_3}^*}^{0.5} \rho_{\text{H}_2\text{O}, T_{\text{H}_2\text{O}}^*}^{0.5} \quad (\text{C.17})$$

$$T_{mix}^* = \frac{T_{mix}}{T_{crit, \text{H}_2\text{O}}} \quad (\text{C.18})$$

$$A = \sum_{i=0}^2 A_{1,i} T_{mix}^{*,i} + \frac{\sum_{i=0}^2 A_{2,i} T_{mix}^{*,i}}{x_{\text{NH}_3}} \quad (\text{C.19})$$

Table C.5: Parameters to determine parameter A

	$i = 0$	$i = 1$	$i = 2$
A_1	-2.410	8.310	-6.924
A_2	2.118	-4.050	4.443

The densities for the pure liquids fluids can be determined using equation C.20 with the parameters given in table C.6.

$$\frac{\rho_{liq}}{\rho_{crit}} = \sum_{i=0}^6 A_i \tau^{b_i} \quad (C.20)$$

Table C.6: Parameters to calculate the pure liquids densities

i	H2O		NH3	
	A	b	A	b
0	1.0	0	1.0	0
1	1.9937718430	1/3	2.02491283	1/3
2	1.0985211604	2/3	0.84049667	2/3
3	-0.5094492996	5/3	0.30155852	5/3
4	-1.7619124270	16/3	-0.20926619	16/3
5	-44.9005480267	43/3	-74.60250177	43/3
6	-723692.2618632	110/3	4089.79277506	70/3

C.3. Vapor properties for ammonia-water

The assumption can be made that the vapor properties only need to be determined for $y_{\text{NH}_3} = 1$ as the pressures and temperature are so low that the chance of water evaporating is negligible.

C.3.1. Specific heat capacity

The specific thermal capacity of the saturated mixture in the vapor phase can be calculated according to equation C.21 under the assumption of an ideal mixture of gases.

$$c_{p_{mix}} = y_{\text{NH}_3} c_{p_{\text{NH}_3}}(T_{\text{NH}_3}^*) + (1 - y_{\text{NH}_3}) c_{p_{\text{H}_2\text{O}}}(T_{\text{H}_2\text{O}}^*) \quad (C.21)$$

For each of the two components the specific heat capacity can be calculated according to equation C.22.

$$c_p(\tau) = A + B\tau^{-1/3} + C\tau^{-2/3} + D\tau^{-5/3} + E\tau - 15/6 \quad (C.22)$$

Where τ is determined from the mixture vapor temperature

$$\tau = 1 - \theta = 1 - \frac{T_{mix}}{T_{crit,mix}} \quad (C.23)$$

The parameters for the equation of the pure substances are:

Table C.7: Parameters for the pure substances

	<i>A</i>	<i>B</i>	<i>C</i>	<i>D</i>	<i>E</i>
NH ₃	-1.199197086	1.240129495	0.924818752	0.018199633	-0.245034E-3
H ₂ O	3.461825651	-4.987788063	2.99431770	6.259308E-3	-8.262961E-6

C.3.2. Thermal conductivity

The thermal conductivity of the mixture in the vapor phase can be calculated according:

$$\lambda_{mix} = \frac{y_{NH_3} \lambda_{NH_3}}{y_{NH_3} + (1 - y_{NH_3}) \phi_{12}} + \frac{(1 - y_{NH_3}) \lambda_{H_2O}}{(1 - y_{NH_3}) + y_{NH_3} \phi_{12}} \quad (C.24)$$

$$\phi_{12} = \frac{\left(1 + \left(\frac{\lambda_{NH_3}}{\lambda_{H_2O}}\right)^{0.5} \left(\frac{M_{H_2O}}{M_{NH_3}}\right)^{0.25}\right)^2}{\left(8\left(1 + \frac{M_{NH_3}}{M_{H_2O}}\right)\right)^{0.5}} \quad (C.25)$$

$$\phi_{21} = \phi_{12} \frac{\lambda_{H_2O} M_{NH_3}}{\lambda_{NH_3} M_{H_2O}} \quad (C.26)$$

The vapor will be pure ammonia vapor, so the equation for the thermal conductivity of pure ammonia is required and can be described by:

$$\lambda_{NH_3} = \sum_{i=0}^3 A_i \left(\ln\left(\frac{1}{\tau}\right)\right)^i \quad (C.27)$$

Table C.8: Parameters to calculate the conductivity of pure ammonia

	<i>A</i> ₀	<i>A</i> ₁	<i>A</i> ₂	<i>A</i> ₃	<i>M</i>
NH ₃	-0.48173	20.04383	0.0	0.0	17.03

C.3.3. Dynamic viscosity

The dynamic viscosity of the mixture in the vapor phase can be calculated according:

$$\eta_{mix} = \frac{y_{NH_3} \eta_{NH_3}}{y_{NH_3} + (1 - y_{NH_3}) \phi_{12}} + \frac{(1 - y_{NH_3}) \eta_{H_2O}}{(1 - y_{NH_3}) + y_{NH_3} \phi_{12}} \quad (C.28)$$

$$\phi_{12} = \frac{\left(1 + \left(\frac{\eta_{NH_3}}{\eta_{H_2O}}\right)^{0.5} \left(\frac{M_{H_2O}}{M_{NH_3}}\right)^{0.25}\right)^2}{\left(8\left(1 + \frac{M_{NH_3}}{M_{H_2O}}\right)\right)^{0.5}} \quad (C.29)$$

$$\phi_{21} = \phi_{12} \frac{\eta_{H_2O} M_{NH_3}}{\eta_{NH_3} M_{H_2O}} \quad (C.30)$$

C.3.4. Density

The density of the saturated vapour of pure ammonia can be calculated with equation C.31 and the required parameters from table C.9.

$$\rho_{mix} = y_{\text{NH}_3} \rho_{\text{NH}_3, T_{\text{NH}_3}^*} + (1 - y_{\text{NH}_3}) \rho_{\text{H}_2\text{O}, T_{\text{H}_2\text{O}}^*} + \Delta \rho_{T_{mix}, y_{\text{NH}_3}} \quad (\text{C.31})$$

The densities of the saturated vapor of pure ammonia can be calculated using:

$$\ln\left(\frac{\rho_{vap}}{\rho_{crit}}\right) = \sum_{i=1}^6 A_i \tau^{b_i} \quad (\text{C.32})$$

Table C.9: Parameters to calculate the pure vapor densities

i	H2O		NH3	
	A	b	A	b
1	-2.025450113	1/3	-1.143097426	1/3
2	-2.701341216	2/3	-3.31273638	2/3
3	-5.359161836	4/3	-4.44425769	4/3
4	-17.343964539	3	-16.84466419	3
5	-44.618326953	37/6	-37.79713547	37/6
6	-64.869052901	71/6	-97.82853834	71/6

D

Optimal operating conditions

In this appendix, the operating condition settings of the OTEC on-design model will be substantiated. These settings can be optimum values or usual values, which are common in the literature. The analyze of these settings can be done with validated off-design model by changing some input conditions. Herewith, the optimum point can be found or the literature can be confirmed. In order to fairly asses the performance of all conditions and to design a base case for a specific condition, the optimum performance curves need be analyzed.

The evaporator outlet vapour quality will be investigated. The analysis is carried out for select concentration, namely pure ammonia. In the comparison of outlet vapour qualities, the warm water and cold water mass flows are kept constant. The turbine performance is assumed to be constant, with an isentropic efficiency of 85 %, because the design conditions of the turbine should not affect these results. In table D.1, the test inputs are given and in the following section the result will be discussed.

Table D.1: Model inputs to find the optimum evaporator vapour quality outlet

x_{NH_3}	T_{warm}	P_{warm}	\dot{m}_{warm}	T_{cold}	P_{cold}	\dot{m}_{cold}	\dot{m}_{wf}	$\eta_{\text{is,t}}$
[%]	[°C]	[bar]	[kg/s]	[°C]	[kg/s]	[kg/s]	[bar]	[%]
100	27	1.1	28260.9	5	1.1	21195.7	254.5-1431.4	85

D.1. Evaporator outlet vapour quality

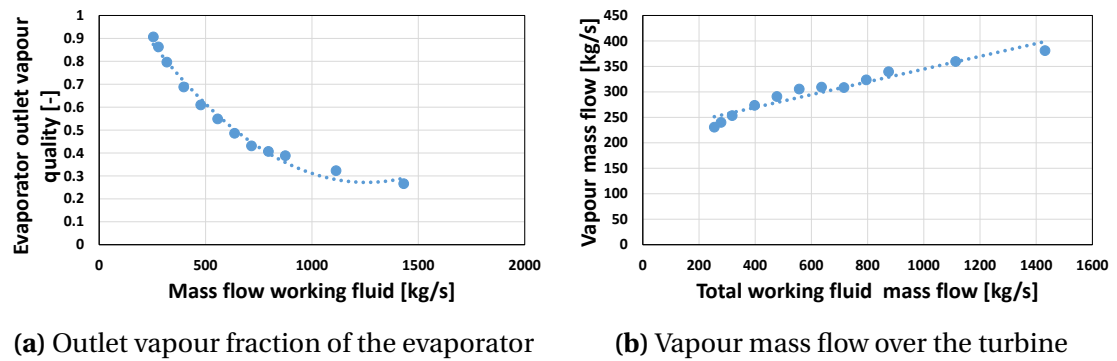
The influence of the vapour quality of the evaporator outlet is investigated by changing the specific working fluid mass flow. So that the mass flow of the working fluid is varied, with fixed cold and hot seawater mass flows and temperatures. The off-design model determines the operation conditions of all cases. This results of the vary of the working fluid mass flow are shown in table D.2.

A decrease of the working fluid mass flow results in a higher vapour fraction of the working fluid, see figure D.1a. The trend of the vapour quality is not quite linear, since the heat input which is extracted from the hot seawater is not totally equal in all off-design conditions. As a result, the outlet temperature of the hot seawater is not the same in all cases. Ultimately, the working fluid mass flow with the obtained vapour quality result in a specific vapour

Table D.2: Model outputs for the optimum performance by vary the working fluid mass flow

x_{NH_3}	\dot{m}_{wf}	\dot{Q}_{evap}	$q_{evap,out}$	\dot{Q}_{cond}	U_{evap}	U_{cond}	\dot{W}_{pump}	\dot{W}_t	η_{th}
[%]	$[\frac{kg}{s}]$	[MW]	[-]	[MW]	$[\frac{W}{m^2K}]$	$[\frac{W}{m^2K}]$	[MW]	[MW]	[%]
100	254.46	280	0.91	-274	962.82	1213.23	0.40	-6.63	2.06
100	278.32	292	0.86	-285	1022.17	1293.02	0.43	-6.91	2.06
100	318.08	309	0.80	-303	1078.48	1520.56	0.99	-7.30	1.89
100	397.60	335	0.69	-328	1194.28	1878.75	1.25	-7.90	1.84
100	477.12	358	0.61	-351	1300.06	2267.79	1.52	-8.43	1.80
100	556.64	376	0.55	-369	1422.83	2546.72	1.77	-8.87	1.76
100	636.16	384	0.49	-377	1427.78	3498.09	2.09	-8.96	1.67
100	715.68	385	0.43	-379	1467.35	4791.47	2.39	-8.90	1.57
100	795.20	403	0.41	-397	1584.09	4857.82	2.65	-9.38	1.55
100	874.72	422	0.39	-415	1717.40	4609.03	2.88	-9.91	1.55
100	1113.28	448	0.32	-441	1952.02	5677.05	3.68	-1.05	1.43
100	1431.36	475	0.27	-468	2224.29	6682.53	4.73	-1.12	1.27

mass flow over the turbine, which is important for the power output of the turbine. The vapour mass flow is not equal in all cases, see figure D.1b.



(a) Outlet vapour fraction of the evaporator (b) Vapour mass flow over the turbine

Figure D.1: Results of varying the mass flow of working fluid.

The conditions which should have no influence on the result of this research are assumed to be constant. The isentropic efficiency of the turbine is assumed to be 85 %. Because of this, the performance of the turbine has no influence. Hereby, the enthalpy drop over the turbine is almost unchanged, see figure D.2. Therefore, the power output of the turbine varies mainly due to the vapour mass flow over the turbine.

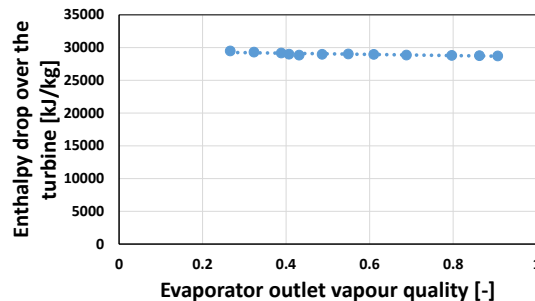


Figure D.2: Enthalpy drop over the turbine

A vary of the working fluid mass flow results in different heat transfer conditions. Whereby, the overall heat transfer coefficient is different in all cases, see figure D.3a. Note that, in

the low vapor fraction range, the overall heat transfer coefficient is higher than usual. Extrapolation of the correlation can be a reason for this, since the Reynolds number is higher than the validated Reynolds number. These values will be out of consideration, since these play not an important role in the result. The result of another heat transfer can be noticed in the outlet temperatures of the sea water flows. Therefore, the log mean temperature difference and the effectiveness of the heat exchangers are different, see figures D.3b and D.3c. The effectiveness of the heat exchangers has an opposite effect for the evaporator or the condenser. This is due to that the maximum temperature difference for the evaporator increases and for the condenser decreases if the evaporator outlet vapour quality increases.

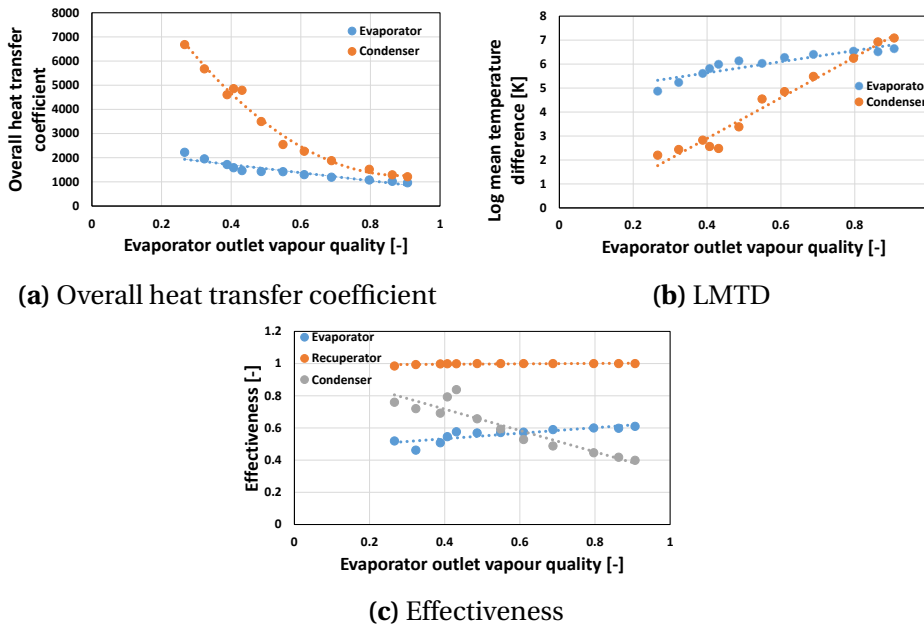


Figure D.3: Results of varying the mass flow of working fluid.

Ultimately the thermal efficiency of the power cycle can be compared. Figure D.4a shows the obtained thermal efficiency per evaporator outlet vapour fraction. The trend shows that the efficiency increases if the vapour fraction of the evaporator outlet is higher. Therefore, the conclusion can be made that the vapour fraction should be high as possible. The extracted heat from the hot source is less if the vapour quality is higher, see figure D.4b. This is due the decrease of the overall heat transfer coefficient, despite an increase of the log mean temperature difference.

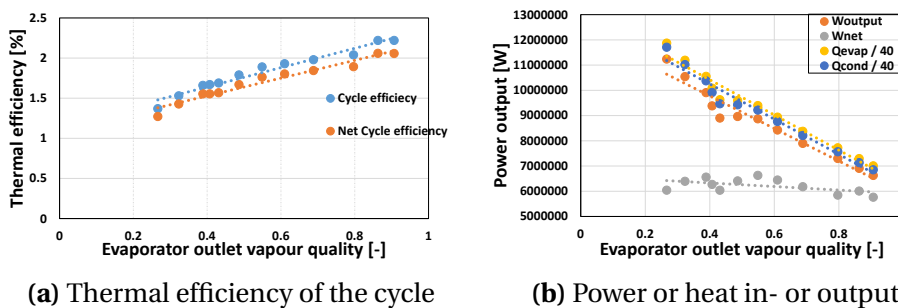
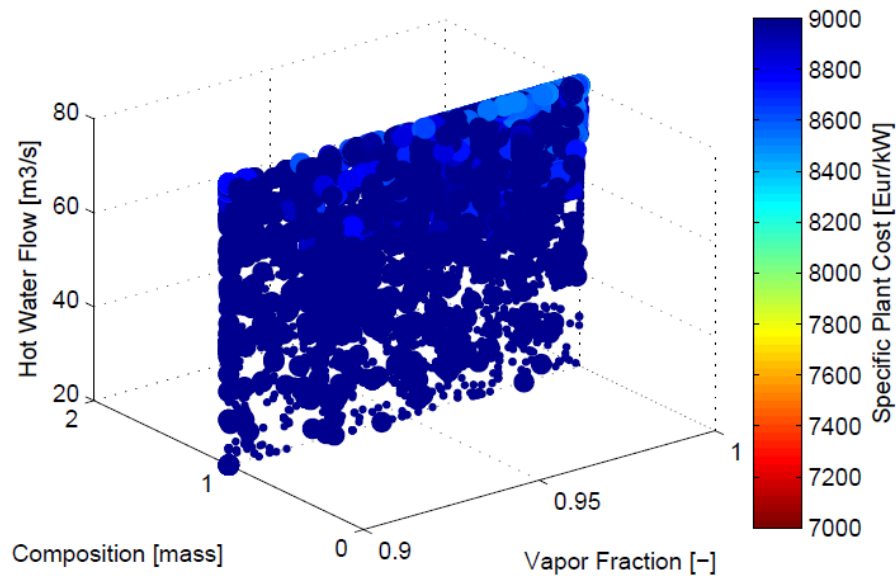


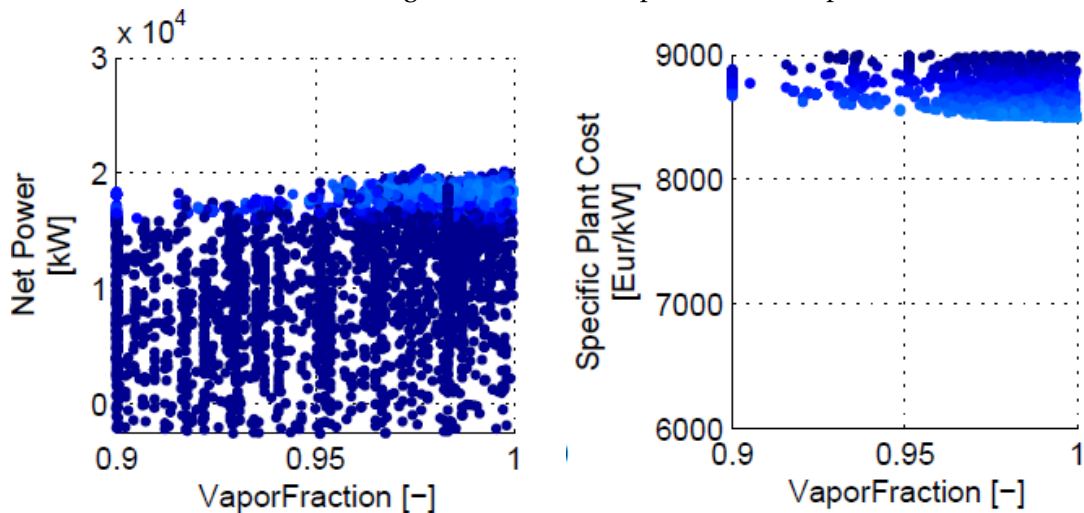
Figure D.4: Results of varying the mass flow of working fluid. Note that the net cycle efficiency is with the work of the sea pumps and the heat input and output in the evaporator and condenser is divided by 40.

The conclusion can be made that an increase of the vapor fraction leads to a higher thermal efficiency. This corresponds to the normal Rankine cycles. Normally, in Rankine cycles super-heating is required at the outlet of the evaporator. Because of this, the outlet of the turbine is dry enough, see section 2.3. In the range of OTEC, the pressure drop over the turbine is small, therefore super-heating is not necessary. The outlet vapor quality of the turbine is never close to the critical value, so super-heating does not have to be taken into account. Figures D.5a, D.5b and D.5c, show the result of the optimum vapor fraction in the thesis of Kirkenier [48], it confirms to evaporate to fully vapor.



(a) 3D scatter plot of optimization run of pure ammonia cycle.

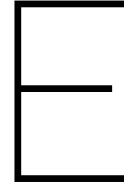
Hot water flow, working fluid mixture composition and vapor fraction.



(b) Net power production

(c) Specific plant cost

Figure D.5: Optimization of the vapor fraction for a pure ammonia cycle. The colors indicate the specific costs [48].



Additional model information

In this appendix, the additional model information is discussed. The on-design model, which is introduced in Chapter 4 and the off-design model from Chapter 5 require some extra explanation of some settings or the method of using the model. First, the extra information of the on-design model is discussed and next the settings and extra requirements for the off-design model will be discussed.

E.1. On-design model

In this section, the components of the on-design model will be discussed. Chapter 4 introduces the on-design model, but some additional information of the on-design model will be explained in more detail. The following items will be discussed, the pressure drops, the cost correlations and the results of the on-design model.

E.1.1. Pressure drop calculations for the sea water pipes

Chapter 4 discusses the pressure drop of the seawater pipe, but not the correlations of the different pressure drops. Since these were taken over from the thesis of Kirkenier [48]. The following equation was given in section 4.3:

$$\Delta P = \Delta P_{fric} + \Delta P_{hy} + \Delta P_{in} \quad (E.1)$$

The pressure drop due to pipe friction, ΔP_{fric} , is calculated with equation E.2. Whereby, the friction number, f , is used, which is derived using the Haaland approximation of the Colebrook-White, see equation E.3.

$$\Delta P_{fric} = f * \rho * L/D * 0.5 * \dot{m}^2 * 10^{-5} \quad (E.2)$$

$$f = (-1/1.8 * \log[(\epsilon_r/3.7)^{1.111} + 6.9/Re])^2 \quad (E.3)$$

In the formula of Colebrook-White, a roughness of the pipes is necessary. A roughness value ϵ of 0.002 m is assumed. This value is acceptable, since all pipes are from Polyethylene.

The hydrostatic pressure drop is given by:

$$\Delta P_{hy} = \Delta \rho_{av} * g * h, \quad (E.4)$$

where ρ_{av} is derived with equation E.5, g is the gravitational acceleration and h is the depth of the deep sea pipe inlet or outlet.

$$\rho_{av} = \rho_{depth} - (\rho_{surface} + (\rho_{depth} + \rho_{surface})/2) \quad (E.5)$$

The pressure drop due to the inlet/outlet resistance is given by:

$$\Delta P_{in} = K * (\dot{m}^2 / 2g), \quad (E.6)$$

where the K factor for all pipes will be set to 0.2, which is a common value for inlets of pipes.

E.1.2. Cost correlations

A number of different components and parts of the offshore power plant are outside of the scope of this thesis. The components with variable costs are the evaporator, condenser, turbine, generator and seawater pipes. The cost of the recuperator and separator, only applies to the ammonia-water cycle, will be neglected since it is relatively small compared to the costs of the evaporator and condenser. The base cost of the system is taken over from the research of Kleute [49], these costs include the transportation, installation and commissioning costs of the entire system. In table E.1, the cost correlation of the different components and the plant base cost are given. The cost calculation are done with equation E.7.

$$C_{component} = C_0 * \left(\frac{P_{ar}}{P_{ar0}} \right)^{PF}, \quad (E.7)$$

where C_0 is the reference cost, P_{ar} is the relevant parameter, P_{ar0} is the value of the relevant parameter corresponding to the reference cost and PF is the power factor. The relevant parameter can vary in which unit it is used.

Table E.1: Cost correlation factors [49]

Component	Property	Symbol	Value	Unit
Evaporator	Reference cost	C_0	20,150,000.00	€
	Reference area	P_{ar0}	97300	m^2
	Power factor	PF	0.9	-
Condenser	Reference cost	C_0	17,750,000.00	€
	Reference area	P_{ar0}	85700	m^2
	Power factor	PF	0.9	-
Turbine	Reference cost	C_0	1,230,000.00	€
	Stages	n	1	-
	Reference Parameter	SP_0	0.18	m
	Power factor	PF	1.1	-
Generator	Reference cost	C_0	200,000.00	€
	Reference power	P_{e0}	5000	kW
	Power factor	PF	0.67	-
Cold water pump	Reference cost	C_0	212,000.00	€
	Reference power	P_{e0}	700	kW

Continued on next page

– continued from previous page

	Power factor	PF	1.0	-
Warm water pump	Reference cost	C_0	150,000.00	€
	Reference power	P_{e0}	700	kW
	Power factor	PF	1.0	-
Working fluid pump	Reference cost	C_0	23,700.00	€
	Reference power	P_{e0}	110	kW
	Power factor	PF	0.67	-
Cold water pipe	HDPE specific cost	C_{HDPE}	2,996.00	€
	Installation costs	$C_{cw,pipe}$	5,000,000.00	€
Warm water pipe	HDPE specific cost	C_{HDPE}	2,996.00	€
	Installation costs	$C_{ww,pipe}$	1,000,000.00	€
Return water pipe	HDPE specific cost	C_{HDPE}	2,996.00	€
	Installation costs	$C_{rw,pipe}$	3,000,000.00	€
Other	Base costs	C_{base}	64,981,000.00	€

E.1.3. Results

The on-design optimization is done with three different environmental conditions, which represents the standard, best and worst scenario. The optimization is discussed in Chapter 4 and the results of the case with a plant designed for the condition of $15MW_{gross}@\Delta T22K$ and $T_H = 27^\circ C$ are given in section 4.7. In this subsection, the optimization results of the other scenario's will be presented.

Plant 1: $15MW_{gross}@\Delta T20K$ and $T_H = 25^\circ C$

In this paragraph, the plant, which is designed for the condition of $15MW_{gross}@\Delta T20K$ will be presented. Figure E.1 shows the convergence of the optimization run. Figure E.2 gives an overview of the optimized operating conditions of the OTEC cycle. Figure E.3 shows an overview of the optimum cost per component and finally figure E.4 shows the optimization variables convergence.

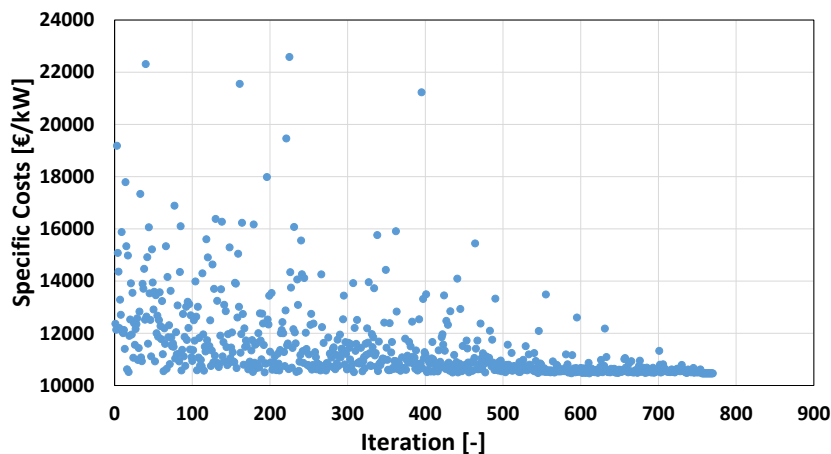


Figure E.1: Convergence of the optimization run. Single stage ORC for $15MW_{gross}@\Delta T20K$ and $T_H = 25^\circ C$.

Kalina cycle

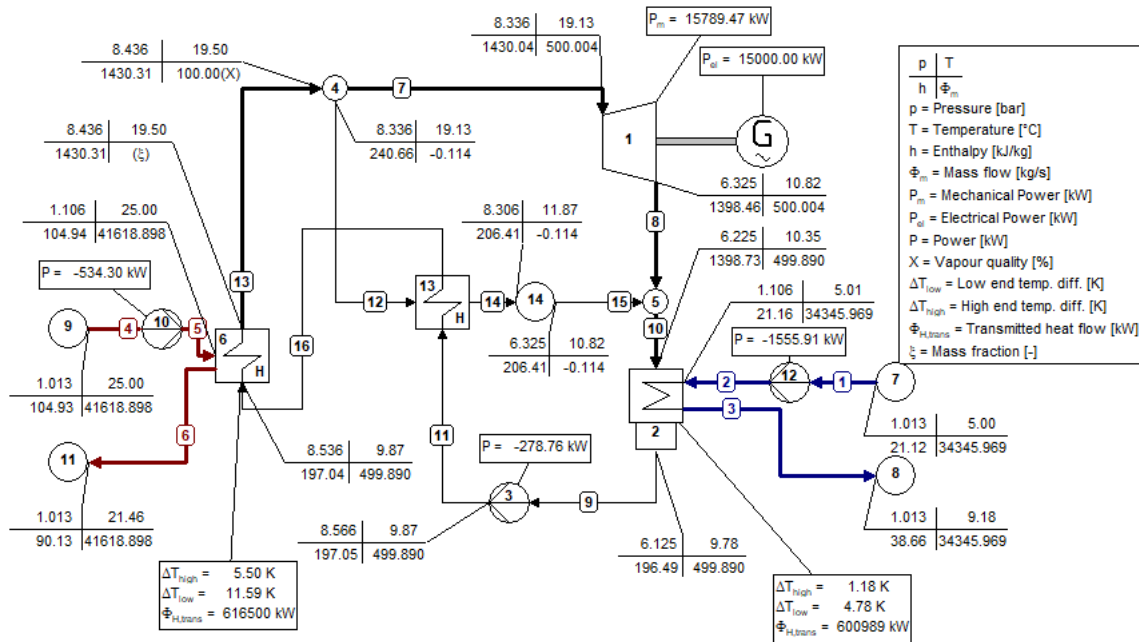


Figure E.2: Cycle tempo model showing the optimal result for the single stage ORC for $15MW_{gross}$ at ΔT_{20K} and $T_H = 25^\circ C$.

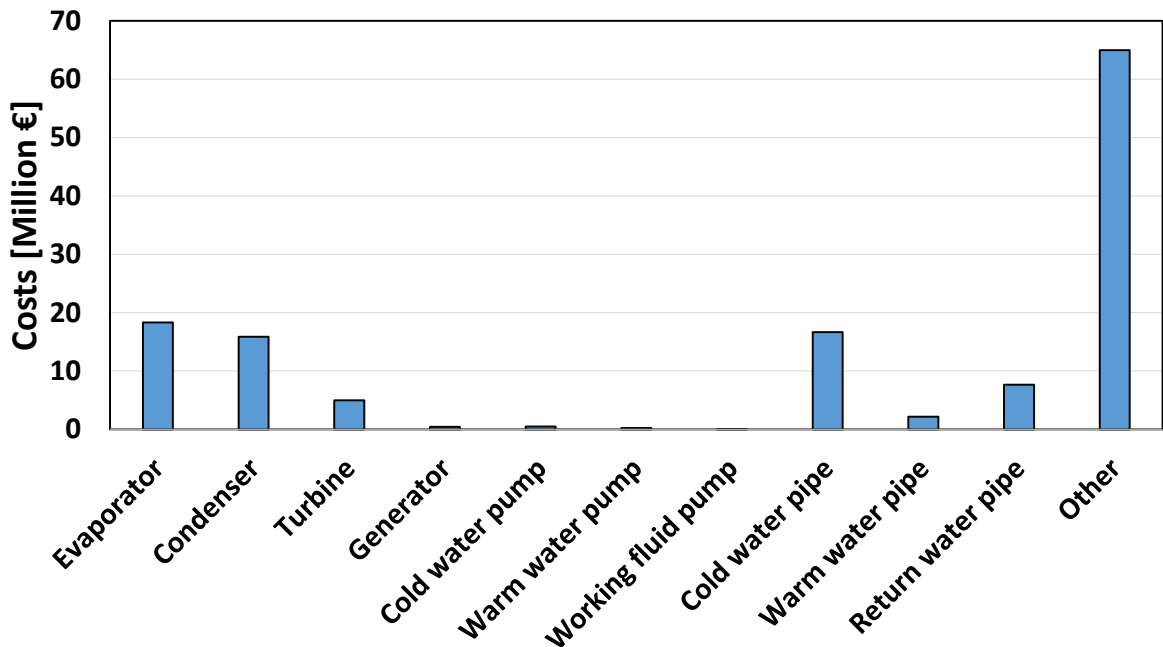


Figure E.3: Cost per component overview for the optimal result for the single stage ORC for $15MW_{gross}$ at ΔT_{20K} and $T_H = 25^\circ C$.

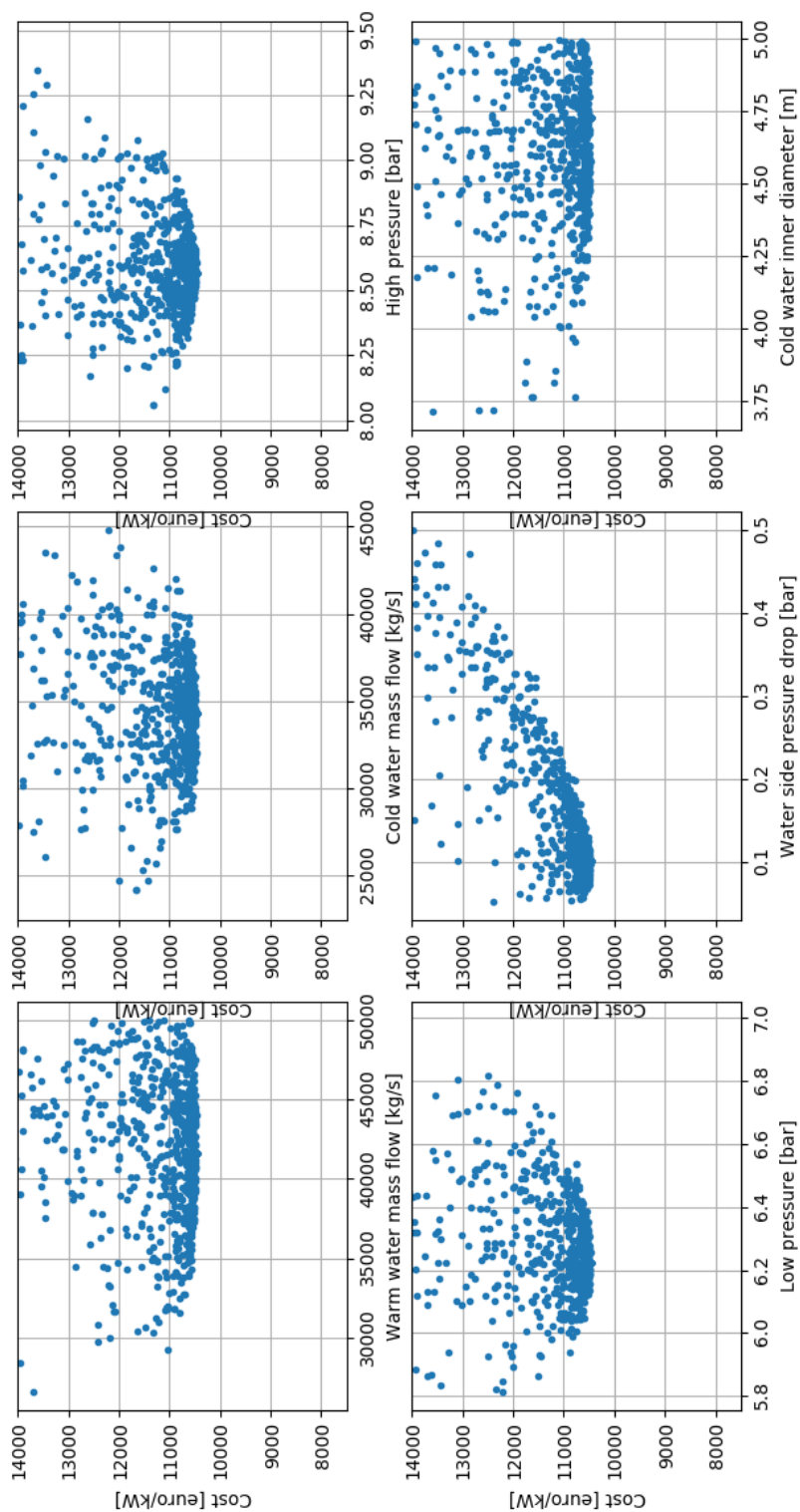


Figure E.4: Optimization results for the single stage ORC for $15MW_{gross}$ at ΔT_{20K} and $T_H = 25^\circ C$.
 Every subplot shows a single optimization variable vs specific cost.

Plant 3: $15MW_{gross}@\Delta T24K$ and $T_H = 29^\circ C$

In this paragraph, the plant, which is designed for the condition of $15MW_{gross}@\Delta T24K$ will be presented. Figure E.5 shows the convergence of the optimization run. Figure E.6 gives an overview of the optimized operating conditions of the OTEC cycle. Figure E.7 shows an overview of the optimum cost per component and finally figure E.8 shows the optimization variables convergence.

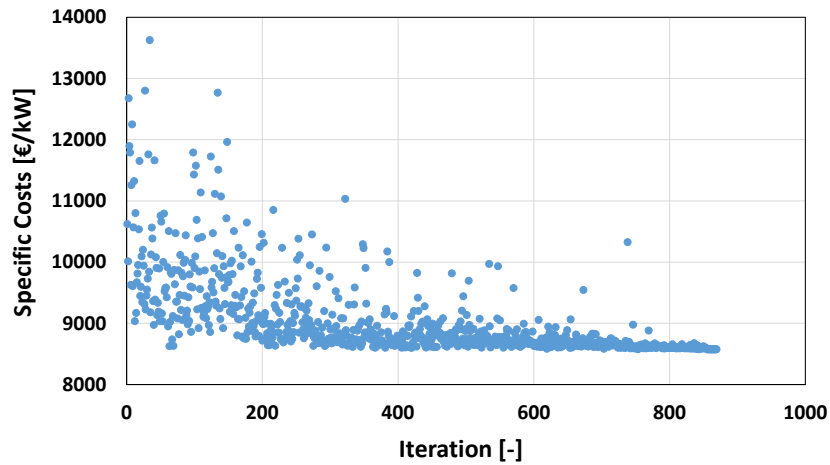


Figure E.5: Convergence of the optimization run. Single stage ORC for $15MW_{gross}@\Delta T24K$ and $T_H = 29^\circ C$.

Kalina cycle

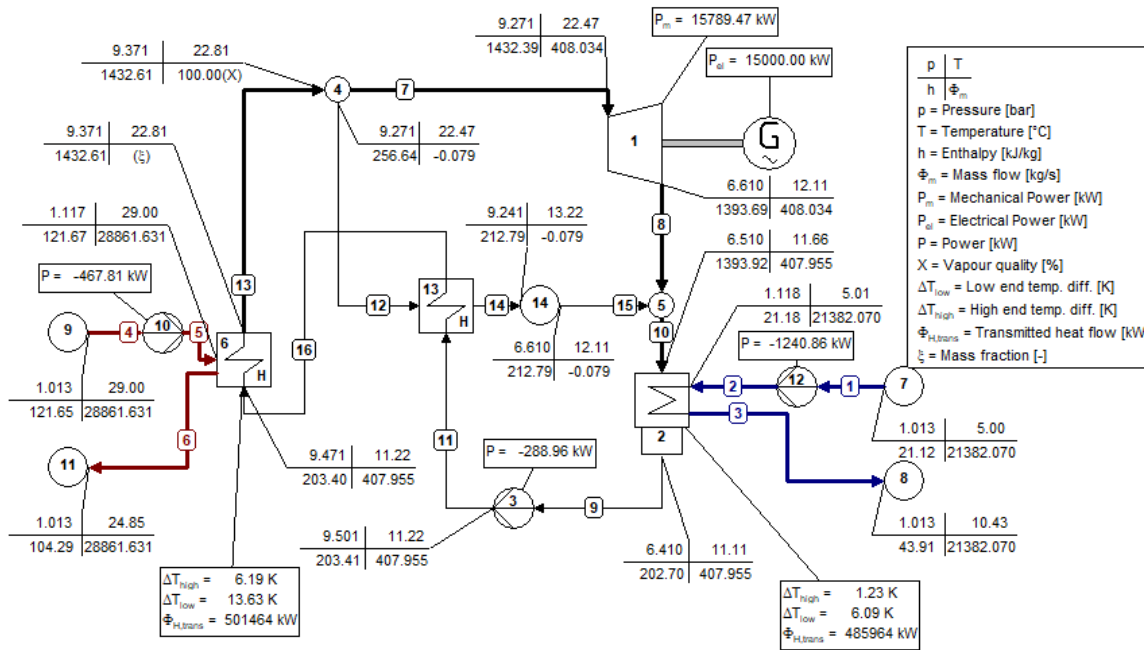


Figure E.6: Cycle tempo model showing the optimal result for the single stage ORC for $15MW_{gross}$ at ΔT_{24K} and $T_H = 29^{\circ}C$.

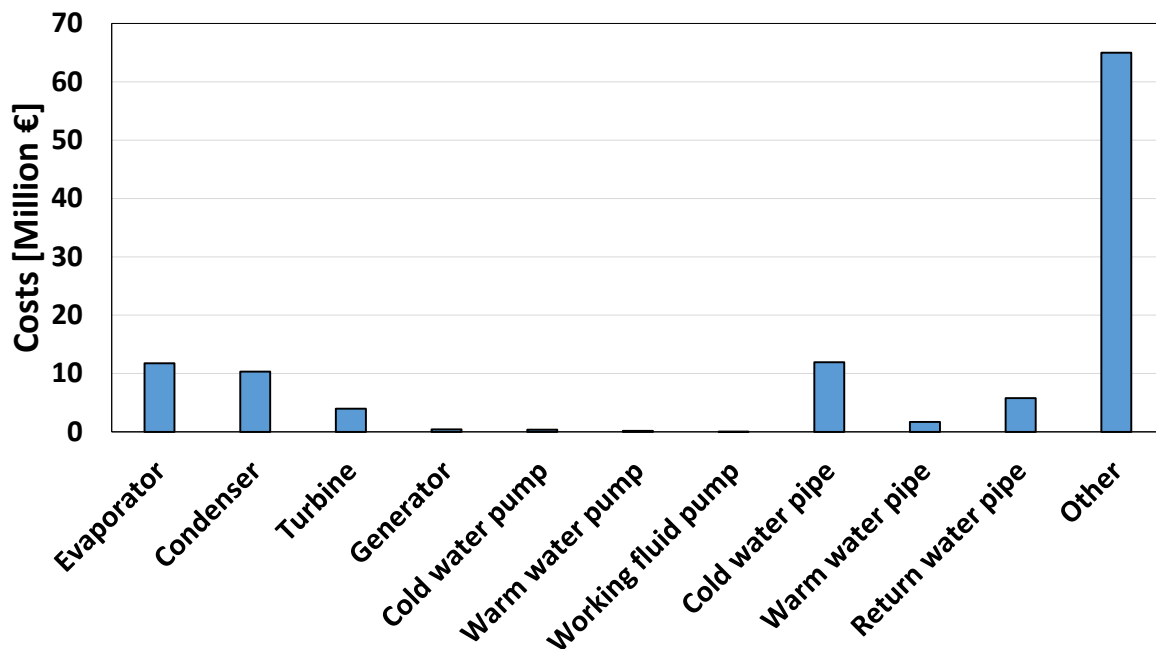


Figure E.7: Cost per component overview for the optimal result for the single stage ORC for $15MW_{gross}$ at ΔT_{24K} and $T_H = 29^{\circ}C$.

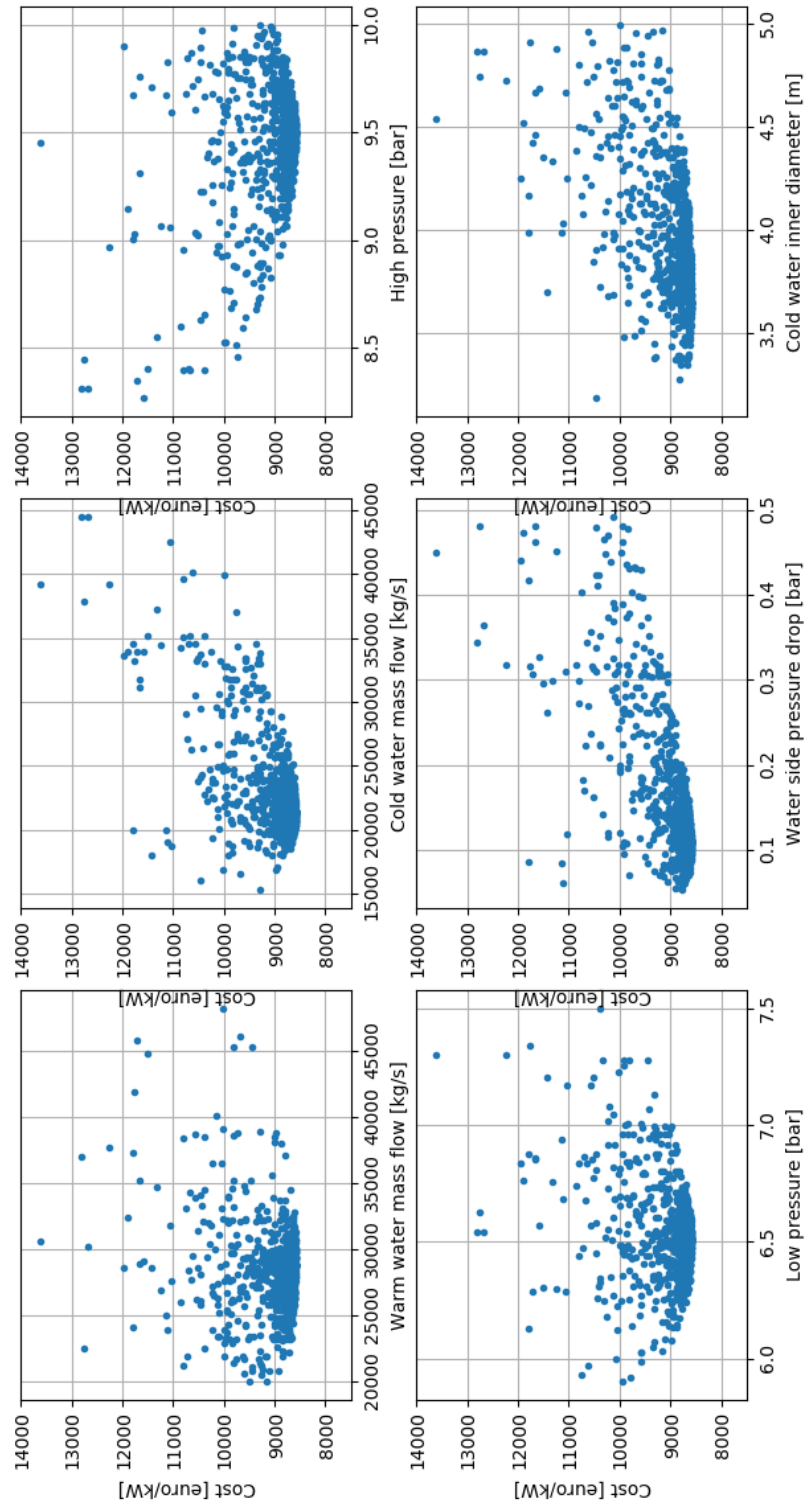


Figure E.8: Optimization results for the single stage ORC for 15MW_{gross} at ΔT_{24K} and $T_H = 29^\circ\text{C}$. Every subplot shows a single optimization variable vs specific cost.

E.2. Off-design model

In this section, the components of the Python off-design model, which require additional model information, will be discussed.

E.2.1. Recuperator

The evaporator can cause that the outlet of the evaporator is fully evaporate. That means that there is no liquid present anymore in the separator. The stream to the recuperator is in this situation zero. In this situation, the system behaves as an ordinary ORC. Since the flow through the recuperator is zero, one control of the mass flow is performed at the beginning of the recuperator. In these situations, the heat transfer is almost zero and therefore can be neglect. The check of the mass flow ensures that the flow never comes close to the minimum mass flow, which is required for the heat transfer correlation used in the recuperator. The recuperator requires a minimal mass flow through the system, so that the heat transfer correlation is valid or another correlation should be selected. The minimum mass flow is derived from the validated Reynolds number, see equation E.8.

$$\dot{m}_{min} = \frac{Re_{min,correlation} * A_f * N_{ch,hot} * \mu}{d_h} \quad (E.8)$$

E.2.2. Heat exchangers

In this thesis, some initial input values are not discussed of the off-design model. These values are necessary to execute a run of the model. Mostly, they are necessary as initial guess. The values are given in table E.2.

Table E.2: Initial values, which are necessary for the model

Component	Parameter	Description	Value	Unit
Evaporator	q_{out}	Guess	1.0	–
	ΔT_{warm}	Guess	0.3	K
	$m_{v,in}$	Guess	0	$\frac{kg}{s}$
Condenser	ΔT_{cold}	Guess	2.5	K
	q_{out}	Guess	0	–
	$m_{v,out}$	Guess	0	$\frac{kg}{s}$
	$T_{subcooling}$	Initial	1	K
	$h_{out\ of\ range}$	Boundary	30	$\frac{kJ}{kg}$

Iteration loop of the heat exchangers

In the heat exchanger algorithm, an initial value is necessary to calculate the outlet temperature of the water flow. For the evaporator the warm outlet flow and for the condenser the cold outlet flow. This temperature is determined by the initial temperature difference and the inlet temperature, see equation E.9 for the evaporator and equation E.10 for the condenser. This temperature difference is the optimization parameter in the algorithm of the heat exchanger.

$$T_{warm,out} = T_{warm,in} - \Delta T_{warm} \quad (E.9)$$

$$T_{cold,out} = T_{cold,in} + \Delta T_{cold} \quad (E.10)$$

Fast calculation method

In the algorithm of the heat exchanger, there is an option to select the fast calculation method. In the fast calculation method, the outlet properties are assumed with a guess value. An initial value of the outlet quality, q_{out} , is used to determine the outlet properties. The value of the outlet quality is overruled with the quality of the previous iteration. The error of the estimated value is less present if the iteration loop is going on. Next to the outlet quality, the vapor mass flow of the inlet of the evaporator inlet and the outlet of the condenser is given. This value is necessary so that no error is occurred in the equation of state. These values are both zero, since no vapor should be present in these in- or out-lets.

Subcooling

Sub-cooling in the condenser can occur, but the degree of sub-cooling is limited. Therefore, a maximum value above the temperature of the inlet of the cold stream determine the minimum temperature of the outlet of working fluid stream, see equation E.11.

$$T_{warm,out,sat} = T_{cold,in} + T_{sub-cooling} \quad (E.11)$$

Unrealistic regime

In the condenser the enthalpy of the working fluid outlet stream is checked, whereby the value is executed if it is realistic. A boundary value, $h_{out\ of\ range}$, is used to check if the enthalpy is higher than the specified value. Otherwise the iteration is not successful and a new iteration is performed.

Correlation range

Each correlation has a specific validation range. Extrapolation of a correlation is possible, but this is accompanied by uncertainty. Therefore, a regime check is executed at every correlation which is used. The user of the model has the freedom to determine whether the boundaries should be adjusted beyond the validation range.

Temperature guess in the evaporator and condenser

The algorithm of the heat exchangers uses a temperature guess of the outlet of the water side. The guess is optimized, so that after all heat transfer calculation the heat transfer area, which is imposed equals the calculated heat transfer area. An initial guess of this temperature guess is required. During the iteration loop, the value is adjusted in the direction so that the area error is converged. Several checks of the temperature guess have been added to the model, to speed up the iteration and to ensure the convergence goes well. If the temperature guess results in a too high heat transfer, the area error should be positive and vice versa. Therefore, the following checks are implemented with the corresponding area error. These checks have a positive effect on the convergence. Another advantage of these checks is that less errors occur in the subsequent calculations. As a result, less iterations go wrong and even unrealistic behaviour is better filtered out.

For the evaporator:

$$T_{water,out} > T_{water,in} \rightarrow (T_{wf,in} - T_{water,out}) \rightarrow [\text{negative}]$$

$$T_{water,out} \leq T_{wf,in} \rightarrow (T_{water,in} - T_{water,out}) \rightarrow [\text{positive}]$$

$$T_{wf,cv} \geq T_{water,cv} \rightarrow (T_{water,in} - T_{water,out}) \rightarrow [\text{positive}]$$

For the condenser:

$$T_{water,out} < T_{water,in} \rightarrow (T_{water,out} - T_{wf,in}) \rightarrow [\text{negative}]$$

$$T_{water,out} \geq T_{wf,in} \rightarrow (T_{water,out} - T_{water,in}) \rightarrow [\text{positive}]$$

$$T_{water,cv} > T_{wf,cv} \rightarrow (T_{water,out} - T_{water,in}) \rightarrow [\text{positive}]$$

E.2.3. perfect insulation or separation in the separator

Kuikhoven [52] concludes that the difference between the assumption of perfect separation or the assumption of perfect insulation has less effect on the separator outputs, but for the orifice outlet temperature it has a significant effect. In the thesis of Kuikhoven, the validation of the separator is done for different ammonia concentrations. Kuikhoven concludes that perfect insulation applies above perfect separation, since the trend of the orifice outlet temperature is correct. An extra check of the difference between the perfect insulation or separation is executed for the pure ammonia case, since the focus will be on pure ammonia. Pure ammonia experiments are compared with off-design model computations. Note that the heat input of all experiments are not equal. Therefore, the trend of the points insinuates nothing. Figure E.9 shows the comparison of the measured value and the predicted value with the model for the separator.

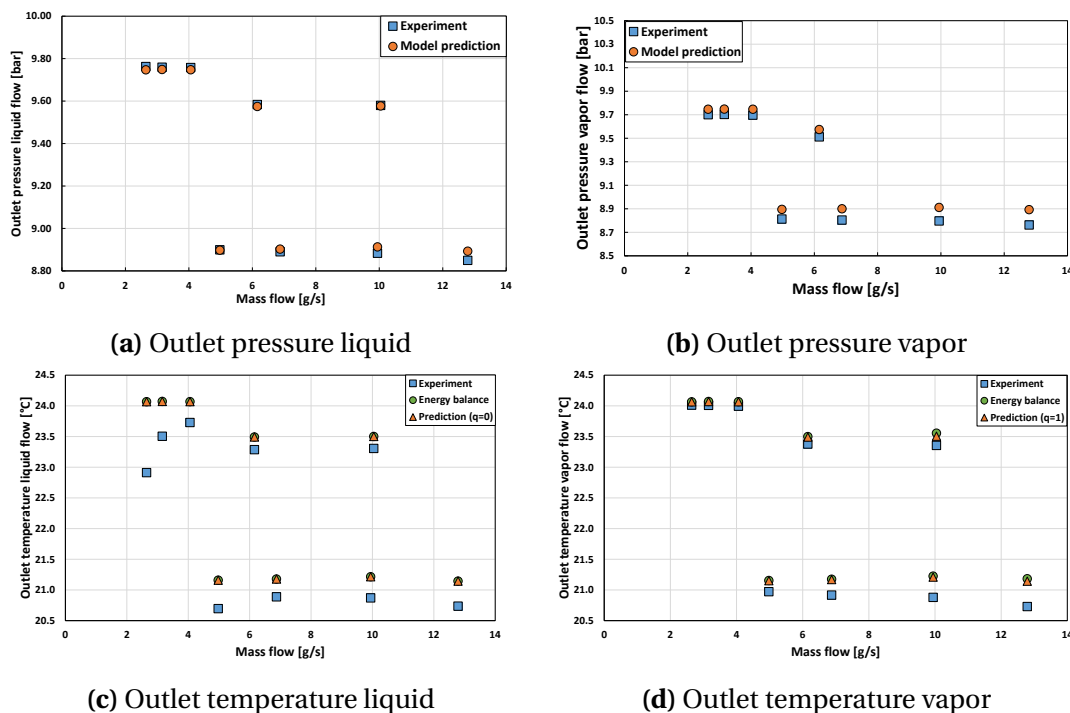
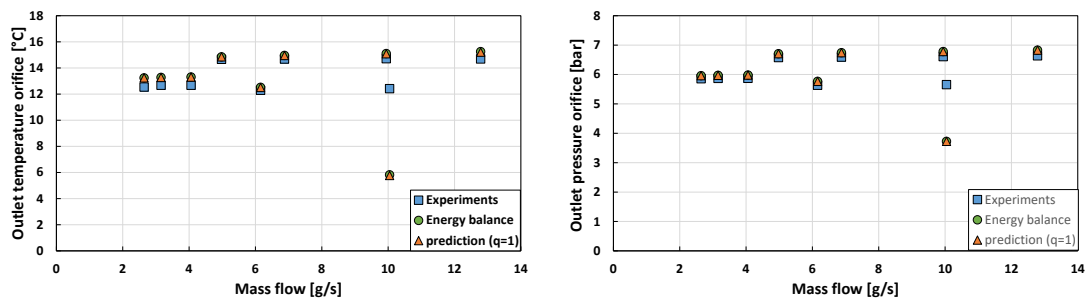


Figure E.9: Measured versus predicted values with the model for the separator. Note that the heat input of all tests is not equal, so the trends do not symbolize anything.

Figures E.9a and E.9b show the outlet pressures of the liquid and vapor flow. It can be concluded that the pressure calculation of the separator is correct, since the average deviation is 0.16% for the liquid flow and 1.7% for the vapor flow. It can be concluded that the

outlet pressure of the vapor flow is overestimated, this was also concluded by Kuikhoven. Kuikhoven supposed that there was some energy loss to the surrounding. Next to the pressure, figures E.9c and E.9d show the outlet temperatures of the liquid and vapor flow. The differences between calculating the outlet temperature with the energy balance or saturated condition, which means $q = 1$ or $q = 0$, is negligible. The deviation of the temperature is 1.99% for the liquid temperature and 0.86% for the vapor temperature in both cases. It can be concluded that the difference between perfect insulation or separation seems no longer have an effect for pure ammonia.

As already mentioned, the difference between perfect separation and insulation should be noticed in the outlet conditions of the orifice. Figures E.10a and E.10b show the outlet conditions of the orifice of the experiments versus the model predictions. The difference of the methods is no longer significant, since pure ammonia is used.



(a) Outlet temperature

(b) Outlet pressure

Figure E.10: Measured versus predicted values with the model for the orifice. Note that one measurement is not correct.

E.3. Optimum off-design pressure drop

Figures E.11 and E.12 show the optimization of the off-design performance of plant 1 and 3. The numbers at the points are the relative opening factor of the vanes

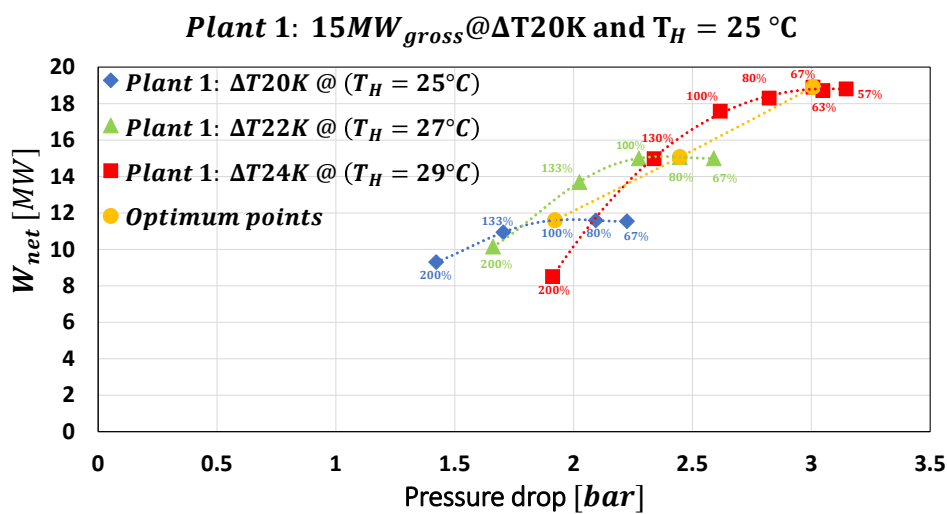


Figure E.11: Optimization of plant 1 in specific environmental conditions. ◆ shows the optimization with a warm seawater temperature of 25 °C, ▲ of 27 °C, ■ of 29 °C and ● shows the optimum operating points. The numbers at the point are the relative opening factor of the vane, $\frac{1}{f_{VTG}}$.

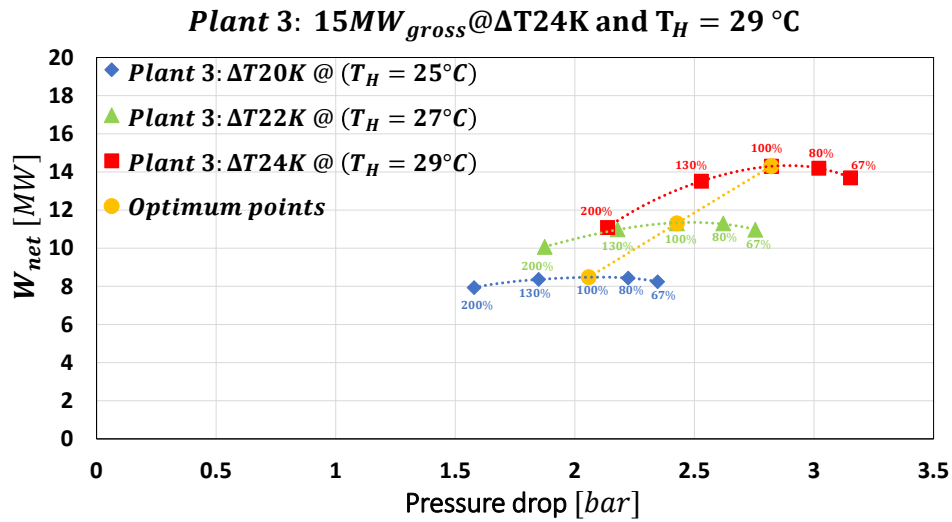
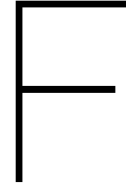


Figure E.12: Optimization of plant 3 in specific environmental conditions. \blacklozenge shows the optimization with a warm seawater temperature of $25^\circ C$, \blacktriangle of $27^\circ C$, \blacksquare of $29^\circ C$ and \bullet shows the optimum operating points. The numbers at the point are the relative opening factor of the vane, $\frac{1}{f_{VTG}}$.



Model decomposition

The model is decomposed into several sub components and for each components the in and outputs are different. In this appendix, an overview of the inputs and outputs per components are given. The state points number corresponds with those given in the process flow diagram, see figure 5.1.

F.1. Heat exchangers

Table E1 gives the inputs and outputs of the evaporator, table E2 for the condenser and table E3 for the recuperator. Be aware that the recuperator is part of the backward loop, so the known parameters are from the outlet of the recuperator for the base solution stream.

Table E.1: Input and outputs of the evaporator

Known inputs			Wanted outputs		
Parameter	Symbol	Unit	Parameter	Symbol	Unit
Inlet water temperature	T_{W1}	[K]	Outlet vapour quality working fluid	q_2	[-]
Inlet water enthalpy	h_{W1}	[J/kg]	Outlet pressure working fluid	P_2	[Pa]
Inlet water pressure	P_{W1}	[Pa]	Outlet temperature working fluid	T_2	[K]
Inlet working fluid temperature	T_1	[K]	Input heat	\dot{Q}_{evap}	[W]
Inlet working fluid pressure	P_1	[Pa]	Outlet water temperature	T_{W2}	[K]
Working fluid mass flow	\dot{m}_1	[kg/s]	Outlet water pressure	P_{W2}	[Pa]
Water mass flow	\dot{m}_{W1}	[kg/s]	Pressure drop sea side	ΔP_{sea}	[Pa]
Heat transfer area	A_{evap}	[m ²]			
Pressure drop working fluid side	ΔP_{wf}	[Pa]			

Table E.2: Input and outputs of the condenser.

Known inputs			Wanted outputs		
Parameter	Symbol	Unit	Parameter	Symbol	Unit
Inlet water temperature	T_{W3}	[K]	Outlet vapour quality working fluid	q_7	[-]
Inlet water enthalpy	h_{W3}	[J/kg]	Outlet pressure working fluid	P_7	[Pa]
Inlet water pressure	P_{W3}	[Pa]	Outlet temperature working fluid	T_7	[K]
Inlet working fluid temperature	T_6	[K]	Heat rejected	\dot{Q}_{cond}	[W]
Inlet working fluid pressure	P_6	[Pa]	Outlet water temperature	T_{W4}	[K]
Working fluid mass flow	\dot{m}_6	[kg/s]	Outlet water pressure	P_{W4}	[Pa]
Water mass flow	\dot{m}_{W3}	[kg/s]	Degree of sub-cooling	ΔT_{sub}	[K]
Heat transfer area	A_{cond}	[m ²]	Pressure drop sea side	ΔP_{sea}	[Pa]
Inlet quality	q_6	[-]			
Pressure drop working fluid side	ΔP_{wf}	[Pa]			

Table F.3: Input and outputs of the recuperator.

Known inputs			Wanted outputs		
Parameter	Symbol	Unit	Parameter	Symbol	Unit
Inlet weak solution temperature	T_{3L}	[K]	Outlet pressure weak solution	P_{4L}	[Pa]
Inlet weak solution enthalpy	h_{3L}	[J/kg]	Outlet temperature weak solution	T_{4L}	[K]
Inlet weak solution pressure	P_{3L}	[Pa]	Inlet temperature base solution	T_8	[K]
Outlet base solution temperature	T_1	[K]	Inlet pressure base solution	P_8	[Pa]
Outlet base solution pressure	P_1	[Pa]	Heat recovered	Q_{recu}	[W]
Base solution mass flow	\dot{m}_1	[kg/s]			
Weak solution mass flow	\dot{m}_{3L}	[kg/s]			
Heat transfer area	A_{recu}	[m ²]			
Pressure drop weak solution side	ΔP_{weak}	[Pa]			
Pressure drop base solution side	ΔP_{base}	[Pa]			

F.2. Other components

The other components, which are part of the model, have also some in and outputs. In the tables F.4, the known inputs and wanted outputs are given for the separator, turbine, valve, mixer, working fluid pump and the sea water pipes.

Table F.4: Input and outputs of the other components

Known inputs			Wanted outputs		
Parameter	Symbol	Unit	Parameter	Symbol	Unit
Separator					
Inlet temperature	T_2	[K]	Liquid outlet temperature	T_{3L}	[K]
Inlet pressure	P_2	[Pa]	Liquid outlet pressure	P_{3L}	[Pa]
Mass flow	\dot{m}_2	[kg/s]	Vapour outlet temperature	T_{3V}	[K]
			Vapour outlet pressure	P_{3V}	[Pa]
			Liquid outlet mass flow	\dot{m}_{3L}	[kg/s]
			Vapour outlet mass flow	\dot{m}_{3V}	[kg/s]
			Liquid outlet concentration	c_{3L}	[-]
			Vapour outlet concentration	c_{3V}	[-]
Turbine/Orifice					
Inlet temperature	T_{3V}	[K]	Outlet temperature	T_{4V}	[K]
Inlet pressure	P_{3V}	[Pa]	Outlet pressure	P_{4V}	[Pa]
Mass flow	\dot{m}_{3V}	[kg/s]	Isentropic efficiency	η_{is}	[-]
			Turbine work	W_{turb}	[W]
			Pressure drop	ΔP_{turb}	[Pa]
Valve					
Inlet temperature	T_{4L}	[K]	Outlet temperature	T_5	[K]
Inlet pressure	P_{4L}	[Pa]			
Outlet pressure	P_{4V}	[Pa]			
Mass flow	\dot{m}_{4L}	[kg/s]			
Mixer					
Inlet temperature vapor stream	T_{4V}	[K]	Outlet temperature	T_6	[K]
Inlet pressure vapor stream	P_{4V}	[Pa]	Outlet pressure	P_6	[Pa]
Inlet temperature liquid stream	T_5	[K]			
Inlet pressure liquid stream	P_5	[Pa]			
Mass flow vapor stream	\dot{m}_{4V}	[kg/s]			
Mass flow liquid stream	\dot{m}_5	[kg/s]			
Working fluid pump					
Outlet temperature	T_8	[K]	Inlet Temperature	T_7	[K]
Outlet enthalpy	h_8	[J/kg]	Inlet enthalpy	h_7	[J/kg]
Outlet pressure	P_8	[Pa]	Pump required power	W_{pump}	[W]
Inlet pressure	P_7	[Pa]			
Mass flow	\dot{m}_7	[kg/s]			
Sea water pipes					
Inlet water temperature	$T_{W,in}$	[K]	Outlet temperature	$T_{W,out}$	[K]
Inlet water pressure	$P_{W,in}$	[Pa]	Outlet pressure	$P_{W,out}$	[Pa]
Water mass flow	\dot{m}_W	[kg/s]			

Bibliography

- [1] Alfa Laval, AlfaLaval - Gasket Plate Heat Exchanger. <http://www.wassertech.net/content/view/42/29/lang,thai/>. (Accessed on 04/05/2018).
- [2] Large Steam System Condensers. https://www.engineersedge.com/heat_exchanger/large_steam_condenser.htm.
- [3] World Ocean Atlas 2013 version 2. <https://www.nodc.noaa.gov/OC5/woa13/>. (Accessed on 07/27/2018).
- [4] *Reference Guide Cycle Tempo, Release 5, ASIMPTOTE, Advanced SIMulation Programs for TOTal Energy systems*. TU Delft, ASIMPTOTE, 2011.
- [5] Gianfranco Angelino and Piero Colonna Di Paliano. Multicomponent working fluids for organic Rankine cycles (ORCs). *Energy*, 23(6):449–463, 1998.
- [6] Marco Astolfi and Ennio Macchi. Efficiency correlations for axial flow turbines working with non-conventional fluids. In *Proceedings of the 3rd International Seminar on ORC Power Systems, Brussels, Belgium*, pages 12–14, 2015.
- [7] Marco Astolfi, Matteo C Romano, Paola Bombarda, and Ennio Macchi. Binary ORC (Organic Rankine Cycles) power plants for the exploitation of medium–low temperature geothermal sources–Part B: Techno-economic optimization. *Energy*, 66:435–446, 2014.
- [8] VDI Heat Atlas. VDI-Gesellschaft Verfahrenstechnik und Chemieingenieurwesen, 2010.
- [9] Zahid H Ayub. Plate heat exchanger literature survey and new heat transfer and pressure drop correlations for refrigerant evaporators. *Heat transfer engineering*, 24(5): 3–16, 2003.
- [10] R Blokker. Cost reduction of Ocean Thermal Energy Conversion- Exploratory analysis of a Supercritical Rankine cycle. *Mbe thesis, Delft University of Technology*, 2012.
- [11] Godfrey Boyle. *Renewable energy: power for a sustainable future*. Oxford University Press, 1996.
- [12] B Cable. NAVFAC OTEC System Design Report. *CDRL A003, Lockheed Martin MS2*, 2010.
- [13] Francesco Calise, Claudio Capuozzo, Alberto Carotenuto, and Laura Vanoli. Thermoeconomic analysis and off-design performance of an organic Rankine cycle powered by medium-temperature heat sources. *Solar Energy*, 103:595–609, 2014.

- [14] Yunus A Cengel and Michael A Boles. *Thermodynamics: an engineering approach. Sea*, 1000:8862, 2002.
- [15] Huijuan Chen, D Yogi Goswami, and Elias K Stefanakos. A review of thermodynamic cycles and working fluids for the conversion of low-grade heat. *Renewable and sustainable energy reviews*, 14(9):3059–3067, 2010.
- [16] Piero Colonna. Cycle-Tempo. <http://www.asimptote.nl/software/cycle-tempo/>, 2011. (Accessed on 07/19/2018).
- [17] James R Couper, W Roy Penney, and James R Fair. *Chemical Process Equipment-Selection and Design (Revised 2nd Edition)*. Gulf Professional Publishing, 2009.
- [18] HRM Craig and HJA Cox. Performance estimation of axial flow turbines. *Proceedings of the Institution of Mechanical Engineers*, 185(1):407–424, 1970.
- [19] Luca Da Lio, Giovanni Manente, and Andrea Lazzaretto. New efficiency charts for the optimum design of axial flow turbines for organic Rankine cycles. *Energy*, 77:447–459, 2014.
- [20] M.E. Dahlgren. Experimental study of transport phenomena in the condenser of an OTEC-cycle. *Master's thesis, Delft University of Technology*, 2018.
- [21] P. R. Dankerlui. Ammonia Turbine Design for Ocean Thermal Energy Conversion systems. *Master's thesis, Delft University of Technology*, 2016.
- [22] Paul Denissen, Thomas Bjelkeman-Petterson, and Richard Meyer. OTEC foundation. <http://otecfoundation.org/otec/index.html>, 2016. (Accessed on 04/23/2018).
- [23] Rémi Dickes, Olivier Dumont, Ludovic Guillaume, Sylvain Quoilin, and Vincent Lemort. Charge-sensitive modelling of organic Rankine cycle power systems for off-design performance simulation. *Applied Energy*, 212:1262–1281, 2018.
- [24] Vincent D Donowski and Satish G Kandlikar. Correlating evaporation heat transfer coefficient of refrigerant R-134a in a plate heat exchanger. In *Engineering Foundation Conference on Pool and Flow Boiling, Alaska*, 2000.
- [25] A Fenghour, William A Wakeham, V Vesovic, JTR Watson, J Millat, and E Vogel. The viscosity of ammonia. *Journal of Physical and Chemical Reference Data*, 24(5):1649–1667, 1995.
- [26] Karen Anne Finney. Ocean thermal energy conversion. *Guelph Engineering Journal*, 1:17–23, 2008.
- [27] WW Focke, J Zachariades, and I Olivier. The effect of the corrugation inclination angle on the thermohydraulic performance of plate heat exchangers. *International Journal of Heat and Mass Transfer*, 28(8):1469–1479, 1985.
- [28] Eric Gaba. Carnot heat engine 2 - Carnot heat engine - Wikipedia. https://en.wikipedia.org/wiki/Carnot_heat_engine#/media/File:Carnot_heat_engine_2.svg, 2006. (Accessed on 09/09/2018).

- [29] Roberto Gabbrielli. A novel design approach for small scale low enthalpy binary geothermal power plants. *Energy Conversion and Management*, 64:263–272, 2012.
- [30] EN Ganic and J Wu. Comparative study of working fluids for otec power plants. Technical report, Illinois Univ., Chicago (USA). Dept. of Energy Engineering, 1979.
- [31] F. Geschiere. OTEC condenser heat exchanger analysis. *Master's thesis, Delft University of Technology*, 2018.
- [32] Jerome C Glenn, Theodore J Gordon, and Elizabeth Florescu. State of the future. *Washington DC*, 2014.
- [33] R. J. Goudriaan. Performance analysis of ammonia and ammonia-water as working fluids for Ocean Thermal Energy Conversion power plants. *Master's thesis, Delft University of Technology*, 2017.
- [34] V. Gudjonsdottir. Analysis of external influences on an OTEC cycle. *Master's thesis, Delft University of Technology*, 2015.
- [35] Jorge AW Gut and José M Pinto. Optimal configuration design for plate heat exchangers. *International Journal of Heat and Mass Transfer*, 47(22):4833–4848, 2004.
- [36] Fredrik Haglind. Variable geometry gas turbines for improving the part-load performance of marine combined cycles—gas turbine performance. *Energy*, 35(2):562–570, 2010.
- [37] Cesare Hall and S Larry Dixon. *Fluid mechanics and thermodynamics of turbomachinery*. Butterworth-Heinemann, 2013.
- [38] Dongshuai Hu, Saili Li, Ya Zheng, Jiangfeng Wang, and Yiping Dai. Preliminary design and off-design performance analysis of an Organic Rankine Cycle for geothermal sources. *Energy Conversion and Management*, 96:175–187, 2015.
- [39] Marcia L Huber, Richard A Perkins, A Laesecke, Daniel G Friend, Jan V Sengers, Marc J Assael, Ifigenia N Metaxa, Eckhard Vogel, R Mareš, and Kiyoshi Miyagawa. New international formulation for the viscosity of H₂O. *Journal of Physical and Chemical Reference Data*, 38(2):101–125, 2009.
- [40] Marcia L Huber, Richard A Perkins, Daniel G Friend, Jan V Sengers, Marc J Assael, Ifigenia N Metaxa, Kiyoshi Miyagawa, Robert Hellmann, and Eckhard Vogel. New international formulation for the thermal conductivity of H₂O. *Journal of Physical and Chemical Reference Data*, 41(3):033102, 2012.
- [41] Eric Jones, Travis Oliphant, Pearu Peterson, et al. SciPy: Open source scientific tools for Python, 2001–. URL <http://www.scipy.org/>. [Online; accessed <today>].
- [42] Marc Judes and George Tsatsaronis. Design optimization of power plants by considering multiple partial load operation points. In *ASME 2007 International Mechanical Engineering Congress and Exposition*, pages 217–225. American Society of Mechanical Engineers, 2007.

- [43] Marc Jüdes, Stefan Vigerske, and George Tsatsaronis. Optimization of the design and partial-load operation of power plants using mixed-integer nonlinear programming. In *Optimization in the energy industry*, pages 193–220. Springer, 2009.
- [44] Alexander I Kalina. Generation of energy by means of a working fluid, and regeneration of a working fluid, August 31 1982. US Patent 4,346,561.
- [45] Derviş Karaboğa and Selçuk Ökdem. A simple and global optimization algorithm for engineering problems: differential evolution algorithm. *Turkish Journal of Electrical Engineering & Computer Sciences*, 12(1):53–60, 2004.
- [46] KR Keeley. A theoretical investigation of the part-load characteristics of LP steam turbine stages. *CEGB memorandum RD/L/ES0817 M*, 88, 1988.
- [47] Dong-Seon Kim. *Solar absorption cooling*. PhD thesis, TU Delft, Delft University of Technology, 2007.
- [48] J.A. Kirkenier. Techno-economic optimization of Organic Rankine Cycles using working fluid mixtures for 10 to 25 MW OTEC power plants. *Master's thesis, Delft University of Technology*, 2014.
- [49] B. J. Kleute. System sensitivity and cold water pipe analysis of a 10 MW offshore OTEC - ocean thermal energy conversion plant. *Master's thesis, Delft University of Technology*, 2014.
- [50] B. J. Kleute and M. Vroom. Offshore Ocean Thermal Energy Conversion- Feasibility study of a 10 MW installation. *Technical report, Bluerise B.V.*, 2014.
- [51] C. H. Kostors and S. P. Vincent. Ammonia Turbine Design for Ocean Thermal Energy Conversion (OTEC) Plants. *Journal of Solar Energy Engineering*, 103, 1981.
- [52] L. J. Kuikhoven. Influence of the ammonia concentration on the performance of OTEC power cycles. *Master's thesis, Delft University of Technology*, 2017.
- [53] Suriyan Laohalertdecha and Somchai Wongwises. The effects of corrugation pitch on the condensation heat transfer coefficient and pressure drop of R-134a inside horizontal corrugated tube. *International Journal of Heat and Mass Transfer*, 53(13):2924–2931, 2010.
- [54] Andrea Lazzaretto and Giovanni Manente. A new criterion to optimize ORC design performance using efficiency correlations for axial and radial turbines. *International Journal of Thermodynamics*, 17(3):192–200, 2014.
- [55] E Macchi and M Astolfi. Axial flow turbines for Organic Rankine Cycle applications. *Organic Rankine Cycle (ORC) Power Systems: Technologies and Applications*, page 299, 2016.
- [56] E Macchi and A Perdichizzi. Efficiency prediction for axial-flow turbines operating with nonconventional fluids. *Journal of engineering for power*, 103(4):718–724, 1981.

- [57] Holger Martin. A theoretical approach to predict the performance of chevron-type plate heat exchangers. *Chemical Engineering and Processing: Process Intensification*, 35(4):301–310, 1996.
- [58] Michael J Moran, Howard N Shapiro, Daisie D Boettner, and Margaret B Bailey. *Fundamentals of engineering thermodynamics*. John Wiley & Sons, 2010.
- [59] Leonid Moroz. Turbomachinery Blog - Working Fluids in Organic Rankine Cycles | SoftInWay | Turbomachinery blog. <http://blog.softinway.com/cn/working-fluid-in-organic-rankine-cycles/>, 01 2014. (Accessed on 09/04/2018).
- [60] A Mulero, I Cachadiña, and MI Parra. Recommended correlations for the surface tension of common fluids. *Journal of Physical and Chemical Reference Data*, 41(4):043105, 2012.
- [61] Sirko Ogriseck. Integration of kalina cycle in a combined heat and power plant, a case study. *Applied Thermal Engineering*, 29(14):2843–2848, 2009.
- [62] Naomi Oreskes, Kristin Shrader-Frechette, and Kenneth Belitz. Verification, validation, and confirmation of numerical models in the earth sciences. *Science*, 263(5147):641–646, 1994.
- [63] Milan V Petrovic and Walter Riess. Off-design flow analysis and performance prediction of axial turbines. In *ASME 1997 International Gas Turbine and Aeroengine Congress and Exhibition*, pages V001T03A013–V001T03A013. American Society of Mechanical Engineers, 1997.
- [64] Kenneth Price and Rainer Storn. Differential Evolution (DE) for continuous function optimization. <http://www1.icsi.berkeley.edu/~storn/code.html>, 1997. [Online; accessed 19-2-2018].
- [65] A Kai Qin, Vicky Ling Huang, and Ponnuthurai N Suganthan. Differential evolution algorithm with strategy adaptation for global numerical optimization. *IEEE transactions on Evolutionary Computation*, 13(2):398–417, 2009.
- [66] Kiyarash Rahbar, Saad Mahmoud, and Raya K Al-Dadah. Optimized efficiency maps and new correlation for performance prediction of ORC based on radial turbine for small-scale applications. In *3rd International Seminar on ORC Power Systems*, pages 12–14, 2015.
- [67] Kiyarash Rahbar, Saad Mahmoud, Raya K Al-Dadah, Nima Moazami, and Seyed A Mirhadizadeh. Review of organic Rankine cycle for small-scale applications. *Energy conversion and management*, 134:135–155, 2017.
- [68] A.S. Rattner and S. Garimella. Fast, stable computation of thermodynamic properties of ammonia-water mixtures. *International journal of refrigeration*, 2016.
- [69] Asok Ray. Dynamic modelling of power plant turbines for controller design. *Appl. Math. Modell*, 4(2):109–112, 1980.

- [70] Michael J. Reader-Harris. VENTURI METERS. <http://www.thermopedia.com/content/1241/>, 1991. (Accessed on 07/13/2018).
- [71] Nabakishore Satnami. Off design performance prediction of steam turbines. <https://www.slideshare.net/nabakishoresatnami/off-design-performance-prediction-of-steam-turbines>, January 2013. (Accessed on 10/10/2018).
- [72] Ramesh K Shah and Dusan P Sekulic. *Fundamentals of heat exchanger design*. John Wiley & Sons, 2003.
- [73] Raymond K Sinnott and Gavin Towler. *Chemical engineering design: SI Edition*. Elsevier, 2009.
- [74] Thomas Stocker. *Climate change 2013: the physical science basis: Working Group I contribution to the Fifth assessment report of the Intergovernmental Panel on Climate Change*. Cambridge University Press, 2014.
- [75] A Stodola. Steam and gas turbines, 1927. *New York, NY, USA, McGraw-Hill*, 1945.
- [76] Rainer Storn. On the usage of differential evolution for function optimization. In *Fuzzy Information Processing Society, 1996. NAFIPS., 1996 Biennial Conference of the North American*, pages 519–523. IEEE, 1996.
- [77] Bengt Sundén and Raj M Manglik. *Plate heat exchangers: design, applications and performance*, volume 11. Wit Press, 2007.
- [78] X Tao, MP Nuijten, and CA Infante Ferreira. Two-phase vertical downward flow in plate heat exchangers: flow patterns and condensation mechanisms. *International Journal of Refrigeration*, 2018.
- [79] R Tillner-Roth, F Harms-Watzenberg, and HD Baehr. Eine neue fundamentalgleichung für ammoniak. *DKV TAGUNGSBERICHT*, 20:67–67, 1993.
- [80] Elias Tsoutsanis, Nader Meskin, Mohieddine Benammar, and Khashayar Khorasani. Transient gas turbine performance diagnostics through nonlinear adaptation of compressor and turbine maps. *Journal of Engineering for Gas Turbines and Power*, 137(9): 091201, 2015.
- [81] R Tufeu, DY Ivanov, Y Garrabos, and B Le Neindre. Thermal conductivity of ammonia in a large temperature and pressure range including the critical region. *Berichte der Bunsengesellschaft für physikalische Chemie*, 88(4):422–427, 1984.
- [82] HJ Van Antwerpen and GP Greyvenstein. Use of turbines for simultaneous pressure regulation and recovery in secondary cooling water systems in deep mines. *Energy Conversion and Management*, 46(4):563–575, 2005.
- [83] L.M. Vonk. Working fluid selection for a diesel engine waste heat recovery ORC module. *Master's thesis, Delft University of Technology*, 2016.

- [84] Wolfgang Wagner and Andreas Pruß. The IAPWS formulation 1995 for the thermodynamic properties of ordinary water substance for general and scientific use. *Journal of physical and chemical reference data*, 31(2):387–535, 2002.
- [85] Philip P Walsh and Paul Fletcher. *Gas turbine performance*. John Wiley & Sons, 2004.
- [86] Jianyong Wang, Jiangfeng Wang, Yiping Dai, and Pan Zhao. Assessment of off-design performance of a Kalina cycle driven by low-grade heat source. *Energy*, 138:459–472, 2017.
- [87] Daniel Winkelmann. *Condensation of pure refrigerants and their zeotropic mixtures in plate heat exchangers*. Deutscher Kälte-und Klimatechnischer Verein, 2010.
- [88] Feng Xu and D Yogi Goswami. Thermodynamic properties of ammonia–water mixtures for power-cycle applications. *Energy*, 24(6):525–536, 1999.
- [89] Y-Y Yan and T-F Lin. Evaporation heat transfer and pressure drop of refrigerant R-134a in a plate heat exchanger. *Journal of Heat Transfer*, 121(1):118–127, 1999.
- [90] Yi-Yie Yan, Hsiang-Chao Lio, and Tsing-Fa Lin. Condensation heat transfer and pressure drop of refrigerant R-134a in a plate heat exchanger. *International Journal of Heat and Mass Transfer*, 42(6):993–1006, 1999.
- [91] Suk Young Yoon, Min Jae Kim, In Seop Kim, and Tong Seop Kim. Comparison of micro gas turbine heat recovery systems using orc and trans-critical co2 cycle focusing on off-design performance. *Energy Procedia*, 129:987–994, 2017.
- [92] Xinxin Zhang, Maogang He, and Ying Zhang. A review of research on the Kalina cycle. *Renewable and Sustainable Energy Reviews*, 16(7):5309–5318, 2012. doi: 10.1016/j.rser.2012.05.040.